FIRST-PRINCIPLES APPROACH TO SCREENING MULTI-COMPONENT METAL ALLOYS FOR HYDROGEN PURIFICATION MEMBRANES

A Thesis
Presented to
The Academic Faculty

by

Lymarie Semidey Flecha

In Partial Fulfillment
of the Requirements for the Degree
Doctor of Philosophy in the
School of Chemical & Biomolecular Engineering

Georgia Institute of Technology
December 2009

FIRST-PRINCIPLES APPROACH TO SCREENING MULTI-COMPONENT METAL ALLOYS FOR HYDROGEN PURIFICATION MEMBRANES

Approved by:

Dr. David S. Sholl, Advisor
School of Chemical & Biomolecular Engineering
Georgia Institute of Technology

Dr. Victor Breedveld
School of Chemical & Biomolecular Engineering
Georgia Institute of Technology

Dr. William Koros
School of Chemical & Biomolecular Engineering
Georgia Institute of Technology

Dr. Andrei G. Fedorov
School of Mechanical Engineering
Georgia Institute of Technology

Dr. Ron R. Chance
School of Chemical & Biomolecular Engineering
Georgia Institute of Technology

Date Approved: October 15, 2009

To my husband,

Paul,

For never letting me quit and always being there to support me.

To my brother,

Daniel,

Who would be so proud of me.

To my parents,

For always insisting upon education.

ACKNOWLEDGEMENTS

There are several people that I would wish to thank who have assisted me in the course of my research work and contributed to my career and personal development.

First I would like to express my gratitude to my thesis advisor, Dr. David S. Sholl for the confidence he has bestowed upon me, his guidance, and his overall support. Dr. Sholl has not only aided in my growth as a professional but as an overall human being by introducing both aspects of life through his own example.

I would like to thank former group members Dr. Rankin and Dr. Newsome for their kindness and friendship, but most of all for their patients. I would also like to thank current group members Dr. Hao and Chen Ling for their cooperation in making a collaborative work a complete success; and Seda Keskin for her friendship, support, and example.

I would like to thank all our former experimental collaborators at NETL Pittsburgh, PA in particular Dan Sorescu for guiding me while working there. I would like to thank our current experimental collaborators Dr. Douglas Way at the Colorado School of mines and Kent Coulter at the South West Research Institute for their support.

Special thanks to Dr. William Koros, Dr. Ronald Chance, Dr. Victor Breedveld, and Dr. Andrei Federov for their comments and questions as members of my thesis committee.

I am grateful to my parents, Benicia Flecha and Raul Semidey, for their constant love and support. And I am especially thankful to my husband for giving me the courage to continue, for believing in me, and for always standing by my side.

TABLE OF CONTENTS

LIST OF TABLES

LIST OF FIGURES

Page

SUMMARY

Metal membranes play a vital role in hydrogen purification. Defect-free membranes can exhibit effectively infinite selectivity for hydrogen. Membranes must meet multiple objectives, including providing high fluxes, resistance to poisoning, long operational standards, and be cost effective. Alloys offer an alternate route in improving upon membranes based on pure metal such as Pd. Development of new membranes is hampered by the large effort and time required not only to experimentally develop these membranes but also to properly test these materials. We show how first principle calculations combined with coarse-grained modeling can accurately predict H_2 fluxes through binary and ternary alloy membranes as a function of alloy composition, temperature and H_2 pressures. Our methods require no experimental input apart from the knowledge of the bulk crystal structure. Our approach is demonstrated for pure Pd, Pd-rich binary alloys, PdCu binary alloys, and PdCu-based ternary alloys. PdCu alloys have been experimentally shown to have potential for resistance to sulfur poisoning. First, we used plane wave Density Functional Theory to study the binding and local motion of hydrogen for the alloys of interest. This data was used in combination with a Cluster Expansion Method along with the Leave-One-Out analysis to generate comprehensive models to predict hydrogen behavior in the interstitial binding sites within the bulk of the alloys of interest. These models not only were required to correctly fit our calculated data, but they were also required to properly predict behaviors for local conditions for which we had not collected information. These models were then used to predict hydrogen solubility and diffusivity at elevated temperatures.

Although we are capable of combining first principle theory calculations with coarse grain modeling, we have explored a prescreening method in order to determine which particular materials are worth performing additional calculations. Our heuristic lattice model is a simplified model involving as few factors as possible. It is by no means intended to predict the exact macroscopic H properties in the bulk of fcc materials, but it is intended as a guide in determining which materials merit additional characterization.

CHAPTER 1

INTRODUCTION

Fossil fuels form the backbone of today's economy, yet environmental issues and global supply concerns associated with fossil fuels have created enormous interest in alternative fuels. Hydrogen is one of the fuels that has received a great deal of attention[1]. Many uses that are envisioned for hydrogen require high purity hydrogen[2, 3]. Advances in membrane technologies have the potential to improve the efficiency and cost of hydrogen separation and recovery[4-7].These membranes must be able to satisfy multiple specifications, including providing a high flux of hydrogen as well as allowing long term operation within a wide range of temperatures and pressures.

Metal membranes have received much attention for H_2 purification since they have the potential for perfect selectivity over other gas species[8]. Several recent reviews are available describing the large body of experimental work that exists for metal membranes[5, 9-11]. Pd films are perhaps the most widely known examples of metal membranes. The permeability of hydrogen through nonporous metal membranes is a multistep process[12-15], as illustrated in Figure 1.1. The process of hydrogen permeability across these metal membranes consists of

1. Dissociative chemisorption of molecular hydrogen on the upstream surface
2. Diffusion of atomic hydrogen from the surface into the bulk of the membrane
3. Diffusion of atomic hydrogen through the bulk
4. Recombinative desorption of molecular hydrogen from the downstream surface.

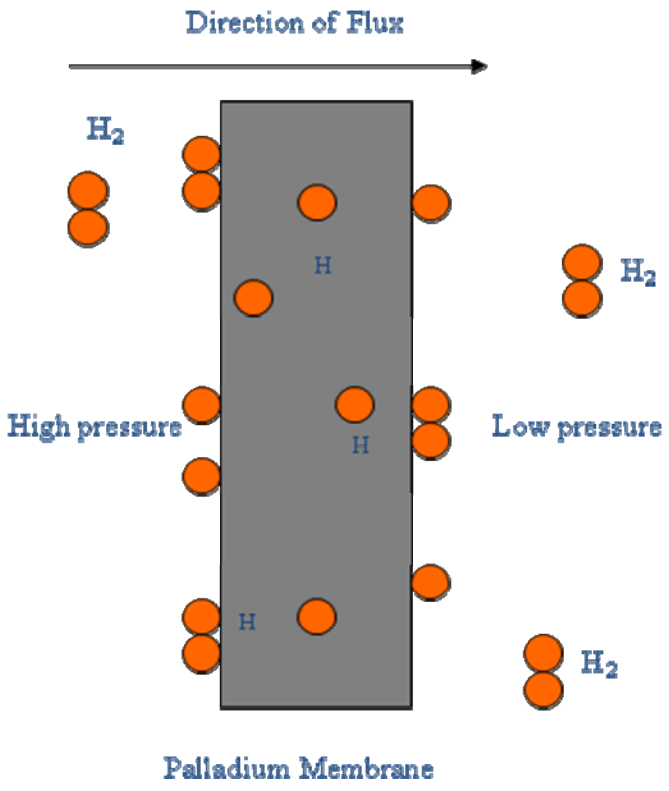

Figure 1.1: Illustration of hydrogen transport through palladium membranes.

Unfortunately, pure Pd membranes are prone to H_2-induced embrittlement at temperatures below 300˚C[16]. Pd membranes are also prone to poisoning due to the presence of sulfur or unsaturated carbon compounds[17].

Pd-based alloys can potentially offer improvements to pure Pd membranes while retaining the desired properties of Pd membranes. Pd has been the core material for binary alloy membranes in combination with elements including boron, cerium, copper, gold, iron, nickel, silver, and yttrium, among others[18]. Binary alloys with cerium, copper, gold, silver, and yttrium exhibit higher permeability than each of the metals exhibit individually under at least some circumstances. An ideal hydrogen-selective metal membrane should possess high catalytic activity for H_2 dissociation, high solubility, and

rapid diffusion of interstitial H. Many Pd-based alloys have been experimentally examined, yet these efforts have resulted in a relatively small number of membranes with attractive properties. This situation could be greatly aided with reliable theoretical methods were available to identify alloy compositions with promising properties.

1.2: Methodology

In this thesis we use first principles Density Functional Theory (DFT)[19-22] to calculate the local interaction and motion of hydrogen in the bulk of the Pd-based binary alloys, PdCu-based ternary alloys, and pure Pd. This data is used to parameterize lattice gas models with the aid of the Cluster Expansion (CE)[23-27] method to predict H solubility as a function of temperature and pressure. These CE lattice gas models, developed using our DFT calculations, were used in conjunction with Kinetic Monte Carlo (KMC)[28] algorithm to predict the long-range diffusivity in fcc dense metal membranes as a function of temperature. Finally we combine the solubility and diffusivity data to characterize the net hydrogen flux through dense alloy membranes as a function of pressure and temperature. Our methods are described with further details in Chapter 2.

1.3: Pd-Rich Binary Alloys

Kamakoti and Sholl have performed detailed calculations on a series of PdCu binary alloys[17, 29, 30]. Their efforts were based on experimental observations of increased contamination resistance in some PdCu alloys when compared to pure Pd membranes[1, 31]. Unlike their work, we have focused in our studies of binary Pd-based membranes on the effects observed when small amounts of an additive metal atom replace Pd to form Pd-

rich binary alloys[26]. Throughout this thesis, we will use the notation such as $Pd_{100-x}M_x$ to describe in this case a Pd-based binary alloy of where M is the additive metal atom. The subscripts denote the specific composition in atomic percent. For compositions of $Pd_{96}M_4$, most transition metals are miscible in Pd to form fcc binary alloys.

In Chapter 3 we used the experimental phase diagrams of a series of transition metals to ensure that the addition of these additives to Pd would result in fcc bulk materials. In this work, we described a robust theoretical framework developed to predict macroscopic properties of $Pd_{96}M_4$ metal membranes using quantum chemical calculations and coarse grained lattice gas modeling. The potential value of this method lied in its ability to screen a series of alloys at different operating conditions using only knowledge of the alloy phase diagram.

1.4: PdCu-Based Ternary Alloys

In Chapter 4 we applied the same concepts used for Pd-rich binary alloys to form PdCu-based ternary alloys. As previously mentioned, the combination of Pd and Cu in the development of a binary alloy improves the membrane's contamination resistance. Unfortunately, this increase in contaminant resistance typically comes at a cost of a reduction in H permeability when compared to H permeability in pure Pd. From Chapter 3 we observed the effects of the additive metal atoms at low compositions on the overall performance of the membranes compared with pure Pd. We observed that 4 at.% sufficed in the manipulation of H macroscopic properties of these bulk fcc alloys compared to pure Pd. With this knowledge we introduce 4 at.% of additive metal atoms to form

$Pd_{70}Cu_{26}M_4$ and compare the overall performance of H in these ternary alloys to $Pd_{70}Cu_{30}$ and $Pd_{74}Cu_{26}$.

In Chapter 4 we rely on the phase diagrams of Pd-M and Cu-M. Because little information on the phase diagrams of ternary alloys is available, we chose M so that the additive metal atoms would form fcc structures in both of the host metals, hence making it likely that any ternary alloy formed would also be an fcc structure. We describe a robust theoretical framework to predict macroscopic properties of $Pd_{70}Cu_{26}M_4$ metal membranes using quantum chemical calculations and coarse grained lattice gas modeling.

Unlike the Pd-rich binary alloys, in which a few DFT calculations suffice to sample a large portion of the bulk material, examining a complete set of interstitial sites for these ternary alloys would require an unfeasible number of DFT calculations. The CE lattice models described in Chapter 2 now serve a dual purpose. First, they must accurately fit the DFT data collected for describing these ternary alloys. In addition the CE models are used to determine if additional DFT data is required in order to properly describe H macroscopic properties in the bulk of these ternary alloys. We applied the methodology described in Chapter 2 to predict H solubility, diffusivities, and permeability in the selected $Pd_{70}Cu_{26}M_4$ alloys in Chapter 4.

1.5: A Heuristic Lattice Model for Analyzing H Permeability Through Alloy Membranes

Although we have demonstrated the capability of detailed calculations to describe macroscopic properties of H in a series of Pd-based binary and PdCu based ternary alloys, the concept of rapid screening can be further accelerated. In Chapter 5 we explore

the possibility of pre-screening materials used to form Pd-based binary alloys with a simple model that would require a minimal number of DFT calculations. This heuristic lattice model is based on the physical effects on the lattice of the membrane in comparison to pure Pd due to the presence of an additive metal atom, and the chemical effect of the M atom to interstitial sites. Unlike the detailed calculations in Chapters 3 and 4 we only perform DFT calculations on a small set of interstitial sites to extract the chemical effect parameter of the heuristic lattice model.

Due to the simplicity of the lattice model we are capable of performing large sets of comparisons among the transition metal atoms that form substitutionally random fcc structure with pure Pd at the desired composition. Once we collect the relevant data we can rapidly predict the properties of H in these binary alloys. We validate the heuristic lattice model predictions with the detailed calculations performed on the $Pd_{96}M_4$ and $Pd_{74}Cu_{26}$ alloys from Chapters 3 and 4. Once convinced that this method is sufficient to assess the effects of the additive metal atoms with semi-qualitative accuracy, we perform a series of calculations for 27 transition metal atoms that form fcc structures with Pd at the composition $Pd_{96}M_4$. Once known which M atoms are predicted to have improved H properties at this alloy composition, we continue our pre-screening calculations to include Pd-based alloys with increased M atom content. This is done for alloys containing up to 40.7 at.% of the additive metal atoms.

1.6: H Isotope Separation

The great majority of work on metal membranes has focused on the purification of hydrogen from mixed gas streams. There are applications, however, where the

separation of isotopes of hydrogen is important, such as the design and operation of fusion reactors[32, 33]. In Chapter 6, we consider how metal membranes can be chosen to achieve effective separations of hydrogen isotopes at elevated temperatures.

1.7: References

1 F. Roa, M. J. Block, and J. D. Way, Desalination **147**, 411 (2002).

2 K. Komiya, Y. Shinzato, H. Yukawa, M. Morinaga, and I. Yasuda, Materials Science Forum **475**, 2497 (2005).

3 J. Zhang, H. Xu, and W. Li, J Membr. Sci. **227**, 85 (2006).

4 L. Schlapbach and A. Züttel, Nature **414**, 353 (2001).

5 D. Edlund, D. Friesen, B. Johnson, and W. Pledger, Gas Sep. & Purif. **8**, 131 (1994).

6 B. H. Howard, R. P. Killmeyer, K. S. Rothenberger, A. V. Cugini, B. D. Morreale, R. M. Enick, and F. Bustamante, J. Membr. Sci. **241**, 207 (2004).

7 B. D. Morreale, M. V. Ciocco, B. H. Howard, K. S. Rothenberger, A. V. Cugini, and R. M. Enick, J. Membr. Sci. **241**, 219 (2004).

8 C. Su, T. Jin, K. Kuraoka, Y. Matsumara, and T. Yazawa, Ind. Eng. Chem. Res. **44**, 3053 (2005).

9 D. S. Sholl and Y. H. Ma, MRS Bulletin **31**, 770 (2006).

10 S. Uemiya, W. Kato, A. Uyama, M. Kajiwara, T. Kojima, and E. Kikuchi, Separ. Purif. Tech **22-23**, 309 (2001).

11 J. W. Phair and R. Donelson, Ind. Eng. Chem. Res **45**, 5637 (2006).

12 R. M. Barrer, *Diffusion In and Through Solids* (Cambridge University Press, London, 1951).

13 F. Roa and J. D. Way, Ind. Eng. Chem. Res. **42**, 5827 (2003).

14 W. T. Shmayda, LLE Review **91**, 125 (2002).

15 T. L. Ward and T. Dao, J. Membr. Sci. **153**, 211 (1999).

16 X. Ke and G. J. Kramer, Phys. Rev. B **66**, 184304 (2002).

17 P. Kamakoti and D. S. Sholl, J. Membr. Sci. **225**, 145 (2003).

18 S. N. Paglieri and J. D. Way, Sep. Purif. Methods **31**, 1 (2002).

19 D. R. Alfonso, A. V. Cugini, and D. S. Sholl, Surf. Sci. **546**, 12 (2003).

20 W. Koch and M. C. Holthausen, *A Chemist's Guide to Density Functional Theory* (Wiley-VCH: Berlin, 2001).

21 O. M. Løvvik and R. A. Olsen, J. Alloys and Compounds **330**, 332 (2002).

22 D. S. Sholl and J. A. Steckel, *Density Functional Theory: A Practical Introduction* (John Wiley & Sons, Inc., 2009).

23 H. Y. Geng, M. H. Sluiter, and N. X. Chen, Phys. Rev. B **73**, 012202 (2006).

24 H. Y. Geng, M. H. F. Sluiter, and N. X. Chen, J. Chem. Phys **122**, 214706 (2005).

25 L. LaFuente and J. A. Cuesta, J. Phys. A: Math. Gen. **38**, 7461 (2005).

26 L. Semidey-Flecha and D. S. Sholl, J. Chem. Phys. **128**, 144701 (2008).

[27] M. H. F. Sluiter and Y. Kawazoe, Phys. Rev. B **68**, 085410 (2003).
[28] H. Kurokawa, Bada, K., Koyama, M., Kubo, M., Miyamoto, A, in *Eighth International Conference on Inorganic Membranes*, edited by F. T. Akin, Lin, Y.S (Adams Press, Cincinnati, OH, 2004), p. 607.
[29] P. Kamakoti, B. D. Morreale, M. V. Ciocco, B. H. Howard, R. P. Killmeyer, A. V. Cugini, and D. S. Sholl, Science **307**, 569 (2005).
[30] P. Kamakoti and D. S. Sholl, Phys. Rev. B **71**, 014301 (2005).
[31] S. E. Nam and K. H. Lee, J. Membr. Sci. **192**, 177 (2001).
[32] J. Evans and I. R. Harris, J. Less-Common Metals **89**, 407 (1983).
[33] S. Tosti and V. Violante, Fusion Eng. Des. **43**, 93 (1998).

CHAPTER 2

METHODS

Systematic experimental study of the large number of binary metal alloys that could potentially be used as metal membranes would be extremely time consuming and expensive. If the number of binary metal alloys is great, then the number of probable ternary metal alloys is far greater. The field of ternary metal alloy development is an experimental challenge few have attempted to solve[1-7], partly due to the fact that there are plentiful binary alloys that are still being analyzed. Nevertheless, ternary metal alloys are prospective membranes for hydrogen purification in addition to those binary metal alloys. A binary alloy that has desirable properties such as resistance to contaminants found in the source stream could potentially be modified into a ternary alloy with metals that will improve the flux while retaining the desired properties. The identification of potential ternary alloys would first require that a good binary alloy candidate is found, bringing us back to the initial problem of overabundance of binary metal alloys and the difficulty experimentalists face in assessing these alloys.

In recent years, theoretical approaches based on first principles calculations have begun to offer a complementary route to gather information on the performance of metal alloys in H_2 purification. These approaches are typically based on plane wave density functional theory (DFT), which is well suited for describing the properties of H on the surfaces and interstitial sites of pure metals, ordered intermetallics, disordered alloys, and metal hydrides[8-12]. Kamakoti and Sholl used DFT-based calculation to examine H solubility, diffusion, and permeability in a series of Pd-Cu alloys[13, 14], showing that the

predictions from these calculations are in good accordance with experimental measurements[15]. Sonwane *et al*. recently used the same methods to examine PdAg and PdAu alloys[16, 17].

A key challenge in using DFT calculations to describe interstitial H in alloys such as PdCu is that in substitutionally disordered materials there is a plethora of structurally distinct binding sites where H can reside. Kamakoti and Sholl[13, 14] (and subsequently Sonwane *et al*. [16, 17]) approached this challenge by performing DFT calculations for H in a collection of distinct interstitial sites, then fitting the observed results for binding energies and transition state energies to a simple lattice model in terms of parameters that describe the local environment of each site. Although this method of fitting data has proven to be effective, there is little information on whether or not the amount of DFT data collected is sufficient to accurately describe the properties of H in the material of interest. In addition, these simple models may not be effective if used to predict binding sites for which no DFT calculations have been performed.

An alternative to this previous approach is the determination of a model derived by the implementation of the cluster expansion (CE) method[18-20]; a mathematical framework that subdivides the binding sites into a series of characteristic figures that define the local structure of the site in used. Many models can be derived from the use of the CE method, by simply altering which characteristic figures will be used to define the interstitial H. In order to determine which of these potential models is best, an additional analysis is performed known as the leave-one-out (LOO)[18, 20] analysis. The LOO method consists of performing an analysis on the predictive capability of a particular CE model. In doing so we are capable of discovering the CE model that is best suited to describe the

distinct binding sites found in the bulk of an alloy. Combining the CE with the LOO method, we are capable determining if the initial data collected is sufficient to describe the particular alloy.

In this chapter, we will describe the method implemented in our research to analyze and describe the properties of H in a series of binary and ternary alloys through the course of this thesis. First, we will describe the use and the accuracy of the plane wave DFT. All DFT calculations we report were performed with the Vienna *Ab Initio* Simulation Package (VASP)[21]. Second, the CE method will be outlined, including the characteristic figures used to describe the binding sites in our analysis. The LOO method will also explained in detail, including how it complements the CE model selection. We will also compare how the CE models selected by the LOO method compare with models used by previous researchers. Finally, we will describe how the solubility, diffusion, and ultimately the permeability of H are computed in the materials of interest with the use of the CE models.

2.1: Density Functional Theory (DFT)

We used plane wave density functional theory (DFT) calculations to characterize interstitial H in fcc PdM and PdCuM where M represents a small amount of an additive metal atom used to form the binary alloys or ternary alloys. The M atoms of interest include Ag, Au, Cu, Ni, Pt, Rh (in the binary case), and Y. These additive metal atoms have been selected for several reasons that we will discuss in later chapters. DFT is a first principles theory of electronic ground state structure based on the electronic density distribution [22, 23]. Calculations in bulk solids are performed by specifying a central

supercell typically containing a few tens of distinct atoms. The periodic calculation is performed by repeating this supercell in three dimensional space to replicate an infinitely large bulk solid. A recent review of DFT calculations for interstitial alloys is available[8].

2.1.1: Calculation Details

All our calculations were performed using VASP, while using the ultra-soft pseudopotentials introduced by Vanderbilt to describe the interactions between the ions and the electrons. All calculations were performed using the generalized gradient approximation (GGA) to describe electron exchange correlation effects using the Perdew-Wang 91 functional[24]. A plane wave expansion with a cutoff of 233.7 eV was used in all calculations. Total energy calculations used the residual minimization method for electron relaxation, accelerated using Methfessel-Paxton Fermi-level smearing with a width of 0.2 eV. Geometry relaxations were done using a conjugate gradient algorithm until the forces on all atoms were less than 0.03 eV/Å. A Γ-centered grid of $4\times4\times4$ k points was used to sample reciprocal space for all calculations with bulk materials. Each calculation used a 27 atom supercell with rhombohedral geometry (that is, $3\times3\times3$ primitive fcc cells) with basis vectors oriented along the three cubic face diagonals starting from origin as can be seen from Figure 2.1. It is important to note that these calculations apply periodic boundary conditions to the supercell used in each calculation, so the calculations describe a 3-D material with no external surfaces or interfaces.

As a first step towards predicting the properties H in the bulk of the materials of interest, we performed DFT calculations for pure Pd. There are two types of interstitial

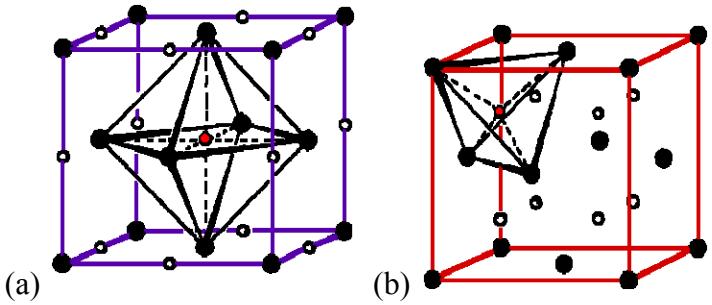

Figure 2.1: Schematic of (a) octahedral (O) and (b) tetrahedral (T) binding sites in an fcc lattice. Filled spheres represent metal atoms defining the fcc lattice, empty circles represent possible interstitial sites, and the red sphere represents an interstitial site currently occupied by hydrogen.

sites, also known as binding sites, available for hydrogen occupation in fcc metals: the sixfold octahedral (O) and the fourfold tetrahedral (T) sites. These two interstitial sites are shown in Figure 2.1. Pure Pd was modeled using the 27 atom supercell described above. For binary alloys, we focused on alloys with atomic compositions of $Pd_{96.3}M_{3.7}$ (in at.%). A 27 atom supercell with one M atom has precisely this composition. For convenience, we will refer to these alloys as having composition $Pd_{96}M_4$ below. For the ternary alloys we focused on alloys with compositions of $Pd_{70.4}Cu_{25.9}M_{3.7}$ (in at.%); a 27 atom supercell with 19 Pd atoms, 7 Cu atoms, and one M atom has this precise composition, which we will refer to as having composition $Pd_{70}Cu_{26}M_4$ below.

Calculations involving interstitial hydrogen were performed by inserting a single H atom in a given interstitial site using the supercells described above. These calculations correspond to dilute hydrogen loadings. Specifically, the H/M loading is 1/27, where M denotes a metal atom. All calculations including interstitial H were performed for supercells with the lattice constant optimized using DFT prior to inserting H. This approach neglects the lattice expansions induced by H, but under the very dilute H concentrations relevant for high temperature membrane applications, this is a reasonable approximation.

2.1.2: Bulk Calculations

Lattice constants were optimized using DFT for each metal system without the presence of H. For all alloys, the lattice parameter was optimized using the 27 atom supercell containing the specific material composition for either the binary or the ternary alloy, after initial estimations with Vegard's law[25]:

$$a_{PdCuM} = x_{Pd}a_{Pd} + x_{Cu}a_{Cu} + x_{M}a_{M} \tag{2.1}$$

where a_{PdCuM}, a_{Pd}, a_{Cu}, a_{M} are the lattice constants for the fcc alloy, pure Pd, pure Cu, pure M, and x_{Pd}, x_{Cu}, x_{M} are the atomic composition of Pd, Cu, and the additive metal atoms M in the material of interest. Vegard's Law predictions are well suited for materials of the same crystal structure. Vegard's Law was also used in the initial estimation of the lattice constant of binary alloys formed from materials with distinct crystal structures without any modifications to account for the differences in crystal structures. For mixtures of materials with distinct pure component crystal structures that form fcc alloys, using Vegard's law in this way is less accurate than for mixtures of fcc materials. In every case, we performed a series of calculations to determine the correct lattice constant of the binary alloys of interest by examining a range of lattice parameters using the Vegard's Law estimates as a starting point. In these calculations, the lattice parameters were varied over a range of values using increments of ±0.01 Å. To facilitate and reduce our calculations, we used the experimental known lattice constants of the pure metals to estimate the lattice constant using Eq.(2.1). In doing this our Vegard's Law approximation was an experimental lattice constant prediction. Using the difference in the DFT calculated and experimentally obtained pure Pd lattice parameter we could

easily approximate the DFT lattice constants of the alloys from the experimentally predicted values, as follows:

$$a_{PdCuM}^{DFT} = a_{Pd}^{DFT} + (a_{PdCuM}^{Exp} - a_{Pd}^{Exp}) \quad (2.2)$$

Here a_{PdCuM}^{Exp} is the prediction using the experimental lattice parameters of the pure metals in Eq.(2.1), a_{Pd}^{Exp} is the lattice parameter experimentally observed for pure Pd, and a_{Pd}^{DFT} is the DFT calculated lattice parameter for pure Pd. In Table 2.1 we compare the results

Table 2.1: Comparison between Vegard's Law approximations for the lattice parameters of $Pd_{96}M_4$ with the DFT calculated values for a series of additive metals atoms. The crystal structure of pure M is also listed.

Crystal structure of pure M	M atom used for $Pd_{96}M_4$	Vegard's Law approximation (Å)	DFT calculated lattice parameter (Å)
Bcc	Cr	3.920	3.950
Bcc	Fe	3.919	3.948
Bcc	Mo	3.930	3.959
Bcc	Nb	3.936	3.962
Bcc	Ta	3.937	3.961
Bcc	V	3.925	3.953
Bcc	W	3.931	3.957
Fcc	Ag	3.968	3.966
Fcc	Au	3.968	3.968
Fcc	Cu	3.949	3.953
Fcc	Ir	3.958	3.956
Fcc	Ni	3.945	3.947
Fcc	Pt	3.961	3.961
Fcc	Rh	3.956	3.956
Hex	Co	3.905	3.945
Hex	Hf	3.932	3.968
Hex	Os	3.914	3.957
Hex	Re	3.915	3.957
Hex	Ru	3.912	3.963
Hex	Tc	3.914	3.956
Hex	Ti	3.922	3.956
Hex	Y	3.950	3.982
Hex	Zr	3.934	3.970

for the Vegard's Law lattice parameters using Eq.(2.2) and the DFT calculated values for a series of metal additive used to form a Pd-rich binary alloy. It can be observed that the M atoms with fcc crystal structures have the best correlation between the predicted lattice parameters and the DFT calculated values. For the other metal atoms with bcc or hex crystal structures, it can be observed that Vegard's law underpredicts the lattice parameters, yet it provides a reasonable starting point for locating the correct lattice parameter of these Pd-rich binary alloys. We further compared the DFT calculated lattice parameters for some of the Pd-rich binary alloys with experimental reported values. Table 2.2 summarizes and compares our DFT optimized lattice constants (LC) for the binary systems with experimental values. In all cases, it can be observed that there is less than a two percent difference between the DFT lattice constants and the experimental lattice constants from difference sources.

Up to this point the discussion has mainly focused the discussion on Pd-based binary alloys. Another aim of our work is to describe PdCu-based ternary alloys. Similar

Table 2.2: Lattice constant comparison between DFT calculations for Pd-rich alloys in this study with experimental Pd-rich alloys at similar compositions. [5, 26, 27]

System	Composition (x at.%)	DFT predicted LC (Å)	Experimental composition (x at.%)	Experimental LC (Å)
$Pd_xY_{(100-x)}$	96	3.982	94	3.930
$Pd_xAu_{(100-x)}$	96	3.968	94	3.903
$Pd_xAg_{(100-x)}$	96	3.966	95	3.899
$Pd_xPt_{(100-x)}$	96	3.961	95	3.890
pure Pd	100	3.960	100	3.889
$Pd_xRh_{(100-x)}$	96	3.956	95	3.886
$Pd_xCu_{(100-x)}$	96	3.953	95	3.877
$Pd_xNi_{(100-x)}$	96	3.947	95	3.878

to previously described binary alloys, the PdCu-based ternary alloys we will be analyzing are treated as substitutionally random disordered materials. Regardless of the alloy composition, we performed DFT calculations with 27 atom supercells as described earlier. To properly describe these disordered materials, we randomly distribute the atoms within these 27 atoms supercells at the desired alloy composition. The only limitation in distributing the atoms for both $Pd_{96}M_4$ binary alloys and $Pd_{70}Cu_{26}M_4$ ternary alloys is to avoid statistically unlikely clustering of the M atoms for the binary systems and the Cu atoms for the ternary systems. This is done to create a representation of well distributed arrangement of the atoms involved in the alloy composition of interest. We also intentionally created supercells with clustering of the M (Cu) atoms for the binary (ternary) systems and optimized the lattice constant of these supercells. The lattice constants obtained using both types of representation resulted in consistent lattice parameters, suggesting that the distribution of atoms within the supercell does not greatly affect the lattice constant.

In dealing with substitutionally random disordered materials, H can encounter many distinct combinations of metal atoms which form the interstitial site. In our Pd-rich alloys, due to the dilute amount of the additive metal atoms used in our binary alloys, we are capable of performing a small number of DFT calculations that encompass a large percentage of the distinct environments H can encounter within the interstitial site of these bulk materials. Using a 27 atom supercell to describe a $Pd_{96}M_4$ alloy most naturally requires the supercell to be composed of 26 Pd atoms and a single M atom. Although there is a small percentage of an M atom in the bulk material, we also perform calculations that include M atom concentrations of up to 3 M atoms within the supercell

while using the lattice parameter for the composition of interest. By doing these additional calculations, we are able to analyze a larger percentage of the metal combinations forming the interstitial sites than would be possible using a single supercell with the precise stoichiometry of the alloy of interest.

In the case of the ternary alloys, unlike the binary systems, we only collect data using a single M atom in the supercell. Because the majority of the bulk material in these ternary alloys is composed of a distribution of Pd and Cu atoms, we collect additional DFT data on an additional 27 atom supercell composed of 20 Pd atoms and 7 Cu atoms while using the lattice parameter optimized for the ternary composition of interest. This approach of using a fixed lattice parameter is appropriate because the ternary alloys are mainly composed of Pd and Cu, and by removing the M atom while redistributing the position of the remaining metal atoms in the supercell provides additional H conditions within the bulk of the materials of interest. In addition, a fixed lattice parameter is a reasonable approximation in general with these metal alloys, in which dilute amounts of hydrogen are found in the bulk material.

2.1.3: Interstitial Site Calculations

As previously mentioned, H can be found in the two distinct interstitial sites in fcc metals known as the octahedral (O) sites and the tetrahedral (T) sites. In fcc materials, the O site typically binds H atoms more strongly than T sites[28]. The classical binding energy of interstitial H found in the various possible interstitial sites based on DFT calculations was calculated using[29, 30]:

$$E_b = E_{H+M} - E_M - \tfrac{1}{2} E_{H_2} \tag{2.3}$$

where the energies on the right represent the total energy of the metal with and without interstitial H and the total energy of an isolated H_2 molecule, respectively. With this definition, a more favorable binding energy has a more negative value. In performing these calculations, the lattice constant (and as a result the shape and volume of the supercell) is held constant but all atoms are allowed to relax to find a minimum on the material's potential energy surface. In pure Pd, the binding energy of the O site was calculated to be $E_{b,O} = -0.14$ eV while for the T site it was $E_{b,T} = -0.09$ eV, in agreement with experimental observations that the O site is the more favorable binding site[31]. We will return to the quantitative accuracy of these calculations below.

Zero point energy (ZPE) corrections can be substantial for small interstitial atoms such as H, so we include them by calculating[32, 33] the vibrational frequencies of H, υ_i^H. For H in interstitial sites these energy corrections were computed within the harmonic approximation by assuming that the vibrational modes of interstitial H are decoupled from lattice phonons. Once the υ_i^H are determined, the ZPE is defined by

$$E_H^{ZP} = h\sum_{i=1}^{3}\frac{\upsilon_i^H}{2} \tag{2.4}$$

where *h* is Planck's constant . The ZPE for molecular H_2 was calculated similarly. Table 2.3 lists our DFT calculated values for H and its isotopes as interstitial atoms in an O site of bulk pure Pd and as a molecular gas compared to experimentally reported values[34]. There is excellent agreement between the calculated and experimental values. At low temperatures, the classical binding energy for an interstitial site must be corrected to include ZPE contributions using[13]:

$$E_b^{ZP} = E_b + E_H^{ZP} - \tfrac{1}{2}E_{H_2}^{ZP} \tag{2.5}$$

Table 2.3: Zero point energy comparison between our DFT calculated results and experimentally reported values for hydrogen and its isotopes by Alefeld and Völkl[34]. Isotopes are represented as interstitial atoms in an O site of pure Pd and in the molecular gas.

Isotope	DFT calculated results [eV]	Experimental results [eV][34]
H (H_2)	0.100 (0.270)	0.102 (0.269)
D (D_2)	0.071 (0.191)	0.072 (0.192)
T (T_2)	0.058 (0.156)	-

For H in an O site in pure Pd this method gives $\upsilon_i^H = 1.63\times10^{13}\,s^{-1}$ and $E_H^{ZP} = 0.10$ eV, in good agreement with experimental values obtained by Wicke *et al.* of $\upsilon_i^H = 1.56\times10^{13}\,s^{-1}$ and $E_H^{ZP} = 0.10$ eV [31]. The ZPEs defined above account only for the lowest energy vibrational states of H. At elevated temperatures, other vibrational energy states can also contribute to the net energy of an interstitial atom. As defined below, we calculate H solubilities and diffusivities in a way that includes the contributions of multiple vibrational energy states.

In the bulk of a substitutionally random alloy membrane, there are many structurally distinct interstitial sites. A simple way of describing the interstitial sites would be to count the number of a particular metal atom that are found in the nearest-neighboring (NN or $2\times N$) and the next-nearest-neighboring (NNN or $3\times N$) shell, $N_{2\times N}$ and $N_{3\times N}$, respectively. Characterizing the O sites of the substitutional random $Pd_{96}M_4$ alloys in this way, there are three kinds of sites that comprise around 90% of all possible O sites that could be found in the bulk material. If we were to count the number of Pd atoms, these sites include being surrounded by Pd ($N_{2\times N} = 6$, $N_{3\times N} = 8$), followed

by having a single M atom in the $2\times N$ shell ($N_{2\times N}$ = 5, $N_{3\times N}$ = 8), and finally having a single M atom in the $3\times N$ shell ($N_{2\times N}$ = 6, $N_{3\times N}$ = 7). It is important to realize that this description suggests that the properties of these sites can be completely described in terms of these two parameters. This is an approach we do *not* take in the cluster expansion approach described below, but it is useful for conceptually describing these systems. Performing calculations on the three types of binding sites can be made by placing the H in various binding sites within the supercell described previously with the desired composition.

The remaining 10% of the substitutionally random bulk material for $Pd_{96}M_4$ alloys are composed of O sites with multiple M atoms in the two distinct shells used above to characterize the binding sites. In order to analyze the clustering effects in these alloys we used 18 additional 27 atom supercells. Within these additional supercells we only examined the O site that included these clustering effects while retaining the lattice constant that was found for the binary alloy. These clustering effects result in 18 additional O sites ranged from one to three M atoms in the $2\times N$ and $3\times N$ shells. We also analyzed all the geometrically independent T sites that surrounded each O sites used to characterize the binary alloys. As a result we analyzed a total of 21 distinct O sites and a total of 88 T sites with these Pd-rich binary alloys.

Due to the complexity of ternary systems it is infeasible to perform as few calculations as in the binary systems and expect to have sampled a large percentage of the distinct sites within the bulk material. For each ternary material, we performed DFT calculations on two distinct 27 atom supercells. The first supercell consists of 19 Pd, 7 Cu, and 1 M atoms, and is used to optimize the lattice constant for all consequent

calculations for the ternary alloys. The second supercell consists of 20 Pd and 7 Cu atoms, using the optimized lattice constant for the ternary alloy. Because of the complexity of these systems, and the random placement of all the atoms in the supercells, we performed calculations for all binding sites within them. DFT calculations for the ternary alloys using the supercells just described provided us with a total of 54 distinct O sites, 108 distinct T sites, as well as the ZPE of H in each of these individual sites. As a means of comparison between the binary systems and the ternary system, if we were to describe the O sites for the ternary alloys with the simple $2\times N$ and $3\times N$ shells, the 54 binding sites we examined with DFT comprise less than 50% of the O sites that could be found in the bulk of these materials in their substitutionally random state.

Our diffusion calculations are based on transition state theory (TST), given that at elevated temperatures H will diffuse in fcc metals through a discrete series of hops between adjacent O and T sites[35, 36]. To characterize this process, the transition states (TS) that control these hops must be known. For individual hops between interstitial sites, the TS can be located within DFT via the nudged elastic band (NEB) method[37]. Although this is a powerful method of locating the TS, the NEB method is also a time consuming calculation. For complex systems such ternary alloys there are several hundred possible required TS calculations, therefore the need for a faster method of acquiring the TS was required.

Our initial $Pd_{96}M_4$ TS calculations were all calculated solely using the NEB method. Detailed inspection of the original data from these NEB calculations provided insight towards a simple method of estimating an initial position of the TS without need of NEB calculations. From a geometric perspective, the adjacent O and T sites for a

particular hop have a geometric face in common. In pure Pd the TS is located by defining a specific vector from the T site, as seen in Figure 2.2. We identify this distance and define it as a vector, $\overrightarrow{\upsilon_{Pd}}$. In a binary system once a particular T site is located we use the $\overrightarrow{\upsilon_{Pd}}$ identified from pure Pd to estimate the TS' in the binary alloy. The estimate obtained for the TS' is similar to the result we would have obtained in using NEB. We perform geometry optimization on the initial TS' estimation to locate the real TS of the binary system taking advantage of the fact that optimization methods exist that will converge to a transition state if a sufficiently accurate initial estimate is available. Once the final TS is found in the binary alloy, a new vector $\overrightarrow{\upsilon_{PdCu}}$ is calculated from the T site to the TS of the PdCu system, which is then used to estimate the TS' in the ternary alloys.

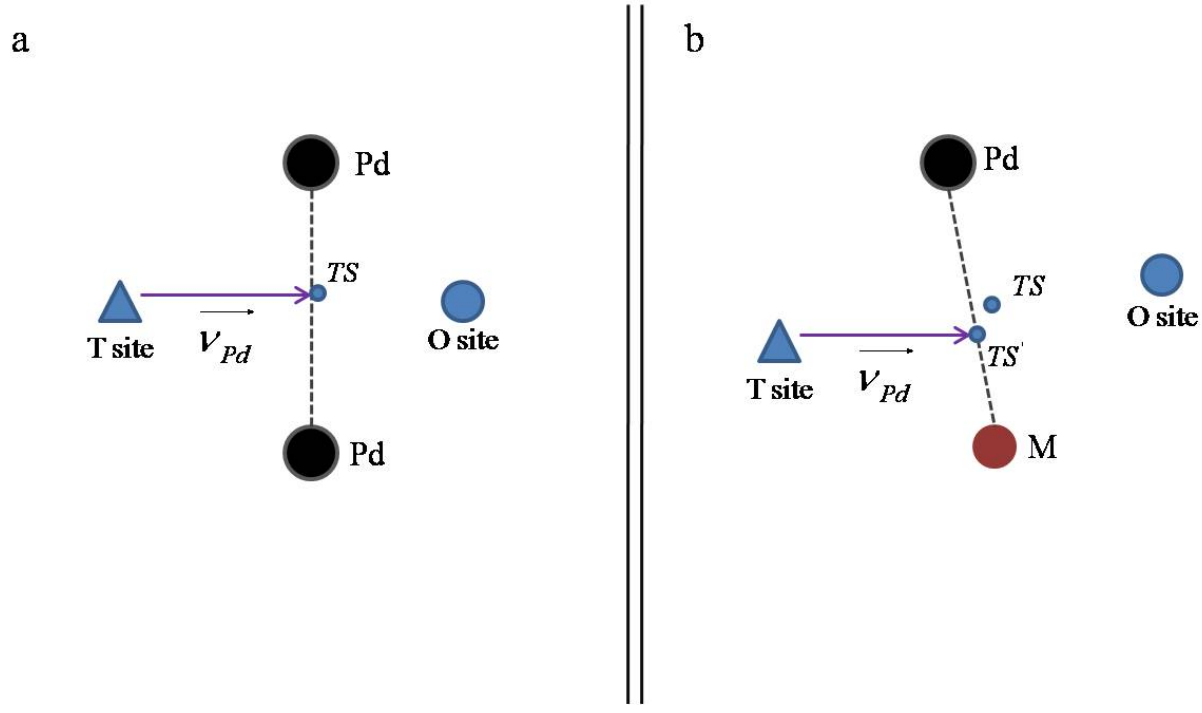

Figure 2.2 Representation displaying how we find the TS for a binary alloy: (a) first the vector between the T site and the TS in pure Pd, $\overrightarrow{\upsilon_{Pd}}$ (b) using the fixed vector identified from pure Pd, an initial estimate, TS', to the true transition state, TS, is made in the binary alloy.

In using the vectors to identify an initial estimation for the TS, we reduce the number of calculations needed to identify the TS, greatly reducing the computational time required for this process. When compared to NEB results, this approach provides initial, TS', positions that differ less than 0.01Å from each other.

In Pd-rich binary alloys, we calculated all the TS possible from the 21 O sites to the 88 T sites using the NEB method. This procedure resulted in a total of 92 geometrically independent TS. For all other alloys in this study we used the approach described above. Also, similarly to the O and T site calculations, all TS found within a supercell were calculated, for supercells associated with the ternary alloys regardless of the geometry. Once the TS are identified, we calculated the vibrational frequencies of H at the TS in the same way as for the interstitial sites. At each well defined TS, this yields two real frequencies and one imaginary frequency.

2.2: Theory of the Cluster Expansion Method

Having a collection of DFT data, we need to find a way to accurately capture the data collected for each individual alloy in order to be able to describe the macroscopic properties of H in the bulk materials. To illustrate the application of the cluster expansion (CE) to Pd-based and PdCu-based alloys, consider the problem of defining the binding energy of H in the O sites of a disordered binary Pd alloy. The labeling scheme introduced above involving the $2\times N$ and $3\times N$ shells is one straightforward way to characterize each site. Kamakoti and Sholl used this characterization to define a model connecting the identity of the site with the H binding energy in this site[13-15]:

$$E_{b,O} = E_o + aN_{2\times N} + bN_{3\times N} \tag{2.6}$$

In this model a , b and E_o are parameters that can be fitted in a least-squares sense to the set of DFT binding energies that are available for different sites. Sonwane *et al*. adopted a similar approach in their treatment of PdAg and PdAu alloys[16, 17]. Although this procedure provides good agreement with experimental studies in PdCu alloys[38, 39], it does not offer a natural means to verify whether the model is sufficient to describe the available DFT data or the majority of the bulk material.

Cluster expansions provide a general mathematical framework for the problem outlined above based on a formally infinite series of characteristic figures such as pairs, triplets, four-body terms, and so on that represent multiple body interactions that sum together to define the energy of a configuration[18, 19, 40-42]. For a situation involving binary and ternary alloys it is convenient to express the lattice model as an Ising model by associating a spin variable with each of the metals of the alloy[43-45]. For our Pd-based binary alloys, we define S_i = -1 (1) for Pd (M) atoms. For our PdCu-based alloys, we similarly define S_{Pd} = -1, S_{Cu} = 1 and S_M = 0.11. We used a fraction to define the M atoms in the ternary alloys to ensure that if we were to sum the number of M atoms in either the $2\times N$ and $3\times N$ shells this sum would not equal the value associated with the other metals in the system. The precise numerical value of S_M does not affect the outcome of these calculations.

The general cluster expansion for the energy of the binding energy or the zero point energy (ZPE) correction of a single interstitial H has the form:

$$E_{b(ZPE)} = E_o + \sum_i J_i^{(1)}\sigma_i^{(1)} + \sum_i J_i^{(2)}\sigma_i^{(2)} + \sum_i J_i^{(3)}\sigma_i^{(3)} + \ldots \qquad (2.7)$$

where each $J_i^{(n)}$ is a parameter defining the interaction energy of an H atom where the superscript denotes the number of bodies involved in the interaction and the subscript

denotes the clusters of i metal atoms in the particular shell. It is useful to consider specific examples for some of the terms in this expansion. The simplest one-body contribution is related to the sum of the number of a particular metal atom in the $2\times N$ shell, so $\sigma_{2\times N}^{(1)} = \sum S_i$, the sum over the six atoms defining the $2\times N$ shell of an O sites. Other contributions to the first sum in the general expansion above can include the $3\times N$ shell and so on. An example of a two-body interaction is $\sigma_{2\times N}^{(2)} = \sum S_i S_j$, where the sum is now taken over all pairs of i and j corresponding to adjacent metal atoms in the $2\times N$ shell. This kind of interaction was not considered in the work of Kamakoti and Sholl[13-15] (and the subsequent work by Sonwane *et al.*[16, 17]) shown in Eq.(2.6).

Table 2.4 gives an example of the types of data that is available for several of these interactions. If we were only to take into consideration the interactions listed in Table 2.4 the CE would be:

$$E_b = E_o + J_{2\times N}^{(1)}\sigma_{2\times N}^{(1)} + J_{3\times N}^{(1)}\sigma_{3\times N}^{(1)} + J_{2\times N}^{(2)}\sigma_{2\times N}^{(2)} + J_{2\times N}^{(3)}\sigma_{2\times N}^{(3)} \tag{2.8}$$

Table 2.4: Brief examples of the interactions used in the CE development of the O site binding energies for $Pd_{96}M_4$. The columns show four types of interactions from a total of 20 that were considered. The rows list information for six distinct O sites from a total of 21 sites that were considered. The classical binding energy for each site is also shown. The four interactions listed here characterize the number of Pd atoms in the $2\times N$ and the $3\times N$ shells ($\sigma_{2\times N}^{(1)}$ and $\sigma_{3\times N}^{(1)}$), two-body interactions involving adjacent atoms in the $2\times N$ shell ($\sigma_{2\times N}^{(2)}$), and three-body interactions involving adjacent atoms in the $2\times N$ shell ($\sigma_{2\times N}^{(3)}$).

Site	E_b (eV)	$\sigma_{2\times N}^{(1)}$	$\sigma_{3\times N}^{(1)}$	$\sigma_{2\times N}^{(2)}$	$\sigma_{2\times N}^{(3)}$
1	-0.118	-2.5	-2.667	1.413	0
2	-0.165	-3	-2.333	4.240	2.823
3	-0.159	-3	-2.667	4.240	2.823
4	-0.173	-3	-2	4.240	2.823
5	-0.165	-3	-2	4.240	2.823
6	-0.169	-3	-2	4.240	2.823

This expression includes single-body contributions from the $2\times N$ and the $3\times N$ shells, a two-body interaction that counts only the adjacent metal atoms in the $2\times N$ shell, and a three-body interaction that counts triplets of adjacent metal atoms in the $2\times N$ shell. The first three terms on the right hand side of Eq.(2.8) are equivalent to the lattice model used by Kamakoti and Sholl [*cf*. Eq.(2.6)].

Because we are working with both binary and ternary alloys, the parameters used to describe the binding sites need to be sufficient to describe each of the systems. In our experience in working with CE, 2-body terms were typically sufficient to accurately describe the binary systems. Upon attempting to apply the same terms used to describe the binary systems to the ternary systems, we realized that 3-body terms were necessary to describe these more complex systems. Our CE models consist of up to 20 parameters to describe the O sites, ranging from counting the number of a particular metal atom in various shells surrounding the site up to 4-body contributions. For further detail of the interactions used to describe the O binding sites, refer to Appendix A. Similarly, we have a distinct set of 30 parameters used to describe the T sites, spanning from the number of a particular metal atom in the surrounding shells up to 3-body interactions. Further details of the characteristic figures used to describe the T sites can be found in Appendix A.

As previously mentioned, high temperature H diffusion in fcc metals occurs via hops over a TS between adjacent O and T sites. A convenient way of defining the transition states would be to identify the O site and the T site that are connected by the TS of interest. Hence, the parameters used to define the TS are a combination of the parameters of the O site and the parameters used to define the T site. This results in a total of 50 parameters that are considered to define each TS.

To apply the CE expansion, it is necessary to truncate the infinite expansion, which we have done by selecting a set of characteristic figures to define each binding site, as described above. Within the selected set of parameters we have chosen to describe the binding sites, we are capable of further truncating the CE by using a limited set of the parameters. If a particular truncation is selected, then it is straightforward to determine the interaction parameters, $J_i^{(n)}$, by least squares minimization of the deviation between the truncated form of the CE and the DFT data that is available. To determine which set of interactions within the list we have used to define the binding sites would be the most suitable truncated form of the CE to produce reliable predictions we used the 'leave-one-out' (LOO) method[18, 46]. With the LOO method, we are able to harness the power of the CE by not only fitting a model to our DFT data, but also compare models with different number of parameters in order determine which set of interactions forms a model that is best suited for predicting data.

The LOO method can be easily applied to a series of CE model calculations. In fitting the CE parameters for any particular truncation, a least square minimization is performed using *X* independent pieces of data, in our case from the DFT calculations. A LOO analysis consists of performing a least squares minimization of the model being considered *X* independent times where in each case, one data point from the complete set of *X* values is left out. From these calculations, the LOO error is defined as

$$R_{LOO}^2 = \frac{1}{X}\sum_{k=1}^{X}(E_{pred,k} - E_k)^2 \tag{2.9}$$

where E_k is the *k*-th data point and $E_{pred,k}$ is the value for this point predicted by the model fitted to all the data except the *k*-th data point. Reducing the value of R_{LOO}^2

represents a better model, since the restricted data set is able to more accurately predict the missing data point. This also suggests that the model will be able to predict data points that were not included in the initial data set. In our work, we applied the LOO analysis to large sets of possible CE truncations for each of the binding sites and ZPE for each individual alloy of interest. In each case, the model with the lowest LOO error was used to define a lattice model for future calculations.

In truncating the CE, we use limited collection of the interactions used to describe a binding site resulting in different sets of models having distinctive number of parameters. The LOO analysis provides a means to compare these models that involve different numbers of parameters. All possible truncated forms of the CE, with the exception of truncations containing only a single parameter, were considered as potential CE models. This action meant that for the O site binding energy having a total of 20 parameters, there are 1,048,555 potential CE models. Similarly for the T sites, considering a total of 30 parameters to define the binding site energy results in 1,073,741,793 possible CE models. In the case of the TS, having as many as 50 parameters to define the site creates a computational problem. Due to the factorial dependence of the number of models on the number of parameters, completely considering 50 parameters would generate $>10^{15}$ possible models. Scanning through this number of potential model would take an enormous amount of computational time. In order to reduce the computational time required to scan through all the potential models for the TS, we have developed two ways of intrinsically discarding truncated CE models before actual application of the LOO method. In both methods we assume that since the

TS are defined by the parameters of the O and T sites, then if a set of parameters is not appropriate to define those sites then the same will be true for the TS.

The first method for developing a truncated CE to describe TS consists of taking the all the parameters used to define TS and dividing them into two groups. First we define the TS only using the O site parameters and perform the CE-LOO analysis to determine which of these best defines the TS. We also perform a separate CE-LOO analysis on the TS solely using the T site parameters, in order to determine which of these parameters is best suited to define the TS. From these two independent analyses we combine the parameters that were selected to form a reduced set of parameters from the possible 50 parameters originally available. By initially dividing the parameters used to define the TS, what we have essentially done is pre-screened the parameters and removed any interaction that would not aid significantly in defining the properties of the TS. This procedure works well with our Pd-based binary alloys. Although this method is effective for finding the CE model for the TS, there are cases were the amount of DFT data in combination with the large set of potential truncated CE models results in time consuming calculations.

When a large set of TS DFT data is also a factor, as it is for some of our ternary alloys, we use a second approach to find the truncated CE model for the TS. In this second approach, the pre-screening process of the interactions consists of using the results of the CE-LOO analysis for the truncated CE model of the O site binding energy in combination with the results for the truncated CE of the T site binding energy models. We combine the predicted parameters best suited to define these other binding sites as the initial set of parameters used to define the TS. In doing this we have reduced the

parameters used to define the TS from the possible 50 interactions available. With this reduced set of interaction to define the TS we perform the CE-LOO analysis in order to determine the truncated CE model suited for describing these binding sites. Although this second method is an approximate approach, given that we have limited the initial interactions used to define the TS, our assumption is that the interactions selected by the truncated CE models for the O sites and the T sites binding energies of a particular system will also be well suited to define the TS.

In presenting the general CE, we briefly mentioned that we calculated the binding energy separately from the ZPE correction to the binding energy for each type of site. The binding site energies and ZPEs are treated as separate expansions to facilitate the prediction of macroscopic properties of H in the bulk materials, as discussed below in section 2.4. In separating these energies, the CE model determination procedures to determine a model for the ZPEs are entirely analogous to what is done for the binding energies in each site. The result is that six truncated CE models are used to describe the behavior of H in the bulk of the alloys of interest, namely models for the binding energy of the O, T, and TS sites, and ZPE energy for each of these sites.

2.3: Validating CE-LOO Selected Models

Although we have a model capable of describing our DFT data, we need models that are not only capable of describing our calculated data, but also binding sites that we have not observed with DFT. This requires us to test our models and validate their capability of describing binding sites that we have not previously analyzed. Before a truncated CE model is selected we perform a validation process that consists of two steps.

The first step consists of calculating the standard deviation of the model in fitting the DFT data, defined as:

$$\sigma = \sqrt{\frac{\sum_{i=1}^{N}\left(X_i - \overline{X}\right)^2}{N}}, \overline{X} = \left|\left(E_{m,k} - E_k\right)\right| \tag{2.10}$$

where $E_{m,k}$ is the E_b predicted from model m for the binding site k to the E_b of the DFT data set of N data points. The standard deviation of the selected models for the O site, T site, and TS binding site energies for the $Pd_{70}Cu_{30}$ were $\sigma(\text{O site}) = 0.0065\,\text{eV}$, $\sigma(\text{T site}) = 0.0053\,\text{eV}$, and $\sigma(\text{TS}) = 0.0115\,\text{eV}$ respectively. The lower the standard deviation between the DFT fitted values and the calculated values the better the model selected describes this DFT dataset. In Figure 2.3 we have plotted the CE predicted binding energy values versus the DFT calculated energies for the $Pd_{70}Cu_{30}$. This figure shows the predicting power of the CE models selected for each of the binding sites in the

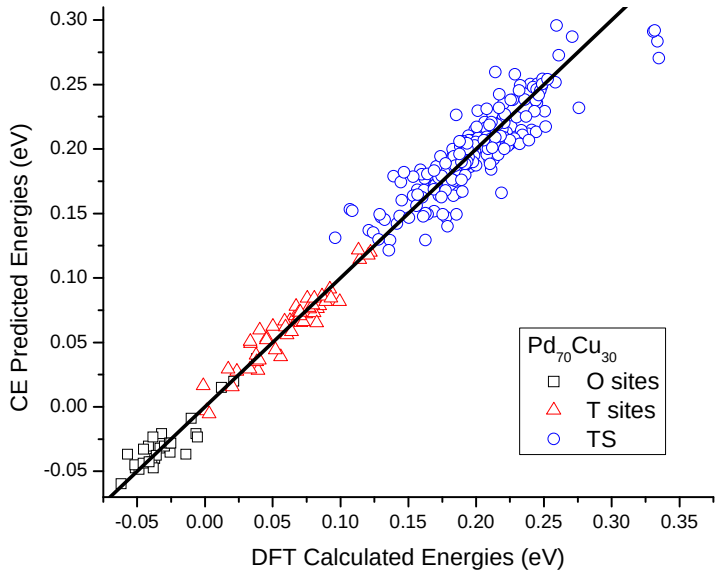

Figure 2.3: CE model prediction vs. DFT calculated data for O site, T site and TS classical binding energies of the $Pd_{70}Cu_{30}$, with all energies in eV.

$Pd_{70}Cu_{30}$ alloy system. From Figure 2.3 it can be observed that our CE models for the O sites and the T sites have greater accuracy than the model for the TS, further discussion will be found in Chapter 4. Nevertheless, the standard deviation for this model is less than 0.02 eV which is an acceptable value in dealing with DFT data.

Once we are convinced that the CE model can appropriately describe the DFT data, we can proceed to the second step in the validation process. This step consists of testing the truncated CE models in a truly random representation of the bulk material and predicting the binding energy values of all the sites within this representation. The representation of the bulk material consists of constructing a randomly generated volume containing $4,000$ atoms. This is equivalent to $10\times10\times10$ primitive fcc cells shown in Figure 2.1. Larger volumes, up to $30\times30\times30$ primitive fcc cells were used and it was determined that the smaller volume size was sufficient for our validation procedures. The atoms in the generated volume are randomly distributed to the desired alloy composition with precision of 0.001%. Once the volume meets the required composition, we scan through the volume calculating the binding site energies of all available O sites, T sites and TS using the truncated CE model selected for each site.

In order to compare how the CE model performs with solely the DFT data and the randomly generated volume, we perform a cumulative probability analysis for the O sites, T sites, and the TS of each alloy. Figure 2.4 shows the results of our cumulative probability analysis of the binding site energies of the O sites, T sites, and TS selected truncated CE models for $Pd_{70}Cu_{30}$ alloy. The solid symbols represent the DFT calculated data, the open symbols represent the CE fitted solely to the DFT data, and the dotted lines represent the CE applied to the random volume. From Figure 2.4 we can see that the

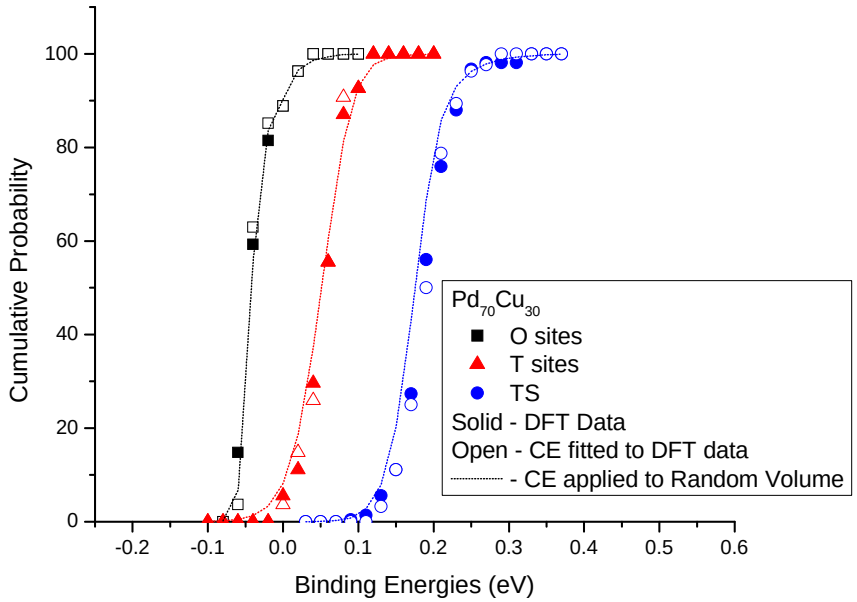

Figure 2.4: Cumulative probability analysis of the truncated CE selected model via LOO for $Pd_{70}Cu_{30}$. The O sites are represented by squares, triangles represent the T sites, and circles represent the TS. Solid symbols signify DFT calculated data, open symbols represent the truncated CE model fitted using only DFT data, while the dotted lines represent the same truncated CE model applied to the randomly generated volume.

selected CE models for each of the binding sites individually have relatively good overlap between the plotted data. More importantly, no binding sites with lower energies, hence more favorable sites, are observed. This suggests that we have sampled sufficient DFT data to describe the bulk of the substitutionally random $Pd_{70}Cu_{30}$. If the CE model predicted binding sites with lower binding energies than had been observed with DFT, we would be required to perform DFT calculations on these sites in order to understand whether this CE model prediction was accurate. Fortunately, this was not the case for the $Pd_{70}Cu_{30}$ alloy where we can observe excellent agreement between the DFT data and the CE model in its multiple applications.

Our DFT calculations were based on supercells that contained $3\times3\times3$ primitive fcc unit cells. Although in a binary system $3\times3\times3$ primitive fcc cells may be sufficient to capture the distribution of the binding sites within the bulk material, this may not be true for the ternary systems. The previous methods for defining the binding sites, such as Eq.(2.6) could potentially work properly as long a good distribution of sample points have been considered. The concern we now encounter is whether we have sampled a sufficient distribution of data points to consider our calculated DFT data a complete data set for our ternary systems. This can easily be determined with the validation procedure of the truncated CE models described above. Figure 2.5(a) shows the cumulative probability analysis on our truncated CE model selected for the O sites of the ternary system $Pd_{70}Cu_{26}Au_{4,}$ while Figure 2.5(b) shows the cumulative probability analysis on Eq.(2.6) applied to the O sites of this same ternary alloy. Although both graphs are analyzing the same data the poor fitting and prediction of the model used in Figure 2.5(b) would limit the accuracy of predictions made with this model. This reinforces the observation that the use of a CE models selected via the LOO analysis results in lattice models that are well suited to describe the bulk of the Pd-based and PdCu-based alloys.

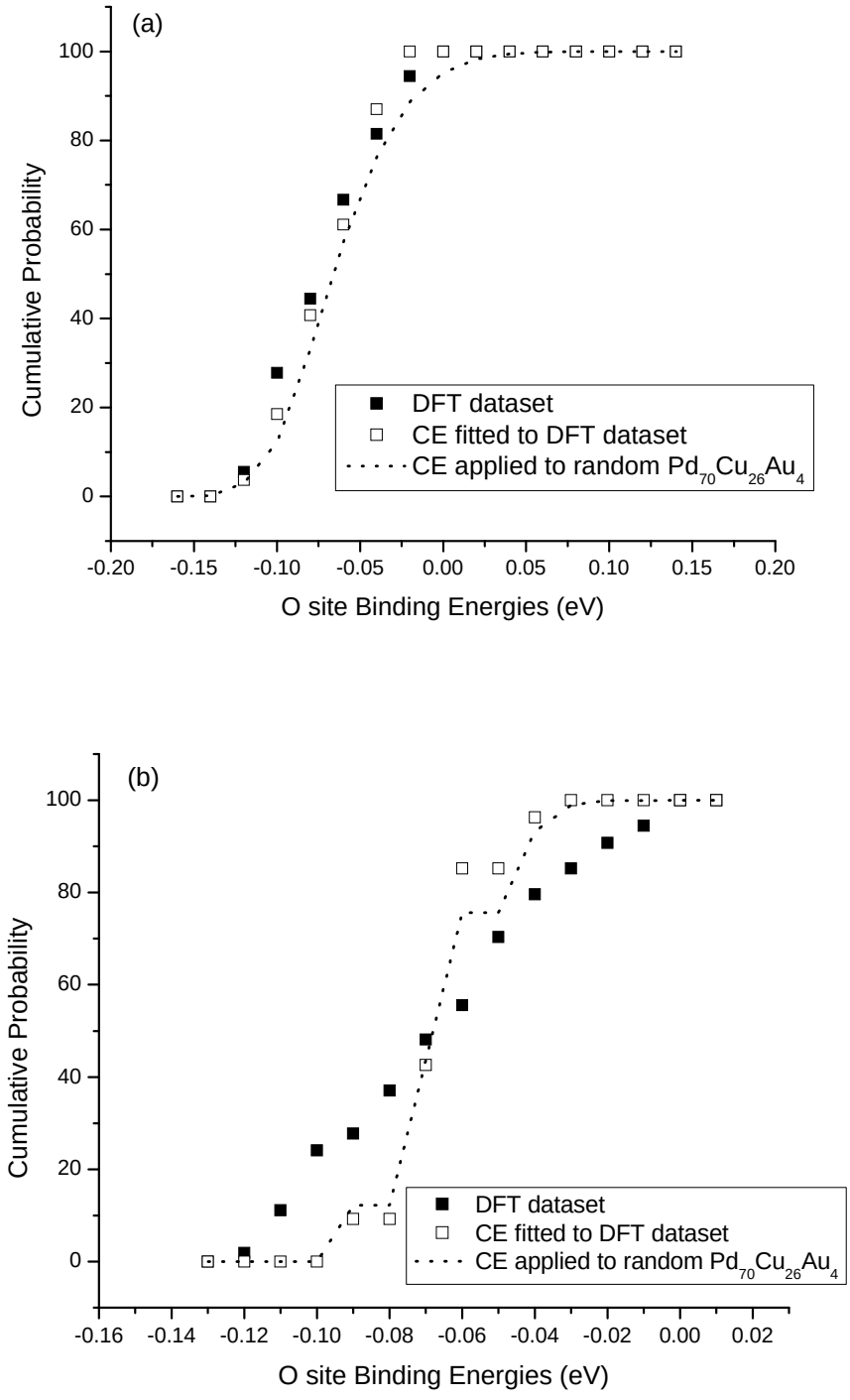

Figure 2.5: Model validation process for $Pd_{70}Cu_{26}Au_4$ (a) for the optimal CE-LOO selected model (b) model following Eq. (2.6) as used by Kamakoti and Sholl. Closed symbols represent the DFT calculated data, open symbols represent CE fitted using only DFT data, and the dotted line represents CE applied to the randomly generated volume representing the alloy of interest.

2.4: Solubility, Diffusion, and Permeability from Lattice Models

Once a lattice model has been defined that gives the binding energies of each interstitial site and transition state in a disordered alloy, the macroscopic properties of H in the alloy such as the net solubility, diffusivity, and membrane permeability can be calculated. Our calculations for these quantities follow Kamakoti and Sholl[13, 14].

2.4.1: Solubility Analysis

We define the concentration of H atoms, Θ_H, as the ratio of the number of H atoms dissolved to the total number of metal atoms in the system. The solubility of dilute amounts of atomic H in metals and alloys can be found using Sieverts' Law[47], which relates the interstitial concentration of atomic H to the gas phase H_2 pressure by:

$$\Theta_H = K_s \sqrt{P_{H_2}} \tag{2.11}$$

where, K_s is the Sieverts' constant[48]. Although the O sites are strongly favored over T sites in most alloys, our analysis of solubility includes both O site and T site contributions. The Sieverts' constant for an individual site, $K_{s,ind}$, with known binding energy can be calculated using:

$$K_{s,ind} = \alpha' \delta e^{-\beta E_b^{ZP}} \tag{2.12}$$

where E_b^{ZP} is the ZPE corrected binding energy of a site, α' represents the translational and rotational effects in the partition function of gas phase H_2[15, 49], and δ incorporates effects of vibrational modes for H in both the interstitial site and as molecular H_2[15]. The net K_s used to define the solubility of H with Eq. (2.11) is the sum of the averages of the $K_{s,ind}$ for the O sites and the T sites in the bulk material.

In order to compute the solubility of H in the bulk of the material of interest we develop a representative volume of the randomly ordered alloy. Specifically, a volume consisting of over 66,000 atoms is generated at the given alloy composition and we calculate the individual contribution towards the solubility of each binding site in order to obtain the net K_s. This procedure is repeated for ten distinct volumes in which the atoms of each volume have been randomly arranged, and the results averaged to determine the final prediction of the material's H solubility. For crystalline materials, such as the ones in this study, the concentration of interstitial H is low at elevated temperatures where the Sieverts' Law is valid. For materials with relatively high solubility of H, such as amorphous material Sieverts' Law can no longer be used to determine the solubility. Instead, methods such as the Grand Canonical Monte Carlo calculations are required to predict the net solubility of interstitial atoms[50].

2.4.2: Diffusion Analysis

Hydrogen diffuses in fcc metals at high temperatures through a series of hops from O sites to T sites via TS. Once all the sites have been characterized, the rate of hopping for an O-T jump can be computed using quantum corrected harmonic transition state theory [13, 14] giving,

$$k_{OT} = \frac{\prod_{i=1}^{3} f(h\nu_i^O / 2k_B T)}{\prod_{i=1}^{2} f(h\nu_i^{TS} / 2k_B T)} \frac{\prod_{i=1}^{3} \nu_i^O}{\prod_{i=1}^{2} \nu_i^{TS}} e^{\frac{-E_a}{k_B T}} \tag{2.13}$$

Here, $f(x) = \sinh(x)/x$, ν_i are the real vibrational frequencies of the binding site or TS, and E_a is the classical activation energy for the particular hop. This expression explicitly includes contributions from the multiple vibrational energy levels available to the

interstitial H at the temperature of interest. Other hops such as from T to O sites or the direct hops from O to O sites, which will be discussed in detail in further chapters, can be described in a similar fashion. This formulation can be extended to include contributions to hopping rates from tunneling between sites[51]. We have not included tunneling contributions in our calculations because they are known to be negligible in the temperature range we considered[51].

The explanation above defines the hopping rate between adjacent interstitial sites, but this is not sufficient to describe the net diffusivity of interstitial H in the bulk of disordered alloys. In order to predict H diffusivity in the materials of interest, the local hopping rates have to be linked with the long range H transport across the bulk. This can be done with Kinetic Monte Carlo simulations (KMC). KMC simulations use the hopping dynamics within a lattice model with local hopping rates defined, as previously described to determine the net diffusivity of interstitial H in the alloys of interest.

2.4.3: KMC Algorithm and Simulation Details

Using the hopping rates we can calculate the diffusivity of H in bulk materials with KMC, given that it is ideally suited to model stochastic systems defined by a succession of events with known rates. KMC can be regarded as a class of algorithm that by randomly choosing from various possible transitions and accepting or rejecting these with appropriate probabilities numerically calculate a stochastic realization of the translation of the atoms. This is accomplished by mapping out all the energy minima in the system and associating the hops with the rates as calculated from Eq. (2.13) via quantum modified harmonic transition state theory. The time scale is incorporated via transition rates for H motion between adjacent binding sites. We used the following KMC

algorithm to follow the time evolution of non-interacting H atoms in fcc Pd-based and PdCu-based alloys, which follow a similar approach to the one utilized by Kamakoti and Sholl[13, 14].

1. Define a simulation volume consisting of randomly arranging the atoms of the alloy at the desired composition.
2. Scan through the entire simulation volume using the CE models for the alloy under study to identify the fastest rate of hopping within all possible hops in the volume, identified as k_{fast}.
3. Randomly position N_H, H atoms among the volume in O sites.
4. At each time step in our KMC an interstitial H is randomly selected from all the H atoms that have been placed in the simulation volume. Next a move direction is chosen randomly from the 8 (4) possible directions available for an O (T) site.
5. Hops are accepted depending on the direction of the hop
    a. O site to T site hops are accepted with probability $2k_{OT}/k_{fast}$
    b. T site to O site hops are accepted with probability k_{TO}/k_{fast}
    c. O site to O site hops are (when they exist) accepted with probability $3k_{OO}/k_{fast}$

    The factors in these acceptance probabilities arise from the different number of hopping directions available to the different types of possible hops.
6. Regardless of the outcome of the attempted hop, time is incremented by $\Delta t = 1/\left(4N_H k_{fast}\right)$, where N_H is the total number of interstitial H atoms in the simulation volume.

It is straightforward to show that this algorithm correctly defines the local hopping rates of all possible processes in our lattice model. Similarly to Kamakoti and Sholl, we have not included site blocking effects in our simulations since we are working with dilute H concentrations. These effects could easily be incorporated in these simulations if simulations of concentration-dependent diffusion were of interest.

A notable contribution to previous work done by Kamakoti and Sholl, is that we have discovered the possibility of additional paths for hopping between interstitial sites. Originally it was thought that if H was found in an O site, labeled A, in order to reach a neighboring O site, labeled B, first the H would have to pass through a T site found between these two O sites. We now know that depending on the additive metal atom used to form an alloy a path directly connecting O site A and O site B can be available. We have briefly mentioned this as O site to O site hopping in this chapter, but further details will be discussed in Chapter 3.

Our simulation volume consisted of $4,000$ metal atoms randomly distributed in an fcc lattice representing the composition of interest. In each simulation, 150 H atoms were randomly distributed in the O sites of the simulation volume. A large number of KMC steps (typically 50,000 steps per H atom) were used to thermally equilibrate the system. After equilibration a further 500,000 MC steps per H atom were performed while collecting data on the trajectory of each atom. After observing a large number of hops in a KMC simulation, the mean square displacement of each H atom is calculated. After correcting for passage across the periodic boundaries, the self diffusivity, D_s, is determined using an Einstein expression relating the diffusivity to the mean square displacement. All of our calculations were performed for substitutionally random alloys.

KMC calculations of this kind can be used to examine the effect of short-range order in metal alloys[14], but we have not pursued this topic here.

2.4.4: Permeability Analysis

The ability of a membrane to transport hydrogen is typically quantified in terms of either flux or permeability. The permeability, *k*, through a membrane can be obtained from[38, 52-54] :

$$k = \frac{N_{H_2} L}{(P_{H_2,ret}^{0.5} - P_{H_2,perm}^{0.5})} \tag{2.14}$$

where N_{H_2} is the H_2 flux, L is the thickness of the membrane, and $P_{H_2,ret}^{0.5}$ and $P_{H_2,perm}^{0.5}$ are the H_2 partial pressures in the retentive and permeate, respectively. This expression is valid when the diffusion of H through the bulk of the membrane is the rate-limiting step of the process and solubility is described accurately with Sieverts' law, assumptions that appear to be accurate for many practical membranes[15]. The importance of other transport resistances in ultra-thin alloy films has been examined recently by Chen and Sholl[55, 56]. Using the definitions above, we can express the permeability of H as[15, 38]:

$$k = \frac{D_s K_s}{2} \tag{2.15}$$

This expression assumes that the interstitial H concentration is dilute, so the diffusion coefficient for H atoms can be accurately represented using the self diffusion coefficient, D_s.

2.5: Summary

In this chapter we have discussed how bulk Pd-based binary and PdCu-based ternary alloys have been analyzed. We began with performing DFT calculations to find

the binding energy of H in a collection of interstitial sites for each material of interest. We then applied the CE method to a set of selected interactions to define interstitial H. A truncated CE model was decided on by performing the LOO analysis to a series of potential truncated CE. Once a CE model was validated, it could be used to determine the macroscopic properties of H in the bulk of the dense metal membranes of interest.

The macroscopic properties of H in the bulk of these materials include the solubility, diffusion, and the permeability. The solubility of H in crystalline materials at high temperatures is relatively low, allowing us to use Sieverts' Law. At elevated temperatures, H diffuses across these membranes via a series of discrete hop between interstitial sites through a TS. Using KMC simulations we are capable of describing the diffusion of H across the membranes. Once both the solubility and the diffusion of H are known for a particular system the permeability is easily obtained. All the methods of analysis described in this chapter have been applied to $Pd_{96}M_4$ for M = Ag, Au, Cu, Ni, Pt, Rh, and Y and to $Pd_{70}Cu_{26}M_4$ for M = Ag, Au, Cu, Ni, Pd, Pt, and Y in subsequent chapters.

2.6: References

1 K. Ohira, Y. Sakamoto, and T. B. Flanagan, J. Alloys and Compounds **236**, 42 (1996).

2 S. Ramaprabhu, Int. J. Hydrogen Energy **23**, 787 (1998).

3 Y. Sakamoto, F. L. Chen, M. Furukawa, and K. Mine, J. Less-Common Metals **166**, 45 (1990).

4 Y. Sakamoto, F. L. Chen, M. Furukawa, and M. Noguchi, J. Alloys and Compounds **185**, 191 (1992).

5 Y. Sakamoto, K. Ohira, N. Ishimaru, F. L. Chen, M. Kokubu, and T. B. Flanagan, J. Alloys and Compounds **217**, 226 (1995).

6 D. Wang, T. B. Flanagan, and K. L. Shanahan, J. Alloys and Compounds **348**, 152 (2003).

7 A. Weiss, Ramaprabhu, S., Rajalakshmi, N., Zeit. Phys. Chem **199**, 165 (1997).

8 D. S. Sholl, J. Alloys and Compounds **446**, 462 (2007).

[9] S. V. Alapati, J. K. Johnson, and D. S. Sholl, Phys. Chem. Chem. Phys. **9**, 1438 (2007).
[10] D. E. Jiang and E. Carter, Phys. Rev. B **70**, 064102 (2004).
[11] B. Bhatia and D. S. Sholl, J. Chem. Phys **122**, 204707 (2005).
[12] O. M. Løvvik and R. A. Olsen, J. Alloys and Compounds **330**, 332 (2002).
[13] P. Kamakoti and D. S. Sholl, J. Membr. Sci. **225**, 145 (2003).
[14] P. Kamakoti and D. S. Sholl, Phys. Rev. B **71**, 014301 (2005).
[15] P. Kamakoti, B. D. Morreale, M. V. Ciocco, B. H. Howard, R. P. Killmeyer, A. V. Cugini, and D. S. Sholl, Science **307**, 569 (2005).
[16] C. G. Sonwane, J. Wilcox, and Y. H. Ma, J. Chem. Phys **125**, 184714 (2006).
[17] C. G. Sonwane, J. Wilcox, and Y. H. Ma, J. Phys. B. **110**, 24549 (2006).
[18] R. Drautz and A. Diaz-Ortiz, Phys. Rev. B **73**, 224207 (2006).
[19] H. Y. Geng, M. H. Sluiter, and N. X. Chen, Phys. Rev. B **73**, 012202 (2006).
[20] L. Semidey-Flecha and D. S. Sholl, J. Chem. Phys. **128**, 144701 (2008).
[21] http://cms.mpi.univie.ac.at/vasp/.
[22] C. Fiolhais, F. Norguera, and M. A. L. Marques, *A Primer in Density Functional Theory* (Spinger-Verlag: Berlin, 2003).
[23] D. S. Sholl and J. A. Steckel, *Density Functional Theory: A Practical Introduction* (John Wiley & Sons, Inc., 2009).
[24] J. P. Perdew, J. A. Chevary, S. H. Vosko, K. A. Jackson, M. R. Pederson, D. J. Singh, and C. Fiolhais, Phys. Rev. B **46**, 6671 (1992).
[25] A. R. Denton and N. W. Ashcroft, Phys. Rev. A **43**, 3161 (1991).
[26] A. K. M. F. Kibria and Y. Sakamoto, Int. J. Hydrogen Energy **25**, 853 (2000).
[27] Y. Sakomoto, F. L. Chen, M. Ura, and T. B. Flanagan, Ber. Buns. Gesell **99**, 807 (1995).
[28] K. W. Kehr, in *Topics in Applied Physics* (Springer-Verlag, Berlin, 1978), Vol. 28, p. 197.
[29] X. Ke and G. J. Kramer, Phys. Rev. B **66**, 184304 (2002).
[30] O. M. Løvvik and R. A. Olsen, J. Chem. Phys. **118**, 3268 (2003).
[31] E. Wicke and H. Brodowsky, *Hydrogen in Metals II* (Springer-Verlag, Berlin, 1978).
[32] C. P. Flynn and A. M. Stoneham, Phys. Rev. A **1**, 3966 (1970).
[33] J. Greeley, Mavrikakis, M, Surf. Sci **540**, 215 (2003).
[34] G. Alefeld and J. Völkl, *Hydrogen in Metals I* (Springer-Verlag, Berlin, 1978).
[35] H. Barlag, L. Opara, and H. Zuchner, J. Alloys and Compounds **330**, 434 (2002).
[36] S. Fujita and A. Garcia, J. Phys. Chem. Solids **52**, 351 (1991).
[37] G. Henkelman, Uberuga, B.P., Jonsson, H, J. Chem. Phys **113**, 9901 (2000).
[38] B. D. Morreale, M. V. Ciocco, R. M. Enick, B. I. Morsi, B. H. Howard, A. V. Cugini, and K. S. Rothenberger, J. Membr. Sci. **212**, 87 (2003).
[39] S. N. Paglieri and J. D. Way, Sep. Purif. Methods **31**, 1 (2002).
[40] M. H. F. Sluiter and Y. Kawazoe, Phys. Rev. B **71**, 212201 (2005).
[41] A. Seko, K. Yuge, F. Oba, A. Kuwabara, I. Tanaka, and T. Yamamoto, Phys. Rev. B **73**, 094116 (2006).
[42] H. Y. Geng, M. H. F. Sluiter, and N. X. Chen, J. Chem. Phys **122**, 214706 (2005).
[43] S. Muller, Surf. Interface Anal. **38**, 1158 (2006).
[44] T. Morita, J. Math. Phys. **13**, 115 (1972).

[45] R. Kikuchi, Phys. Rev. **81**, 988 (1951).
[46] H. A. Martens and P. Dardenne, Chemometics and Intelligent Lab. Syst. **44**, 99 (1998).
[47] T. L. Ward and T. Dao, J. Membr. Sci. **153**, 211 (1999).
[48] B. D. Morreale, M. V. Ciocco, B. H. Howard, K. S. Rothenberger, A. V. Cugini, and R. M. Enick, J. Membr. Sci. **241**, 219 (2004).
[49] D. A. McQuarrie, *Statistical Mechanics* (University Science Books, 2000).
[50] S. Hao and D. S. Sholl, Energy Environ. Sci. **1**, 175 (2008).
[51] B. Bhatia and D. S. Sholl, Phys. Rev. B **72**, 224302 (2005).
[52] L. Schlapbach and A. Züttel, Nature **414**, 353 (2001).
[53] R. C. Brouwer, E. Salomons, and R. Griessen, Phys. Rev. B **38**, 10217 (1988).
[54] K. S. Rothenberger, B. H. Howard, R. P. Killmeyer, A. V. Cugini, R. M. Enick, F. Baustmante, M. V. Ciocco, B. D. Morreale, and R. E. Bauxbaum, J. Membr. Sci. **218**, 19 (2003).
[55] C. Ling and D. S. Sholl, J. Membr. Sci. **303**, 162 (2007).
[56] L. Mc. Leod, F. L. Degertekin, and A. Fedorov, J. Membr. Sci. **(in review)** (2007).

CHAPTER 3

Pd-BASED BINARY ALLOYS FOR H PURIFICATION

Metal membranes have received much attention for H_2 purification given their wide range of operational standard and the high selectivity over other gas species[1]. Several reviews are available describing the large body of experimental work that exists for metal membranes[2-5]. Pd membranes are the most widely studied films for hydrogen purification purposes. Unfortunately pure Pd membranes are prone to problems such as H_2-induced embrittlement at temperatures below 300 ˚C[2]. Pd membranes are also prone to poisoning due to the presence of sulfur or unsaturated carbon compounds such as those found in flue gases[3].

Pd-based alloys can potentially offer improvements to pure Pd membranes while retaining the desired properties Pd membranes have to offer. Pd has been the core material for binary alloy membranes, in combination with elements including boron, cerium, copper, gold, iron, nickel, silver, yttrium, among others[4]. The properties of hydrogen in Pd and Pd-based binary alloys have been well documented for many alloy compositions given the large number of experiments performed on these systems. Binary alloys composed of Pd and larger additive atoms such as Au, and Ag have been extensively studied by Sakamoto *et al*., Wang *et al*., Okazaki *et al*., Zhang *et al*., Chen *et al*., Fort *et al*., and Maestas *et al*. [5-13]. Other transition metals similar to Pd in size such as Pt and Rh have also been extensively studied for alloy stability, separation applications, and resistance to sulfur contamination resistance[14-22]. Copper as an additive metal atom to form $Pd_{100-x}Cu_x$ alloys has been widely studied both experimentally and theoretically

given the improved sulfur resistance these alloys have over pure Pd membranes[3, 23-29]. Ni has been widely used to form binary alloys with other metals such as Ta and V as well as for the study of ternary alloys for both H purification and stability of membranes[30-35].

In Figure 3.1 we have plotted the experimentally reported solubility of H in $Pd_{100-x}M_x$ (in at.%) normalized by the solubility of H in pure Pd at the same experimental conditions for M = Au, Ag, Pt, Cu, and Ni[8, 22, 26, 27, 36]. It can be observed that the alloys formed with M atoms larger in size than Pd, that is Ag and Au, enhance the solubility of H. This suggests that a connection exists between the changes in lattice constant of the alloy in comparison to the lattice of pure Pd, and the net solubility of H in the alloy. Although at

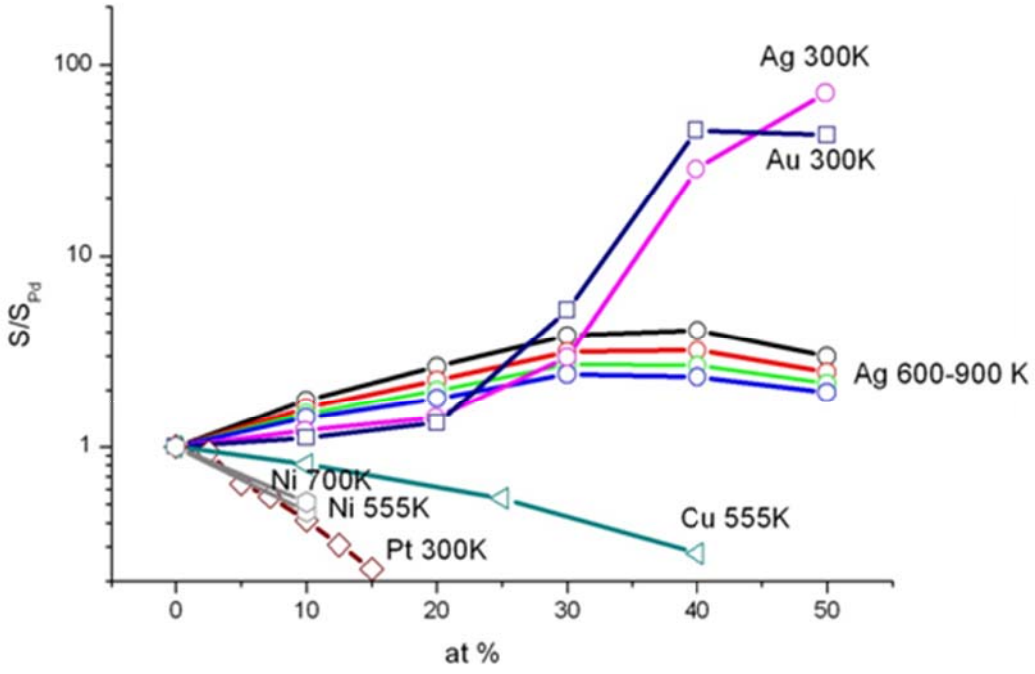

Figure 3.1: Experimental results for the solubility of H in Pd-based binary alloys as the content of the additive metal atom is increased, normalized with respect to the solubility of H in pure Pd at the same conditions[8, 22, 26, 27, 36]. The temperature associated with each data set is indicated.

low temperatures Sieverts' Law may not be as accurate as it is for higher temperatures, the purpose of Figure 3.1 was to portray the effects of $Pd_{100-x}M_x$ on H solubility in comparison to H solubility in pure Pd.

Binary alloys with cerium, copper, gold, silver, and yttrium exhibit higher permeability than each of the metals exhibit individually under at least some circumstances. In Figure 3.2 we have plotted a compilation of key experimental results observed for permeability of H in $Pd_{100-x}M_x$ for M = Y, Au, Ag, and Cu normalized with respect to pure Pd under the same experimental conditions[8, 12, 37, 38]. We note that there are some alloys such as $Pd_{100-x}Y_x$ for which permeability data is readily available but not solubility data. One difference from the solubility plot is that the addition of Au in Pd-based binary alloys is not advantageous for H separation in comparison to pure Pd, at

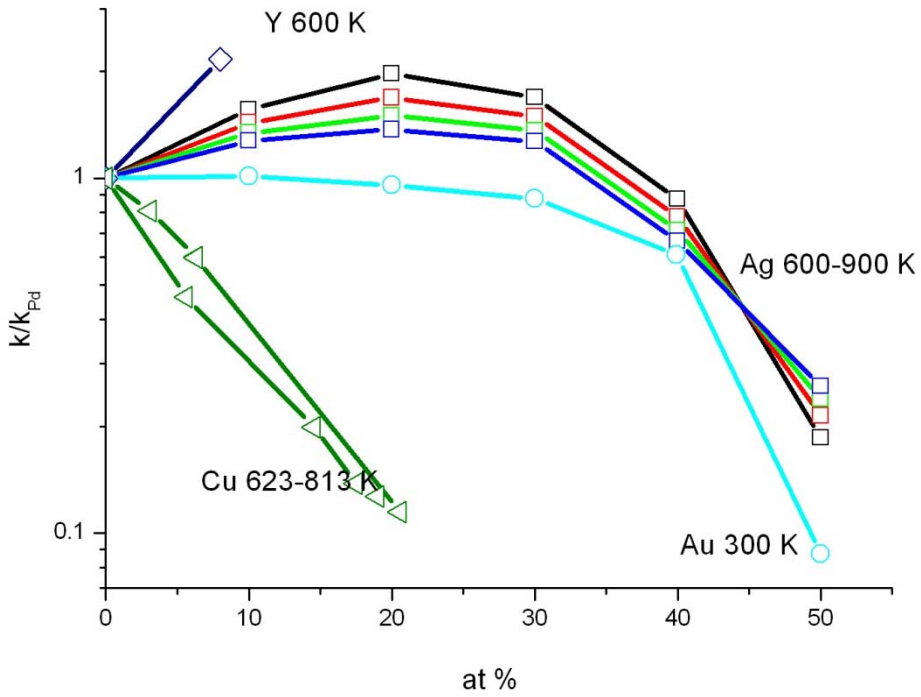

Figure 3.2: Experimental results for permeability of H in Pd-based binary alloys as the content of the additive metal atom is increased, normalized with respect to the permeability of H in pure Pd at the same conditions[8, 12, 37, 38]. The temperature associated with each data set is indicated.

least in terms of H_2 flux under these conditions. Another observation is that increasing the Ag content improves H permeability up to roughly 23 at.% of Ag in the $Pd_{100-x}Ag_x$. However a reduction in permeability is observed in $Pd_{100-x}Ag_x$ for Ag content over 35 at.%.

The ultimate goal of using binary alloys in membranes is to have high hydrogen fluxes while remaining active under conditions where pure Pd would normally not function. The flux of hydrogen depends on the properties of H in the bulk of these membranes. These properties include the solubility and diffusion of H in the bulk of these materials, both of which contribute to permeability, as explained previously in Chapter 2. Although experimentally some binary alloy compositions have been shown to improve the behavior of H in these dense membranes, it is not clearly understood known how these metals contribute to the improvements. The focus of the work in this chapter will be in understanding the effects of dilute amounts of an additive metal in a Pd-rich binary membrane. The Pd-based binary alloys examined in this chapter will have composition $Pd_{96}M_4$ (at.%), where M represents the additive metal atoms used. Results will be presented for M = Ag, Au, Cu, Ni, Pt, and Rh.

In this chapter we will discuss the reasons behind selecting M = Ag, Au, Cu, Ni, Pt, and Rh as additive atoms used in the binary alloys. We will also discuss our calculated density functional theory (DFT) results for the binding site of H in the bulk of these membranes. In Chapter 2 we outlined the cluster expansion (CE) method, and now we will present the results of using this methods for the seven $Pd_{96}M_4$ alloys listed above. Having accurate CE models to describe the binding sites in the bulk of the Pd-rich alloys

enabled the calculation of H solubility, diffusion and permeability as described in Chapter 2 for the temperature range of 400 – 1200 K.

3.1: Selection of Additive Metal Atoms

Although the work to be described in based on first principles quantum chemistry calculations, we do not attempt to use these calculations to predict the phase diagrams of the metal alloys of interest. The phase diagrams of binary metal alloys are well known experimentally[39-41]. We used these phase diagrams to examine if material we examined would be influenced by immiscibility gaps or changes in crystal structure. Kamakoti and Sholl have previously worked on PdCu alloys with both fcc and bcc crystal structures[23]. Their aim was to develop a theoretical framework capable of screening through alloys at different compositions and operating conditions only using only knowledge of the phase diagrams. Experimentally it has been shown that PdCu alloys in the bcc structure tend to have higher H permeability than in the fcc structure[23]. For the purpose of this work, however, we have focused all our efforts on fcc structures. This decision was made because the bcc material examined by Kamakoti and Sholl is only thermodynamically stable over a limited temperature range.

Most metals are at least partially miscible in Pd. In analyzing the phase diagrams of Pd and M = Ag, Au, Cu, Ni, Pt, and Rh we can group the formation tendencies of these binary alloys into three categories. The first category is when the two metals are both fcc crystals as single elements and are completely miscible. In this case, randomly ordered fcc alloys form regardless of the composition of the alloy. Ag and Ni show this behavior when alloyed with Pd. When Au is alloyed with Pd, fcc crystals are formed at

all temperatures, although there are compositions where ordered fcc alloys are formed. There are three ordered fcc regions. One occurs for composition of approximately 12 to 30 at.% Au for temperatures between 973– 1143 K forming the $AuPd_3$ structure. Another ordered region is found for compositions of approximately 68 - 88 at.% Au with structures of Au_3Pd for temperatures between 873 – 1123 K. The third region has an alloy structure known as AuPd, and is observed for compositions of 43 - 57 at.% for temperatures up to 373 K. The existence of this AuPd ordered structure is controversial[39]. According to the phase diagrams, the $Pd_{100-x}Au_x$ experimental data shown in Figure 3.1 for T = 300 K should cross between the ordered and disordered regions. No ordering was reported in that study[8,13]. In the second category, formation of both ordered and disordered fcc alloys are observed for the majority of alloy compositions with the exception of one or more gaps in which the alloys formed have different crystal structures. This situation occurs when Cu is alloyed with Pd. At temperatures lower than 873 K, a broad region of the PdCu phase diagram including all alloys with greater than 60 atomic percent of Pd exists as a disordered fcc phase. For a range of compositions centered around 40 atomic percent of Pd, the stable phase in this region at low temperatures is an ordered bcc phase. In the third and final category, fcc alloys form but a large miscibility gap exist in the phase diagram. If alloys with compositions lying inside the miscibility gap are prepared, they will phase separate into phases defining the envelope of the miscibility gap at equilibrium. This kind of miscibility gap exists when Pt and Rh are used as additive metal atoms in Pd to form alloys. For Pt in Pd this miscibility gap exist for compositions of approximately 10 to 90 atomic percent of Pt for

Table 3.1: Binary alloys at the compositions of this study, their DFT calculated lattice constants in Å, and the percent difference between the lattice constant of the alloys and that of pure Pd.

Alloy Composition	Lattice Constant (Å)	% of Difference with pure Pd
$Pd_{96}Au_4$	3.968	0.202
$Pd_{96}Ag_4$	3.966	0.151
$Pd_{96}Pt_4$	3.961	0.025
Pure Pd	3.960	0.000
$Pd_{96}Rh_4$	3.960	0.000
$Pd_{96}Cu_4$	3.950	-0.253
$Pd_{96}Ni_4$	3.947	-0.329

temperatures between 573 K – 1043 K. A continuous fcc structure is observed for all other composition and temperatures. For Rh in Pd the miscibility gap exists when about 6to 90 atomic percent of Rh is used in the alloy for temperatures of 773 – 1118 K.

In determining which additive metal atoms were to be used, in addition to forming fcc structures, we included selections which expand and contract the lattice of the structure in comparison to pure Pd. Table 3.1 lists the DFT optimized lattice constants for Pd-rich binary alloys using M = Ag, Au, Cu, Ni, Pt, and Rh as the additive metal atoms. For additional information of how to calculate the lattice constants, please refer to Chapter 2. In Table 3.1 a positive difference between the lattice of the alloy and pure Pd corresponds to a lattice expansion. The additive metal atoms used in this study can be classified into three distinct groups. The first group consist of M = Au and Ag. These metal additives represent a lattice expansion of the alloy in comparison to pure Pd. The second group consists of M = Pt and Rh; these metal additives cause little to no expansion of the lattice. The third group consists of metal additives that contract the lattice in comparison to pure Pd, namely M = Cu and Ni.

3.2: Binding Sites and Transition States for Site to Site Hopping

In fcc crystal structures H can reside within the bulk of these materials in two distinct binding sites. These binding sites are known as the 6-fold octahedral (O) site and the 4-fold tetrahedral (T) site. In fcc materials, the O site typically binds H atoms more strongly than T sites[42]. More details of these binding sites can be found in Chapter 2. In the bulk of a substitutionally random alloy membrane, there are many structurally distinct interstitial sites. A simple way of describing the interstitial sites would be to count the number of Pd atoms in the nearest neighboring ($2\times N$) shell and in the next to nearest neighboring ($3\times N$) shell. Characterizing the O sites of the substitutionally random $Pd_{96}M_4$ alloys in this way, we performed DFT calculations for 21 distinct O sites. The 21 O sites we examined would represent about 99% of all possible sites in the substitutionally random material if the simple characterization of the sites just described were used. These O sites ranged from having 0 – 3 M atoms in the $2\times N$ and $3\times N$ shells. We also analyzed the geometrically independent T sites that surrounded these 21 O sites, resulting in a total of 88 DFT calculated T sites.

At elevated temperatures, H diffuses in fcc metals through discrete hops between adjacent O and T sites via transition states (TS)[43, 44]. In order to characterize this process, the TS that control these hops must be known. For individual hops between interstitial sites, the TS can be located within DFT via the Nudged Elastic Band (NEB) method[45]. We analyzed the TS defined by each pair of adjacent O and T sites from the set of interstitial sites listed above in this way. From NEB calculations we were able to identify the TS between all the O and T sites analyzed. This procedure results in a total of 92 TS calculations. The NEB method is a multistep process, consisting of first locating an

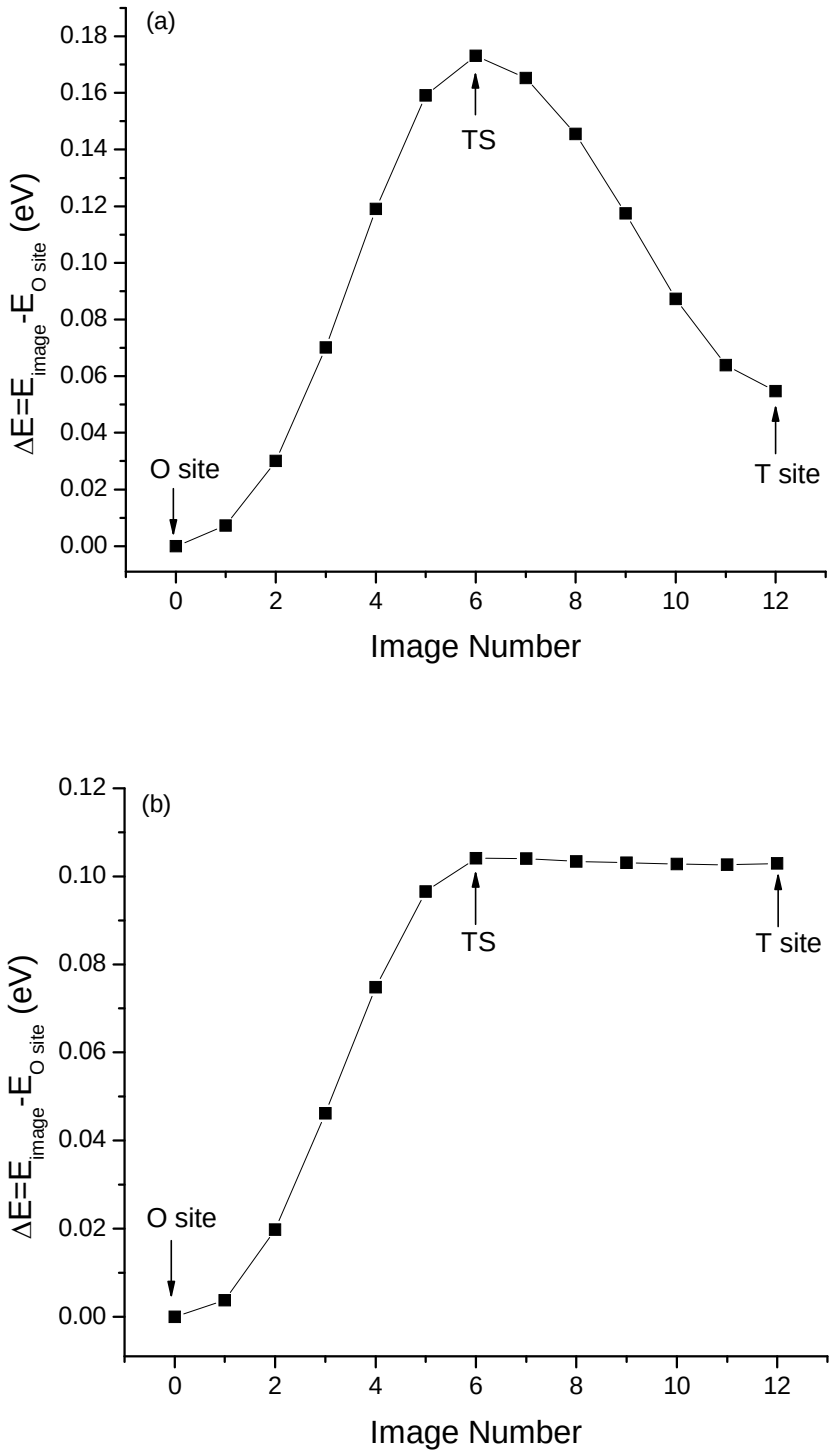

Figure 3.3: NEB results for H hopping from an O site to a T site in (a) pure Pd and (b) $Pd_{96}Ag_4$ alloy with Ag in the $2\times N$ shell of the T site. In both cases, energy is defined relative to the energy in the initial O site.

estimated location of the TS, followed by a final calculation to find the TS. We performed NEB calculations for $Pd_{96}M_4$ for M = Ag, Rh and Cu in order to account for a range in lattice expansion and contractions. Upon completion of the first step in the NEB calculations we realized the initial estimates of the TS for these three alloys were very similar. This does not mean that the final location of the TS in different alloys were identical, but it showed that converged results for the TS in one alloy could be used to give accurate estimates to start calculations in other alloys. When accurate initial estimates are available for a TS, a well converged result can be obtained using a standard geometry optimization calculation rather than a more computationally intensive NEB calculation. This approach was adopted to determine the precise geometry and energy of the 92 TS in each of the remaining alloys.

For our $Pd_{96}M_4$ alloys when M = Pt, Rh, Cu, and Ni all TS calculations gave well defined TS for every pair of O and T sites we examined. For $Pd_{96}M_4$ alloys in which the additive metal atom expands the lattice constant (M = Au and Ag) however, a complication arose in a number of cases. These cases have important implications for accurately modeling Pd-based alloys containing these additive metal atoms. Hence, we describe these complications in some detail. Figure 3.3 shows the outcome from two NEB calculations for H hopping between an O and a T site, one in pure Pd and another in $Pd_{96}Ag_4$. In pure Pd, the TS between the interstitial sites is clearly defined. In the $Pd_{96}Ag_4$ example, however, no distinct TS exists between the O and T sites. Analysis of many examples in this alloy, as well as in the alloy with M = Au, showed that this situation occurs whenever an H atom moves through a triangular face in an O site defined by three Pd atoms into a T site where the fourth atom (i.e., the metal atom opposite the entering H)

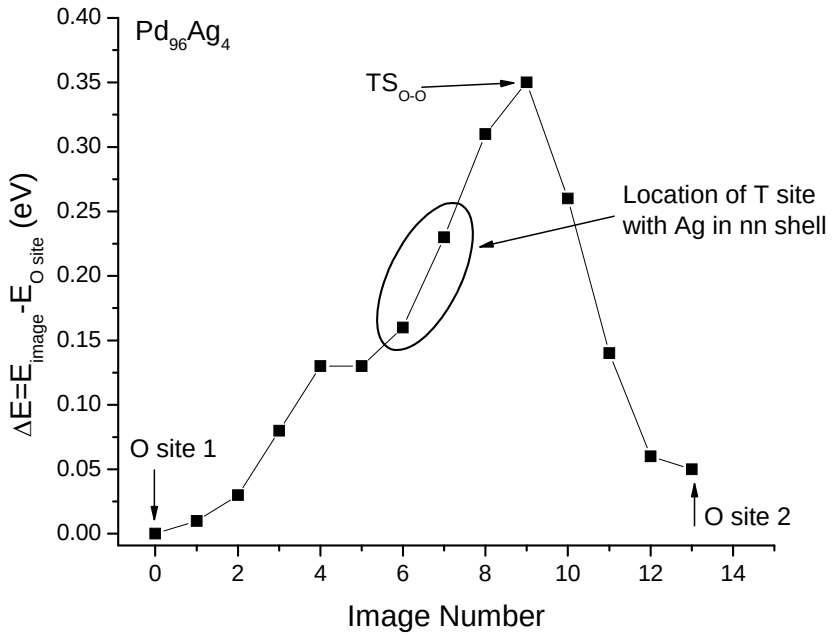

Figure 3.4: NEB results for hopping of H between adjacent O sites in $Pd_{96}Ag_4$ via a T site that includes one Ag (larger than Pd) atom. Energy is defined relative to the energy of the first O site.

is M. An example of an NEB result for $Pd_{96}Ag_4$ that indicates how to interpret the H hopping through these sites is shown in Figure 3.4. As an H atom moves from an O site into a T site along a path that approaches an M atom, there is no distinct TS and the T site is no longer a local minimum in energy. If the H atom moves away from the T site toward one of the other adjacent O sites, it passes over a well defined TS. This is, H can move via a direct hop between two O sites. This situation cannot occur when a TS exist between every adjacent pair of O and T sites, as in the case for $Pd_{96}M_4$ with M = Pt, Rh, Cu, and Ni.

The physical origin of this result is straightforward. Au and Ag atoms are considerably larger than Pd, and the repulsion associated with these atoms partially fills the region that is typically available to define the interstitial T site. We have performed

similar calculations for the ternary Pd-Cu-Ag alloys; these calculations show the same phenomenon for each T site that includes an Ag atom. In dealing with interstitial H we calculate the zero point energy (ZPE) for all interstitial binding sites; additional information on this topic can be found in Chapter 2. For these particular T sites the vibrational frequencies of H, υ_i^H, behave as TS, where one of the three frequencies is imaginary. This is an added way to identify T sites that are no longer local energy minima. This behavior does not seem to have been previously recognized for H diffusion in Pd-based alloys containing additive metal atoms considerably larger than Pd such as Au and Ag[46, 47].

3.3: Cluster Expansion Model Results for $Pd_{96}M_4$ Alloys

Because we are working with substitutionally disordered alloys membranes with many structurally distinct binding sites, the simple method of characterizing these sites consisting of counting of Pd atoms in the $2\times N$ and the $3\times N$ shells cannot fully distinguish between sites. In order to properly distinguish and characterize the DFT calculated binding sites, a cluster expansion (CE) method combined with the leave-one-out (LOO) analysis was used to determine an appropriate lattice model. For detailed information of how to apply the CE and the LOO analysis please refer to Chapter 2. To maintain clarity, the binding energy (E_b) model coefficients are listed separately from the zero point energy (ZPE) model coefficients for all binding sites of each individual $Pd_{96}M_4$ alloy membrane in Appendix B.

As described in Chapter 2, we first need to find a model that is capable of describing the DFT calculated interstitial binding sites. This is done by calculating the

standard deviation between the values predicted by the CE model and the DFT calculated results. The standard deviation σ is computed as follows:

$$\sigma = \sqrt{\frac{\sum_{i=1}^{N}\left(X_i - \overline{X}\right)^2}{N}}, \overline{X} = \left|\left(E_{m,k} - E_k\right)\right| \tag{3.1}$$

where the binding energy E_b determined from a model *m* for binding site *k* to the E_b of the DFT data set of *N* data points. Table 3.2 lists the standard deviation for the CE models selected for each of the Pd-rich binary alloys. We can see that all the models have good capability in describing the DFT calculated binding energies as well as the ZPE of

Table 3.2: Standard deviation between the DFT calculated data and the CE models for the E_b and the ZPE for each of the $Pd_{96}M_4$ binary alloys in this study.

	$Pd_{96}Cu_4$		$Pd_{96}Ni_4$	
	E_b (eV)	ZPE (eV)	E_b (eV)	ZPE (eV)
O sites	0.0029	0.0022	0.0011	0.0013
T sites	0.0065	0.0066	0.0103	0.0017
TS	0.0070	0.0024	0.0169	0.0037

	$Pd_{96}Pt_4$		$Pd_{96}Rh_4$	
	E_b (eV)	ZPE (eV)	E_b (eV)	ZPE (eV)
O sites	0.0016	0.0033	0.0002	0.0029
T sites	0.0020	0.0005	0.0049	0.0036
TS	0.0170	0.0016	0.0010	0.0008

	$Pd_{96}Au_4$		$Pd_{96}Ag_4$	
	E_b (eV)	ZPE (eV)	E_b (eV)	ZPE (eV)
O sites	0.0089	0.0086	0.0012	0.0035
T sites	0.0090	0.0017	0.0040	0.0027
TS	0.0403	0.0022	0.0339	0.0040

H in these sites. The standard deviation was calculated using only the sites that were true energy minima.

In order to further convince ourselves that the CE models are capable of properly fitting the DFT calculated data, we plot the DFT data and the fitted CE model. This allows a visual aid in determining how well the CE model fits the DFT data. It is of course important that the model accurately describes sites for which no DFT data has been gathered. Hence we also compare the predictions of the CE model for a randomly generated volume, representing the bulk of these Pd-rich binary alloys, with the set of sites examined in our DFT results. In order to simplify the explanation of our results we will continue separating the binary alloys into three groups consisting of M contracting the lattice constant, making only small changes in the lattice constant, and M expanding the lattice constant of the alloy in comparison to pure Pd.

To compare results from our CE model on a randomly generated volume with DFT data, we must decide how to weight our DFT data. As described in Chapter 2, the sites examined by DFT were selected using a simple characterization of counting the nearest-neighboring and next-to-nearest-neighboring metal atoms, $N_{2\times N}$ and $N_{3\times N}$. This approach identified 21 distinct O sites. From this set of O sites, 90% of the bulk material would be composed of only three of the 21 O sites calculated if this simple characterization was valid. A CE model is obtained by performing a least squares fit treating all sites equally. This approach is not suitable, however, for the validation approach based on calculating the cumulative probability of sites observed as a function of energy that was explained in Chapter 2. Instead, the relative weighting for each site examined with DFT in a random volume had to be determined. To accomplish this task in

a way that was independent of the CE model being examined, we used a randomly generated volume at the alloy composition of interest and examined all available binding sites. These sites are characterized by counting the number of Pd atoms in the shells surrounding the binding site up to the next-to-next-nearest-neighboring metal atom shell, $N_{4\times N}$. Once the sites have been characterized in this way, the probability of finding each site in the bulk of the random volume was recorded. The sites associated with DFT data were each characterized in the same way. The weighting defined by this procedure was applied to our DFT calculated O sites, T sites, and TS in performing the validation procedure outlined in Chapter 2.

We will begin by analyzing M atoms that reduce the lattice constant of the binary alloys in comparison to pure Pd, that is M = Cu and Ni. Figure 3.5(a) shows the DFT and CE model data for $Pd_{96}Cu_4$. The nomenclature for this figure and the similar figures that follow is that the O sites are represented by squares, T sites are represented by triangles, and the TS are represented by circles. The same energy range is shown in each figure of this type to facilitate comparison of different alloys. It can be observed that the low standard deviation results in an excellent fit between the CE model and the DFT data for the O sites, T sites, and TS. This agreement allowed us to proceed in analyzing the CE model for each binding site within a randomly generated volume at the desired composition as shown in Figure 3.5(b). The same nomenclature as in Figure 3.5(a) is applied in Figure 3.5(b).

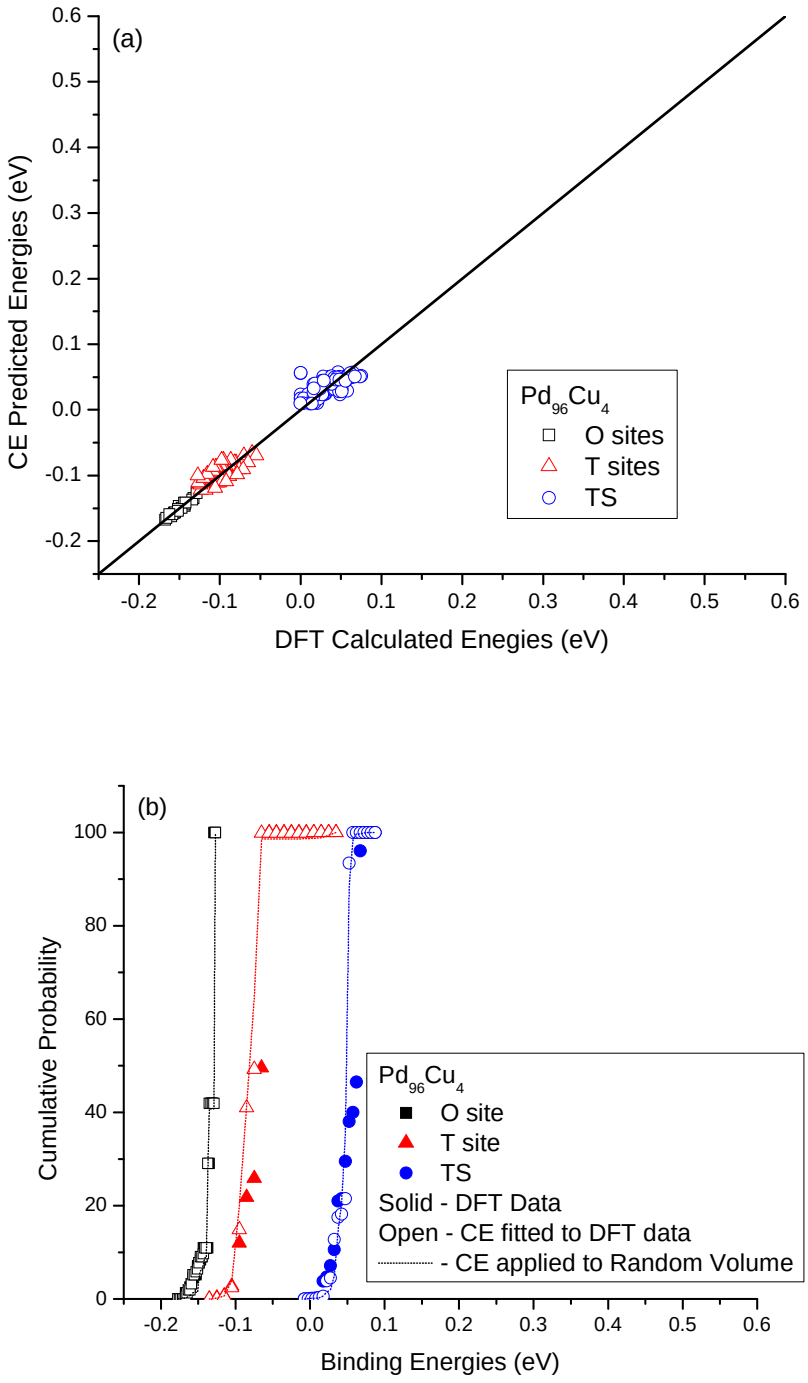

Figure 3.5: Cluster expansion for $Pd_{96}Cu_4$. The O sites are represented by squares, triangles represent the T sites, and circles represent TS. (a) A comparison of the CE model and the DFT data. (b) The DFT data and the CE model fitted using only DFT data (open symbols), and the CE model applied to a randomly generated volume (lines).

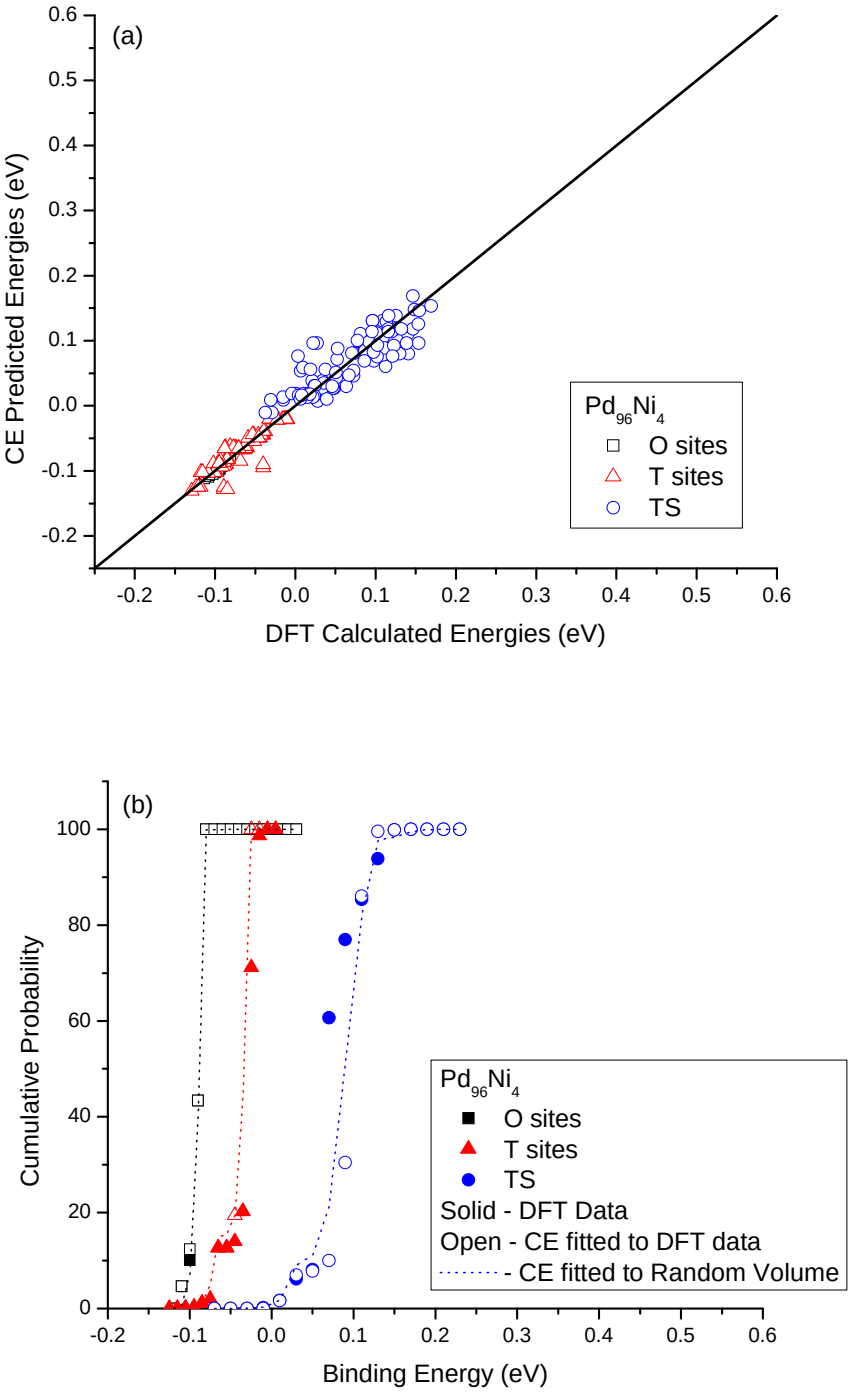

Figure 3.6: Cluster expansion for $Pd_{96}Ni_4$. The O sites are represented by squares, triangles represent the T sites, and circles represent TS. (a) A comparison of the CE model and the DFT data. (b) The DFT data and the CE model fitted using only DFT data (open symbols), and the CE model applied to a randomly generated volume (lines).

Focusing on the O sites, Figure 3.5(b) shows that the CE model not only fits the DFT data but has excellent performance within the randomly generated volume. Within the randomly generated volume, the CE model has not predicted any O sites that were lower in binding energy than the sites already examined with DFT. A binding site with lower energy would force us to perform additional DFT calculations, because the lowest energy sites dominate H solubility and therefore must be described with precision. Similarly the CE models for the T sites and TS performed well. Figure 3.5(b) suggests that the DFT calculated data was sufficient in encompassing the H behavior in $Pd_{96}Cu_4$.

Figure 3.6(a) shows the DFT and CE model data for $Pd_{96}Ni_4$. For all interstitial binding sites, each individual CE model has good agreement with the DFT data. The cumulative probability analysis for this alloy is shown in Figure 3.6(b). Figure 3.6(b) shows there is a good correlation between the DFT data and the CE model. Generally in fcc materials the O sites are the most favorable interstitial binding sites. Comparing the O site and T site binding energies in Figure 3.6(a) this generalization is not the case for all interstitial binding sites in the $Pd_{96}Ni_4$ alloy. Figure 3.6(a) illustrates that the T sites are the binding sites with the lowest energy values for this alloy. Analyzing these T sites showed that when two Ni atoms are found in the nearest neighbor shells, low energy binding T sites are formed. A physical explanation for this phenomenon is the presence of multiple Ni atoms causing there to be a distortion in the cage area of the T site. Because Ni atoms are smaller than Pd atoms, the space of the T site cage is increased in comparison to one composed of pure Pd. This allows for additional volume for an interstitial H, allowing the T sites to become more favorable, and in some cases enhanced over some O sites.

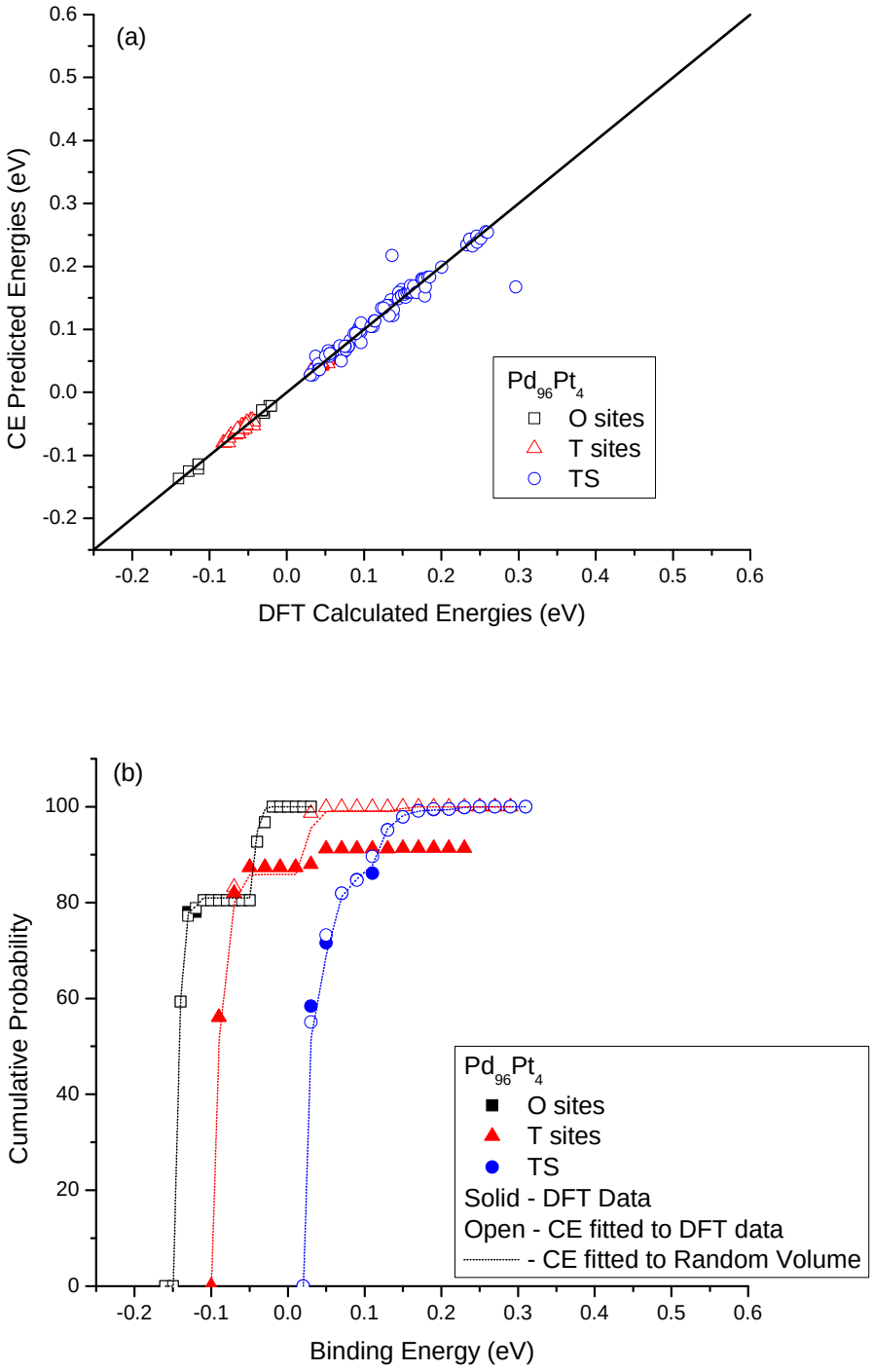

Figure 3.7: Cluster expansion for $Pd_{96}Pt_4$. The O sites are represented by squares, triangles represent the T sites, and circles represent TS. (a) A comparison of the CE model and the DFT data. (b) The DFT data and the CE model fitted using only DFT data (open symbols), and the CE model applied to a randomly generated volume (lines).

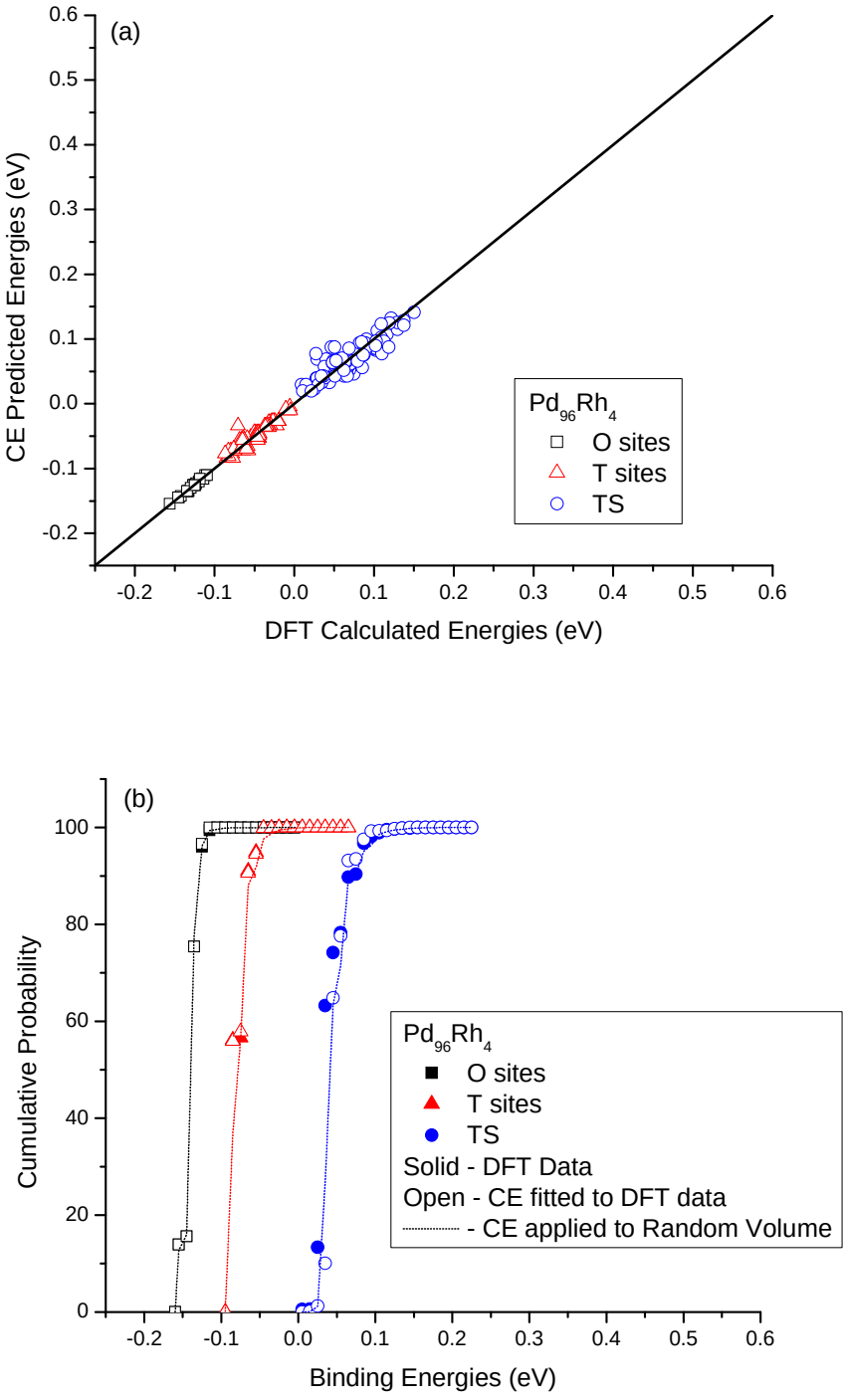

Figure 3.8: Cluster expansion for $Pd_{96}Rh_4$. The O sites are represented by squares, triangles represent the T sites, and circles represent TS. (a) A comparison of the CE model and the DFT data. (b) The DFT data and the CE model fitted using only DFT data (open symbols), and the CE model applied to a randomly generated volume (lines).

We continue with M = Pt and Rh, which have little to no effect to the lattice constant of the alloy in comparison to pure Pd. We compare the DFT and CE data for M = Pt in Figure 3.7(a). Table 3.2 shows that the $Pd_{96}Pt_4$ standard deviation for the TS is higher than for the O sites or the T sites. Figure 3.7(a) indicates that the reason for this outcome is that two TS are poorly fitted by the CE models for these binding sites. It is important to remember that in dealing with the complete set of TS, this CE model is capable of properly describing the remaining 90 TS that were examined with DFT. Although the CE model for the TS has some discrepancies, we performed the validation procedure using a randomly generated volume representing $Pd_{96}Pt_4$ bulk material. The CE model validation for the O sites, T sites, and TS has been plotted in Figure 3.7(b). An important observation from this figure is that the two TS mentioned above have at most a minor effect on the total energy distribution of the TS available in $Pd_{96}Pt_4$.

$Pd_{96}Rh_4$ is an interesting alloy for analysis from the standpoint that addition of Rh at this alloy composition does not change the lattice constant of the alloy in comparison to pure Pd. This implies that any change in the behavior of H in the alloy is a result of a chemical effect due to the presence of Rh. Figure 3.8(a) plots the CE analysis for this binary system. From both Figure 3.8(a) and Figure 3.8(b) it is observed that the CE models for all binding sites have excellent agreement.

The final set of binary alloys is $Pd_{96}M_4$ for M = Au and Ag. Figure 3.9(a) shows the DFT and CE data for $Pd_{96}Au_4$. Similarly to what was observed for $Pd_{96}Pt_4$, two TS are poorly predicted by the CE model for these binding sites. Due to the excellent fit to the remaining TS, we proceed to perform the validation procedure. We compare the CE model for each binding site with a randomly generated volume in Figure 3.9(b).

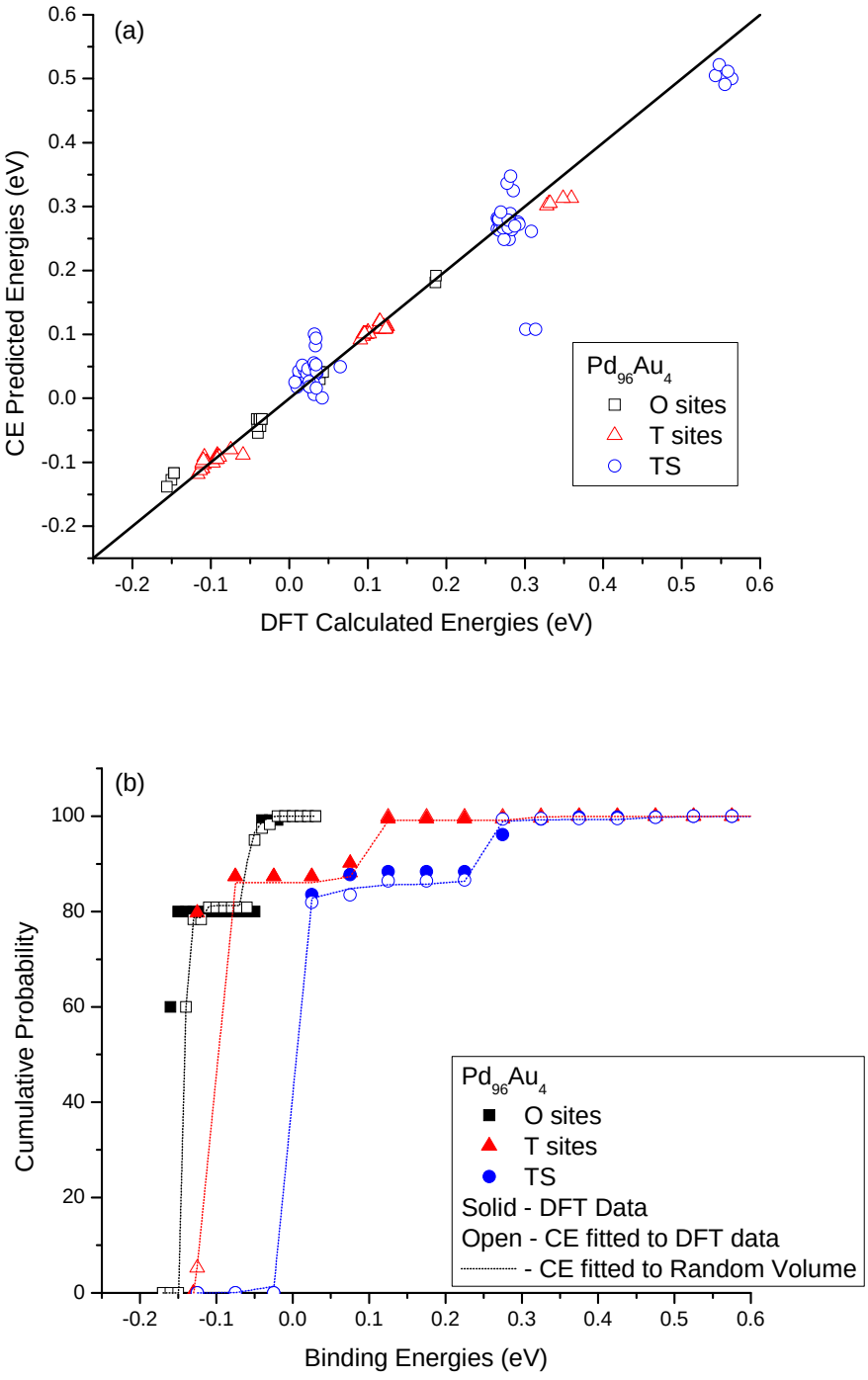

Figure 3.9: Cluster expansion for $Pd_{96}Au_4$. The O sites are represented by squares, triangles represent the T sites, and circles represent TS. (a) A comparison of the CE model and the DFT data. (b) The DFT data and the CE model fitted using only DFT data (open symbols), and the CE model applied to a randomly generated volume (lines).

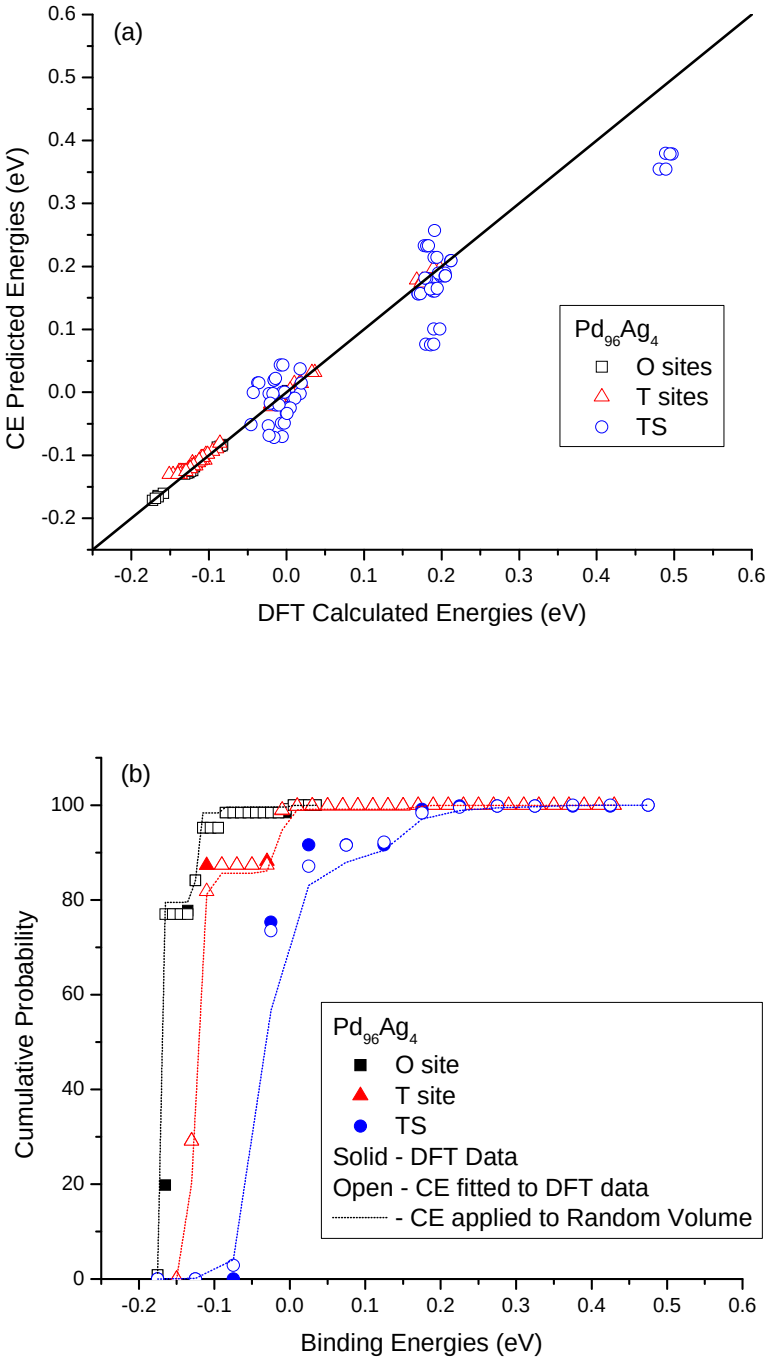

Figure 3.10: Cluster expansion for $Pd_{96}Ag_4$. The O sites are represented by squares, triangles represent the T sites, and circles represent TS. (a) A comparison of the CE model and the DFT data. (b) The DFT data and the CE model fitted using only DFT data (open symbols), and the CE model applied to a randomly generated volume (lines).

In Figure 3.9(b) shows that the CE models are capable of properly describing the bulk material of the $Pd_{96}Au_4$. Interestingly the $Pd_{96}Ag_4$ CE models have very similar behavior to the models for $Pd_{96}Au_4$. In Figure 3.10(a) both the O site CE model as well as the T site CE model have excellent fit with the DFT data, but there are a number of TS in $Pd_{96}Ag_4$ that are poorly predicted by the CE model. As noted in section 3.2, some T sites in $Pd_{96}M_4$ (M= Ag, Au) are not local energy minima for H in our DFT calculations. These sites were not included in fitting the CE model, so they are not shown in Figure 3.9(a) and Figure 3.10(a). In calculating the macroscopic properties of H in the bulk materials, a random volume is also generated. We identify the T sites that are not local energy minima by counting the number of Au or Ag atoms in the $2 \times N$ shell. Once identified, we search for the three possible O sites that are now available for O to O hopping.

In comparing $Pd_{96}M_4$ DFT and CE data for M = Au, Ag, Pt, Rh, Cu, and Ni a trend can be observed in the energy values of the data. For systems in which the M atoms are larger than Pd there are gaps between the energy values of a particular binding site. For example in Figure 3.9(a) we can see that there are multiple groups of O sites in different energy ranges. These gaps disappear as the M atoms become equal to the size of Pd as observed in Figure 3.8(a). Furthermore, as the M atoms become smaller than Pd, overlaps between distinct binding sites can be observed, as illustrated in Figure 3.6(a).

For $Pd_{96}M_4$ alloys for M = Au, Ag, Pt, Rh, Cu, and Ni the CE models selected to describe the O sites, T sites and TS perform well in both fitting to the calculated DFT data as well as predicting the binding site energies of a random volume. More importantly for all the systems analyzed, the CE models have not predicted binding sites

lower in energy than those calculated via DFT. This is a strong indication that we have sufficiently sampled conditions found in the bulk material. Although we have primarily focused in the validation of the binding energy, E_b, CE models for O sites, T sites, and TS we have also performed this rigorous validation process to the ZPE CE models for each individual binding site for each alloy of interest.

3.4: Macroscopic Properties of H in $Pd_{96}M_4$ Alloys

The binary alloys we focused on have composition $Pd_{96}M_4$ (in at.%) for M = Au, Ag, Pt, Rh, Cu, and Ni. We performed extensive analysis in order to determine a CE model describing the behavior of H in these alloys. Using these CE models, we are able to describe the solubility, diffusion and permeability of H in the bulk of these materials at the temperature range of T = 400 – 1200 K.

3.4.1: Results for Solubility of H in $Pd_{96}M_4$ Alloys

In general it is thought that an expansion of the lattice parameter in comparison to pure Pd improves the solubility of H in the bulk of dense metal membranes. For the most part this assumption holds true, however there are many exceptions. One exception is found when Pd-based binary alloys are formed using M = Pt. Pt is slightly larger than Pd, hence when used to form binary alloys with Pd there is an expansion of the lattice parameter of the alloy formed when compared to pure Pd. Although there is a lattice expansion in $Pd_{100-x}Pt_x$ alloys, experiments performed on these alloys report drastic reduction of H solubility as atomic the Pt content of the alloy increase[36]. This discrepancy to the general observation above suggests that in addition to the lattice correlation, chemical effects have to be considered when describing the solubility of H in Pd alloys.

The solubility for H in each alloy was calculated as $\Theta_H = K_s\sqrt{P_{H_2}}$, where K_s is the sum of the averages of the Sieverts' constant for an individual site, $K_{s,ind} = \alpha'\delta e^{-\beta E_{b,O}^{ZP}}$, using the CE models for each $Pd_{96}M_4$ alloy. Further details on the theory of solubility can be found in Chapter 2. The predicted solubility for H each alloy is reported in Figure 3.11(a). At first glance, the general correlation of the lattice parameter seems to be also observed, with Au and Ag having greater H solubility than pure Pd while the addition of Cu and Ni reduces H solubility. To assist the explanation of our results, we have plotted the predicted H solubility of the alloys normalized with respect to predicted H solubility in pure Pd in Figure 3.11(b). Here, any data plotted above the solid line is an indication of an alloy with favorable H solubility. As expected larger M atoms (square symbols) have the best performance. Interestingly, when Au is used as an additive in $Pd_{96}M_4$, the solubility of H in the alloy relative to pure Pd is approximately independent of T. In contrast when Ag is used as the temperature increases the favorability of H solubility decreases, while remaining more favorable than pure Pd throughout the temperature range we examined. Our results are qualitatively consistent with experimental work done by Boureau *et al*. on $Pd_{90}Ag_{10}$ showing that the solubility of H in these alloys was more favorable than in pure Pd[48]. Comparing our solubility results using $\Theta_H = K_s\sqrt{P_{H_2}}$ with experiments performed by Yoshihara and McLellan at 1000 K and hydrogen pressure of 1 atm, our model predicts H solubility in pure Pd to be $\Theta_{Pd} = 0.011\ \text{atm}^{-0.5}$, while an experimental value of $\Theta_{Pd} = 0.009\ \text{atm}^{-0.5}$ was observed[29].

Our analysis of H solubility is based on treating interstitial H as a dilute species in the metal alloy. In this limit, using Sieverts' Law to describe the net solubility in each

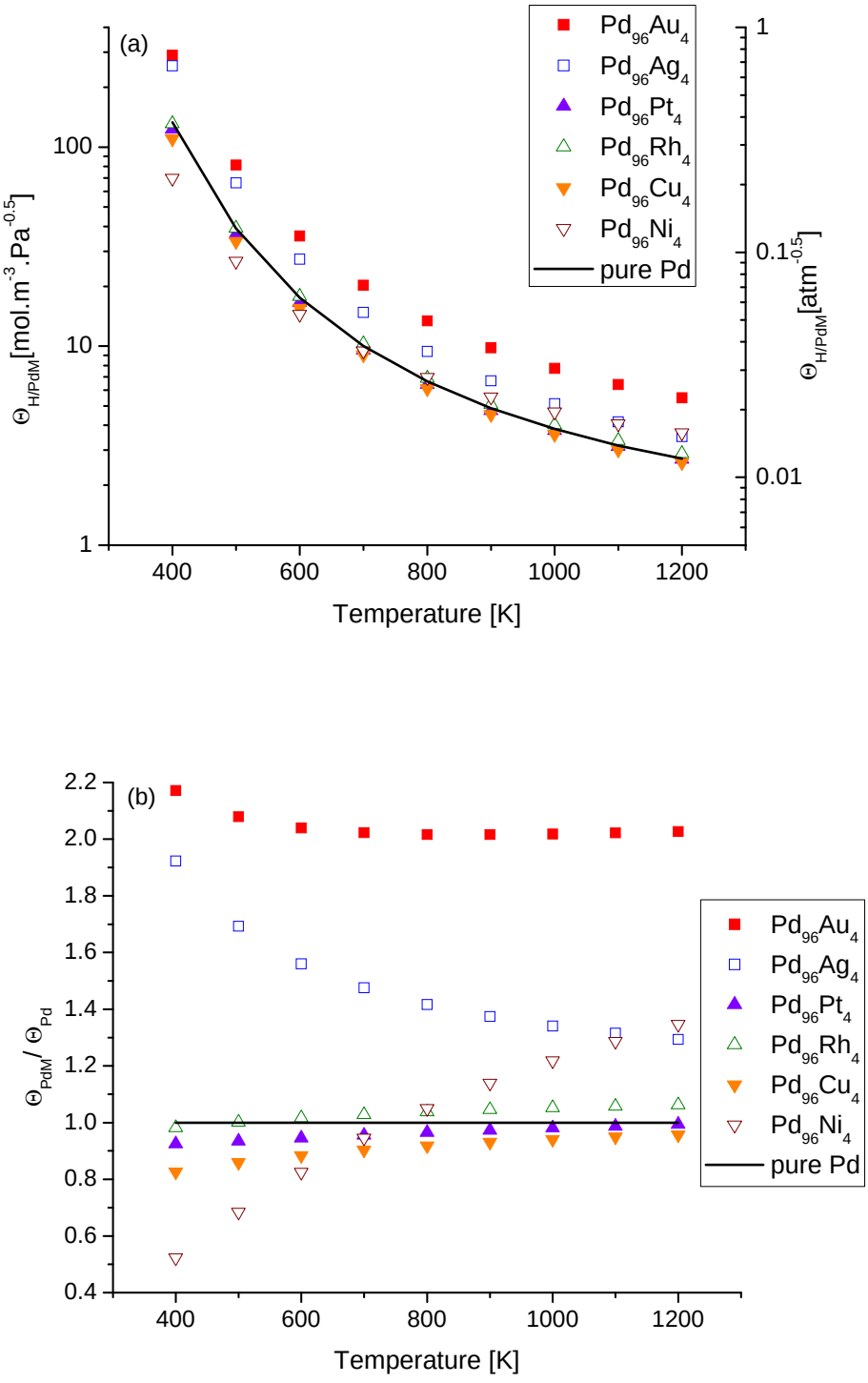

Figure 3.11: Hydrogen solubility predictions for (a) $Pd_{96}M_4$ for M = Au, Ag, Pt, Rh, Cu, and Ni compared to H solubility prediction in pure Pd (two axis are shown for the same data to facilitate experimental comparison);(b) solubility results normalized with respect to pure Pd.

interstitial site is valid. In Figure 3.11(a), for pressures of 1 atm, at 600 K we predict H solubility in pure Pd to be $\Theta_H = 0.05$. This suggests for materials with calculated solubilities higher than this our assumptions of dilute interstitial H concentration may be inaccurate. This estimate implies that our calculated results are most accurate at temperatures above 600 K. Fortunately, this is the temperature range that is most relevant for high temperature H_2 purification.

Based on the general expectation of solubility based on the lattice constant, the use of M = Cu and Ni was expected to result in lower H solubility than pure Pd. $Pd_{96}Cu_4$ behaves consistently with this expectation through the entire temperature range of study, as seen in Figure 3.11(b). Yoshihara and McLellan experimentally performed solubility analysis on a series of PdCu alloys. Comparing our results on $Pd_{96}Cu_4$ at T = 663 K and pressures of 1 atm, our model predicts H solubility of $\Theta = 0.03\ \text{atm}^{-0.5}$, while an experimental value of $\Theta = 0.02\ \text{atm}^{-0.5}$ was observed[29]. Our results are consistent with experimental results indicating a reduction of H solubility with increased Cu content in fcc PdCu alloys[38, 49].

For T ≤ 700 K, $Pd_{96}Ni_4$ also has the expected behavior of alloys with lattice constants smaller than pure Pd. For T ≥ 800 K, however, the H solubility for this alloy is predicted to surpass H solubility in pure Pd. As the temperature increases, the importance of the vibrational energy levels also increases. In pure Pd the binding energy of H in an O site is $E_b^O = -0.14$ eV and the ZPE for H in an O site is $E_O^{ZPE} = 0.10$ eV while the majority of the O sites in $Pd_{96}Ni_4$ have an average binding energy of $E_b^O = -0.08$ eV and average ZPE of $E_O^{ZPE} = 0.08$ eV. At low temperatures, the less favorable binding energy

in the alloy for H dominates the solubility in $Pd_{96}Ni_4$, resulting in a reduction in H solubility as compared to pure Pd. As the temperature increases the dependence on the vibrational energy increases and due to the reduction of ZPE energy in $Pd_{96}Ni_4$ an increase in H solubility is observed. Experiments on $Pd_{90}Ni_{10}$ performed by Shamsuddin *et al*. report that normalized solubility results with pure Pd increase as the temperature increases in these alloys[30]. This is consistent with our predicted trends for $Pd_{96}Ni_4$.

Rh and Pt as additive metal atoms in these $Pd_{96}M_4$ alloys have very similar lattice parameters to pure Pd. Figure 3.11(b) indicates that the chemical effects of these additives on H solubility are contrasting; use of Rh slightly improves H solubility at T > 400 K, but the same amount of Pt has reduced H solubility. In $Pd_{96}Pt_4$ the reduction of H solubility is stronger at lower temperatures, yet even as the temperature increases the H solubility remains lower than 98% of the H solubility in pure Pd. These results are consistent with experimental observations that the addition of Pt reduces H solubility in the bulk of these materials. Noh *et al*. performed experiments to determine the thermodynamic properties for hydrogen solubility in a series of Pd-Pt alloys[22]. From the data of Noh *et al*. we calculated the normalized solubility for $Pd_{98}Pt_2$ and $Pd_{95}Pt_5$ in order to compare the trends with our calculated results for $Pd_{96}Pt_4$. At 400 K, the experiments yield normalized solubilities for $Pd_{98}Pt_2$ of $\Theta_{PdPt}/\Theta_{Pd} = 0.93$ and for $Pd_{95}Pt_5$ $\Theta_{PdPt}/\Theta_{Pd} = 0.73$ [22]. At these same conditions our model predicts $\Theta_{PdPt}/\Theta_{Pd} = 0.93$ for $Pd_{96}Pt_4$. This comparison suggests that our DFT-based model slightly overpredicts the solubility of H in PdPt alloys relative to pure Pd. Nevertheless our results are consistent with experimental observations given experimental uncertainties.

3.4.2: Results for Diffusion of H in $Pd_{96}M_4$ Alloys

At elevated temperatures hydrogen diffuses via a series of hops between interstitial sites in the fcc lattice through the transition state connecting these interstitial sites. Using the CE models in combination with a Kinetic Monte Carlo (KMC) scheme we can characterize the diffusion of H in the bulk of our Pd-based alloys. Further details of the KMC scheme can be found in Chapter 2. Figure 3.12(a) shows our results for each alloy for T = 400 – 1200 K. We also normalize the diffusivity predicted for each alloy with the analogous result for pure Pd and plot these results in Figure 3.12(b).

In Figure 3.12(b) the most noticeable effect is that the additive metal predicted to have the greatest H solubility also reduces H diffusion. For $Pd_{96}Au_4$ we see that the increase in trap sites, or sites in for which H stronger affinity (has longer residence time), which aided in solubility also hinder the diffusion of H in this material. Au atoms affect the binding sites by creating local trap sites, yet the chemical affect is not of a single Au atom is not limited to the local environment, also affecting neighboring sites. Similarly to the solubility analysis, the reduction in H diffusion throughout the entire temperature range of study remains relatively temperature independent resulting in approximately 46% of H diffusion in pure Pd. For $Pd_{96}Ag_4$, the increase in trap sites which aided in the solubility have not hindered the diffusion of H in this material. Unlike Au, Ag atoms create local trap sites; the chemical effect due to the presence of Ag atoms is not as substantial to surrounding binding sites. From Figure 3.12(b) it can be observed that as the temperature increases the favorability decreases.

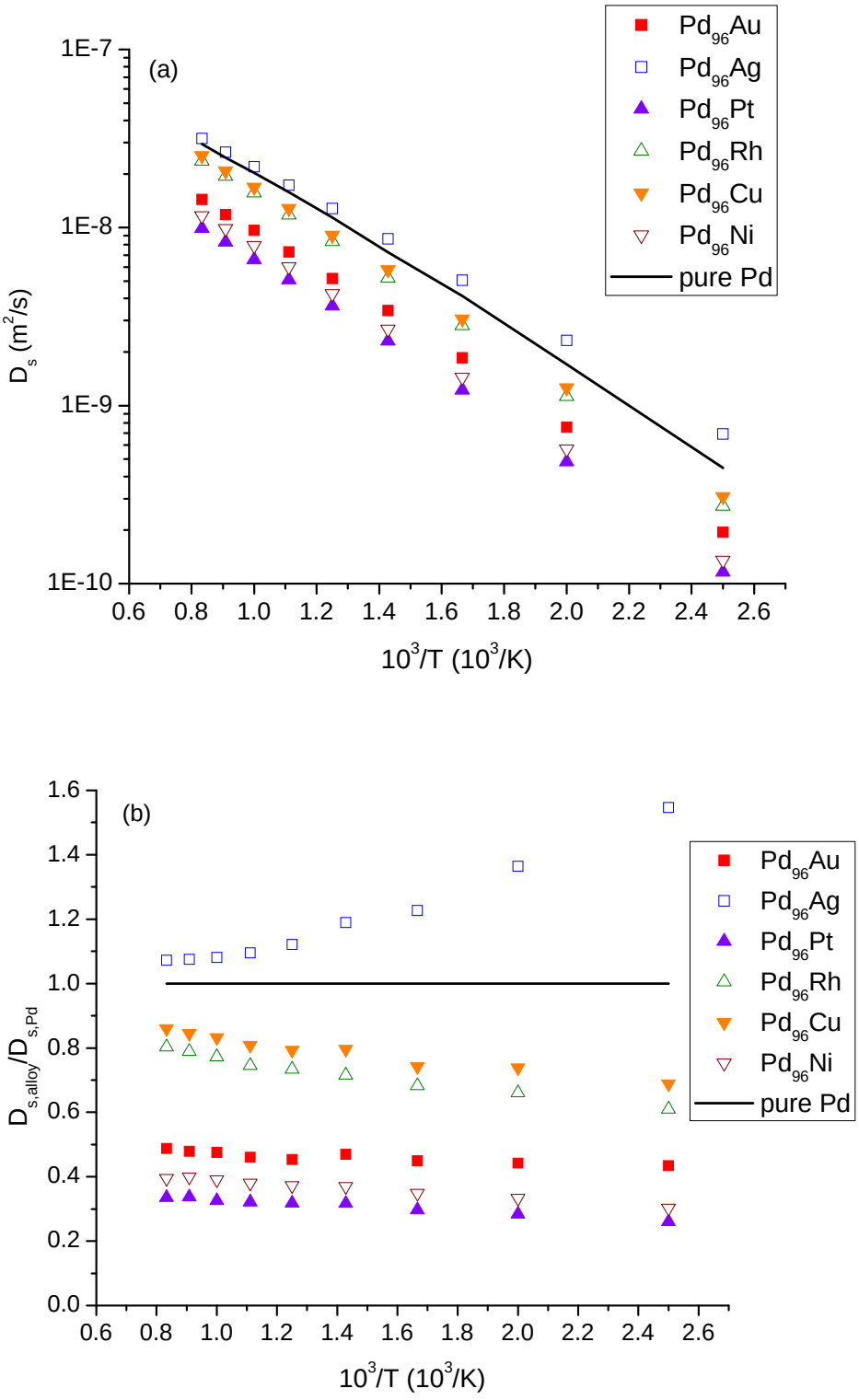

Figure 3.12: H diffusion predictions determined from KMC simulations for pure Pd and Pd rich binary alloys in this study. (a) Arrhenius plot of H diffusion, (b) H diffusion predictions normalized with respect to pure Pd for the temperature range of T = 400 - 1200 K.

From Figure 3.12(a) we are capable of determining the diffusion pre-exponential factor as well as the effective activation energy from the Arrhenius diffusion equation

$$D_s = A_o e^{E_{a,eff}/k_b T} \tag{3.2}$$

where A_o is the pre-exponential factor, $E_{a,eff}$ is the effective activation energy, and k_b is the Boltzmann constant. Table 3.3 lists the calculated factors from Eq.(3.2), using our diffusion predictions, plotted in an equally spaced temperature range, for $Pd_{96}M_4$ alloys. From this table we can see that a prediction in diffusion could not solely rely on the activation energy prediction, otherwise it would be concluded that $Pd_{96}Au_4$, $Pd_{96}Cu_4$ and $Pd_{96}Pt_4$ would have similar H diffusion rates. Maestas *et al*. examined H diffusion at low temperature in a series of experiments on pure Pd and PdAu alloys[13]. Maestas *et al*. concluded that the addition of additive Au atoms would not greatly vary the diffusion of H in the alloy in comparison to pure Pd up to approximately 20 at.% of Au content was reached; this conclusion was also extended to the usage of Ag as an additive to develop Pd-based binary alloys[13]. From Table 3.3 we see that there is a slight difference between

Table 3.3: Diffusion pre-exponential factor $(m^2 \cdot s^{-1})$ and effective activation energies (eV) for Pd and Pd-rich binary alloys in this study for the full temperature range of T = 400 – 1200 K.

System	$A_o (m^2 \cdot s^{-1})$	$E_{a,eff}$ (eV)
$Pd_{96}Au_4$	1.27×10^{-7}	0.222
$Pd_{96}Ag_4$	2.17×10^{-7}	0.196
$Pd_{96}Pt_4$	1.04×10^{-7}	0.230
$Pd_{96}Rh_4$	2.27×10^{-7}	0.230
$Pd_{96}Cu_4$	2.37×10^{-7}	0.227
$Pd_{96}Ni_4$	1.15×10^{-7}	0.230
Pure Pd	2.51×10^{-7}	0.216

Table 3.4: Diffusion pre-exponential factor $(\mathrm{cm}^2 \cdot \mathrm{s}^{-1})$ **and effective activation energies** $(\mathrm{kcal} \cdot \mathrm{mol}^{-1})$ **for Pd and Pd-rich binary alloys in this study for the full temperature range of T = 400 – 600 K compared to experimental results reported by Maestas *et al*.[13].**

System	$A_o(\mathrm{cm}^2 \cdot \mathrm{s}^{-1})$	$E_{a,eff}(\mathrm{kcal} \cdot \mathrm{mol}^{-1})$
$Pd_{96}Au_4$	1.69×10^{-3}	5.58
$Pd_{96}Ag_4$	2.74×10^{-3}	4.93
Pure Pd (this study)	3.52×10^{-3}	5.50
Pure Pd Maestas *et al*.	4.00×10^{-3}	5.75

the A_o and the $E_{a,eff}$ of $Pd_{96}Au_4$, $Pd_{96}Ag_4$, and pure Pd. However these constants were obtained using the full temperature range of this study. We calculated the diffusion coefficients only considering T = 400 – 600 K in Table 3.4. Our results for pure Pd in this temperature range are very similar to the experimental results of Maestas *et al*. They reported H diffusion for $Pd_{95}Au_5$ at T = 310 K to be $D_s = 3.5\times10^{-7}\,\mathrm{m}^2 \cdot \mathrm{s}^{-1}$ while in this study we obtained $D_s = 2.5\times10^{-7}\,\mathrm{m}^2 \cdot \mathrm{s}^{-1}$ for $Pd_{96}Au_4$[13]. Similarly, Barlag *et al*. performed H diffusion experiments on $Pd_{100-x}Ag_x$ alloys for several alloys. At the alloy composition of $Pd_{95}Ag_5$ and T = 294 K, they report a diffusion of $D_s = 4.0\times10^{-7}\,\mathrm{m}^2 \cdot \mathrm{s}^{-1}$ while in this study we obtained $D_s = 7.0\times10^{-7}\,\mathrm{m}^2 \cdot \mathrm{s}^{-1}$ for $Pd_{96}Ag_4$[43]. Both of the experimental comparisons are within reasonable agreement due to the experimental uncertainties.

Previous theoretical calculations performed on $Pd_{100-x}Ag_x$ and $Pd_{100-x}Au_x$ by Sonwane *et al*. suggested that at low concentrations these additive metal atoms reduce H diffusion relative to pure Pd[46,47]. This interpretation, however, was based on extrapolation from a limited set of DFT calculations performed for $Pd_{100-x}M_x$ for M = Ag and Au and $x = 14.81,\ 25.93,\ 37.04,$ and 48.51 at.% to alloys with $x < 10$ at. %[46, 47]. Our calculations are based on detailed calculations for the specific alloy composition we have

discussed, and we feel that our results are more reliable than the extrapolated results of Sonwane *et al*.[46, 47].

From Figure 3.12 we observe that the remaining $Pd_{96}M_4$ alloys (M = Pt, Rh, Cu, and Ni) all reduce the diffusion of H relative to pure Pd. Rh as an additive may have improved the solubility of H, but in turn it has reduced the diffusion. Both Cu and Pt are the only metal additive to have been predicted to reduced both H solubility and diffusion relative to H behavior in pure Pd. Similar to Au as an additive metal atom, using Pt results temperature independent constant reduction in diffusion, approximately 31% of H diffusion in pure Pd. Experimentally it has been observed that as more Pt content is present in the binary alloy H diffusion is further reduced in comparison to pure Pd[19]. For M = Ni, there is a similar reduction in the diffusion of H as observed for the addition of Pt. Although at elevated temperatures the diffusion rate slightly improves, $Pd_{96}Ni_4$ provide approximately 37% of the H diffusion rate obtained from pure Pd. Yoshihara and McLellan performed diffusion experiment on a set of binary alloys which included $Pd_{96}Ni_4$. In their experiments they report $E_a = 0.24$ eV for the $Pd_{96}Ni_4$ while our model predicts $E_{a,eff} = 0.23$ eV [50, 51]. These activation energies are in excellent agreement.

It is interesting to consider the general physical effects that lead to the observed trends in diffusion in these Pd rich binary alloys. Two separate effects contribute to the net diffusion of H in the alloys when compared to pure Pd. First, the lattice constant of the alloys are different from the lattice constant of pure Pd. Test calculations on pure Pd with expanded or compressed lattice parameter showed that lattice expansion (contraction) reduces (increases) the activation energy for site to site hopping. One way to think about the impact of small amounts of large M atoms in the $Pd_{96}M_4$ alloy is that it

reduces the activation barrier between many adjacent sites that otherwise are very similar to the sites in pure Pd. This effect is simply attributed to the lattice expansion due to the size of large M atoms. If this were the only relevant effect, we would expect H diffusion to be faster for all alloys composed with large M atoms. There is, of course, another contribution that is also important: the heterogeneity in the binding site energies in the alloys means that the long range diffusion of H must involve hops over activation barriers with various different heights. Because the presence of a large M generally increases the solubility of H, sites near M atoms effectively act as traps for H, slowing down the net diffusion of H. These two effects have qualitatively different effects on the overall diffusivity of H, so it is not possible from this qualitative argument to predict the overall trend in the diffusion of H relative to pure Pd.

For M atoms smaller in size than Pd, the sites near M atoms do not act as trap sites, unlike the previous situation large M-containing alloy, so it is reasonable to expect that the diffusivity of H will follow the trend dictated by the expansion or contraction of the lattice constant. Because M is a smaller atom than Pd, the alloy's lattice constant is smaller than pure Pd. This leads to larger activation energy for diffusion in sites that are similar to those in pure Pd, suggesting, in agreement with our detailed results, that H diffusion is slowed in the Cu and Ni-containing alloy.

For M atoms similar in size to Pd such as Pt and Rh, the lattice expansion or contraction is minor factor. The effects of trap site formations and heterogeneity of the binding sites is what controls the outcome of the long range diffusion in these alloys. For the cases involving Pt and Rh as additive metals atoms, the result is in a reduction of H diffusion at distinct magnitudes.

3.4.3: Results for Permeability of H in $Pd_{96}M_4$ Alloys

Having obtained results for both solubility and diffusion, we can predict the permeability of membranes made from the binary alloys that have been studied. It is worth noting that these predictions did not require the availability of any experimental data for these alloys. The permeability of H for $Pd_{96}Au_4$, $Pd_{96}Ag_4$, $Pd_{96}Pt_4$, $Pd_{96}Rh_4$, $Pd_{96}Cu_4$ and $Pd_{96}Ni_4$ was calculated using $k = D_s K_s / 2$ and the results are plotted in Figure 3.13(a). We have also normalized the predicted H permeability of each alloy with respect to pure Pd and compared our results with some experimentally reported results on various alloys with similar composition in Figure 3.13(b)[52-55]. For a detailed explanation of these permeability calculations, refer to Chapter 2.

Permeability is directly proportional to both solubility and diffusion. Although there was high H solubility in the $Pd_{96}Au_4$ alloy, the diffusion of H was sufficiently sluggish to cause reduction in H permeability. The resulting permeability of H in $Pd_{96}Au_4$ was on average only 94% of the H permeability in pure Pd. The temperature seems to have little overall effect on the performance of the $Pd_{96}Au_4$ alloy over pure Pd. Sakamoto *et al*. performed permeability analysis on $Pd_{90}Au_{10}$ at T = 335 K[54]. In their experiments $Pd_{90}Au_{10}$ were capable of only 95% of the H permeability observed in pure Pd[54]. Comparing our results with experiments performed by Sakamoto *et al*., our results are consistent with their observations that small amounts of Au in Pd-based binary alloys reduce H permeability.

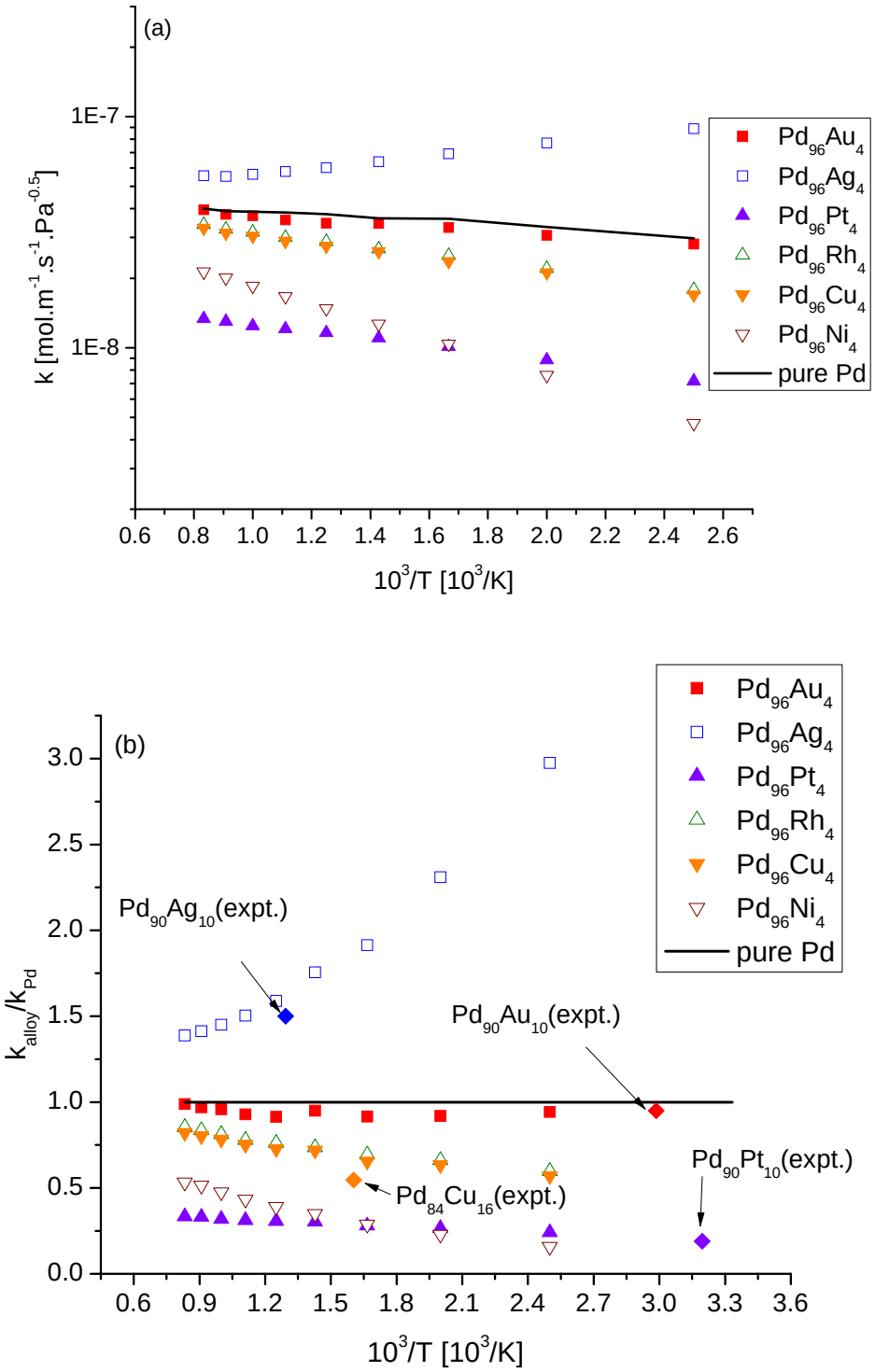

Figure 3.13: Permeability results for Pd rich binary alloys (a) in units of $\mathrm{mol \cdot m^{-1} \cdot s^{-1} \cdot Pa^{-0.5}}$ and (b) normalized with respect to pure Pd for the temperature range of T = 400 – 1200 K. Experimental results are also normalized with respect to the reported pure Pd of each source[52-55].

For the $Pd_{96}Ag_4$ alloy we observe improved performance in both H solubility and diffusion; hence the overall result was improved H permeability in $Pd_{96}Ag_4$ in particular at lower temperatures. These results are qualitatively consistent with the experimental results indicating that the permeability of H is improved for $Pd_{100-x}Ag_x$ alloys up to approximately $x = 23$ at.% of Ag[5, 46]. Gryaznov reported experiments with $Pd_{90}Ag_{10}$ at T = 773 K resulted in H permeability about 1.5 time larger than pure Pd membranes at the same conditions[52]. Again our predicted results for $Pd_{96}Ag_4$ are consistent with these experimental observations in which a small content of Ag is sufficient to improve H permeability in binary alloys over H permeability in pure Pd.

As can be noted from both plots in Figure 3.13 the addition of Pt has a negative effect on the permeability of H in comparison to pure Pd. This is not surprising if we take into account the reduction in both the solubility and diffusion of H for the $Pd_{96}Pt_4$ alloy. Temperature is predicted to have little overall effect on the performance of the $Pd_{96}Pt_4$ alloy relative to pure Pd. Dos Santos *et al*. performed permeability experiments on $Pd_{90}Pt_{10}$ at $T = 313\,K$ and report H permeability of 19% that of pure Pd under the same experimental conditions[55]. Our results are consistent with these experimental observations.

The $Pd_{96}Rh_4$ alloy shows reduced H diffusion with slight improvement in H solubility relative to pure Pd. The reduction of in H diffusion overpowers any improvement over solubility of H in the bulk material resulting in a reduction in H permeability. Although the lattice constant of $Pd_{96}Rh_4$ remained the same as in pure Pd, the presence of Rh produced a reduction in the permeability similar to what would be observed if a smaller additive metal atom such as Cu was used.

For the Cu alloy, the predicted permeability of H is lower than the permeability in pure Pd since both the solubility and the diffusion of H in the alloy were predicted to be lower in value. Our results for Cu are qualitatively consistent with observed experimental results indicating that the addition of Cu reduced the flux of H in the membranes[28, 56]. McKinley reported the permeability of H in pure Pd membrane at T = 623 K to be $1.24\times10^{-8}\ \mathrm{mol\cdot m^{-1}\cdot s^{-1}\cdot Pa^{-0.5}}$ and in a $Pd_{84}Cu_{16}$ membrane at the same temperature to be $6.78\times10^{-9}\ \mathrm{mol\cdot m^{-1}\cdot s^{-1}\cdot Pa^{-0.5}}$ [53]. Our computational methods predict the permeability for H in pure Pd membranes at T = 623 K to be $3.54\times10^{-8}\ \mathrm{mol\cdot m^{-1}\cdot s^{-1}\cdot Pa^{-0.5}}$, in reasonable agreement with the experimental results at this temperature. For $Pd_{96}Cu_4$ at T = 623 K, our model predicts a permeability of $2.42\times10^{-8}\ \mathrm{mol\cdot m^{-1}\cdot s^{-1}\cdot Pa^{-0.5}}$. In fcc PdCu alloys, it has been observed that as the Cu composition increases, the H permeability decreases[38, 57, 58]. Our predicted results for $Pd_{96}Cu_4$ have lower permeability than the predicted results for pure Pd membranes but are greater than the $Pd_{84}Cu_{16}$ experimental results, in agreement with the trend in H permeability versus alloy composition implied by McKinley's data.

Finally, the $Pd_{96}Ni_4$ alloy is predicted to have lowest permeability of all the systems at low temperatures. At elevated temperatures, however, the performance of H in the $Pd_{96}Ni_4$ alloy surpasses that of H in $Pd_{96}Pt_4$. This improvement is due to the increased H solubility at elevated temperatures combined with the improved H diffusion when compared to H diffusion in $Pd_{96}Pt_4$. The general effect of introducing Ni is to produce overall reduction of H permeability in comparison to pure Pd membranes.

3.5: Conclusion

We have successfully analyzed the properties of interstitial H in $Pd_{96}Au_4$, $Pd_{96}Ag_4$, $Pd_{96}Pt_4$, $Pd_{96}Rh_4$, $Pd_{96}Cu_4$, and $Pd_{96}Ni_4$ using DFT calculations. In contrast to earlier DFT-based approached to this situation, we have developed lattice models for interstitial H using a cluster expansion approach that allows us to explore a large number of possible lattice models. Separate models were developed with this method for the binding energy of H in the O sites, T sites, and in the transition states connecting these interstitial sites. At each kind of site, a separate cluster expansion was applied to the classical energy and the ZPE of the interstitial atom. Explicitly separating these two energies make it possible to use quantum corrected transition state theory in a straightforward way to describe the temperature dependent hopping rates of H between adjacent sites. Once a lattice model for interstitial H has been developed in this way, the net solubility and diffusivity of H can be computed. These quantities can be combined to give the net permeability of hydrogen through a bulk sample of the metal alloy being modeled.

In order for the general approach just outlined to be successful, the lattice model must correctly identify all local minima and transition states. A somewhat unexpected outcome from our DFT calculations was that not all T sites in the $Pd_{96}Au_4$ and $Pd_{96}Ag_4$ alloys we examined were stable local minima on the potential energy surface. When one of the four atoms defining these T sites was an M atom, our DFT calculations showed that the T site was not a local minimum. Site to site hopping through these sites from one O site to another O site can occur with H passing through these types of T sites while passing over only one transition state. Preliminary calculations suggest that this situation

occurs not just for the specific binary alloys we examined, but also for ternary alloys in which Au or Ag is present in small quantities. These observations suggest that careful attention should be paid to this issue in any effort to characterize H diffusion in Pd-based alloys including alloying elements with significantly larger atomic sizes than Pd.

The methods we have introduced here are not limited to examining binary alloys in which one component is present in relatively small quantities. Cluster expansion approaches should be useful in developing DFT-based models of other metal alloys that are of more practical interest as membranes, including binary alloys with appreciable concentrations of both metals and ternary alloys; these will be further discussed in Chapter 4. Our interest here has focused on membranes that are dominated by transport of H through the bulk of the material, but cluster expansions can also be useful in efforts to describe the resistances to net mass transport that can occur at the surfaces of ultra-thin membranes[59].

3.6: References:

1 C. Su, T. Jin, K. Kuraoka, Y. Matsumara, and T. Yazawa, Ind. Eng. Chem. Res. **44**, 3053 (2005).

2 X. Ke and G. J. Kramer, Phys. Rev. B **66**, 184304 (2002).

3 P. Kamakoti and D. S. Sholl, J. Membr. Sci. **225**, 145 (2003).

4 S. N. Paglieri and J. D. Way, Sep. Purif. Methods **31**, 1 (2002).

5 J. Okazaki, D. A. Pacheco Tanaka, M. A. Llosa Tanco, Y. Wakui, F. Mizukami, and T. M. Suzuki, J. Membr. Sci. **282**, 370 (2006).

6 Y. Sakamoto, F. L. Chen, M. Furukawa, and K. Mine, J. Less-Common Metals **166**, 45 (1990).

7 Y. Sakamoto, F. L. Chen, M. Furukawa, and M. Noguchi, J. Alloys and Compounds **185**, 191 (1992).

8 Y. Sakamoto, S. Hirata, and H. Nishikawa, J. Less-Common Metals **88**, 387 (1982).

9 D. Wang, T. B. Flanagan, and K. L. Shanahan, J. Phys. Chem. B **112**, 1135 (2008).

10 Y. Zhang, J. Lu, R. Maeda, and C. Nishimura, J. Alloys and Compounds (2007).

[11] F. L. Chen, M. Furukawa, and Y. Sakamoto, J. Less-Common Metals **172-174**, 56 (1991).
[12] D. Fort, J. P. G. Farr, and I. R. Harris, J. Less-Common Metals **39**, 293 (1975).
[13] S. Maestas and T. B. Flanagan, J. Phys. Chem. **77**, 850 (1973).
[14] Y. Chen, S. Liao, and H. Deng, Applied Sur. Sci. **253**, 6074 (2007).
[15] A. K. M. F. Kibria and Y. Sakamoto, Int. J. Hydrogen Energy **25**, 853 (2000).
[16] L. Rubinovich, M. I. Haftel, N. Bernstein, and M. Polak, Phys. Rev. B **74**, 035405 (2006).
[17] D. Wang, J. Clewley, T. B. Flanagan, R. Balasubramaniam, and K. L. Shanahan, Acta Mater. **50**, 259 (2002).
[18] A. K. M. F. Kibria, T. Kubota, A. Kagawa, and Y. Sakamoto, Int. J. Hydrogen Energy **24**, 747 (1999).
[19] B. Coluzzi, C. Costa, A. Biscarini, and F. M. Mazzolai, J. Phys. Cond. Matter **4**, 5155 (1992).
[20] S. Uemiya, W. Kato, A. Uyama, M. Kajiwara, T. Kojima, and E. Kikuchi, Separ. Purif. Tech **22-23**, 309 (2001).
[21] P. Zoltowski and E. Makowska, Phys. Chem. Chem. Phys. **3**, 2935 (2001).
[22] H. Noh, T. B. Flanagan, T. Sonoda, and Y. Sakamoto, J. Alloys and Compounds **228**, 164 (1995).
[23] P. Kamakoti, B. D. Morreale, M. V. Ciocco, B. H. Howard, R. P. Killmeyer, A. V. Cugini, and D. S. Sholl, Science **307**, 569 (2005).
[24] P. Kamakoti and D. S. Sholl, Phys. Rev. B **71**, 014301 (2005).
[25] F. Roa, M. J. Block, and J. D. Way, Desalination **147**, 411 (2002).
[26] F. Roa, J. D. Way, R. L. McCormick, and S. N. Paglieri, Chem. Eng J. **93**, 11 (2003).
[27] P. M. Theon, F. Roa, and J. D. Way, Desalination **193**, 224 (2006).
[28] O. J. Kleppa, Shamsuddin, and C. Picard, J. Chem. Phys. **71**, 1656 (1979).
[29] M. Yoshihara, McLellan, R.B, Acta. Metall **31**, 66 (1983).
[30] M. Shamsuddin and O. J. Kleppa, J. Chem. Phys. **80**, 3760 (1984).
[31] T. M. Adams and J. Mickalonis, Matt. Let. **61**, 817 (2007).
[32] K. Ohira, Y. Sakamoto, and T. B. Flanagan, J. Alloys and Compounds **236**, 42 (1996).
[33] Y. Sakamoto, K. Ohira, N. Ishimaru, F. L. Chen, M. Kokubu, and T. B. Flanagan, J. Alloys and Compounds **217**, 226 (1995).
[34] D. Wang, T. B. Flanagan, and K. L. Shanahan, J. Alloys and Compounds **348**, 152 (2003).
[35] K. W. Wang, S. R. Chung, and C. W. Liu, J. Phys. Chem. C **112**, 10242 (2008).
[36] A. Weiss, Ramaprabhu, S., Rajalakshmi, N., Zeit. Phys. Chem **199**, 165 (1997).
[37] F. L. Chen, Kinari, Y., Sakamoto, F., Nakayama, Y., Sakamoto, Y, Int. J. Hydrogen Energy **21**, 555 (1996).
[38] B. H. Howard, R. P. Killmeyer, K. S. Rothenberger, A. V. Cugini, B. D. Morreale, R. M. Enick, and F. Bustamante, J. Membr. Sci. **241**, 207 (2004).
[39] *Binary Alloy Phase Diagrams, 2nd Edition*, 1990).
[40] M. Hansen, *Constitution of Binary Alloys* (McGraw-Hill, New York, 1958).
[41] W. B. Pearson, *A Handbook of Lattice Spacings and Structures of Metals and Alloys* (Macmillan, New York, 1958).

[42] J. Volkl and G. Alefield, in *Hydrogen in Metals I*, edited by G. Alefield and J. Volkl (Springer-Verlag, Berlin, 1978), Vol. 28, p. 321.
[43] H. Barlag, L. Opara, and H. Zuchner, J. Alloys and Compounds **330**, 434 (2002).
[44] S. Fujita and A. Garcia, J. Phys. Chem. Solids **52**, 351 (1991).
[45] G. Henkelman, Uberuga, B.P., Jonsson, H, J. Chem. Phys **113**, 9901 (2000).
[46] C. G. Sonwane, J. Wilcox, and Y. H. Ma, J. Chem. Phys **125**, 184714 (2006).
[47] C. G. Sonwane, J. Wilcox, and Y. H. Ma, J. Phys. B. **110**, 24549 (2006).
[48] G. Boureau, O. J. Kleppa, and K. C. Hong, J. Chem. Phys **67**, 3437 (1977).
[49] T. B. Flanagan and D. M. Chisdes, Solid. State. Comm **16**, 529 (1975).
[50] R. B. McLellan and M. Yoshihara, Acta. Metall **35**, 197 (1987).
[51] M. Yoshihara and R. B. Mc. Lellan, Acta Metallurgica **30**, 1605 (1982).
[52] V. Gryaznov, Sep. Purif. Methods **29**, 171 (2000).
[53] D. McKinley, in *US Patent* (Union Carbide, 1969).
[54] F. Sakamoto, F. L. Chen, Y. Kinari, and Y. Sakamoto, Int. J. Hydrogen Energy **22**, 369 (1997).
[55] D. S. d. Santos, V. M. Azambuja, L. Pontonnier, S. Miraglia, and D. Fruchart, J. Alloys and Compounds **356-357**, 236 (2003).
[56] H. Amandusson, L. G. Ekedahl, and H. Dannetum, J. Membr. Sci. **193**, 35 (2001).
[57] P. L. Andrew and A. A. Haasz, J. Appl. Phys. **70**, 3600 (1991).
[58] J. Piper, J. Appl. Phys. **37**, 715 (1966).
[59] C. Ling and D. S. Sholl, J. Membr. Sci. **303**, 162 (2007).

CHAPTER 4

PdCu-BASED TERNARY ALLOYS FOR H PURIFICATION

Our work so far involved the development of first principles based models to predict the solubility and transport of H in Pd-rich binary alloys. We implemented a cluster expansion (CE) technique to characterize the interstitial sites of the bulk material of these fcc binary alloys. We successfully applied this methodology to calculate the solubility, diffusion, and permeability of H in $Pd_{96}M_4$ alloys for M = Au, Ag Pt, Rh, Cu and Ni. These results were found to be in quantitative agreement with experimental measurements, as presented in Chapter 3. A key feature in this work was that these models could be developed without requiring any experimental data. Thus, our computational methods are complementary to experimental studies for screening metal alloys for the use as potential hydrogen purification membranes. Motivated by these results, we now aim to make predictions about ternary alloys in the absence of experimental data[1]. Kamakoti and Sholl have done some preliminary first principle-based calculations for the identification of ternary alloys for hydrogen purification membranes[2].

A limited amount of experimental work exists on H solubility and diffusion for ternary alloys. Ramaprabhu and Weiss *et al*. performed H solubility measurements in a wide range of Pd-based binary and ternary alloys of the form $Pd_{1-x}Z_x$ and $Pd_{1-x-y}Z_xZ'_y$ [3, 4]. Their results showed that the ternary alloys Pd-Y-Ag and Pd-Gd-Ag have much greater H solubility than pure Pd. Their results also suggest that there is slight increase in H solubility in Pd-Cu-Au with increased Au content. Ramaprabhu and Ohira *et al*. have similarly reported H solubility for Pd-Ag-Ni [3]. These ternary alloys also show a slight

increase in H solubility in comparison to pure Pd for low Ni content (1.5 at.%), followed by a reduction in H solubility with increasing Ni content[3, 5]. Sakamoto *et al*. and Ramprabhu reported that H solubility in Pd-Ni-Rh alloys is lower than H solubility in pure Pd, with further decreases with additional Ni or Rh content[3, 6]. Sakamoto *et al*. performed a series of diffusion and permeability experiments on $\text{Pd-Y(Gd)}_x\text{-Ag}_y$ alloys[7]. They report that for $\text{Pd-Y(Gd)}_x\text{-Ag}_y$ for $x = 6.3,\ 4.7,\ 2,\ \text{and}\ 1.3$ with $y = 5,\ 10,\ 15,\ \text{and}\ 20$, respectively, in all cases these ternary alloys have greater permeabilities than $Pd_{76}Ag_{24}$ alloys at same experimental conditions[7]. To date, there has been little theoretical work reported studying H transport in ternary alloys.

The objectives of our calculations are to identify ternary alloys that satisfy two criteria:

i. Maintenance of favorable sulfur resistance properties observed experimentally for fcc PdCu binary alloys[8, 9]
ii. Higher net H_2 flux than comparable PdCu binary alloys.

Cu-containing alloys have shown promise in resistance to sulfur poisoning[8-10], so as a result of our first selection criteria we have limited our calculations to PdCu-based ternary alloys. In this chapter we have examined $Pd_{70}Cu_{26}M_4$ (at.%) alloys for M = Au, Ag, Pt, Pd, Cu, and Ni. Our calculations treat each of these materials as substitutionally random fcc alloys. We will discuss the reasons behind selecting M = Au, Ag, Pt, Pd, Cu, and Ni as additive metal atoms used in the ternary alloys. We will also discuss our density functional theory (DFT) results for the binding sites and transition states of H in the bulk of these membranes. In Chapter 3 we applied a CE method to describe interstitial H in the bulk of Pd-rich binary alloys. In this chapter we will use similar models to

describe PdCu-based ternary alloys. Once accurate CE models are defined, we calculate H solubility, diffusion, and permeability in each alloy as described in Chapter 2 for the temperature range of 400 – 1200 K.

4.1: Additive Metal Atom Selection

In addition to limited experimental data of H behavior in ternary alloys, limited experimental data is available on the phase diagrams of ternary metals. In Chapter 3 we analyzed the binary phase diagrams of Pd and Ag, Au, Pt, Rh, Cu and Ni to ensure the addition of four atomic percent of the additive metal atoms would result in an fcc crystal structure. Similarly we now analyze the binary phase diagrams for Cu and Au, Ag, Pt, and Ni to examine the miscibility between these additive metals and Cu[11,12]. The assumption made, in light of the lack of experimental data, is that if the additive metal atoms form fcc crystals with the two host metals, Pd and Cu, independently, then it is reasonable to assume that the combination of these metals to form a ternary alloy would also form fcc crystal structures.

Similar to the binary phase diagram comparison between Pd and the additive metal atoms, the formation tendencies between the additive metal atoms we considered and Cu can be divided into three groups. The first and simplest formation tendency is the alloying of Cu and Ni. When these two metals are combined, fcc crystal structures are formed regardless of the alloy composition for temperatures above 638 K. Below this temperature, compositions involving greater >20 at.% Ni, show a phase separation between two distinct phases. The second category involves the alloying of Cu and Ag, for which a limited range of compositions form fcc alloys. When these metals are combined

to form an alloy, fcc crystal structures exist for compositions involving greater than 94 at.% Cu or less than 15 at.% Cu in the binary alloy. For other compositions, phase separation occurs. In the third group, the formation of an fcc alloy is observed for the majority of alloy compositions with the exception of several gaps in which the alloys have different crystal structures. This situation occurs with Au and Pt alloyed with Cu. Au and Cu form disordered fcc materials for all temperatures above 683 K. For temperatures below 683 K, alloys with $10 \le x_{Cu} \le 82$ at.% have five regions involving distinct crystal structures and ordered fcc phases. Similarly when Pt is alloyed with Cu several distinct crystal structures along with an ordered fcc crystal structure are formed. For temperatures approximately below 1000 K, alloys with $13 \le x_{Cu} \le 95$ at. % has five regions involving distinct ordered and disorder crystal structures.

Summarizing the results above, for the compositions of interest dealing with 4 at.% of the additive metal atoms, Cu and the additive metal atoms we have considered have disordered fcc crystal structures. Because the additive metal atoms we have considered tend to form fcc crystals with both Pd and Cu, it is reasonable to assume that ternary alloys involving these metals will also have similar crystal structures.

In determining which additive metal atoms could potentially form fcc crystals, we included selections that expand and contract the lattice structure in comparison to $Pd_{74}Cu_{26}$ and $Pd_{70}Cu_{30}$. Although pure Pd is the reference material for all Pd based alloys, our goals for the ternary alloys are to observe the effects of additive metal atoms in comparison to PdCu binary alloys. Therefore we have decided to compare the macroscopic properties between the ternary alloys and $Pd_{74}Cu_{26}$ and $Pd_{70}Cu_{30}$. These two binary alloys share either the same content of Pd or Cu with those present in the ternary

Table 4.1: Ternary alloys considered in this study, their DFT calculated lattice constant, and the difference between the lattice constant of the alloys and $Pd_{74}Cu_{26}$, $Pd_{70}Cu_{30}$, and pure Pd.

Alloy composition	Lattice constant (Å)	% difference with $Pd_{74}Cu_{26}$	% difference with $Pd_{70}Cu_{30}$	% difference with pure Pd
Pure Pd	3.960	1.629	2.144	0.000
$Pd_{70}Cu_{26}Au_4$	3.901	0.128	0.643	-1.501
$Pd_{70}Cu_{26}Ag_4$	3.899	0.077	0.592	-1.552
$Pd_{74}Cu_{26}$	3.896	0.000	0.515	-1.629
$Pd_{70}Cu_{26}Pt_4$	3.896	0.000	0.515	-1.629
$Pd_{70}Cu_{26}Ni_4$	3.881	-0.386	0.129	-2.015
$Pd_{70}Cu_{30}$	3.876	-0.515	0.000	-2.144

alloys. We will refer to these two binary alloys as the reference alloys. Our ternary alloys have compositions of $Pd_{70}Cu_{26}M_4$, allowing us to replace M with either Pd or Cu to obtain the two reference binary alloys. In Table 4.1 we list the DFT optimized lattice constant for the PdCu-based ternary alloys using M = Au, Ag, Pt, and Ni as the additive metal atoms. Additional information on calculating these lattice constants is given in Chapter 2. Table 4.1 also lists the percent difference between the ternary lattice constants and the two PdCu reference binary alloys, and pure Pd. In comparing the ternary alloys and $Pd_{74}Cu_{26}$, the additive metal atoms can be classified into three distinct groups. The first group is M = Au and Ag. These two additives create a lattice expansion in comparison to $Pd_{74}Cu_{26}$. The second category consists of M = Pt; which causes no dilation of the lattice. The third group is the additive that contracts the lattice in comparison to $Pd_{74}Cu_{26}$, namely M = Ni. In contrast, the lattice constant of all the ternary alloys in this study expand the lattice compared to $Pd_{70}Cu_{30}$.The lattice constants of the ternary alloys and the reference binary alloy are much smaller than pure Pd due to the Cu in these alloys.

4.2: Binding Sites and Transition States for Site to Site Hopping

Similarly to the binary alloys studied in Chapter 3, the ternary alloys we examined are assumed to be fcc crystal structures. This implies that interstitial H resides in the bulk material in the octahedral (O) and the tetrahedral (T) sites. In the bulk of substitutionally random alloys membranes there are many structurally complex interstitial sites. Recalling Chapter 3, a simple way of describing the interstitial sites would be to count the number of Pd atoms in the nearest neighboring $(2\times N)$ shell and in the next to nearest neighboring $(3\times N)$ shell. If we were to characterize the O sites of $Pd_{96}M_4$ alloys in this way, DFT calculations for 21 distinct O sites could represent approximately 99% of the bulk material. Within these 21 O sites, three types account for around 90% of the bulk material, as can be observed from Figure 4.1(a). If we were to use a similar simple characterization of the interstitial sites by additionally counting the number of Cu in the same $2\times N$ and $3\times N$ shells it would be infeasible to perform a small number of DFT calculations and sample a large percentage of the distinct sites within the ternary material. Figure 4.1(b) represents the possible types of O sites a $Pd_{70}Cu_{26}M_4$ alloy if the simple characterization outlined above was used is used.

For each ternary alloy we performed DFT calculations on a minimum of two distinct 27 atom supercells. Further details related to applying DFT to ternary systems can be found in Chapter 2. DFT calculations for the ternary alloys using these supercells provided a total of 54 distinct O sites, 108 distinct T sites, as well as the ZPE of H in each of these individual sites. As a means of comparison between the completeness of the binary systems and the ternary systems, if we were to describe these 54 O sites using the simple characterization discussed above, they comprise less than 50% of the O sites that

could be found the substitutionally random state represented in Figure 4.1(b). For the reference binary alloys, $Pd_{70}Cu_{30}$ and $Pd_{74}Cu_{26}$, we performed DFT calculations using the single supercell. This supercell provided 27 distinct O sites, 54 distinct T sites and the ZPE of H in each of these individual sites.

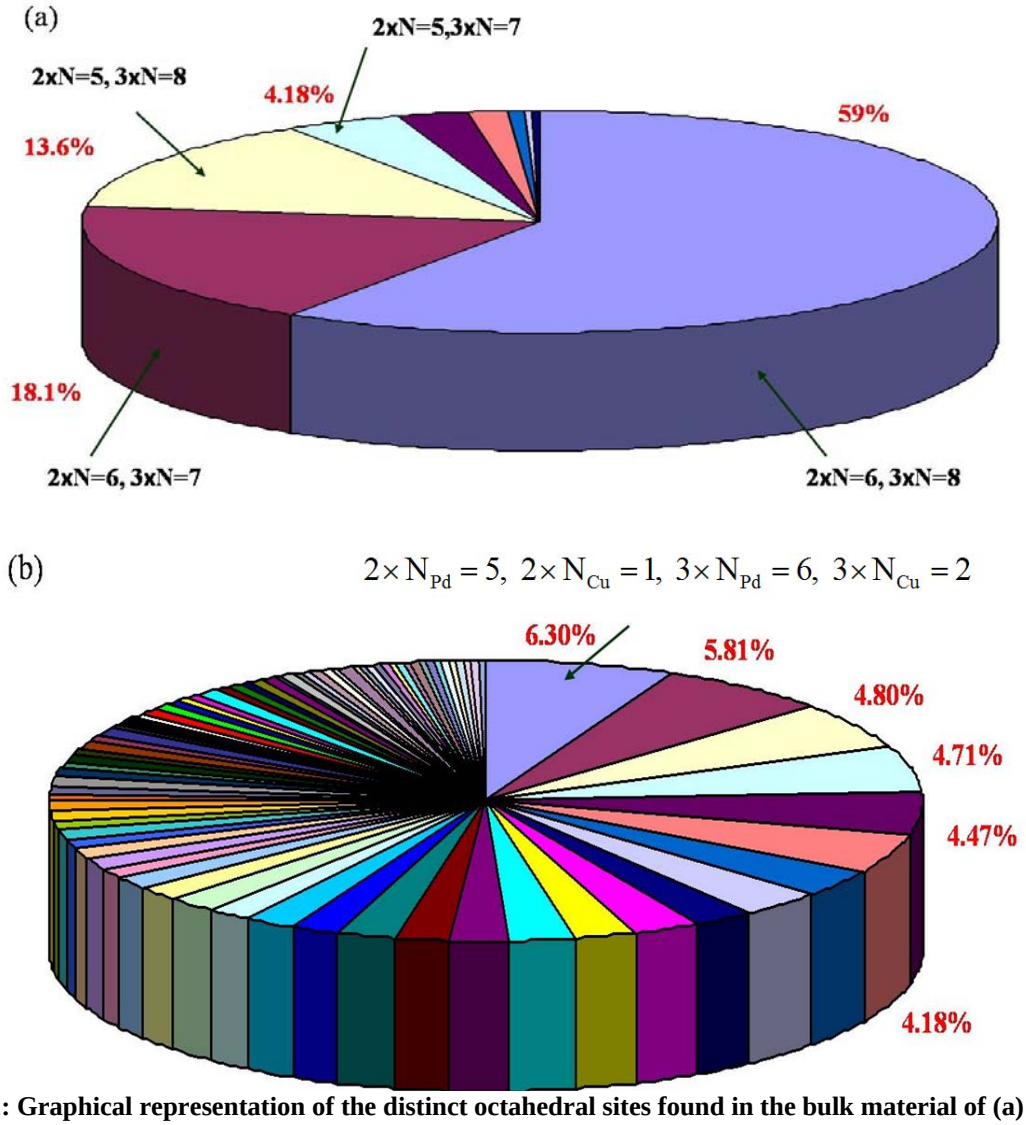

Figure 4.1: Graphical representation of the distinct octahedral sites found in the bulk material of (a) $Pd_{96}M_4$ alloys, characterized by counting the number of Pd in the $2\times N$ and $3\times N$ shell and (b) $Pd_{70}Cu_{26}M_4$ characterized by counting the number of Pd and Cu in the $2\times N$ and $3\times N$ shells.

We will be analyzing these ternary alloys at elevated temperatures where H diffuses by discrete hops between adjacent binding sites via transitions states (TS)[13, 14]. In Chapter 2 we introduced a simple method of identifying the initial estimate for a TS using a geometric approximation. In general a TS is found in the center of the geometric face shared by adjacent O and T sites. Using a vector $\vec{\nu}_{Pd}$ defined as the distance from a T site to the TS in pure Pd we are able to estimate the general location of a TS in a binary alloy. We perform geometry optimization of the initial TS estimations to locate the real TS in the $Pd_{70}Cu_{30}$ binary alloy. Once the TS in the binary system are located, we can now find a new vector $\vec{\nu}_{PdCu}$ defining the distance between a T sites and a TS in the $Pd_{70}Cu_{30}$ alloy. Using $\vec{\nu}_{PdCu}$, we identify an estimated location for the TS in the ternary systems, which is then optimized to find the real TS in the ternary alloy supercell. For further details involving the identification of the TS, refer to Chapter 2. This approach was adopted to determine the precise geometry and energy of the 432 TS in each of the ternary alloys and 216 TS in the two PdCu binary alloys. ZPE values were additionally computed for each TS for all alloys of interest.

In our $Pd_{70}Cu_{26}M_4$ alloys with M = Pd, Pt, Cu and Ni, all TS calculations gave a well defined TS for every pair of O and T sites we examined. For $Pd_{70}Cu_{26}M_4$ alloys in which additive metal atoms were substantially larger than Pd (M = Au and Ag) however, the complication observed in $Pd_{96}M_4$ binary alloys was also found in these ternary alloys. For ternary alloys $Pd_{70}Cu_{26}M_4$ with M = Au and Ag several T sites were found to no longer be energy minima when an M atoms was near the binding site. Additional information pertaining to the non-local energy minimum T sites can be found in Chapter 3.

4.3: Cluster Expansions for $Pd_{70}Cu_{26}M_4$ Alloys

Similar to the binary alloys examined in Chapter 3, the simple characterization of binding sites used for ternary alloys in Figure 4.1(b) is, at best, a significant simplification of the factors that define the properties of each binding site. In order to properly characterize the binding site energies in ternary alloys a cluster expansion (CE) method combined with the leave-one-out (LOO) analysis was employed. For additional detailed information describing the CE and LOO analysis, refer to Chapter 2. The resulting binding energy (E_b) model coefficients are listed separately from the zero point energy (ZPE) model coefficients for all binding sites in each ternary alloy and the two reference binary alloys in Appendix C. Only binding sites that were found to be local energy minima were included in developing these CE models.

As described in Chapter 2, and demonstrated for $Pd_{96}M_4$ in Chapter 3, we first have to find a CE model that accurately fits the DFT data. We characterize this property

Table 4.2: Standard deviation between DFT data and the CE models for the E_b and the ZPE for each of the $Pd_{70}Cu_{26}M_4$ ternary alloys in this study.

	$Pd_{74}Cu_{26}$		$Pd_{70}Cu_{30}$		$Pd_{70}Cu_{26}Pt_4$	
	E_b (eV)	ZPE (eV)	E_b (eV)	ZPE (eV)	E_b (eV)	ZPE (eV)
O sites	0.0060	0.0018	0.0055	0.0025	0.0094	0.0052
T sites	0.0064	0.0004	0.0074	0.0040	0.0091	0.0014
TS	0.0156	0.0054	0.0144	0.0044	0.0159	0.0076

	$Pd_{70}Cu_{26}Au_4$		$Pd_{70}Cu_{26}Ag_4$		$Pd_{70}Cu_{26}Ni_4$	
	E_b (eV)	ZPE (eV)	E_b (eV)	ZPE (eV)	E_b (eV)	ZPE (eV)
O sites	0.0118	0.0020	0.0099	0.0015	0.0043	0.0018
T sites	0.0094	0.0006	0.0203	0.0014	0.0071	0.0004
TS	0.0204	0.0032	0.0169	0.0061	0.0143	0.0051

with the standard deviation between the values predicted by the CE model and the DFT results. Table 4.2 lists the standard deviation for the CE models selected for $Pd_{74}Cu_{26}$, $Pd_{70}Cu_{30}$, and each of the $Pd_{70}Cu_{26}M_4$ ternary alloys. Only DFT data from local energy minima for H in O and T sites was used for this comparison. The CE models fit the DFT data with a good level of accuracy. We also plot the DFT and CE data for visual inspection below.

Although the CE models must fit the DFT data, it is equally important that these models accurately describe sites for which no DFT data has been gathered. This aspect is especially important in ternary alloys, where it is not practical to use DFT to sample the enormous range of distinct sites that exist. To address this issue, we compare the predictions of the CE model applied to all sites in a large substitutionally random volume with the set of sites examined in our DFT results. The interpretation of this comparison is discussed below.

In order to facilitate the explanation of our results, we consider separately the three groups of alloys. The first group is $Pd_{74}Cu_{26}$, $Pd_{70}Cu_{30}$, and $Pd_{70}Cu_{26}Pt_4$; for these alloys the set of DFT data defined above was sufficient to describe the bulk material. For the second category, $Pd_{70}Cu_{26}M_4$ with M = Au and Ag, the original set of DFT data collected was sufficiently complete to describe the bulk material, but interstitial sites exist that are not local energy minima. The third category is $Pd_{70}Cu_{26}Ni_4$. This ternary alloy required additional DFT data in order to find appropriate CE models.

Figure 4.2(a) shows the DFT and CE model data for $Pd_{74}Cu_{26}$. The nomenclature for this figure and all similar figures to follow is that the O sites are represented by squares, T sites by triangles, and the TS by circles. The same energy range is shown in

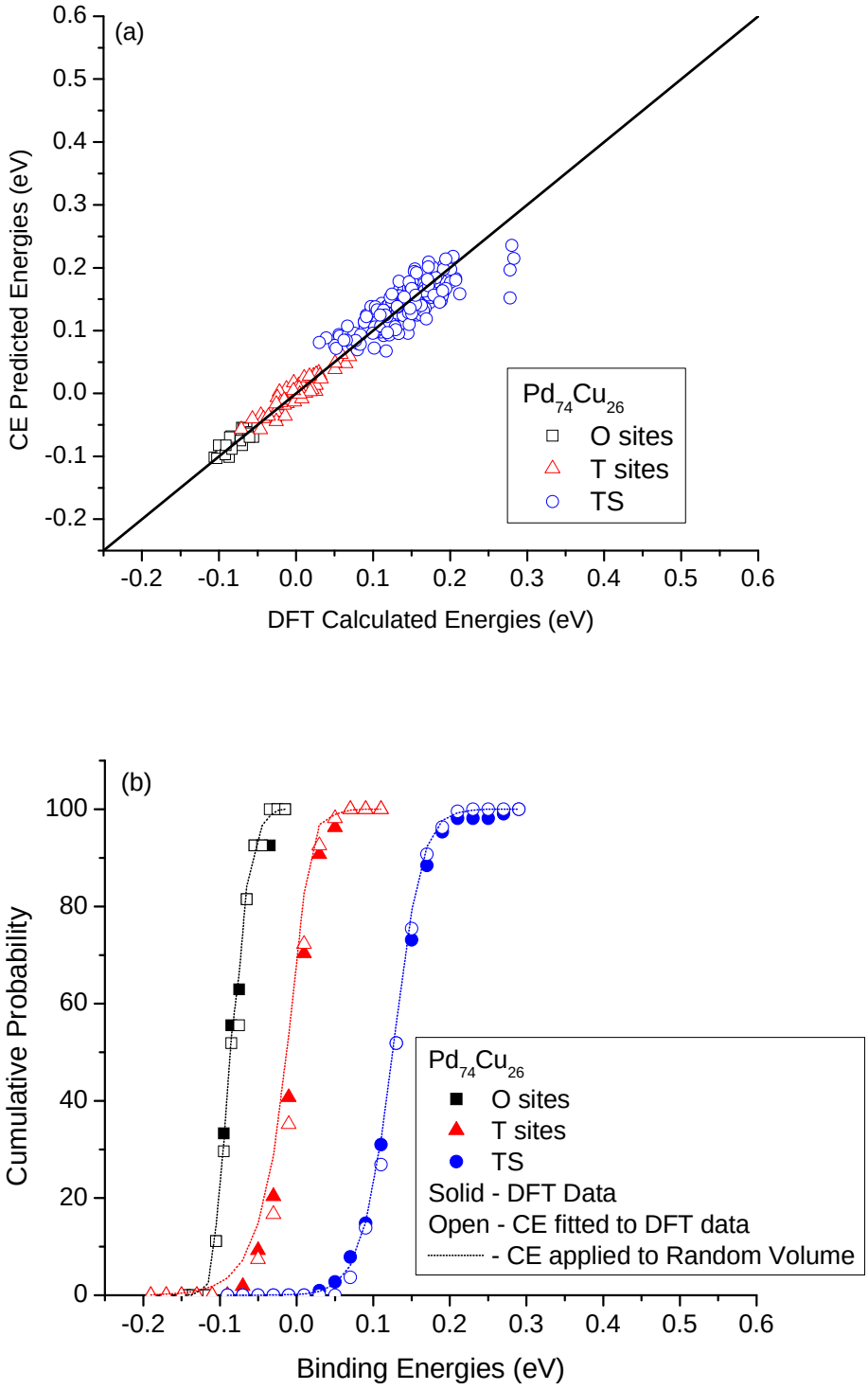

Figure 4.2: Cluster expansion for $Pd_{74}Cu_{26}$. The O sites are represented by squares, triangles represent the T sites, and circles represent TS. (a) A comparison of the CE model and the DFT data. (b) The DFT data and the CE model fitted using only DFT data (open symbols), and the CE model applied to a randomly generated volume (lines).

each figure of this type to facilitate comparison of different alloys. There are four TS that are poorly fitted by the CE, causing the variance for the TS to be higher than the variance for the O sites and T sites, but the remaining 212 TS are very well fitted.

We analyzed the CE model for each binding site within a representative randomly generated volume containing 4,000 atoms for the $Pd_{74}Cu_{26}$ alloy as shown in Figure 4.2(b). The same nomenclature as in Figure 4.2(a) is used in Figure 4.2(b). The truncated CE model for the O sites not only fits the DFT data, but has excellent performance for the randomly generated volume. Specifically, within the randomly generated volume, the CE model has not predicted any O sites that were lower in binding energy than the set of sites observed with DFT. If binding sites with this property were predicted, it would be necessary to perform additional DFT calculations, because the lowest energy sites dominate H solubility and therefore need to be described with precision. In order for our models to precisely mimic the random volume, our DFT data most entail a truly random sampling of sites in the alloy. Nevertheless, a good match between DFT and the CE applied to a random volume over the full range of binding energies heightens our confidence in the CE model. In the CE model predictions for the T sites, there are a small number of binding sites in the random volume lower in energy than the sites included in our DFT data. This situation is much less significant than for the O sites, since it is the low energy O sites that dominate H solubility. The agreement between our DFT data and the CE model for the random volume for the TS is excellent.

Figure 4.3(a) shows the DFT and CE model data for $Pd_{70}Cu_{30}$. The CE models show good agreement with the DFT data. For the TS, there are three TS that are poorly predicted, similar to the previous alloy. The remaining 213 TS that were examined with

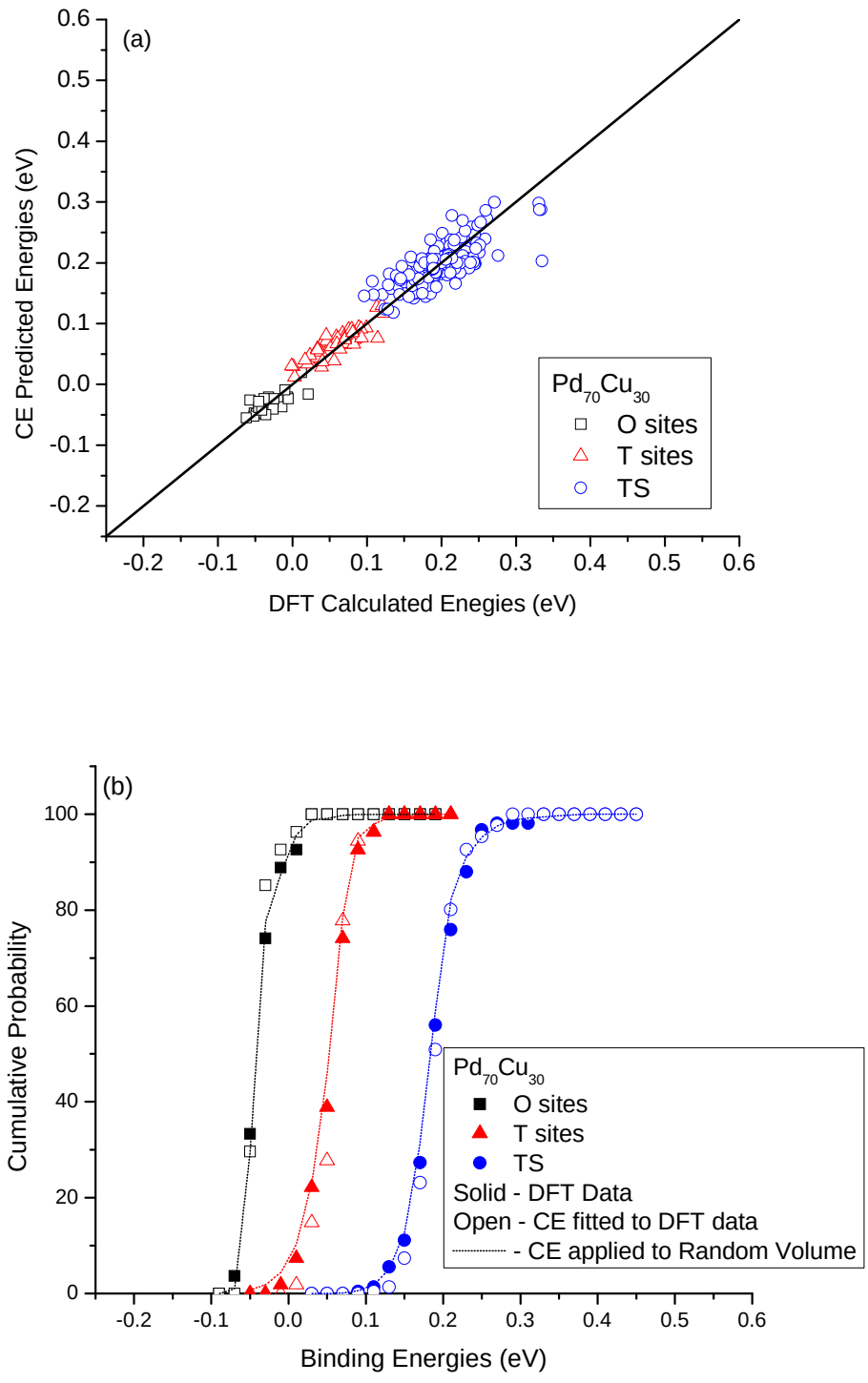

Figure 4.3: Cluster expansion for $Pd_{70}Cu_{30}$. The O sites are represented by squares, triangles represent the T sites, and circles represent TS. (a) A comparison of the CE model and the DFT data. (b) The DFT data and the CE model fitted using only DFT data (open symbols), and the CE model applied to a randomly generated volume (lines).

DFT are properly described by the CE model. The cumulative probability analysis for this alloy and is shown in Figure 4.3(b). There is good correlation between the DFT data and the CE model applied to the random volume.

Next we analyze the CE model for the first ternary system, $Pd_{70}Cu_{26}Pt_4$. Figure 4.4(a) plots the CE for each site fitted to the calculated DFT data. The standard deviations in Table 4.2 for the two PdCu binary alloys and $Pd_{70}Cu_{26}Pt_4$ are similar, and the O site and T site models have lower standard deviations than the TS model. Five of the 432 TS shown in Figure 4.4(a) are predicted somewhat inaccurately by the CE model. The results of using the CE model for a representative randomly generated volume for $Pd_{70}Cu_{26}Pt_4$ are shown in Figure 4.4(b). The energy distribution of the O sites in the random volume is similar to the DFT data for the lowest binding energies observed, but a broader distribution of energies is seen in the random volume than from DFT at higher energies. As mentioned above, this does not necessarily imply that the CE model is inaccurate. Because the variance of this model is acceptably low and the binding sites which are most critical are those in the lower energy regime, we accept this model for H in the O sites. The results for the T sites are similar to the situation in $Pd_{74}Cu_{26}$. We accept the selected CE for the T sites of $Pd_{70}Cu_{26}Pt_4$ for the same reasons as this binary alloy. We also judged the CE model for the TS in Figure 4.4(b) to be an acceptable description of the full range of sites available in $Pd_{70}Cu_{26}Pt_4$.

We turn now to $Pd_{70}Cu_{26}M_4$ for M = Au and Ag. Similar to what was observed for $Pd_{96}Au_4$ and $Pd_{96}Ag_4$ in Chapter 3, the presence of Au and Ag causes some T sites to no longer be local energy minima for H in our DFT calculations for $Pd_{70}Cu_{26}Au_4$

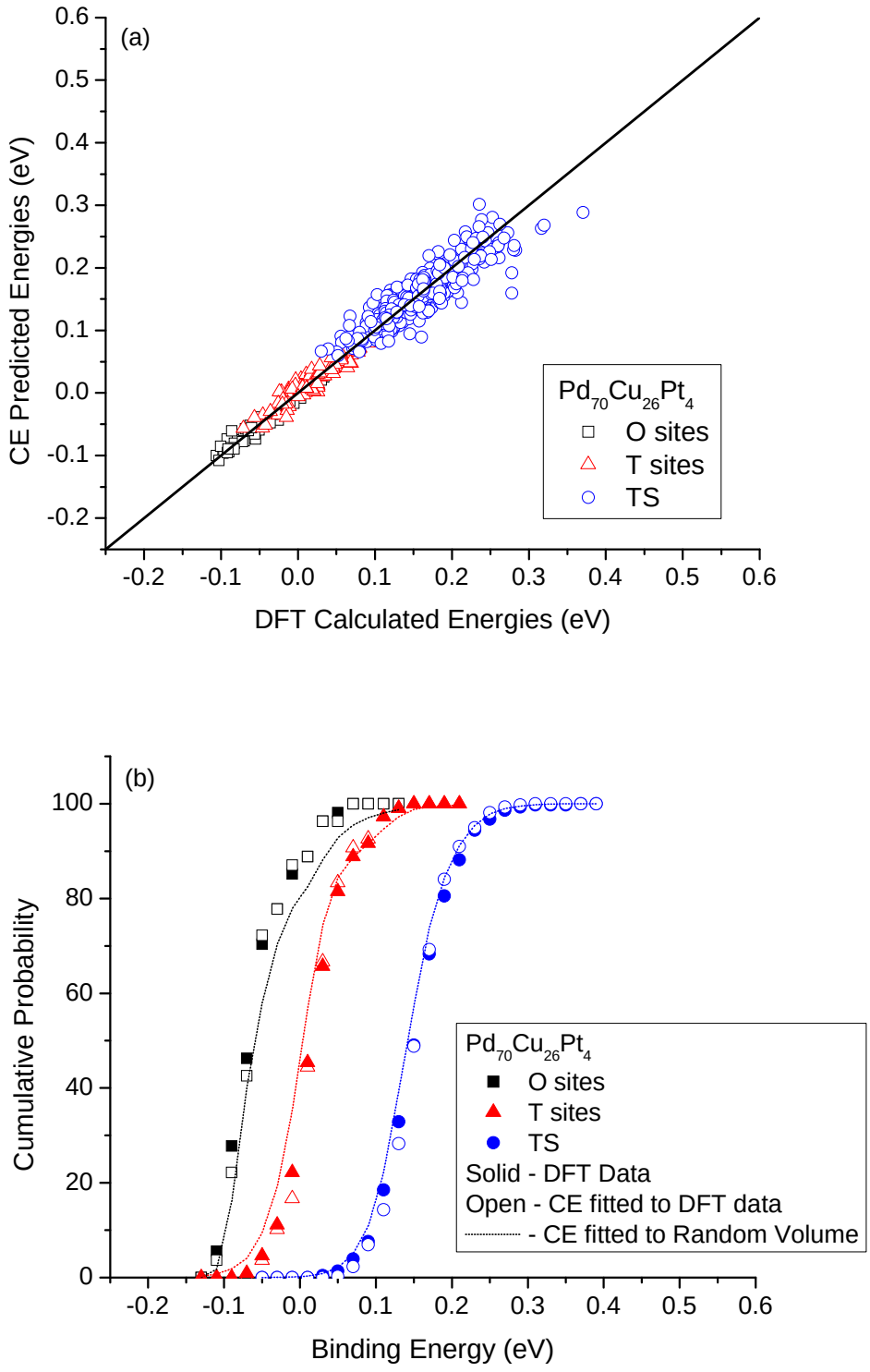

Figure 4.4: Cluster expansion for $Pd_{70}Cu_{26}Pt_4$. The O sites are represented by squares, triangles represent the T sites, and circles represent TS. (a) A comparison of the CE model and the DFT data. (b) The DFT data and the CE model fitted using only DFT data (open symbols), and the CE model applied to a randomly generated volume (lines).

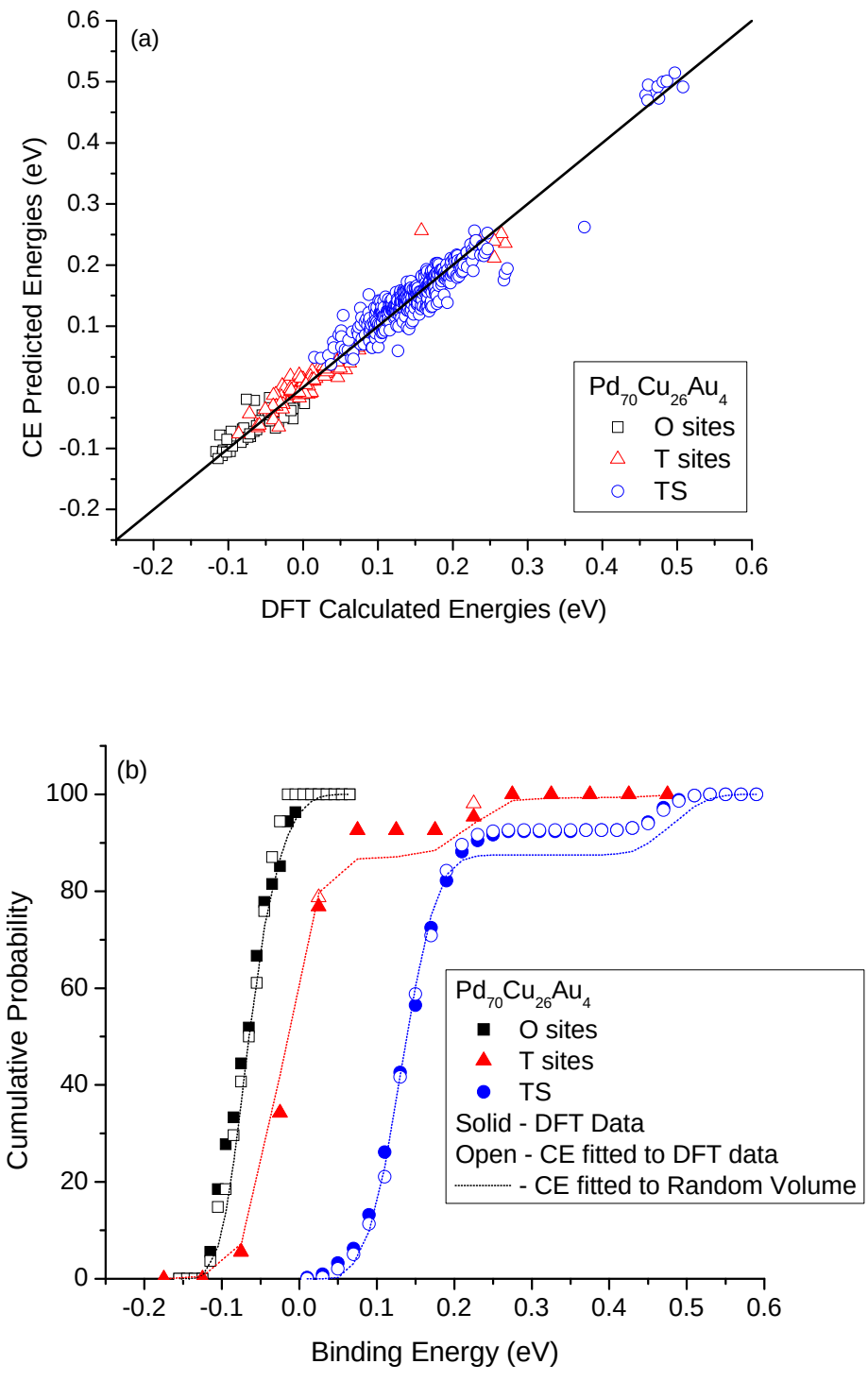

Figure 4.5: Cluster expansion for $Pd_{70}Cu_{26}Au_4$. The O sites are represented by squares, triangles represent the T sites, and circles represent TS. (a) A comparison of the CE model and the DFT data. (b) The DFT data and the CE model fitted using only DFT data (open symbols), and the CE model applied to a randomly generated volume (lines).

and $Pd_{70}Cu_{26}Ag_4$. The physical origin of this result is straightforward. Au and Ag atoms are considerably larger than either Pd or Cu, and the repulsion associated with these atoms partially filling the region that is typically available to define the interstitial T site. These calculations show the same phenomenon for each T site that includes an Au (Ag) atom. These sites were not included in fitting the CE model.

Figure 4.5(a) shows the DFT data and CE data for all sites that are real energy minima in $Pd_{70}Cu_{26}Au_4$. One T site and one TS is poorly predicted by the CE models, but the other 99 T sites and 399 TS are predicted by these models. The results of using the CE model for a representative randomly generated volume for $Pd_{70}Cu_{26}Au_4$ are shown Figure 4.5(b). Because we only include local energy minimum binding sites in our CE model analysis, we identified the T sites that were no longer energy minima as any T site that included an M atom in the $2\times N$ shell. The O site CE model has excellent performance. The energy distribution of the T sites and TS in the random volume is similar to the DFT data for the lowest binding energies observed. A broader energy distribution is observed in the random volume than from DFT at higher energies for both T sites and TS. This does not imply that the CE models are inaccurate, as mentioned earlier.

The $Pd_{70}Cu_{26}Ag_4$ CE models have similar behavior to the models for $Pd_{70}Cu_{26}Au_4$. In Figure 4.6(a) the O site CE model and the T site CE model are excellent fits for the DFT data, but there are a small number of TS are poorly predicted by the truncated CE model. Figure 4.6(b) shows the comparison between the CE models for each binding site with the randomly generated volume and the DFT data. In Figure 4.6(b) we note similarities in the discrepancy as in Figure 4.5(b). Although these models do not

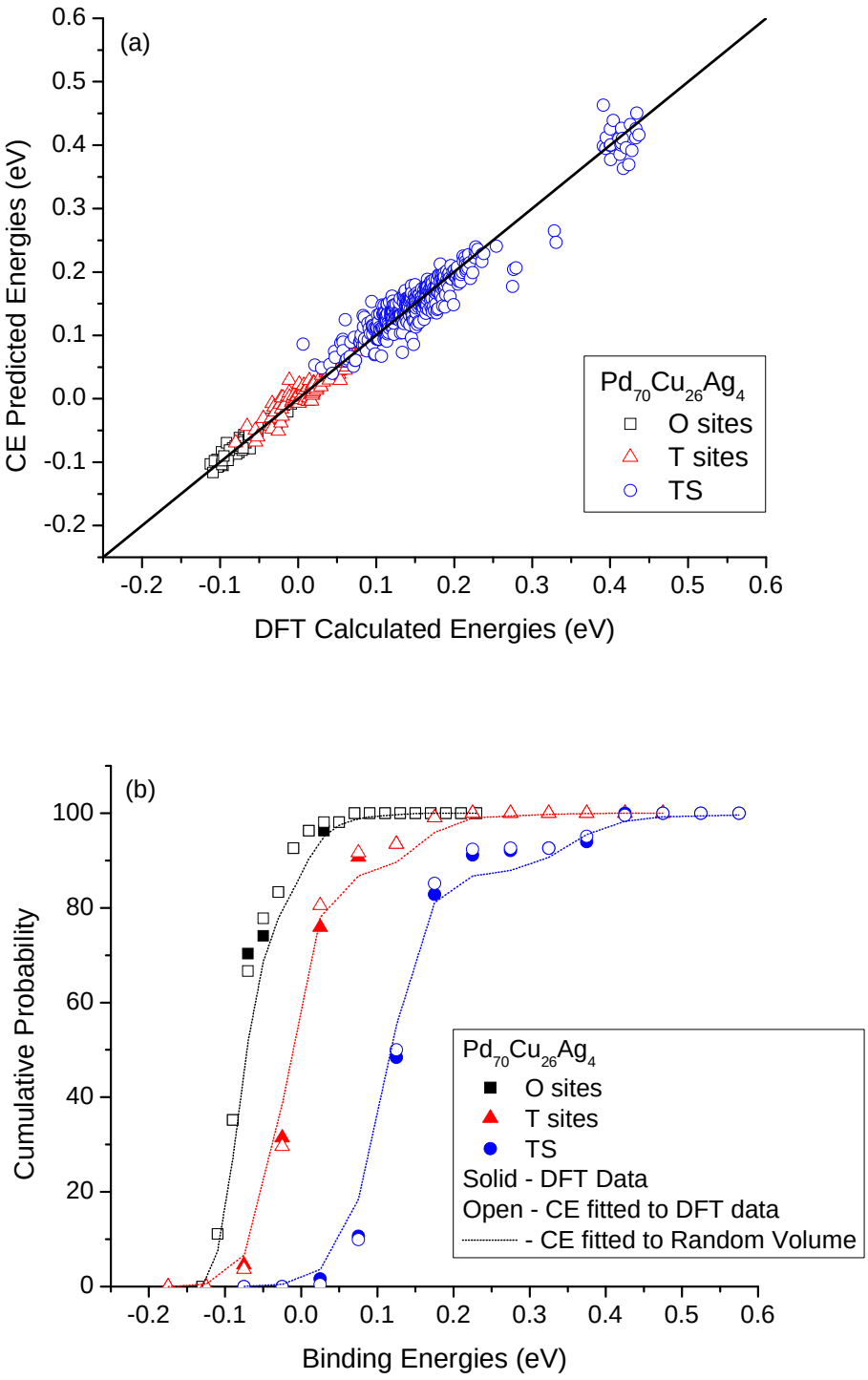

Figure 4.6: Cluster expansion for $Pd_{70}Cu_{26}Ag_4$. The O sites are represented by squares, triangles represent the T sites, and circles represent TS. (a) A comparison of the CE model and the DFT data. (b) The DFT data and the CE model fitted using only DFT data (open symbols), and the CE model applied to a randomly generated volume (lines).

precisely mimic the random volume a reasonable match is observed between the DFT data and the CE applied to the random volume over the full range of binding energies, providing confidence in the CE models.

Up to this point, for all binary and ternary alloys, the DFT data obtained from the supercells described in Chapter 2 proved to be sufficient in finding a CE model capable of both fitting the DFT data as well as predicting binding sites in the random volume. This was not the case for $Pd_{70}Cu_{26}M_4$ when M = Ni. For $Pd_{70}Cu_{26}Ni_4$ we performed the CE selection procedure as it has been done for all other alloys. In analyzing the resulting CE modes for the O sites and the T sites with the randomly generated volume, the CE predicted that a variety of sites we had not examined with DFT gave lower binding energies than all the DFT data. Specifically, the sites that were predicted to have lower energy dealt with two Ni atoms in the $2\times N$ shell of the interstitial sites. Unlike our O and T site CE model determination analysis, in determining the TS CE model, we did not observe any need for additional DFT calculations. These circumstances dictated the need to perform additional DFT calculations for the O sites and the T sites of the $Pd_{70}Cu_{26}Ni_4$ alloy. An additional 27 atom supercell ternary alloy representation was created containing 2 Ni, 7 Cu, and 18 Pd atoms using the optimized lattice constant for the ternary alloy of 3.811Å. In this new supercell, the Ni atoms were chosen to be nearest neighbors to create sites with 2 Ni atoms in the $2\times N$ shell of some interstitial sites. We performed DFT calculations for all available O and T sites within this supercell. Combining all our DFT data gave 81 O sites, 165 T sites, and 432 TS. In Figure 4.7(a) we compare the DFT and CE data for $Pd_{70}Cu_{26}Ni_4$ using the full set of DFT data. The results are similar in quality to the other alloys we have already discussed.

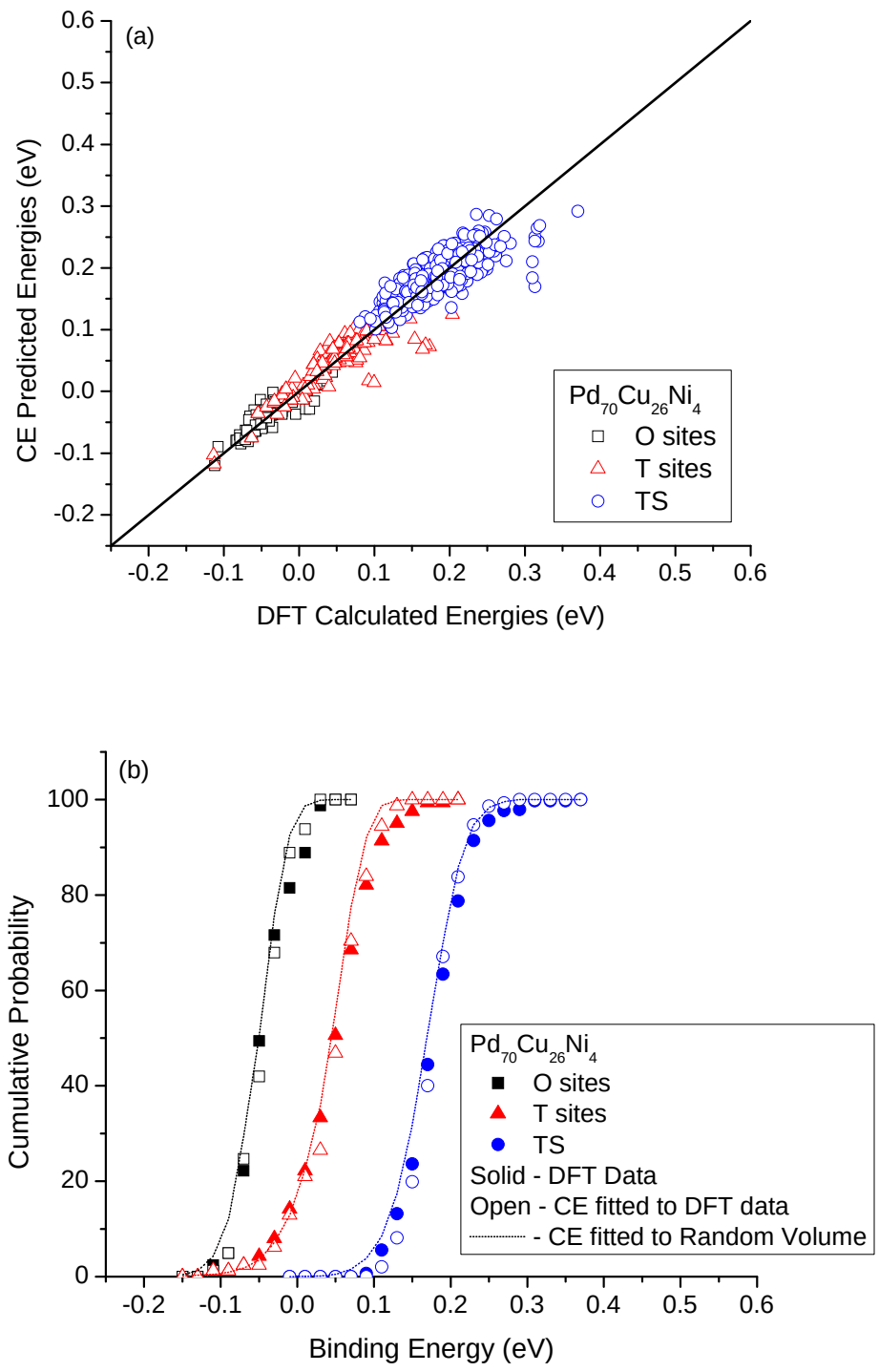

Figure 4.7: Cluster expansion for $Pd_{70}Cu_{26}Ni_4$. The O sites are represented by squares, triangles represent the T sites, and circles represent TS. (a) A comparison of the CE model and the DFT data. (b) The DFT data and the CE model fitted using only DFT data (open symbols), and the CE model applied to a randomly generated volume (lines).

From Figure 4.7(a) it can be observed that there are a several T sites that are similar in energy to the lowest energy O sites. These T sites have two Ni atoms in the $2 \times N$ shell. The physical origin of this result is straightforward. Ni atoms are considerably smaller than both Pd and Cu. When these atoms are present in the set of atoms forming a T site, the region that is typically available to define the interstitial T site becomes larger, hence more favorable than other binding sites of this type.

The CE model validation for the O site, T sites, and TS in $Pd_{70}Cu_{26}Ni_4$ is shown in Figure 4.7(b). An important observation from this figure is that the CE model for T sites shows good agreement when the DFT data and the random volume results are compared for the most favorable sites. From Figure 4.7(b) we conclude that the CE models provide a valid description of $Pd_{70}Cu_{26}Ni_4$.

4.4: Macroscopic Properties of H in $Pd_{70}Cu_{26}M_4$ Alloys

In this chapter we have focused on ternary alloys with composition $Pd_{70}Cu_{26}M_4$ for M = Au, Ag, Pt, and Ni. We have also worked on $Pd_{74}Cu_{26}$ and $Pd_{70}Cu_{30}$ to use as reference materials in order to measure the performance of the ternary alloys. We performed extensive analysis in order to determine a CE model that was capable of describing and predicting H behavior in the bulk of each of these alloys. Using these CE models, we now examine the solubility, diffusion, and permeability of H for the temperature range of T = 400 – 1200 K.

4.4.1: Solubility of H in $Pd_{70}Cu_{26}M_4$ Alloys

As we have already discussed, there is limited experimentally reported solubility data for ternary alloys. Ramaprabhu performed solubility experiments on Pd-rich ternary

alloys of involving Pd-Y-Ag, Pd-Cu-Au, Pd-Ag-Er, Pd-Au-Er, Pd-Cu-Er, Pd-Ni-Rh, and Pd-Ag-Ni[3]. His results suggest that there is a strong correlation between the lattice constant and the solubility. This is similar to what is generally assumed for binary alloys when compared to pure Pd[4, 15].

The H solubility for each alloy was calculated as $\Theta_H = K_s\sqrt{P_{H_2}}$, where $K_s = \sum K_{s,ind}$, $K_{s,ind} = \alpha^{'}\delta e^{-\beta E_b^{ZPE}}$, using the CE models for each particular $Pd_{70}Cu_{26}M_4$ alloy. Further details on the theory of solubility can be found in Chapter 2. We report solubility data as a function of temperature for $Pd_{74}Cu_{26}$, $Pd_{70}Cu_{30}$, and $Pd_{70}Cu_{26}M_4$ for M = Au, Ag, Pt, and Ni in Figure 4.8. In this figure, and in the figures to follow, the solid

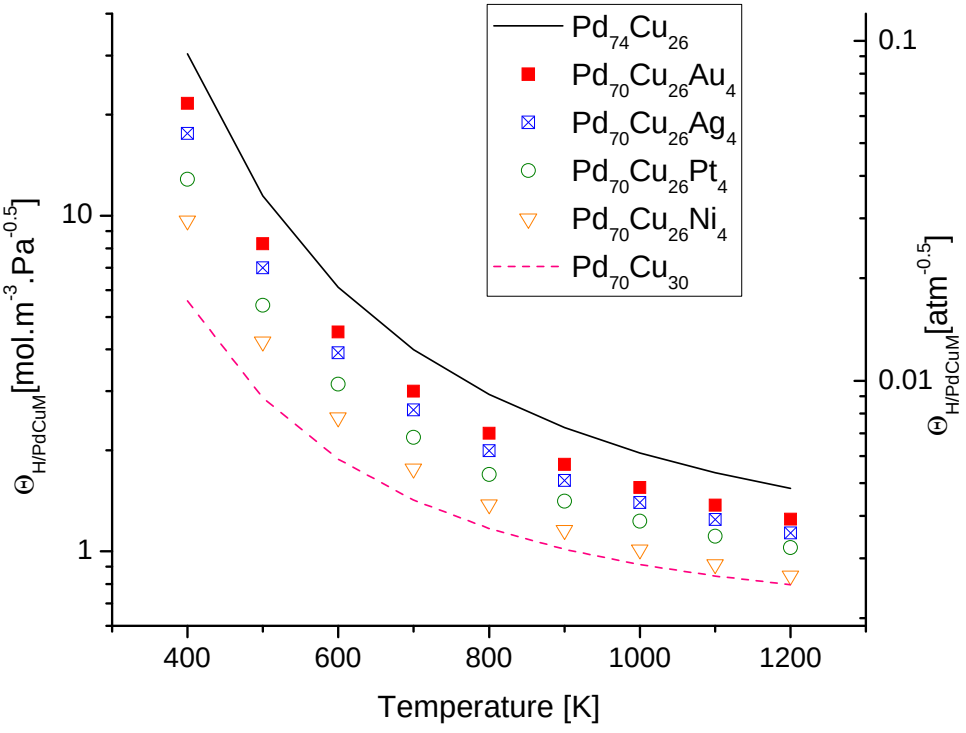

Figure 4.8: Hydrogen solubility predictions for $Pd_{70}Cu_{26}M_4$ for M = Au, Ag, Pt and Ni compared to H solubility predictions in $Pd_{74}Cu_{26}$ and $Pd_{70}Cu_{30}$ for T = 400 – 1200 K.

curves represent $Pd_{74}Cu_{26}$ and $Pd_{70}Cu_{30}$, while open symbols represent the ternary alloys. The predicted H solubility of all four $Pd_{70}Cu_{26}M_4$ ternary alloys falls between the solubility predicted for $Pd_{74}Cu_{26}$ and $Pd_{70}Cu_{30}$. Unlike our observation for H solubility inPd-rich binary alloys, all the additive metal atoms have reduced (increased) H solubility when compared to the PdCu alloy with higher (lower) Pd content. Similar to results in Chapter 3, in the ternary alloys the addition of Au improves the H solubility more than the addition of Ag. The addition of Pt results in reduced H solubility when compared to the previous two additive metal atoms, but has improved H solubility when compared to using Ni.

Before we discuss the ternary alloy results, it is important to note the large difference in the predicted H solubility between the two PdCu binary alloys in Figure 4.8. In Figure 4.9 we have plotted the O site binding energy distribution using the CE models

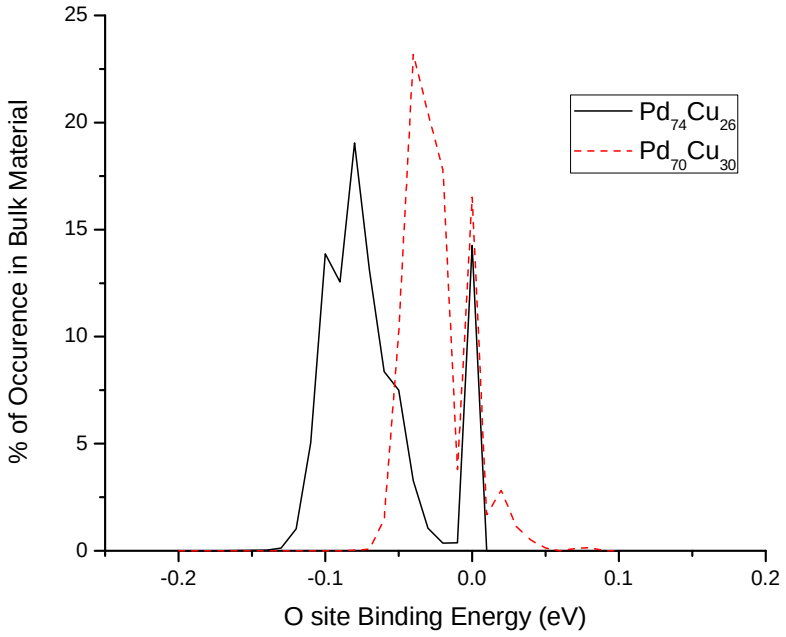

Figure 4.9: Energy distribution using CE models applied to random volume for the O sites of $Pd_{74}Cu_{26}$ (black curve) and $Pd_{70}Cu_{30}$ (red dotted curve).

applied to a random volume for the $Pd_{74}Cu_{26}$ and $Pd_{70}Cu_{30}$ alloys. When we compare the O site energy distribution from Figure 4.9, it can be observed that the majority of the O sites in the $Pd_{74}Cu_{26}$ alloy are lower in energy than for the $Pd_{70}Cu_{30}$ alloy. These two PdCu binary alloys differ by 4 at. % in their Cu content resulting in a 0.51% difference in lattice constant, yet their solubility for H differs by 60% at 800 K. In our results for pure Pd and $Pd_{96}Cu_4$ from Chapter 3, there was lattice constant difference of 0.25% and a reduction of 10% in H solubility at 800 K.

The predicted solubility of H in the ternary alloys normalized by the results for $Pd_{74}Cu_{26}$ is shown in Figure 4.10(a). It is useful to think of these ternary alloys, which have composition $Pd_{70}Cu_{26}M_4$, as replacing 4 at.% of the Pd in the binary alloy with M. Even though the lattice constant of the ternary alloys with M = Ag and Au are larger than the binary alloy, the solubility of H in all the ternary alloys is lower than the binary alloy.

It is useful to examine the solubility of H in these alloys in terms of the effects of lattice strain and chemical interactions. We first consider lattice strain. We collected DFT data for a supercell with composition $Pd_{74}Cu_{26}$ at three different lattice constant, namely the lattice constants for bulk $Pd_{74}Cu_{26}$, $Pd_{70}Cu_{26}Au_4$, and $Pd_{70}Cu_{26}Ag_4$ materials. The two latter lattice constants are 0.13 and 0.08 % larger than for bulk $Pd_{74}Cu_{26}$, respectively. The resulting O site binding energies are shown in Figure 4.11. The only difference between the three calculations for each site in Figure 4.11 is the lattice constant. It is clear from Figure 4.11 that lattice expansion of this binary PdCu alloy makes all O sites more favorable for H. That is, the lattice expansion induced by adding Au or Ag to $Pd_{74}Cu_{26}$ enhances H solubility.

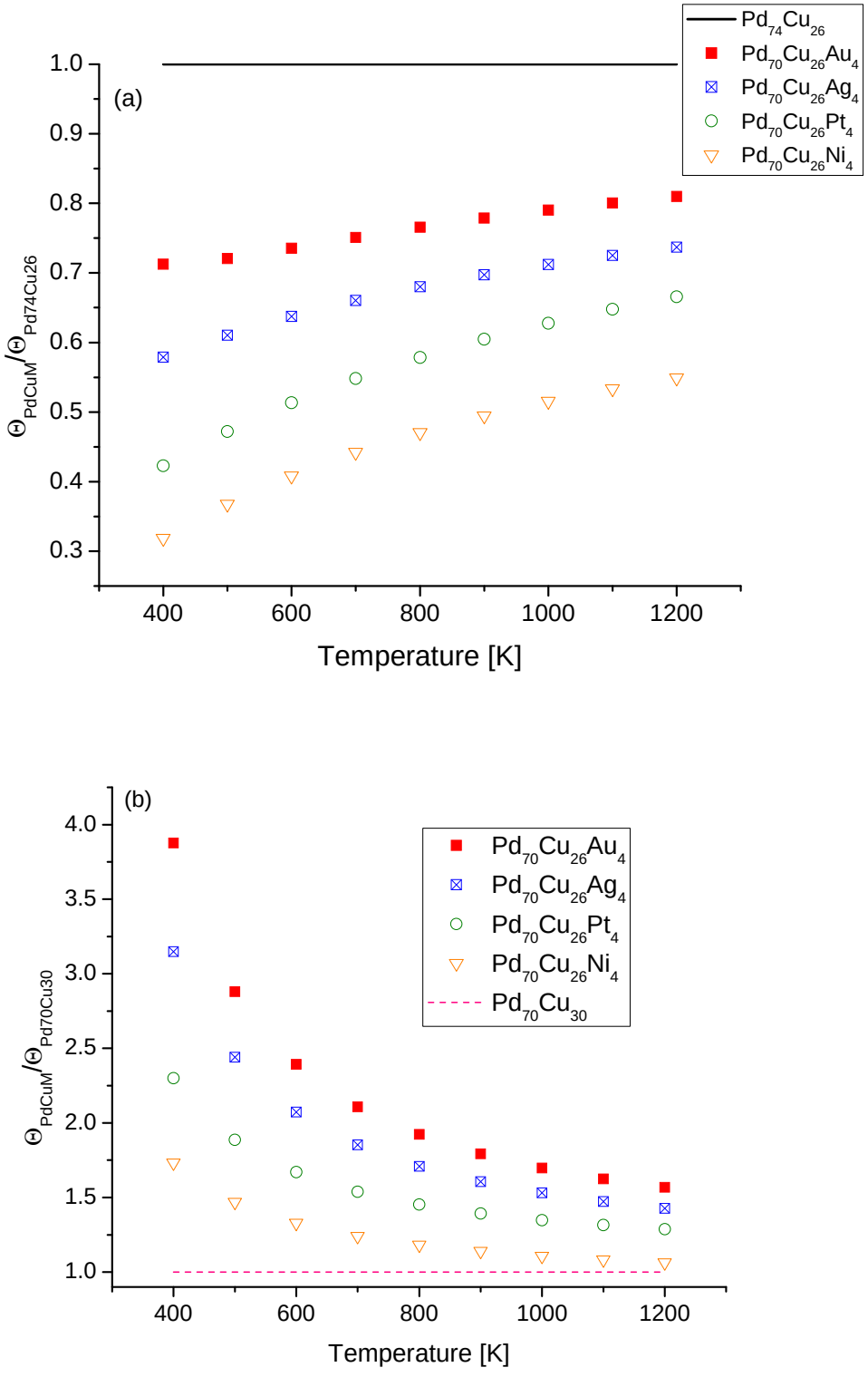

Figure 4.10: Hydrogen solubility predictions for $Pd_{70}Cu_{26}M_4$ for M = Au, Ag, Pt and Ni (a) results normalized with respect to $Pd_{74}Cu_{26}$; (b) results normalized with respect to $Pd_{70}Cu_{30}$.

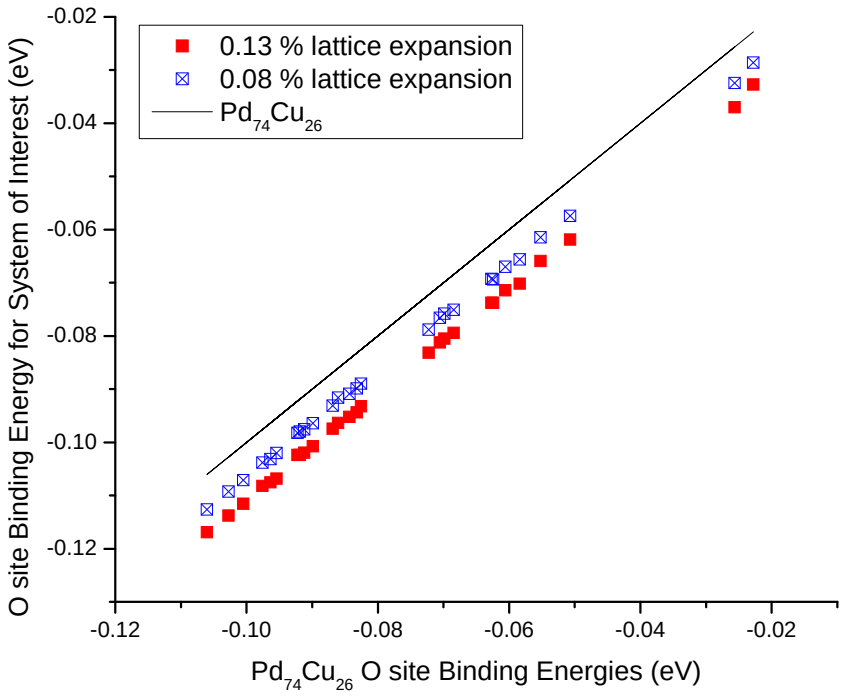

Figure 4.11: DFT calculated O site binding energy for a $Pd_{74}Cu_{26}$, supercell at the three lattice constants described in the text.

The solubility of H in $Pd_{70}Cu_{26}Au_4$, and $Pd_{70}Cu_{26}Ag_4$ relative to $Pd_{74}Cu_{26}$ is of course also influenced by the local chemical interactions between H and Au or Ag atoms. To characterize these effects, we examined our DFT data for groups of O sites that had identical arrangement of nearby Cu atoms in the binary and ternary alloys. The results of this analysis are shown in Figure 4.12. In this figure, each circle represents a shell of neighboring metal atoms around an O site. The innermost circle, for example, denotes the six metal atoms in the $2\times N$ shell, which are located approximately $L/\sqrt{2}$ Å away from the H in an O site. For each coordination shell, we defined ΔE_b to be the average binding energy difference between O sites in the binary and ternary alloy, with this average taken over only those sites that differ by the presence of a single additive atom in the shell of

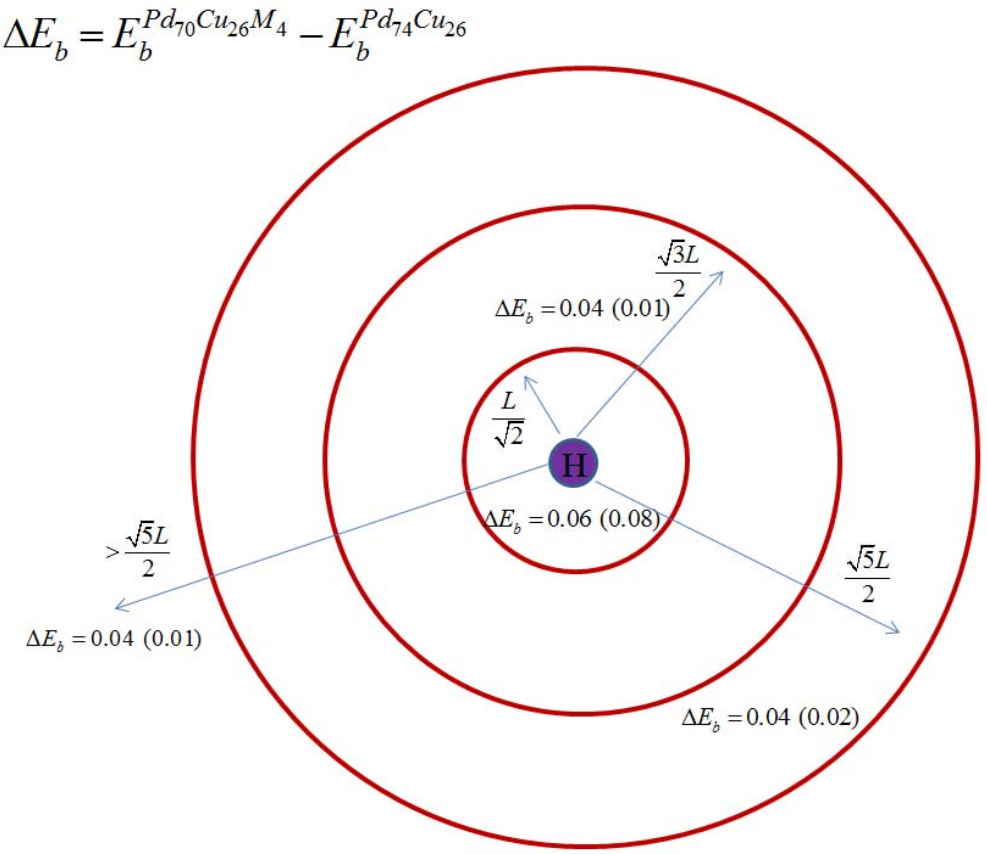

Figure 4.12: DFT calculated O binding site energy difference between O sites in $Pd_{74}Cu_{26}$ and O sites with an M atom in the neighboring shells in $Pd_{70}Cu_{26}Au_4$ ($Pd_{70}Cu_{26}Ag_4$) where $\Delta E_b = E_b^{Pd_{74}Cu_{26}} - E_b^{Pd_{70}Cu_{26}M_4}$.

interest. For the nearest neighbor shell, we find $\Delta E_b = 0.06\ (0.08)$ eV for $Pd_{70}Cu_{26}Au_4$ ($Pd_{70}Cu_{26}Ag_4$). That is, the binding energy of H in sites with Au (Ag) in the $2 \times N$ shell is less favorable by 0.06 (0.08) eV, on average, than similar sites in $Pd_{74}Cu_{26}$. This change in binding energy has the opposite sign to the lattice expansion effect shown in Figure 4.11, and has a larger magnitude than the lattice expansion effect.

As shown in Figure 4.12, the effect of a Au or Ag atom in the second, third, or fourth neighbor shell of an O site also make an O site less favorable for H. As might be expected, the effects from these shells are smaller than for the nearest neighbor shell, particularly for Ag. Because of the periodic boundary conditions in our supercell

calculations, we are unable to unambiguously examine chemical effects beyond the fourth neighbor shells.

The overall solubility of H in $Pd_{70}Cu_{26}Au_4$ and $Pd_{70}Cu_{26}Ag_4$ relative to $Pd_{74}Cu_{26}$ is governed by a combination of lattice expansion effects, which depress solubility in sites near Ag or Au atoms. Because the latter effect has stronger net effect than lattice expansion, these two ternary alloys have lower net solubility for H than $Pd_{74}Cu_{26}$, as seen in Figure 4.10(a). The same qualitative idea can be applied when comparing the ternary alloys to $Pd_{70}Cu_{30}$. In this case the lattice expansion due to adding Au or Ag is larger, with changes of 0.64 (0.59) % in going from the binary alloy to the Au-based (Ag-based) ternary alloy. As a result, lattice expansion effects dominate over local chemical effects in influencing the overall H solubility, leading to higher solubility in the ternary alloys than in $Pd_{70}Cu_{30}$ (see Figure 4.10(b)).

4.4.2: Diffusion of H in $Pd_{70}Cu_{26}M_4$ Alloys

At elevated temperatures hydrogen diffuses via a series of hops between interstitial sites in the fcc lattice through transition states connecting these interstitial sites. Using the CE models derived earlier in combination with a Kinetic Monte Carlo (KMC) scheme, we can characterize H diffusion in each alloy of interest. Further details of the KMC scheme can be found in Chapter 2. In Chapter 3 we introduced O to O hopping that occurred for some sites in alloys with increased lattice constants relative to pure Pd. In our study of $Pd_{70}Cu_{26}M_4$ ternary alloys we find that O to O hopping occurs for ternary alloys with M = Au and Ag. When these additive atoms are present in the bulk material, there are T sites for which an M atom is present in the $2\times N$ shell that are no longer energy minima. When this occurs, a path for H to pass from an O site directly to

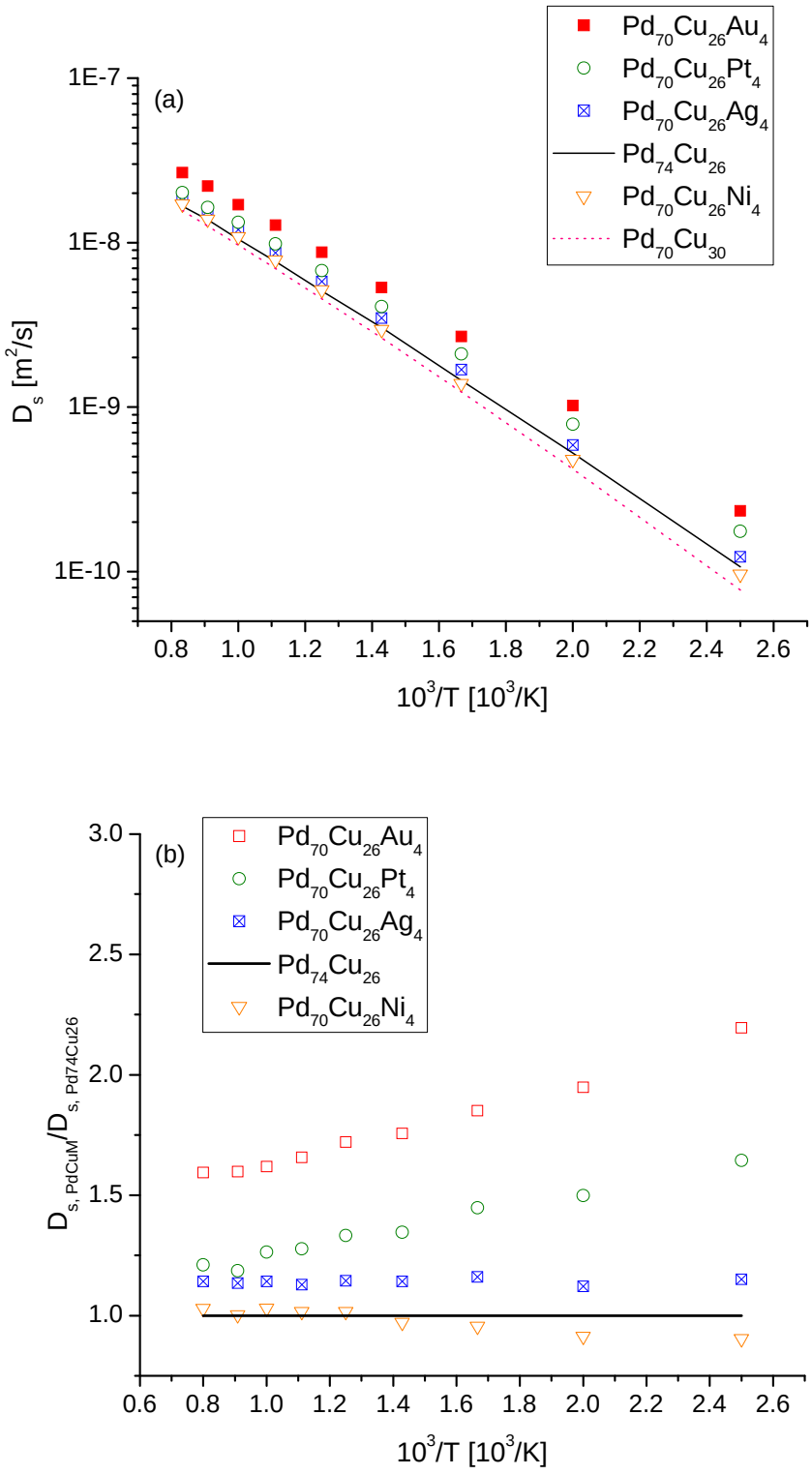

Figure 4.13: H diffusion predictions determined from KMC simulations for $Pd_{74}Cu_{26}$, $Pd_{70}Cu_{30}$, $Pd_{70}Cu_{26}Au_4$, $Pd_{70}Cu_{26}Ag_4$, $Pd_{70}Cu_{26}Pt_4$, and $Pd_{70}Cu_{26}Ni_4$ alloys in this study. (a) Arrhenius plot of H diffusion, (b) H diffusion predictions normalized with respect to $Pd_{74}Cu_{26}$ for the temperature range of 400 – 1200 K.

another O site is opened. For additional information on O to O hopping, refer to Chapter 3. Figure 4.13(a) shows our results for each ternary alloy compared to H diffusion results for $Pd_{74}Cu_{26}$ and $Pd_{70}Cu_{30}$ for T = 400 – 1200 K.

The diffusivities of H in $Pd_{74}Cu_{26}$ and $Pd_{70}Cu_{30}$ are comparable, unlike the H solubility predictions, which were noticeably different. One way to understand why the diffusivities in the two reference binary alloys are similar is to analyze the activation energies for H hops in each alloy. We did this using the CE models applied to a substitutionally random volume for $Pd_{74}Cu_{26}$ and $Pd_{70}Cu_{30}$. We define the activation energy required for H to hop out of an O site by $E_a = E_b^{TS} - E_b^O$. Figure 4.14(a) shows the E_a energy distribution for all sites in $Pd_{74}Cu_{26}$ and $Pd_{70}Cu_{30}$. Recall that the O site energy distributions for these binary alloys, which are plotted in Figure 4.9, shows a noticeable difference between $Pd_{74}Cu_{26}$ and $Pd_{70}Cu_{30}$. This distribution of hopping activation energies, E_a, in contrast are relatively similar for the two alloys.

A complication with this analysis is that looking at E_a give no information about which hops are the most important in net diffusion. It is conceivable, for example, that the lowest energy hops shown in the E_a distribution are associated with unfavorable binding sites and therefore make only limited contribution to H diffusion. To address this issue, we determine the distribution of hopping energies in the range $-0.06 \le E_b^O \le 0.05$ eV. This range corresponds to the most favorable sites in common in each alloy (see Figure 4.9). The results of this analysis are shown in Figure 4.14(b). It can be seen that the hopping energies in $Pd_{74}Cu_{26}$ are slightly lower, on average, than in $Pd_{70}Cu_{30}$, but the magnitude of this difference is relatively small. This is entirely

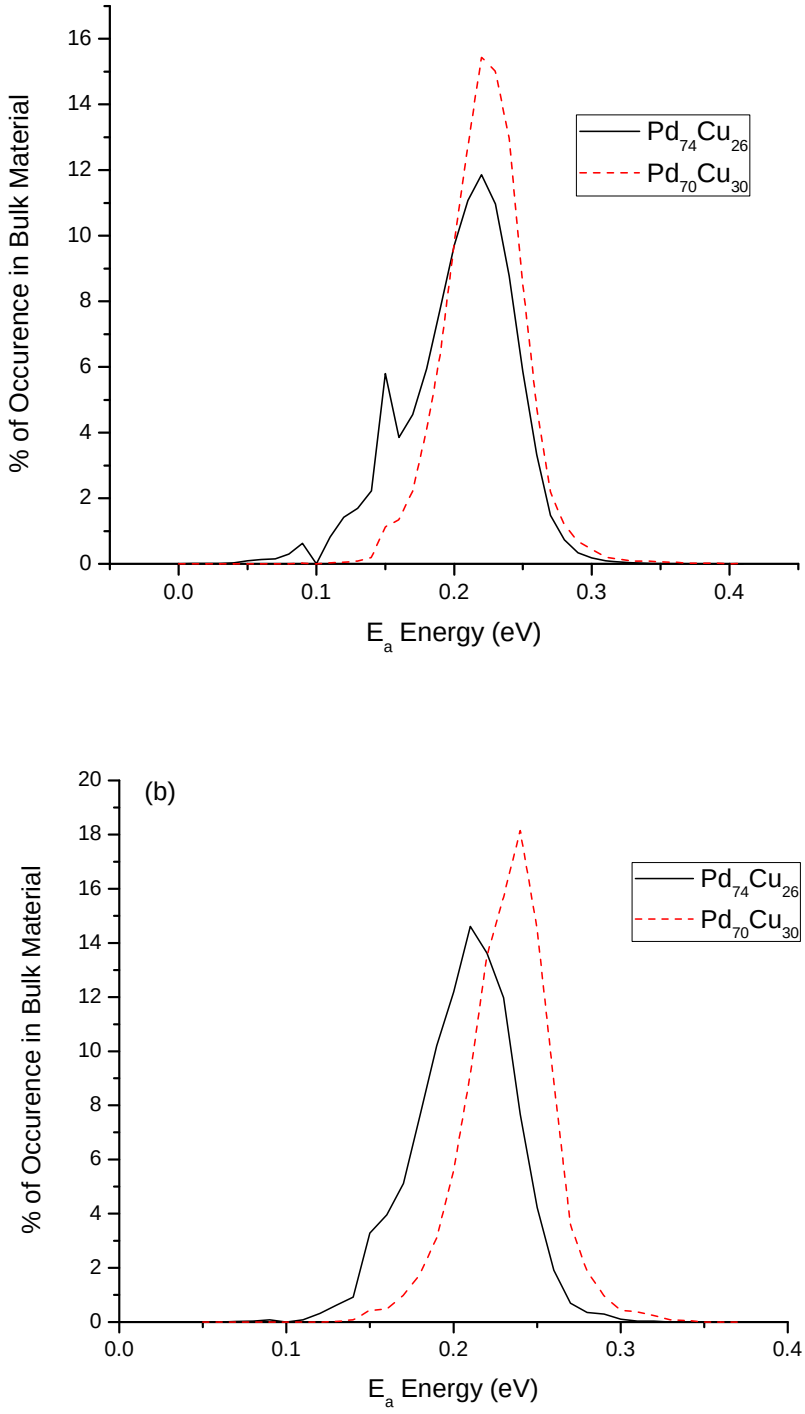

Figure 4.14: Activation energy, E_a, distribution using CE models (a) applied to random volume for $Pd_{74}Cu_{26}$ (black curve) and $Pd_{70}Cu_{30}$ (red dotted curve). (b) E_a distribution for O sites within this volume with binding energy of $-0.06 \le E_b^O \le -0.05$ eV.

consistent with the observation that H diffusion is similar in the two alloys with the $Pd_{74}Cu_{26}$ alloy showing slightly larger diffusivities than $Pd_{70}Cu_{30}$.

From Figure 4.13(a) we also observe that H diffuses faster in the $Pd_{70}Cu_{26}M_4$ for M = Au, Ag, and Pt than in either of the reference PdCu binary alloys, while $Pd_{70}Cu_{26}Ni_4$ is predicted to have similar H diffusion as $Pd_{74}Cu_{26}$. In our solubility analysis we discussed the effects of lattice contributions and chemical effects due to the presence of the M atoms to an interstitial site compared to our reference materials. Again, if we were only to consider the lattice contributions, then it would be expected that any ternary alloy resulting with lattice expansion (contraction) reduces (increases) the activation energy for site to site hopping. If this were the only contribution then we would expect $Pd_{70}Cu_{26}Pt_4$ and $Pd_{70}Cu_{26}Ni_4$ to have lower H diffusion predictions than $Pd_{74}Cu_{26}$ predictions. Because the M atoms are not only affecting local interstitial sites, but surrounding sites as well, the variation of heights of the activation energies for these hops is slightly reduced. The diffusion of H still involves hops over activation barriers of various different heights, it is just that the difference in these heights has been reduced. Because the lattice contributions and the chemical effects are qualitatively different effects on the overall diffusivity of H, it is not possible from this qualitative argument to predict the overall trend in the diffusion of H relative to the binary reference alloys.

To offer another comparison among the alloys, we fitted the data in Figure 4.13(a) to

$$D_s = A_o e^{E_{a,eff}/k_b T} \tag{4.1}$$

where A_o is the pre-exponential factor, $E_{a,eff}$ is the effective activation energy, and k_b is the Boltzmann constant. Table 4.3 lists the fitted parameters from Eq.(4.1), based on data

Table 4.3: Diffusion pre-exponential factor $(m^2 \cdot s^{-1})$ and effective activation energies (eV) for Pd, $Pd_{74}Cu_{26}$, $Pd_{70}Cu_{30}$, $Pd_{70}Cu_{26}Au_4$, $Pd_{70}Cu_{26}Ag_4$, $Pd_{70}Cu_{26}Pt_4$, and $Pd_{70}Cu_{26}Ni_4$ for the low temperature range of T = 400 – 600 K.

System	$A_o(m^2 \cdot s^{-1})$	$E_{a,eff}$ (eV)
Pure Pd	3.52×10^{-7}	0.230
$Pd_{70}Cu_{26}Au_4$	3.58×10^{-7}	0.253
$Pd_{70}Cu_{26}Ag_4$	3.19×10^{-7}	0.271
$Pd_{74}Cu_{26}$	2.75×10^{-7}	0.271
$Pd_{70}Cu_{26}Pt_4$	3.05×10^{-7}	0.257
$Pd_{70}Cu_{26}Ni_4$	2.90×10^{-7}	0.276
$Pd_{70}Cu_{30}$	3.24×10^{-7}	0.288

for equally spaced temperatures for T = 400 K – 600 K . The fitted $E_{a,eff}$ for $Pd_{70}Cu_{26}M_4$ for M = Ag, and Ni are relatively similar in value to $Pd_{74}Cu_{26}$. The larger difference between these alloys lies in the pre-exponential factor. The $E_{a,eff}$ for $Pd_{70}Cu_{26}M_4$ for M = Au and Pt are similar and lower than the activation energy for $Pd_{74}Cu_{26}$.

Because the H diffusion predictions between the two reference alloys are similar we normalized the H diffusivity predictions for $Pd_{70}Cu_{26}M_4$ with respect to $Pd_{74}Cu_{26}$ Figure 4.13(b). Unlike the solubility analysis from Figure 4.13(b) the $Pd_{70}Cu_{26}M_4$ for M = Au, Ag, and Pt are predicted to have increased H diffusion when compared to the H predicted diffusion for $Pd_{74}Cu_{26}$. $Pd_{70}Cu_{26}Au_4$ is predicted to have the fastest H diffusion, followed by the H diffusion in $Pd_{70}Cu_{26}Pt_4$. Compared to these additive metal atoms, the addition of Ag has less of a favorable contribution to H diffusion, with Ni resulting in the least favorable additive metal atoms used in our ternary analysis of H diffusion.

With the exception of M = Ni compared to $Pd_{74}Cu_{26}$ at low temperatures the ternary alloys of interest are predicted to have increased H diffusion than our two reference PdCu alloys. A simplified manner of explaining these results is that for M = Au

and Ag, the expanded lattice reducing the activation energy of H hopping was sufficient to increase H diffusion in these alloys. This is the general observation for all the ternary alloys of interest compared to $Pd_{70}Cu_{30}$. For $Pd_{70}Cu_{26}Pt_4$, the lattice parameter correlation has no consequence to the H diffusion, given that they both have the same lattice parameter. For $Pd_{70}Cu_{26}Pt_4$ anti-trap sites or sites which are less favorable are formed when compared to $Pd_{74}Cu_{26}$, resulting in decreased H solubility, and increased H diffusion in this ternary alloy. For $Pd_{70}Cu_{26}Ni_4$ the lattice is reduced, yet we have previously discussed how there are several T sites with multiple Ni atoms that have more favorable H binding. This results in a reduction in activation energy for H hopping, making up for the increased in the activation energy barriers due to the lattice reductions. The overall result is similar H diffusion predictions between $Pd_{70}Cu_{26}Ni_4$ and $Pd_{74}Cu_{26}$ at elevated temperatures.

4.4.3: Permeability of H in $Pd_{70}Cu_{26}M_4$ Alloys

Having obtained results for both the solubility and the diffusion, we can predict the permeability of H in the ternary alloys $Pd_{70}Cu_{26}M_4$ for M = Au, Ag, Pt, and Ni and the binary reference alloys $Pd_{74}Cu_{26}$ and $Pd_{70}Cu_{30}$. It is worth noting that these predictions did not require the availability of any experimental data for these alloys. The permeability of H for pure Pd, $Pd_{74}Cu_{26}$, $Pd_{70}Cu_{30}$, $Pd_{70}Cu_{26}Au_4$, $Pd_{70}Cu_{26}Ag_4$, $Pd_{70}Cu_{26}Pt_4$, and $Pd_{70}Cu_{26}Ni_4$ was calculated using $k = D_s K_s / 2$ and the results are plotted in Figure 4.15(a). For a detailed explanation of these permeability calculations, refer to Chapter 2.

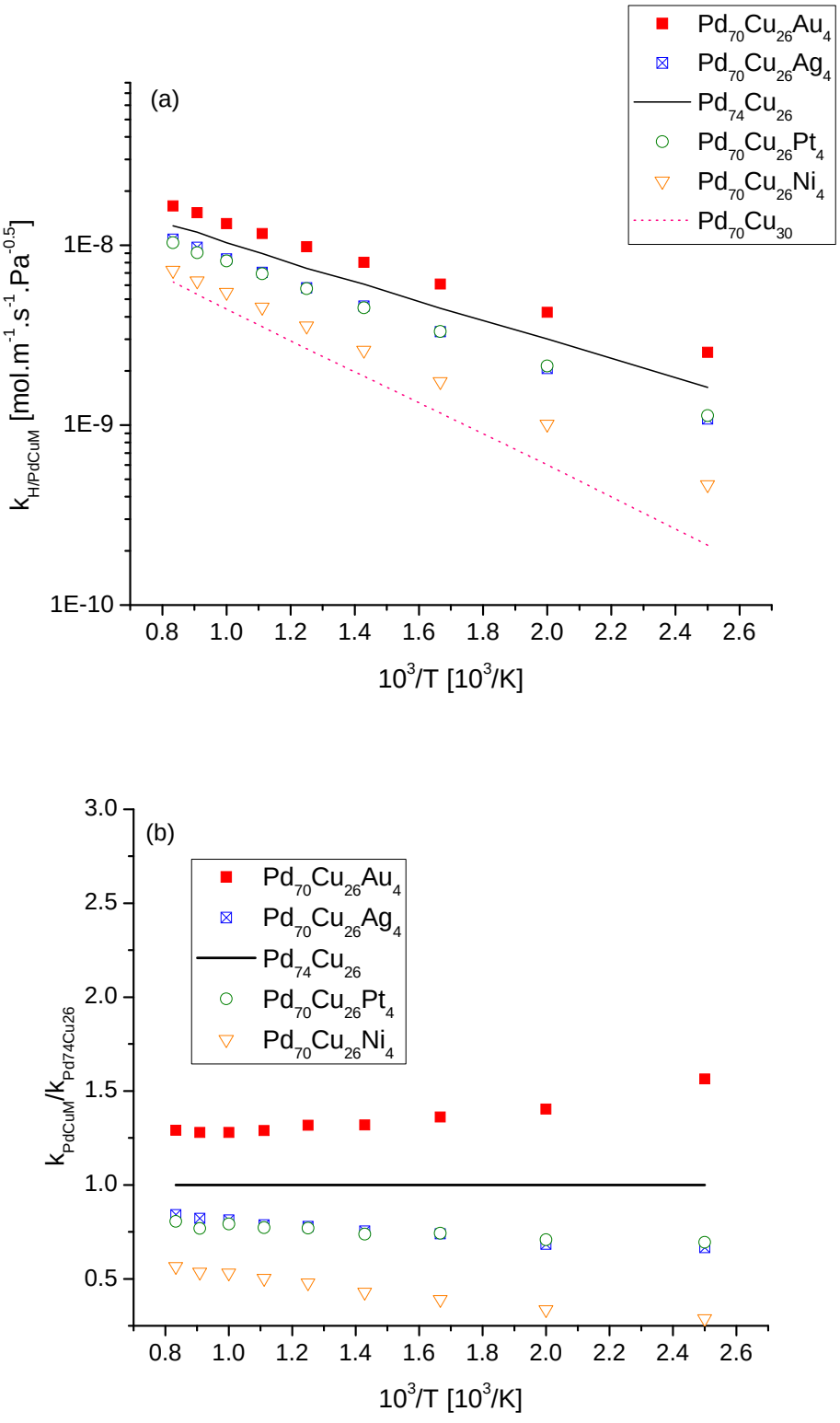

Figure 4.15: Permeability results for PdCu-based ternary alloys (a) in $\mathrm{mol \cdot m^{-1} \cdot s^{-1} \cdot Pa^{-0.5}}$ **and (b) normalized with respect to $Pd_{74}Cu_{26}$ for the temperature range of T = 400 – 1200 K.**

Permeability is directly proportional to both solubility and diffusion. From Figure 4.15(a) we observe that the $Pd_{70}Cu_{26}Au_4$ is predicted to have the overall best H permeability for this temperature range. The remaining ternary alloys are all predicted to have diminished H permeability when compared to $Pd_{70}Cu_{26}Au_4$. From Figure 4.15(a) we observe that all alloys of interest are predicted to have increased H permeability when compared to the reference binary alloys $Pd_{70}Cu_{30}$. This is a useful result, given that while using the same Pd content we are capable of improving H macroscopic properties when ternary alloys are formed using M = Au, Ag, Pt, or Ni. Because all ternary alloys were predicted to have increased H permeability we only present the normalized H permeability results with respect to $Pd_{74}Cu_{26}$ in Figure 4.15(b). The $Pd_{70}Cu_{26}Au_4$ H permeability is observed to be approximately 1.3 times larger than the H permeability in $Pd_{74}Cu_{26}$ for T > 600 K. There is a weak temperature dependence on H permeability predictions when compared to H permeability in $Pd_{74}Cu_{26}$. We observed similar H permeability characteristic for predicted H permeability in $Pd_{96}Au_4$ compared to pure Pd; refer to Chapter 3 for additional information.

The additions of Ag, Pt, and Ni as additive metal atoms results in a negative effect on the permeability of H in comparison to $Pd_{74}Cu_{26}$ as observed in Figure 4.15(b). Although an increase in H diffusion was observed for $Pd_{70}Cu_{26}Ag_4$, $Pd_{70}Cu_{26}Pt_4$, $Pd_{70}Cu_{26}Ni_4$ (at elevated temperatures) it was not sufficient to compensate any reduction predicted in H solubility. The addition of Ag or Pt as additive metal atoms are predicted to have overall similar H permeability effects when compared to H permeability in $Pd_{74}Cu_{26}$. Similar to $Pd_{70}Cu_{26}Au_4$, there seems to be little temperature dependence on the H permeability of $Pd_{70}Cu_{26}Ag_4$ and $Pd_{70}Cu_{26}Pt_4$ as seen in Figure 4.15(b). H permeability

for $Pd_{96}Pt_4$ compared to pure Pd also was predicted to have little temperature dependence on the overall performance, refer to Chapter 3 for additional information. Although there $Pd_{70}Cu_{26}Ni_4$ and $Pd_{74}Cu_{26}$ were predicted to have similar H diffusivity, the H solubility of $Pd_{70}Cu_{26}Ni_4$ was predicted to be the lowest out of all the $Pd_{70}Cu_{26}M_4$ alloys in this study. As a result, the H permeability is at best 57% of H permeability in $Pd_{74}Cu_{26}$.

4.5: Conclusion

We have successfully analyzed the properties of interstitial H in $Pd_{74}Cu_{26}$, $Pd_{70}Cu_{30}$, $Pd_{70}Cu_{26}Au_4$, $Pd_{70}Cu_{26}Ag_4$, $Pd_{70}Cu_{26}Pt_4$, and $Pd_{70}Cu_{26}Ni_4$ using limited DFT calculations. We applied the cluster expansion approach to the development of lattice models for the description of interstitial H. With the cluster expansion approach we are capable of exploring a large number of possible lattice models. Separate models were developed with this method for the binding energy of H in the O sites, T sites, and in the transition states connecting these interstitial sites. For each kind of site, a separate cluster expansion was applied to the classical binding energy and the zero point energy of the interstitial H atom. By separating these two energies it made it possible to use quantum corrected transition state theory in a straightforward way to describe the temperature dependent hopping rates of H between adjacent sites. Once a lattice model of interstitial H has been developed in this manner, the net solubility and diffusivity of H can be computed. These quantities can be combined to give the net permeability of hydrogen through a bulk sample of the metal alloy being modeled.

In order for the general approach just outlined to be successful, the lattice model must correctly identify all local minima and transition states. From our $Pd_{96}M_4$ analysis

we identified that the presence of metal atoms larger in size than Pd would cause some of the T sites to no longer be local energy minima on the potential energy surface. Hence we were not surprised when our DFT calculations for $Pd_{70}Cu_{26}Au_4$ and $Pd_{70}Cu_{26}Ag_4$ showed that not all T sites that we not local energy minima. These T sites were identified when one of the four atoms defining these T sites was an M atom. Site to site hopping through these T sites from one O site to another O site can occur with H moving through these types of T sites while passing over a single transition state.

Although fcc PdCu alloys are known to have reduced H permeability, they are also known to increase contamination resistance compared to pure Pd[8]. Our main goal was to predict if the addition of four atomic percent of a third atom to bulk material mainly composed of Pd and Cu could be sufficient to affect the macroscopic properties of H in the bulk if these membranes. Our results suggest that we can improve the performance of a binary membrane by developing a ternary alloy using Au as the additive. By no means have we found the metal alloy membrane that surpasses the performance of commercially used Pd-based alloys, but we are capable of predicting that we can tweak the alloy performance by introducing additional materials. It would be interesting to see how increased amounts of the additive metals would further affect H macroscopic properties in the bulk of these materials.

4.6: References:

1 L. Semidey-Flecha and D. S. Sholl, J. Chem. Phys. **128**, 144701 (2008).
2 P. Kamakoti and D. S. Sholl, J. Membr. Sci. **279**, 94 (2006).
3 S. Ramaprabhu, Int. J. Hydrogen Energy **23**, 787 (1998).
4 A. Weiss, Ramaprabhu, S., Rajalakshmi, N., Zeit. Phys. Chem **199**, 165 (1997).
5 K. Ohira, Y. Sakamoto, and T. B. Flanagan, J. Alloys and Compounds **236**, 42 (1996).

[6] Y. Sakamoto, K. Ohira, N. Ishimaru, F. L. Chen, M. Kokubu, and T. B. Flanagan, J. Alloys and Compounds **217**, 226 (1995).
[7] Y. Sakamoto, F. L. Chen, M. Furukawa, and M. Noguchi, J. Alloys and Compounds **185**, 191 (1992).
[8] P. Kamakoti, B. D. Morreale, M. V. Ciocco, B. H. Howard, R. P. Killmeyer, A. V. Cugini, and D. S. Sholl, Science **307**, 569 (2005).
[9] B. D. Morreale, M. V. Ciocco, B. H. Howard, K. S. Rothenberger, A. V. Cugini, and R. M. Enick, J. Membr. Sci. **241**, 219 (2004).
[10] O. Iyoha, E. R, R. Killmeyer, and B. D. Morreale, J. Membr. Sci. (2007).
[11] *Binary Alloy Phase Diagrams, 2nd Edition*, 1990).
[12] H. Okamoto, *Desk handbook : phase diagrams for binary alloys* (ASM International, Materials Park, OH, 2000).
[13] S. Fujita and A. Garcia, J. Phys. Chem. Solids **52**, 351 (1991).
[14] H. Barlag, L. Opara, and H. Zuchner, J. Alloys and Compounds **330**, 434 (2002).
[15] G. Alefeld and J. Völkl, *Hydrogen in Metals I* (Springer-Verlag, Berlin, 1978).

CHAPTER 5

A HEURISTIC LATTICE MODEL FOR ANALYZING H PERMEABILITY THROUGH ALLOY MEMBRANES

In previous chapters we have discussed an approach involving numerous DFT calculations in combination with coarse grained statistical models to represent the properties of interstitial H in Pd-based alloys. These calculations were performed for both binary alloys and ternary alloys. These efforts made detailed predictions about which alloys are best suited for H purification relative to other Pd-based dense metal membranes. From a practical standpoint, it would be ideal if this detailed approach could be coupled with a less time consuming method that could identify new alloys with interesting properties. From a general point of view, the solubility of H is correlated with the lattice expansion in an alloy compared to the host lattice, although there are exceptions to the lattice expansion/contraction rule as seen in binary alloys where Pd is alloyed with Pt[1, 2]. A more challenging and less understood concept is how to understand chemical effects on the diffusion of H in alloys. In this chapter we describe a heuristic lattice model that is suitable for rapidly characterizing H solubility and diffusion in alloys, and show how this model can focus the search of new materials for membranes.

5.1: Methodology

We aim to develop a simple lattice model for interstitial H that describes lattice expansion/contraction effects independently from chemical effects due to the presence of the additive metal atom used in binary alloys. We do this assuming that the binding

energy of each interstitial site in a binary alloy in which one metal species i is designated the additive species can be expressed as,

$$E_b^{site} = E_{LC} + E_2 N \tag{5.1}$$

This expression includes the energy due to lattice expansion, E_{LC}, and the (local) chemical effect, E_2, multiplied by the number of additive metal atoms (M) in the nearest neighboring shell ($2 \times N$) of the binding site, N. The lattice distortion effect is assumed to apply uniformly to all interstitial sites. This expression is a severe simplification of the cluster expansion-based model we have used earlier. We reiterate that the idea of the heuristic lattice model is to pre-screen potential alloys and not necessarily provide the most accurate prediction in terms of the H permeability in these alloys.

5.1.1: Lattice Distortion

When a Pd-based binary alloy is formed, the lattice constant of this alloy compared to the lattice constant of pure Pd is influenced by the size of the atoms of the second metal used to form the alloy. Since the heuristic lattice model needs to be general enough to encompass any metal atom introduced with Pd to form a binary alloy, the simplest approach to quantifying E_{LC} is to characterize the properties of bulk pure Pd as the lattice is expanded or contracted. We performed DFT calculations to obtain the octahedral (O) binding energy, tetrahedral (T) binding energy, and transition state (TS) energies of H in pure Pd with lattice expansions and contractions of up to 1 % relative to the DFT-optimized lattice constant. Table 5.1 lists these results for the O and T sites, which show that the binding energies are linearly correlated with the lattice constant. In order to characterize these effects, we performed linear fits to the DFT data in Table 5.1 for the O site and the T sites as follows:

$$E_{LC} = E_o + E_1 \Delta_{LC} \tag{5.2}$$

$$\Delta_{LC} = \frac{(LC_{alloy} - LC_{Pd})}{LC_{Pd}}$$

Here, E_o and E_1 are constants and Δ_{LC} is the lattice distortion between the lattice constant of the alloy and the lattice constant of pure Pd. The results of these linear fits are shown in Table 5.2. We performed similar calculations to quantify the zero point energy (ZPE) dependence on the lattice distortion for each binding site and the TS. Our earlier detailed calculations for Pd-rich binary alloys and PdCu-ternary alloys indicated that the ZPE's of H in the distinct interstitial sites of these materials are relatively insensitive to the local environment. For this reason we decided to employ a model that will account for the lattice distortion effects on the ZPE but not a chemical effect, a factor to be discussed below. We have now accounted for the lattice distortion contribution in Eq. (5.1) and the next step is to determine the local chemical effect contributions. The local chemical effect must be individually determined for each Pd-based binary alloy, a subject of further discussion below.

Table 5.1: Classical binding energies of H in octahedral (O) and tetrahedral (T) sites in pure Pd as a function of lattice constant as computed using DFT.

LC **(Å)**	**%** Δ_{LC}	**O site** E_b (eV)	**T site** E_b (eV)
3.9204	-1.00	-0.0558	0.0434
3.9303	-0.75	-0.0775	0.0119
3.9402	-0.50	-0.0998	-0.0226
3.9501	-0.25	-0.1208	-0.0549
3.9600	0.00	-0.1416	-0.0870
3.9699	0.25	-0.1619	-0.1184
3.9798	0.50	-0.1799	-0.1472
3.9897	0.75	-0.2002	-0.1763
3.9996	1.00	-0.2213	-0.2081

Table 5.2: Lattice distortion energy, E_{LC}, and ZPE parameters for the O site, T site and TS of bulk pure Pd as the lattice is varied from 3.92 Å – 4.00Å.

O site	E_o (eV)	E_1 (eV)
E_{LC}	-0.1399	-8.2093
ZPE_O	0.10067	-0.8000

T site	E_o (eV)	E_1 (eV)
E_{LC}	-0.0843	-12.5547
ZPE_T	0.1827	-0.8000

TS	E_o (eV)	E_1 (eV)
E_{LC}	-	-
ZPE_{TS}	0.1645	-0.8000

5.1.2: Local Chemical Effect E_2

Now that we have a way of quantifying the lattice distortion effects, E_{LC}, all that remains to fully specify Eq. (5.1) is the chemical effect due to the presence of the M atoms in the local environment of the interstitial binding sites. According to Eq. (5.1) an M atom that has a favorable (unfavorable) effect on the H binding energy would have $E_2 < 0$ $(E_2 > 0)$. A general model needs to account for all possible values of the local chemical effect. To do this, we will analyze our heuristic lattice model for all values of E_2 in the range $-0.20 \le E_2 \le 0.40$ eV.

5.1.3: Transition States

H transport at elevated temperatures in fcc metals occurs through a series of hops between neighboring interstitial binding site via TS. Similar to our calculations for the O and T sites, we performed DFT calculations to obtain the TS energy in pure Pd as the lattice constant was varied. The TS are used to obtain the classical activation energy for a

hop, $E_{a(\min)} = E_b^{TS} - E_b^O\left(E_b^T\right)$, which is calculated as a difference in energy between the TS and the interstitial binding site of interest. This definition characterizes the activation energy in terms of $E_a\left(E_{a,\min}\right)$ for hops out of an O (T) site.

lists the results of these calculations. The data shows that $E_{a,\min}$ is the only weakly dependent on the lattice constant, with an average value of $\overline{E_{a,\min}} = 0.1183$ eV. To keep the heuristic lattice model simple, we define the binding energy of the TS as $E_b^{TS} = E_b^T + E_{a,\min}^{Pd}$, where E_b^T is the value of Eq.(5.1) for a T site and $E_{a,\min}^{Pd}$ is the activation energy for a hop out of the T site for the undistorted lattice constant for pure Pd. Once the TS energies are defined, the activation energy for any specific hop is easily obtained. Because the ZPE are generally insensitive to the chemical effect due to the presence of M atoms, the ZPE for all interstitial sites are modeled as being independent of the number of M atoms near the TS.

Table 5.3: DFT classical activation energy for hops out of an O site (E_a) and for hops out of a T site $(E_{a,\min})$ in pure Pd as the lattice constant is expanded and contracted.

LC (Å)	% Δ_{LC}	E_a (eV)	$E_{a,\min}$ (eV)
3.9204	-1.00	0.2246	0.1254
3.9303	-0.75	0.2125	0.1231
3.9402	-0.50	0.1989	0.1216
3.9501	-0.25	0.1857	0.1198
3.9600	0.00	0.1712	0.1165
3.9699	0.25	0.1614	0.1159
3.9798	0.50	0.1477	0.1149
3.9897	0.75	0.1372	0.1132
3.9996	1.00	0.1251	0.1119

5.2: Heuristic Lattice Model Results

In Chapter 2 we discussed our methods for calculating the solubility, diffusion, and permeability of H in the bulk of fcc alloys. A substitutionally random volume containing $4,000$ atoms, equivalent to a $10\times10\times10$ primitive fcc cell, is defined at a desired alloy composition. Below, we analyze six binary alloy compositions, $Pd_{100-x}M_x$ for $x = 3.70$, 11.1, 18.5, 25.9, 33.3 and 40.7 at.%. These compositions were chosen to match the compositions of the 27 atoms supercells used to describe each alloy in our subsequent DFT calculations, and we shall refer to them as $x = 4$, 11, 19, 26, 33, and 41 at.% for simplicity. We intentionally selected these alloy compositions in order to ensure that the majority of the bulk material was Pd. At each alloy composition we explore H solubility, diffusion, and permeability using our heuristic lattice model for values of the lattice constant from $LC = 3.68\,\text{Å} - 4.09\,\text{Å}$, and chemical effects in the range of $-0.20 \le E_2 \le 0.40$ eV. This means that for every alloy composition we analyzed 42 lattice constants and effects of M atoms that varied from highly attractive to highly repulsive for H.

We are going to be working with Pd-based binary alloys for which dilute amounts of H are present in the bulk material. This implies we can predict H solubility using Sieverts' Law[3]. For additional details regarding Sieverts' Law, refer to Chapter 2. For simplicity, we will perform our pre-screening calculations at a fixed temperature. Solubility in general decreases with increased temperature, hence for pre-screening purposes there is no need for a full temperature profile.

Once all the sites within an fcc binary alloys have been characterized, the rates of hopping from interstitial binding site to interstitial binding site via TS can be computed

using quantum corrected harmonic transition state theory (TST)[4, 5]. Additional information regarding TST can be found in Chapter 2. In order to predict H diffusivity these local hopping behaviors need to be linked with long range H transport. This can be done with Kinetic Monte Carlo (KMC)[6] simulations. KMC simulations were used to determine the net diffusivity of interstitial H in alloys described by our heuristic lattice model, as previously described in Chapter 2. Permeability of H in the bulk of thick membranes is directly proportional to the H solubility and diffusivity. Once we have calculated the solubility and diffusion of H we calculate the permeability as described in Chapter 2.

Using the heuristic lattice model we have examined H solubility, diffusion, and permeability for $2,562$ binary alloys. We present the solubility, diffusion, and permeability results normalized with respect to the predicted macroscopic properties of H in pure Pd. By doing this we are capable of determining whether the alloy is predicted to be more or less favorable than pure Pd.

5.2.1: H Solubility Predictions

We calculated the H solubility, Θ_{alloy}, using Sieverts' Law with the heuristic lattice model for 42 distinct lattice constants and 61 distinct local chemical effects at $600\ \mathrm{K}$. Figure 5.1 shows the calculated H solubility for $Pd_{100-x}M_x$ for x = 4 at.% normalized with respect to pure Pd. As the lattice constant of the alloy decreases, a decrease in H solubility is observed. This contour plot includes a curve for which the alloys have equal H solubility to pure Pd, $\Theta_{alloy}/\Theta_{Pd}=1$. Examining this curve shows that in order for alloys with $LC_{alloy} < LC_{Pd}$ to have increased H solubility relative to Pd, E_2 must be negative, indicating an additive with a strong affinity for H.

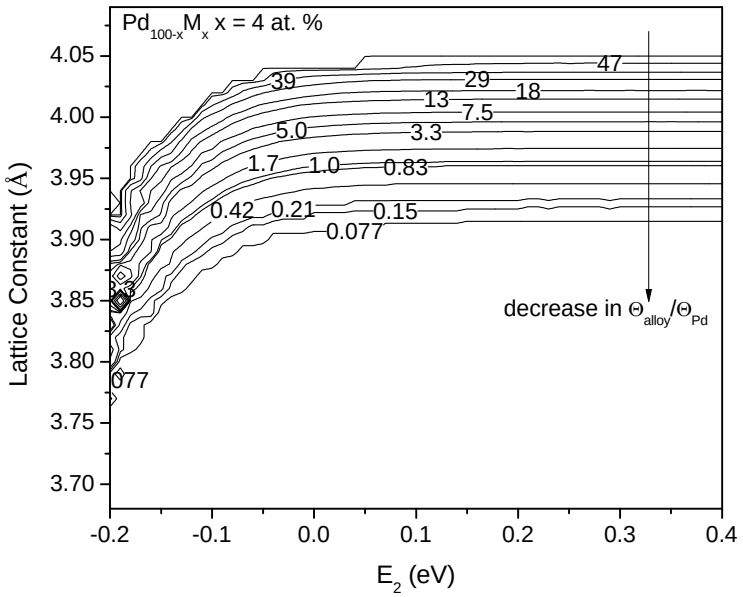

Figure 5.1: Solubility predictions using the heuristic lattice model for Pd-rich binary alloys with composition $Pd_{96}M_4$. The alloy solubility results have been normalized with respect to the hydrogen solubility of pure Pd, so the contours show values of $\Theta_{alloy}/\Theta_{Pd}$ at 600 K.

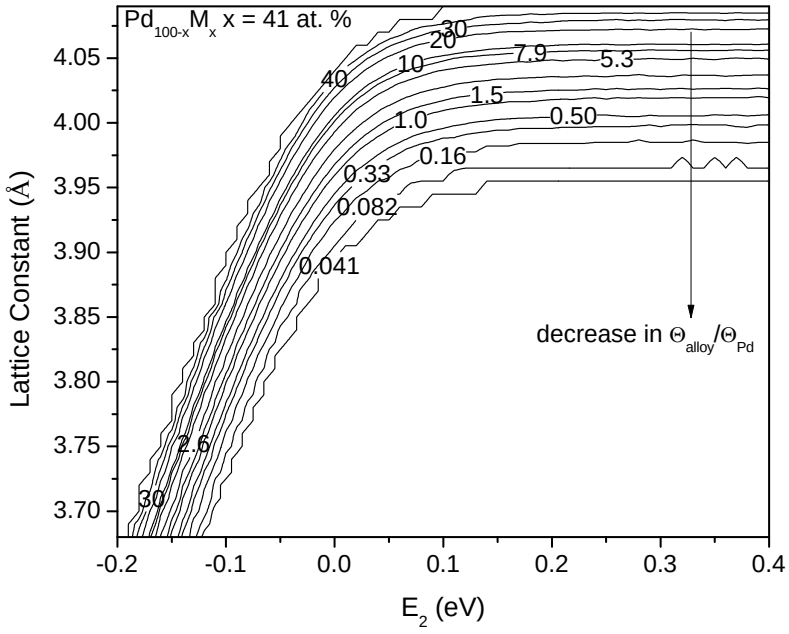

Figure 5.2: Solubility predictions using the heuristic lattice model for Pd-based binary alloys with composition $Pd_{59}M_{41}$. The alloy solubility results have been normalized with respect to the hydrogen solubility of pure Pd, so the contours show values of $\Theta_{alloy}/\Theta_{Pd}$ at 600 K.

Figure 5.2 shows the normalized H solubility results for $Pd_{100-x}M_x$ for x = 41 at.%. The most noticeable difference from Figure 5.1 is the strong curvature in the contours defining curves of equal H solubility in these alloys. This curvature lessens as the amount of the additive metal in the alloy decreases. This is not surprising, since the chemical effect, E_2, in Eq. (5.1) is proportional to the number of M atoms in the system. We also observe that alloys with $LC_{alloy} > LC_{Pd}$, in Figure 5.1 are predicted to have greater H solubility than alloys under similar conditions in Figure 5.2. Here and below, we have only presented contour plots for the lowest and the highest M concentrations we studied. Similar plots for the other alloy composition can be found in Appendix D.

5.2.2: H Diffusion Predictions

KMC was used to calculate the self diffusivity of H, $D_{s,alloy}$, for the same set of alloys described above at T = 600 K. Figure 5.3 plots the H diffusion predictions for $Pd_{100-x}M_x$ for x = 4 at.% normalized with respect to pure Pd, $D_{s,alloy}/D_{s,Pd}$. Unlike the solubility results, the most noticeable feature of the diffusion predictions is that alloys with $LC_{alloy} < LC_{Pd}$, regardless of the E_2 value, are predicted to have a reduction in H diffusion when compared to pure Pd. On the other hand, alloys with an $LC_{alloy} > LC_{Pd}$ are predicted to have faster H diffusion, regardless of the E_2 value. These results are in great part due to the fact that the alloy composition in Figure 5.3 involves a dilute concentration of M atoms.

Figure 5.4 shows the normalized H diffusion results for $Pd_{100-x}M_x$ for x = 41 at.%. The chemical effect has a greater influence over the diffusion predictions in these alloys

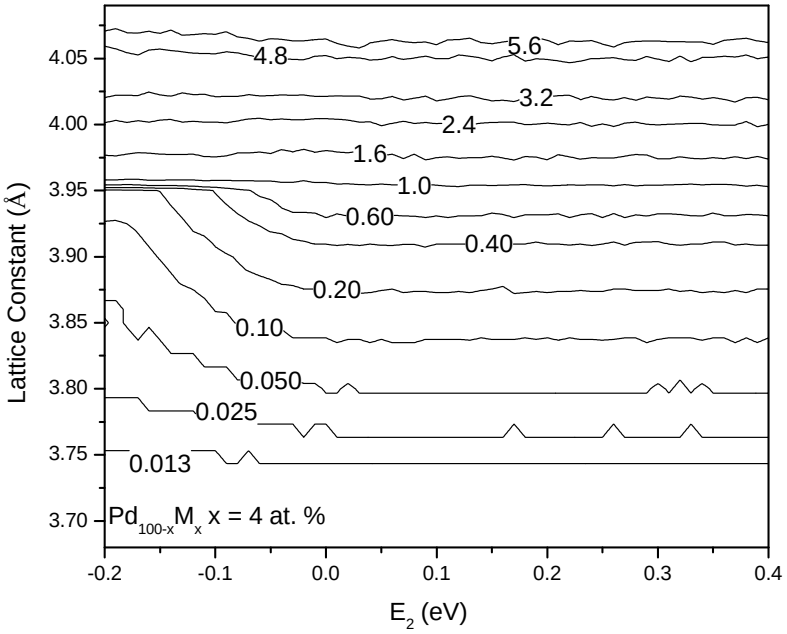

Figure 5.3: Diffusion predictions using the heuristic lattice model for Pd-rich binary alloys with composition $Pd_{96}M_4$. The alloy diffusion results have been normalized with respect to the hydrogen diffusion of pure Pd, so the contours show values of $D_{s,alloy}/D_{s,Pd}$ at 600 K.

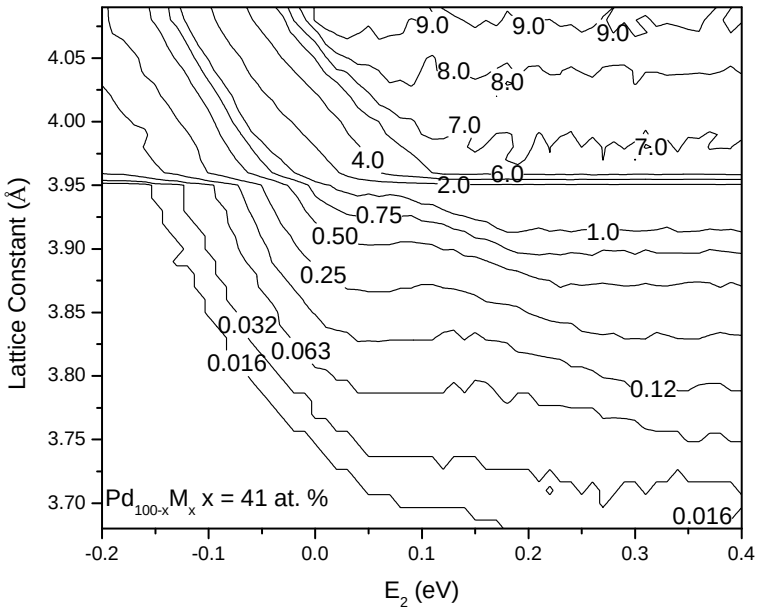

Figure 5.4: Diffusion predictions using the heuristic lattice model for Pd-based binary alloys with composition $Pd_{59}M_{41}$. The alloy diffusion results have been normalized with respect to the hydrogen diffusion of pure Pd, so the contours show values of $D_{s,alloy}/D_{s,Pd}$ at 600 K.

than in Figure 5.3. Similar to $Pd_{96}M_4$, the alloys in Figure 5.4 with $LC_{alloy} < LC_{Pd}$ are predicted to have slower H diffusion than pure Pd for all but the largest positive values of E_2. In comparing our solubility and diffusion predictions we note that the ranges of the solubility values are much larger than for diffusion, regardless of the alloy composition. Our heuristic lattice model suggests that while solubility is equally dependent on both the lattice distortion and chemical effects, diffusion is mainly lattice distortion dependent. Similar diffusion plots for the other alloy compositions we considered can be found in Appendix D.

5.2.3: H Permeability Predictions

Having predicted H solubility and diffusion for each $Pd_{100-x}M_x$ alloy, the permeability of H was calculated at 600 K. Figure 5.5 plots the H permeability results for the $Pd_{100-x}M_x$ for x = 4 at.% normalized with respect to pure Pd, k_{alloy}/k_{Pd}. Although permeability is proportional to both the solubility and diffusivity of H, the solubility of H dominates the overall shape of the contours in Figure 5.5. This is due to the larger range in values observed in our solubility predictions when compared to the diffusion values. Figure 5.6 shows the normalized permeability predictions for $Pd_{100-x}M_x$ for x= 41 at.%. The permeability contours of alloys in Figure 5.6 are also dominated by the solubility of H. Similar permeability plots for the other alloy compositions we considered can be found in Appendix D.

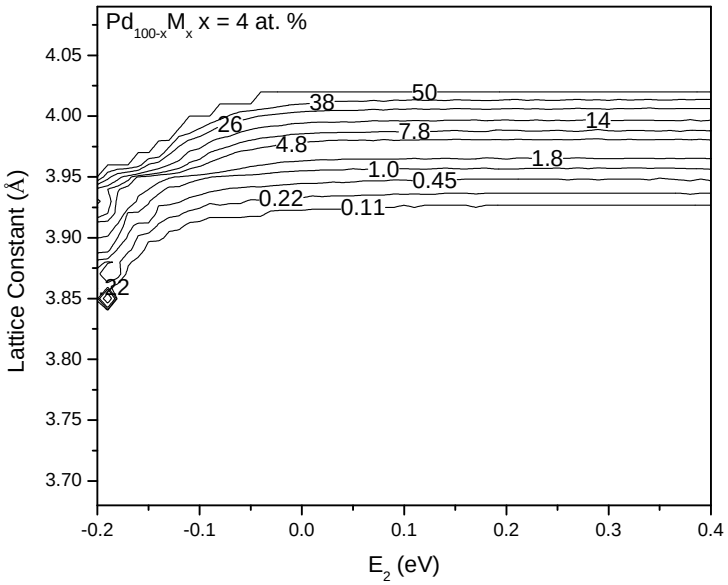

Figure 5.5: Permeability predictions using the heuristic lattice model for Pd-rich binary alloys with composition $Pd_{96}M_4$. The alloy permeability results have been normalized with respect to the hydrogen permeability of pure Pd, so the contours show values of k_{alloy}/k_{Pd} at 600 K.

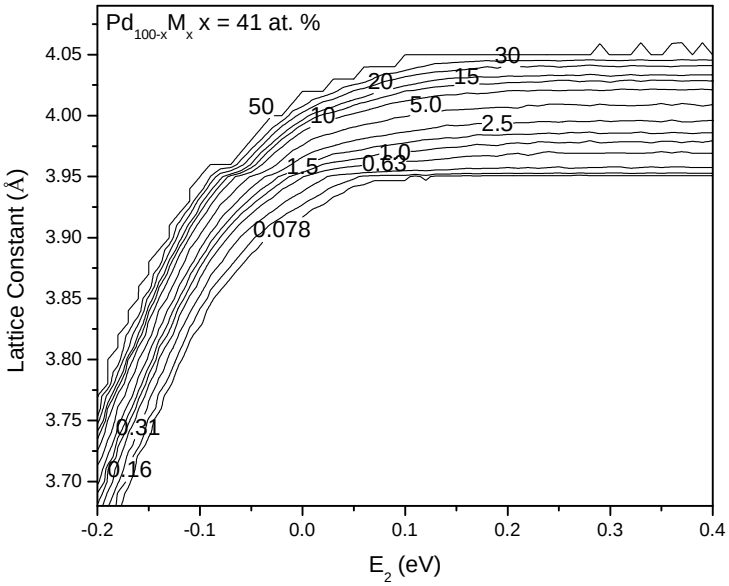

Figure 5.6: Permeability predictions using the heuristic lattice model for Pd-based binary alloys with composition $Pd_{59}M_{41}$. The alloy permeability results have been normalized with respect to the hydrogen permeability of pure Pd, so the contours show values of k_{alloy}/k_{Pd} at 600 K.

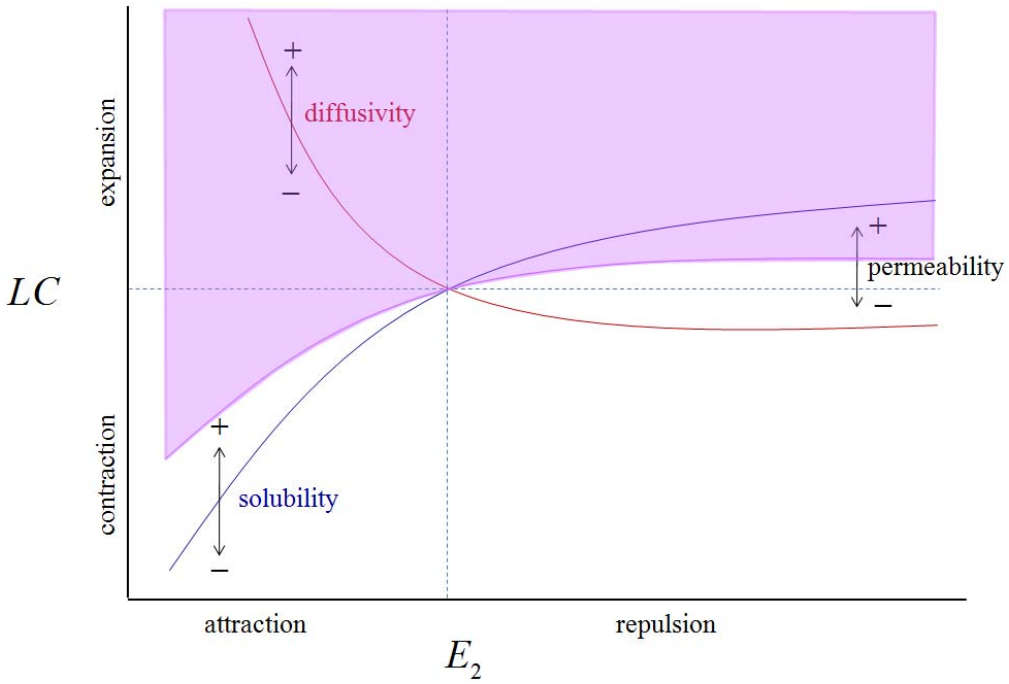

Figure 5.7: A schematic illustration of the normalized macroscopic properties of interstitial H with respect to pure Pd, with curves showing materials the same performance as pure Pd.

In order to determine the ideal conditions for a binary alloy to have improved properties relative to pure Pd we have taken the trends from the calculations above and presented them schematically in Figure 5.7. Each curve in this figure represents one of the macroscopic properties of H and any alloy above the curve has improved performance, relative to pure Pd. The shaded region in this figure represents alloys with greater H permeability than pure Pd. The permeability curve strongly resembles the solubility curve. For low M atom concentrations the difference between the solubility and diffusivity curves is diminished, but the permeability continues to resemble the solubility curve.

5.3: Heuristic Lattice Model Validation

A crucial question to ask about our heuristic lattice model is whether it gives meaningful predictions for real alloys. In this section, we explore this issue using data from our detailed CE / DFT models of $Pd_{96}M_4$ alloys with M = Au, Ag, Pt, Rh, Cu, and Ni. First we examine how to determine the parameters used in the heuristic model for a specific alloy. Once this is done, comparisons between our detailed and heuristic model results are possible.

Our heuristic lattice model requires two parameters. The first parameter is the lattice constant of the alloy of interest. Once the alloy composition is known the lattice constant is rapidly determined using Vegard's Law[7] as an initial estimate, followed by DFT calculations in order to find the appropriate lattice constant. We are aware that Vegard's Law provides a poor lattice constant estimate when working with non-fcc metals; hence we perform the DFT calculations. The second parameter is the chemical effect contribution, E_2. In our heuristic lattice model, the local chemical effect is magnified when the number of M atoms in the $2\times N$ shell increases. This is an indication that the E_2 values for an individual alloy composition must be related to DFT data that includes an M atom or atoms in the $2\times N$ shell. From Eq. (5.1) the chemical effect can be calculated as $E_2 = (E_b^{site} - E_{LC})/N$. From Table 5.1 we note that regardless of the lattice constant the O sites have the most favorable H binding energy between the two types of binding sites. Because the O sites are the most favorable sites, it is reasonable to assume that they too will be the most affected by the presence of the M atoms. Therefore the E_2 value for an individual alloy composition can be estimated based on DFT calculations for O sites binding energies in which an M atom is present in the $2\times N$

shell, $E_2 = E_{2,O} = E_b^O - E_{LC}$. In order to test whether this approach was appropriate we also tested methods using DFT data for T site binding energies with an M atom in the $2 \times N$ shell by using, $E_2 = E_{2,T} = E_b^T - E_{LC}$. We have also explored multiple combinations of $E_{2,O}$ and $E_{2,T}$ values, by using $E_2 = \frac{1}{2} E_{2,O} + \frac{1}{2} E_{2,T}$, $E_2 = \frac{2}{3} E_{2,O} + \frac{1}{3} E_{2,T}$, or $E_2 = \frac{1}{3} E_{2,O} + \frac{2}{3} E_{2,T}$. Using the DFT data collected for $Pd_{96}M_4$ alloys in Chapter 3 we tested all five methods of extracting E_2. For clarity we will only show details of these five methods for the $Pd_{96}Ag_4$ alloy.

In Chapter 3, 21 O sites and 88 T sites were used for describing H in $Pd_{96}Ag_4$ with $LC_{alloy} = 3.968$ Å. 10 of these O sites and 41 T sites have a single M atom in the site's $2 \times N$ shell. We calculated the average binding energy, $\overline{E_b^{O(T)}}$ of each binding site from this collection of sites. The average binding energy $\overline{E_b^{O(T)}}$ was then used in for estimating E_2 with the methods described above. Table 5.4 presents the predicted H solubility and

Table 5.4: Heuristic lattice model prediction for H solubility and diffusion in $Pd_{96}Ag_4$ using $LC_{alloy} = 3.968$ Å and several estimates for E_2 compared to results using the cluster expansion methods described in Chapter 3 at 600 K.

Method	E_2 **(eV)**	K_s **Prediction [** $atm^{-0.5}$ **]**	D_s **prediction [** $m^2 \cdot s^{-1}$ **]**
Cluster Expansion	-	0.082	5.06×10^{-9}
$E_2 = E_{2,O}$	0.04	0.072	5.20×10^{-9}
$E_2 = E_{2,T}$	0.16	0.066	5.65×10^{-9}
$E_2 = \frac{1}{2} E_{2,O} + \frac{1}{2} E_{2,T}$	0.10	0.068	5.64×10^{-9}
$E_2 = \frac{1}{3} E_{2,O} + \frac{2}{3} E_{2,T}$	0.12	0.067	5.48×10^{-9}
$E_2 = \frac{2}{3} E_{2,O} + \frac{1}{3} E_{2,T}$	0.08	0.069	5.69×10^{-9}

diffusivity for the cluster expansion model described in Chapter 3 and the predictions of the heuristic lattice model for each of the five estimates of E_2. In this context, the CE results should be considered the 'correct' results. As might be expected, the estimate of E_2 producing the most similar results to our detailed CE model corresponds to the E_2 estimated solely from O sites. Similar results were found for the other $Pd_{96}M_4$ alloys.

We estimate the E_2 values for $Pd_{96}M_4$ for M = Au, Ag, Pt, Rh, Cu, and Ni alloys using the O site binding energy data from our previous DFT calculations and compared our heuristic lattice model (HLM) H permeability predictions with the CE model predictions at T = 600 K. This comparison is shown in Figure 5.8. In this figure, the symbols represent the H permeability predictions using the cluster expansion models

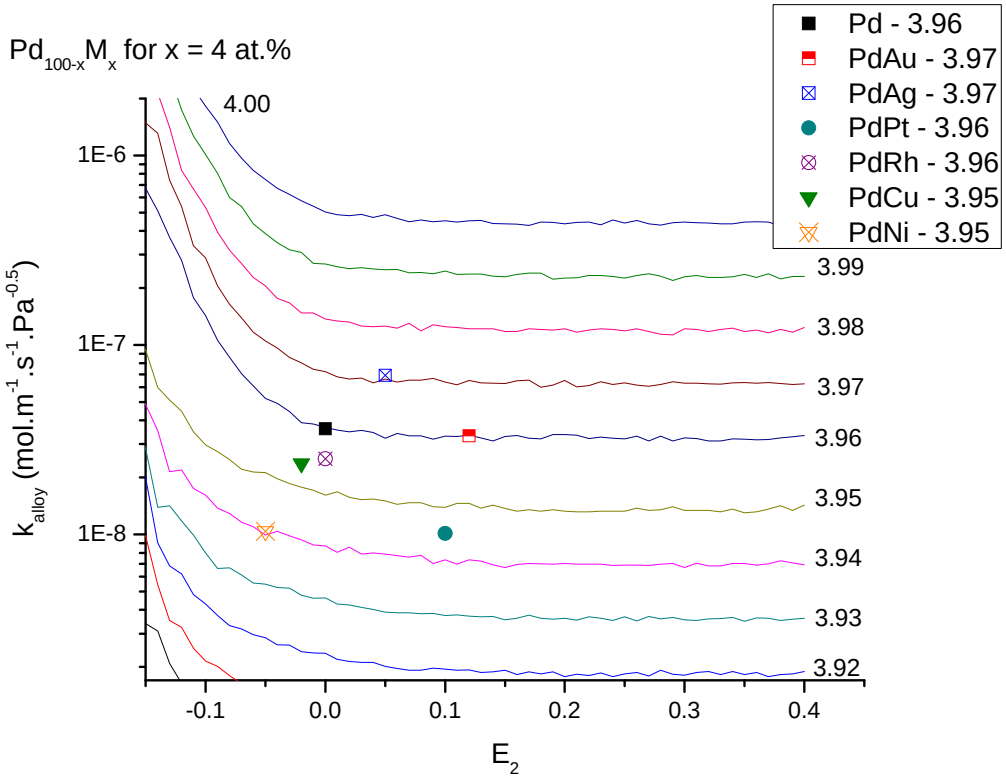

Figure 5.8: Heuristic lattice model permeability predictions at T = 600 K for (a) $Pd_{100-x}M_x$ for x = 4 at.% compared to cluster expansion predictions for $Pd_{96}M_4$ alloys from Chapter 3 at the extracted E_2 values only using O site binding energy data.

Table 5.5: Normalized H permeability predictions for $Pd_{96}M_4$ alloys for M = Au, Ag, Pt, Rh, Cu, and Ni using CE models from Chapter 3 and the heuristic lattice model.

Alloy	E_2 **(eV)**	k_{alloy}^{CE} / k_{Pd}	k_{alloy}^{HLM} / k_{Pd}
$Pd_{96}Au_4$	0.12	0.92	1.91
$Pd_{96}Ag_4$	0.05	1.91	2.00
$Pd_{96}Pt_4$	0.10	0.28	0.99
$Pd_{96}Rh_4$	0.00	0.69	1.16
$Pd_{96}Cu_4$	-0.02	0.66	0.49
$Pd_{96}Ni_4$	-0.05	0.29	0.72

outlined in Chapter 3 and the solid curves represent the heuristic lattice model predictions for an alloy with a specific LC. In Table 5.5 we have tabulated the normalized permeability predictions using the CE models and the heuristic lattice model plotted in Figure 5.8 for further comparison. If our heuristic lattice model agreed exactly with the more detailed CE model predictions, the symbols in Figure 5.8 would lay directly on the curve representing the lattice constant of the alloy at the E_2 value. In every case except M = Cu, the heuristic lattice mode overestimates the alloy permeability relative to the CE models. This indicates that caution should be used in interpreting results from the simplified model quantitatively. At a qualitative level, our detailed CE calculations rank the six additives as Ag > Au > Rh > Cu > Ni > Pt in terms of permeability. The heuristic lattice model gives the same order except for reversing the positions of Cu and Pt. This suggests that this model may be useful for examining trends in large groups of materials.

As a further test of the idea that using the binding energy of O sites with a single M atom in the $2 \times N$ shell was useful for estimating E_2, we applied the heuristic lattice model to the $Pd_{74}Cu_{26}$ alloy described in Chapter 4. For this alloy we had 11 O sites with a single Cu atom in the $2 \times N$ shell with an average O site binding energy of $\overline{E_b^O} = -0.08$

eV. From the CE models described in Chapter 4 we predicted the H permeability at T = 600 K to be $k^{CE}_{Pd_{74}Cu_{26}} = 4.46\times10^{-9}\ mol\cdot m^{-1}\cdot s^{-1}\cdot Pa^{-0.5}$, while the heuristic lattice model (HLM) predicts $k^{HLM}_{Pd_{74}Cu_{26}} = 4.80\times10^{-9}\ mol\cdot m^{-1}\cdot s^{-1}\cdot Pa^{-0.5}$.

We have successfully applied our heuristic lattice model to real alloys. The heuristic lattice model does not provide the exact H permeability predictions, as our CE model would, but this was never the goal of this simplified model. The heuristic lattice model allows us to use small set of DFT calculations to predict whether a binary alloy is an interesting candidate as an H purification membrane that merits detailed study.

5.4: Heuristic Lattice Model Predictions

Having developed a method to extract the chemical effect and the lattice constant of specific alloy from DFT calculations, our goal is to use our heuristic lattice model to examine a large series of potential Pd-based binary alloys. Unlike our detailed calculations for $Pd_{96}M_4$ in Chapter 3, our aim here is to use a number of DFT calculations in order to predict H permeability in alloys using our heuristic lattice model. Because the chemical effect in these calculations is estimated from O site binding energies, we only performed DFT calculations for O sites in each alloy of interest with a single M atom in the $2\times N$ shell. When the supercells for the alloys of interest included multiple distinct O sites with these conditions, the average of the binding energy in these sites, E_b^O was used in estimating E_2.

From the binary phase diagrams[8, 9] we know that Pd forms fcc alloys with most transition metals, including M = Ag, Au, Co, Cr, Cu, Fe, Hf, Ir, Mn, Mo, Nb, Ni, Os, Pt, Re, Rh, Ru, Ta, Tc, Ti, V, W, Y, and Zr. Below, we analyze binary alloys of Pd with all

of these metals at 600 K. We begin with a Pd-rich binary alloy composition, and any alloy predicted to have improved H permeability was further analyzed with increased M atom content. This was done for $Pd_{100-x}M_x$ up to x = 41 at.% for all transition metals forming substitutionally random fcc alloys. When an alloy reaches a boundary in the binary phase diagram, if there was an fcc crystal structure at an elevated temperature we proceed in our analysis, otherwise we removed the alloy from our analysis.

In Chapter 3 we analyzed six $Pd_{96}M_4$ alloys with great detail. Our DFT calculations describing bulk H were done using 27 atom supercells. We now use a similar 27 atom supercell in which a single atom out of the 27 atom supercell is M, and optimized the lattice constant of each individual alloy. We find an initial lattice constant estimate using Vegard's Law regardless of the individual metal crystal structure. This initial lattice constant is used to find the DFT optimized lattice constant while allowing all the metal atoms to relax as the cell volume changes. Because there is a single M atom in the supercell there were six identical O sites with one M atom in the $2\times N$ shell. We therefore needed only to perform a single DFT calculation for this O site to obtain the binding energy. For $Pd_{96}M_4$ for M = Au, Ag, Pt, Rh, Cu and Ni although we have 10 available O sites to estimate the chemical effect, as described earlier, we will only use the O site binding energy pertaining to the supercell in which a single M atoms was used excluding from using all other O site information. This is done in order to maintain a consistent set of data between all the alloys used in this comparison. Once we have the O site binding energy we can extract the E_2 as $E_{2,O} = E_b^O - E_{LC}$. Table 5.6 lists the additive metal atoms used to form $Pd_{96}M_4$ alloys, the parameters used in the heuristic lattice model and the H permeability predictions for each alloy. The additives are listed in this

Table 5.6: Heuristic lattice model parameters used in the H permeability predictions for a series of $Pd_{100-x}M_x$ for x = 4 at.% alloys at T = 600 K.

$Pd_{96}M_4$	Δ_{LC} (%)	E_2 (eV)	k_{alloy}^{HLM} / k_{Pd}
Co	-0.38	-0.06	0.65
Ni	-0.33	-0.06	0.72
Fe	-0.30	-0.02	0.54
Mn	-0.30	0.06	0.44
Cr	-0.25	0.10	0.42
Cu	-0.18	0.00	0.49
V	-0.18	0.11	0.44
Ir	-0.10	0.08	1.01
Rh	-0.10	-0.01	1.16
Tc	-0.10	0.17	0.98
Ti	-0.10	0.09	0.96
Os	-0.08	0.16	1.01
Re	-0.08	0.26	1.00
W	-0.08	0.24	0.97
Mo	-0.03	0.20	1.02
Pd	0.00	-	1.00
Pt	0.03	0.11	0.99
Ta	0.03	0.19	1.02
Nb	0.05	0.16	1.00
Ru	0.08	0.05	0.97
Ag	0.15	0.05	2.00
Au	0.20	0.13	1.91
Hf	0.20	0.13	1.91
Zr	0.25	0.11	1.86
Y	0.56	0.15	3.56

table in order of increasing alloy lattice parameter. The additive metal atoms M = Ag, Au, Hf, Ir, Mo, Nb, Os, Re, Rh, Ta, Y, and Zr are predicted to have H permeability greater than or equal to the H permeability in pure Pd. Because our heuristic lattice model is a simplified model, we widen our acceptance criteria to consider any alloy with

$k_{alloy}^{HLM} / k_{Pd} \geq 0.95$. Our heuristic lattice model predicts that no further calculations are necessary Pd-based alloys with additive metal atoms M = Co, Cr, Cu, Fe, Mn, Ni, and V for H purification purposes because of low H permeability in these alloys. Figure 5.9 shows the permeability prediction for all $Pd_{96}M_4$ alloys as a function of the alloy lattice constant. It is interesting to note that not all the alloys that were predicted to be potentially good for further study are predicted to expand the lattice constant of the alloy when compared to pure Pd.

Based on our permeability predictions for $Pd_{100-x}M_x$ for x = 4 at.% we only performed calculations for those M atoms that were predicted to have $k_{alloy}^{HLM} / k_{Pd} \geq 0.95$

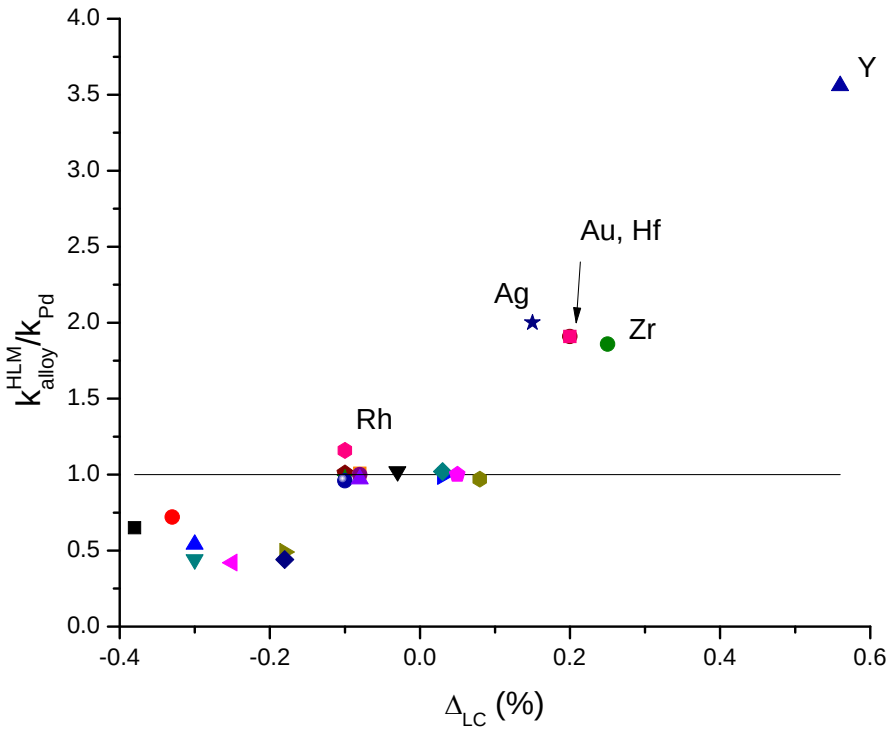

Figure 5.9: Normalized permeability predictions for $Pd_{96}M_4$ from the heuristic lattice model as a function of the lattice constant of the alloys.

normalized H permeabilities at a higher M content alloy. On this basis, we continued our heuristic lattice model permeability predictions for $Pd_{100-x}M_x$ for x = 11 at.% for M = Ag, Au, Hf, Ir, Mo, Nb, Os, Pt, Re, Rh, Ru, Ta, Tc, Ti, W, Y, and Zr. Due to the increased M atom content the 27 atom supercells used to describe these alloy are now composed of 3 randomly placed M atoms and 24 Pd atoms. For each alloy composition of interest the lattice constant was optimized with DFT. Within each supercell we identify the O sites that have a single M atom in the $2\times N$ shell and use DFT to gather the binding energy of H in these interstitial sites. This gives a total of 16 O sites. We averaged the O site

Table 5.7: Heuristic lattice model parameters used in the H permeability predictions for a series of $Pd_{100-x}M_x$ for x = 11 at.% alloys at T = 600 K.

$Pd_{89}M_{11}$	Δ_{LC} (%)	E_2 (eV)	k_{alloy}^{HLM} / k_{Pd}
Re	-0.66	0.29	0.07
Cu	-0.60	-0.04	0.40
Mo	-0.58	0.25	0.14
W	-0.57	0.34	0.14
Tc	-0.56	0.19	0.14
Ru	-0.52	0.08	0.15
Nb	-0.13	0.26	0.27
Ti	-0.12	0.17	0.26
Pd	0.00	-	1.00
Ta	0.15	0.30	2.05
Ag	0.33	0.03	2.14
Au	0.47	0.11	4.05
Ir	0.60	0.08	4.08
Rh	0.62	0.00	4.89
Pt	0.64	0.10	7.49
Hf	0.67	0.25	6.92
Zr	0.68	0.26	6.88
Y	0.82	0.14	7.03

binding energy, $\overline{E_b^O}$, for each alloy and use this average to obtain our E_2. Table 5.7 summarized our result for these alloys. For this and all subsequent analysis we included results for M = Cu. Although Cu is predicted by our calculations to have reduced H permeability, this additive metal atom widely used in experiments and therefore serves as a reference material. From Table 5.7 M = Ag, Au, Hf, Ir, Pt, Rh, Ta, Y, and Zr are predicted to increase H permeability relative to H permeability in pure Pd. Increasing the amount of Mo, Nb, Re, Ru, Tc, Ti, and W as additive metal atoms had a negative outcome for H purification purposes by decreasing H permeability relative to both alloys with composition of $Pd_{96}M_4$ and pure Pd. Unlike the previous alloy composition analysis, all the alloys that are now predicted to have improved H permeability relative to pure Pd have expanded lattices compared to pure Pd.

We continued our analysis for H purification membranes with $Pd_{100-x}M_x$ for x = 19 at.% alloys using M = Ag, Au, Cu, Hf, Ir, Pt, Rh, and Ta. For M = Y and Zr the binary alloys with x = 19 at.% with these additive metal atoms no longer form substitutionally random fcc alloys[8]. We therefore do not consider alloys with these two metal additives at this or compositions with larger amounts of M. The 27 atom supercells used to describe these materials are composed of 5 randomly distributed M atoms and 22 Pd atoms. For each alloy the lattice constant was optimized with DFT. Within each supercell we identify the O sites that have a single M atom in the $2\times N$ shell and we use DFT to calculated the binding energy of H in these sites. $\overline{E_b^O}$ is obtained from the 14 available O sites, which is used for calculating E_2 as $E_{2,O} = \overline{E_b^O} - E_{LC}$. Table 5.8 summarizes our results for the $Pd_{81}M_{19}$ alloys. From this table we can see that with the exception of M =

Table 5.8: Heuristic lattice model parameters used in the H permeability predictions for a series of $Pd_{100-x}M_x$ for x = 19 at.% alloys at T = 600 K.

$Pd_{81}M_{19}$	Δ_{LC} (%)	E_2 (eV)	k_{alloy}^{HLM} / k_{Pd}
Cu	-1.31	-0.07	0.17
Rh	-0.35	0.02	0.38
Pd	0.00	-	1.00
Ir	0.25	0.12	2.23
Ag	0.52	0.04	4.04
Au	0.60	0.12	3.98
Pt	0.63	0.11	7.24
Ta	0.63	0.40	3.50
Hf	0.71	0.37	5.81

Cu and Rh the remaining M atoms examined at this alloy composition are predicted to have increased H permeability performance compared to pure Pd. The added Rh resulted in a lattice contraction. Compared to the results is Table 5.7, the only additive metal atoms to continue improving H permeability are M = Ag, Au, and Ta. Using M = Hf, Ir, and Pt is predicted to have greater H permeability than pure Pd, but when compared to the results in Table 5.7 there has been a decrease in permeability performance with the increased M content in the bulk of these alloys. This is, our heuristic lattice model is suggesting that in order to maximize H permeability for $Pd_{100-x}M_x$ using M = Hf, Ir and Pt the alloy should contain less than 19 at.% of these metal additives.

As we increase the additive metal atom content, we note that $Pd_{100-x}M_x$ for x = 26, 33, and 41 at.% with M = Hf and Ta no longer give substitutionally random fcc alloys[8]. These two additives are, therefore, not considered at these compositions. At these alloy compositions, the 27 atom supercells are now composed of 7, 9, and 11 randomly distributed M atoms and 20, 18, and 16 Pd atoms, respectively. The lattice constant of

Table 5.9: Heuristic lattice model parameters used in the H permeability predictions for a series of $Pd_{100-x}M_x$ for x = 26 at.% alloys at T = 600 K.

$Pd_{74}M_{26}$	Δ_{LC} (%)	E_2 (eV)	k_{alloy}^{HLM} / k_{Pd}
Cu	-1.62	-0.07	0.14
Ir	-0.76	0.20	0.03
Pd	0.00	-	1.00
Pt	0.63	0.15	2.79
Ag	0.68	0.09	6.26
Au	0.77	0.21	4.66

Table 5.10: Heuristic lattice model parameters used in the H permeability predictions for a series of $Pd_{100-x}M_x$ for x = 33 at.% alloys at T = 600 K.

$Pd_{66}M_{33}$	Δ_{LC} (%)	E_2 (eV)	k_{alloy}^{HLM} / k_{Pd}
Cu	-2.07	-0.07	0.07
Pd	0.00	-	1.00
Pt	0.05	0.16	0.63
Au	1.30	0.20	8.48
Ag	1.45	0.10	20.53

Table 5.11: Heuristic lattice model parameters used in the H permeability predictions for a series of $Pd_{100-x}M_x$ for x = 41 at.% alloys at T = 600 K.

$Pd_{59}M_{41}$	Δ_{LC} (%)	E_2 (eV)	k_{alloy}^{HLM} / k_{Pd}
Cu	-2.84	-0.05	0.01
Pd	0.00	-	1.00
Ag	1.47	0.13	9.60
Au	1.71	0.26	12.00

each individual alloy was optimized using DFT. These supercells give 11 O sites for the $Pd_{74}M_{26}$, 9 O sites for the $Pd_{66}M_{33}$, and 4 O sites for the $Pd_{59}M_{41}$. We averaged the O site binding energy, $\overline{E_b^O}$, for each alloy at each composition and use this average to obtain

E_2. Table 5.9, Table 5.10, and Table 5.11 summarize our results for $Pd_{74}M_{26}$, $Pd_{66}M_{33}$, $Pd_{59}M_{41}$ alloys, respectively. From Table 5.9, $Pd_{74}Pt_{26}$ is predicted to have an improved H permeability compared to pure Pd, but a reduction compared to the permeability of $Pd_{81}Pt_{19}$. Further increase in Pt content, as for $Pd_{66}Pt_{33}$ in Table 5.10, causes a drastic reduction in H permeability when compared to pure Pd. From Table 5.9, $Pd_{74}Ir_{26}$ is predicted to have a reduced H permeability relative to pure Pd. For alloys with M composition of x = 33 at.% or greater M = Ag and Au are the only metal additives to have larger H permeability than pure Pd. Our heuristic lattice model predicts H permeability in $Pd_{66}Ag_{33}$ to be over 20 times greater than H permeability in pure Pd at 600 K. We reiterate this heuristic lattice model should be interpreted qualitatively.

We summarize the heuristic lattice model results for all the alloy compositions described above in Figure 5.10. From this figure we observe that $Pd_{100-x}Ag_x$ alloys are

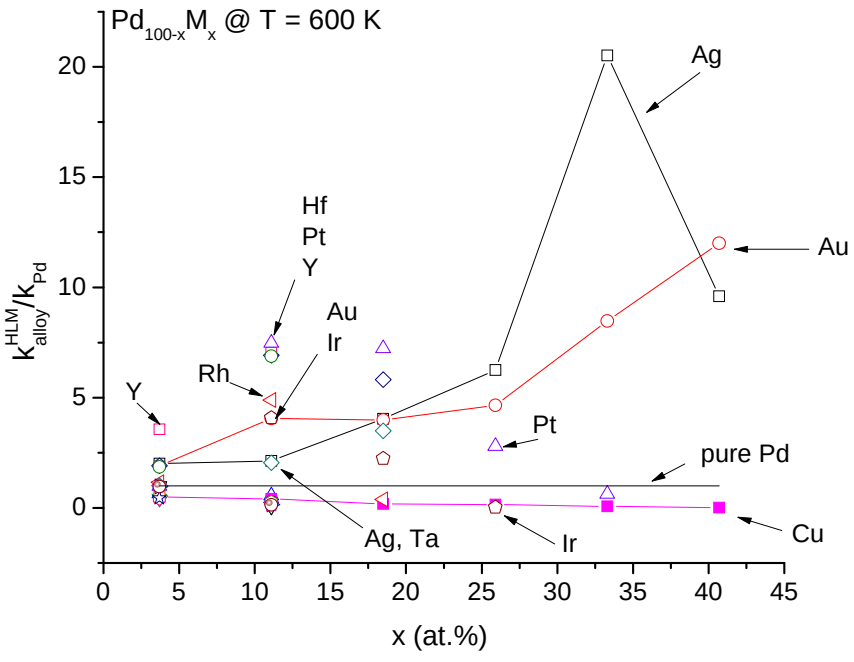

Figure 5.10: Summary of H permeability predictions for 24 transition metals using our heuristic lattice model for $Pd_{100-x}M_x$ alloys for x = 4, 11, 19, 26, 33, and 41 at.%.

predicted to have a maximum for compositions containing approximately 33 at.%. In contrast, our heuristic lattice model predicts that for $Pd_{100-x}Au_x$ alloys, adding Au content will continue to improve H permeability. $Pd_{100-x}Pt_x$ alloys are predicted to have a maximum around 11 – 19 at.%. $Pd_{100-x}Rh_x$ and $Pd_{100-x}Ir_x$ are predicted to have a maximum in permeability for x = 11 at.%. Our heuristic lattice model predicts that at least at some compositions, Pd-based binary alloys with M = Ag, Au, Hf, Ir, Pt, Rh, Ta, Y, and Zr out of the 24 transition metal consider merit detailed analysis as potential H purification membranes.

Figure 5.11 is a collection of experimentally reported H permeabilities for a number of Pd-based binary alloys. Comparing the heuristic lattice model permeability predictions from Figure 5.10 with these experimental values shows that the model

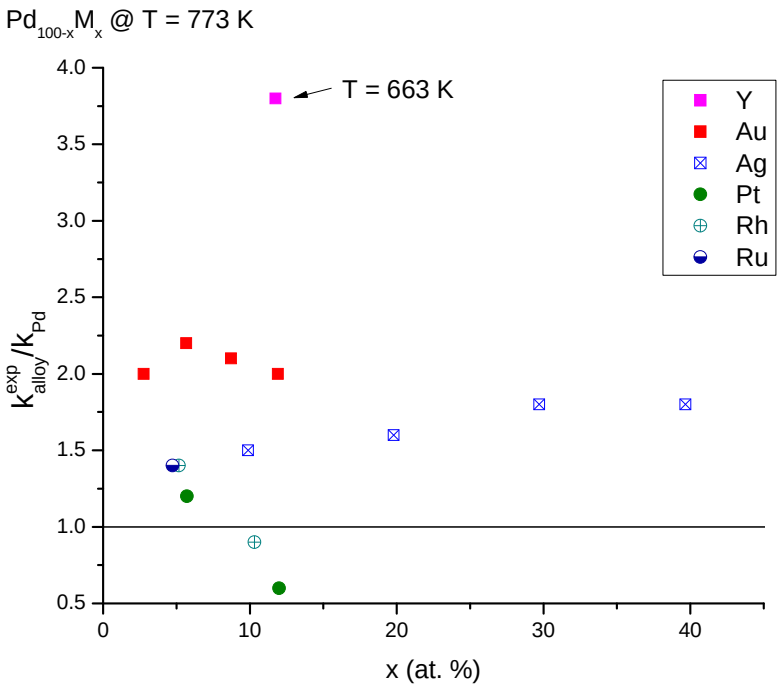

Figure 5.11: Summary of H permeability predictions reported by Gryaznov[10] and Ma *et al.*[11] for a series of Pd-based binary alloys.

typically overestimates the alloy permeability, a result consistent with our earlier comparison of our simplified model with the more detailed predictions from Chapter 3. Crucially, however, our heuristic lattice model appears to capture the key physical trends evident in the experimental data. Gryaznov[10] reported that at 773 K binary alloys with less than 15 at.% Au have greater H permeability than binary alloys with Ag at equal compositions. Our heuristic lattice model has similar predictions. Experimentally it is known that palladium alloys with Y, Ag, and Au at some compositions have greater H permeability than pure Pd[10, 11]. Conversely, the addition of Cu to Pd results in a reduction in H permeability for alloys that are fcc crystals[12, 13]. Our heuristic lattice model captures all of these qualitative observations.

The heuristic lattice model over predicts the range of compositions for which adding Pt to Pd can enhance permeability in the binary alloy. The experimental data shown above shows a slight enhancement in permeability for an alloy with ~5 at.% Pt, but a strong decrease in permeability for alloys with ~10 at.% Pt. It is important to note, however, that our more detailed CE-based models appear to characterize these Pt-based alloys more accurately. At 773 K, the same temperature as the experimental data above, our CE model of $Pd_{96}Pt_4$ predicts $k^{CE}_{Pd_{96}Pt_4} = 1.14\times10^{-8}\ mol\cdot m^{-1}\cdot s^{-1}\cdot Pa^{-0.5}$, which is only 30% of H permeability in pure Pd. That is, our CE-based model correctly identifies this PdPt alloy as a material that does not substantially increase the permeability of H relative to pure Pd, as seen in experiment[1, 14, 15]. This example illustrates the important point that our heuristic model is intended only to identify which alloys show sufficient promise to be examined by a more detailed calculation (or via experiment), and that the methods we have introduced in the earlier chapters provide the tools to make this possible.

Hf, Ir, Ta, and Zr have been identified by our heuristic lattice model as potential additive metals for the formation of Pd-based alloy membranes with permeability exceeding pure Pd. Experimental work for these alloys to date is limited. To our knowledge, no experimental work has been performed using PdHf, PdIr, or PdZr as hydrogen separation membranes. Research has been done with PdIr alloys as catalyst for conversion of methane[16]. In this work Persson *et al.*. found that PdIr have poor but stable catalytic activity for CH_4 relative to pure Pd catalyst[16]. Similarly PdZr alloys have been studied as catalyst for hydrogenation of pentynes[17, 18]. Ta has been suggested as a promising material for hydrogen separation applications[19]. Unfortunately the experimental work done on a series of bulk Ta and PdTa membranes have been found to suffer surface fouling[19]. Although PdTa alloys have been experimentally studied and prove to be easily poisoned, yet if they are capable of improving H permeability, these metal additive could be sparingly used in ternary alloys to improve H permeability. In our view, it would be worthwhile exploring the properties of Pd alloys with Hf, Ir, Ta, and Zr in more detail using the methods that were applied in earlier chapters.

5.5: Conclusion

We have successfully developed a tool that enables us to pre-screen potential Pd-based binary alloys which merit detailed analysis. This tool, our heuristic lattice model, is a simple model only requiring two parameters. In order predict H permeability in substitutionally random fcc bulk alloys, our heuristic lattice model requires the lattice constant of the alloy, along with the local chemical effect on H binding in O sites due to

the presence of the M atom. Once these two factors are available, the H permeability is easily predicted.

We validated our heuristic lattice model predictions with detailed analysis done in Chapter 3 on $Pd_{96}M_4$ alloys as well as with the $Pd_{74}Cu_{26}$ alloy analyzed in Chapter 4. Once convinced of the capability of screening which additive metal atoms have potential to improve H permeability compared to H permeability in pure Pd, we analyzed $Pd_{100-x}M_x$ alloys for six distinct alloy compositions for 24 transition metals. From these 24 transition metals our heuristic lattice model predicts that further study should be performed only for nine of the transition metals at distinct alloy compositions for each candidate as H purification membranes. We compared our heuristic lattice model H permeability predictions with some experimentally reported values. Although our model was never intended to make qualitative predictions for H permeability, we note great similarities with H permeability trends observed experimentally.

Our heuristic lattice model predicts that at least at some compositions, Pd-based binary alloys with M = Ag, Au, Hf, Ir, Pt, Rh, Ta, Y, and Zr are promising materials for future study. Y, Ag, and Au have been experimentally proven to improve H permeability[10, 11]. In Chapter 3, we extensively studied the macroscopic properties of H in $Pd_{96}Pt_4$ and $Pd_{96}Rh_4$ and found these additives to reduce H permeability relative to pure Pd. Little is known on the effects of Hf, Ir, Ta, and Zr to H macroscopic properties in bulk alloys, making these additive metal atoms interesting candidates for additional DFT calculations.

5.6: References

[1] G. Alefeld and J. Völkl, *Hydrogen in Metals I* (Springer-Verlag, Berlin, 1978).

[2] E. Wicke and H. Brodowsky, *Hydrogen in Metals II* (Springer-Verlag, Berlin, 1978).

[3] B. D. Morreale, M. V. Ciocco, B. H. Howard, K. S. Rothenberger, A. V. Cugini, and R. M. Enick, J. Membr. Sci. **241**, 219 (2004).

[4] P. Kamakoti and D. S. Sholl, J. Membr. Sci. **225**, 145 (2003).

[5] P. Kamakoti and D. S. Sholl, Phys. Rev. B **71**, 014301 (2005).

[6] L. Semidey-Flecha and D. S. Sholl, J. Chem. Phys. **128**, 144701 (2008).

[7] A. R. Denton and N. W. Ashcroft, Phys. Rev. A **43**, 3161 (1991).

[8] *Binary Alloy Phase Diagrams, 2nd Edition*, 1990).

[9] H. Okamoto, *Desk handbook : phase diagrams for binary alloys* (ASM International, Materials Park, OH, 2000).

[10] V. Gryaznov, Sep. Purif. Methods **29**, 171 (2000).

[11] Y. H. Ma, I. P. Mardilovich, and E. E. Engwall, Annals NY Acad. Sci. **984**, 346 (2003).

[12] P. L. Andrew and A. A. Haasz, J. Appl. Phys. **70**, 3600 (1991).

[13] P. Kamakoti, B. D. Morreale, M. V. Ciocco, B. H. Howard, R. P. Killmeyer, A. V. Cugini, and D. S. Sholl, Science **307**, 569 (2005).

[14] B. Coluzzi, C. Costa, A. Biscarini, and F. M. Mazzolai, J. Phys. Cond. Matter **4**, 5155 (1992).

[15] P. Zoltowski and E. Makowska, Phys. Chem. Chem. Phys. **3**, 2935 (2001).

[16] K. Persson, A. Ersson, K. Jansson, N. Iverlund, and S. Järås, J. Catalysis **231**, 139 (2005).

[17] M. Varga, Á. Molnár, M. Mohai, I. Bertóti, M. Janik-Czachor, and A. Szummer, Appl. Cat. A. **234**, 167 (2002).

[18] F. Berger, M. Varga, G. Mulas, Á. Molnár, and I. Dékány, Langmuir **19**, 3692 (2003).

[19] K. S. Rothenberger, B. H. Howard, R. P. Killmeyer, A. V. Cugini, R. M. Enick, F. Baustmante, M. V. Ciocco, B. D. Morreale, and R. E. Bauxbaum, J. Membr. Sci. **218**, 19 (2003).

CHAPTER 6

H ISOTOPE SEPARATION USING CRYSTALLINE AND AMORPHOUS METAL MEMBRANES

The great majority of work on metal membranes has focused on the purification of hydrogen from mixed gas streams. There are applications, however, where the separation of isotopes of hydrogen is important, such as the design and operation of fusion reactors[1, 2]. In this chapter, we consider how metal membranes can be chosen to achieve effective separations of hydrogen isotopes at elevated temperatures.

Traditionally hydrogen isotope separation is based on principles of adsorption[3, 4] or cryogenic distillation[1, 3]. Methods involving infrared lasers for molecular separations[5] and magnetic field effects[6] have also been explored. Pure Pd membranes are known to separate H from its isotopes and are an attractive application for cost reduction of processes by developing a continuous operational mode[2]. The phase transition that exists between the α and β-PdH phases at moderate temperatures complicates the use of pure Pd for membrane-based isotopic separations. Pd-based alloys can potentially offer improvements relative to pure Pd membranes[7]. By forming alloys with Pd, the temperature of hydride formation can be reduced, allowing for a wider range of operational temperatures for separation purposes[8].

Pd and Pd-based membranes have been studied for the separation of hydrogen and its isotopes[1, 3, 9, 10] particularly at temperatures below 200 °C, yet interesting opportunities exist for using metal membranes for high temperature isotope separations[11]. Because of the challenges of examining the performance of metal membranes for isotope

separation experimentally, quantitative modeling techniques can play a useful role in considering what materials are well suited for these separations. As we have shown in earlier chapters in this thesis, first-principles calculations based on Density Functional Theory (DFT) have been used to predict H permeation rates through a variety of metal membranes[12-21]. DFT calculations are well suited for describing isotopic effects in the binding energy and site to site hopping energies for interstitial H in metals[22-24].

In this chapter we use DFT-based calculations to predict isotope properties within the bulk of several disordered binary Pd-based alloys with the aim of understanding whether particular binary alloys have useful properties for isotopic separations using membranes. Although most experimental studies of metal membranes have focused on crystalline materials, interest in using amorphous metals as membranes for hydrogen separations is growing rapidly[17, 25]. No experimental information on isotopic separations using amorphous metal membranes is currently available. Hao and Sholl have recently introduced quantitative modeling methods suitable for treating the solubility and mobility of interstitial H in amorphous metals[13, 26]. To explore whether the characteristics of isotopic separations in amorphous metal membranes may hold some advantages over crystalline materials, we use DFT-based calculations to explore this topic in crystalline and amorphous Fe_3B membranes.

6.1: DFT Calculations for Interstitial Atoms

We performed plane wave Density Functional Theory (DFT) calculations with the PW91 GGA exchange-correlation functional using the Vienna *Ab-initio* Simulation Package (VASP)[27] to characterize interstitial H in substitutionally disordered fcc $Pd_{96}M_4$

alloys (M = Ag, Cu, and Rh), amorphous Fe_3B (*a*-Fe_3B) and crystalline Fe_3B (*c*-Fe_3B) with Pearson symbol oP16[13, 18]. Further details our calculations for crystalline materials can be found in Chapter 2. The methods used for amorphous Fe_3B have been described in detail by Hao and Sholl[13, 26].

In fcc crystals H can be located in two distinct interstitial sites, the octahedral (O) or and tetrahedral (T) sites, as mentioned in Chapter 3. In the *c*-Fe_3B material we examined, H can reside in three types of interstitial sites that include O sites composed of 6 Fe atoms, T sites composed of 4 Fe atoms, and T sites composed of 1 B and 3 Fe atoms. The majority of the interstitial sites in the *a*-Fe_3B structure can be described as distorted versions of the interstitial sites found in the *c*-Fe_3B structure. The binding energy of interstitial H found in the various possible interstitial sites, based on DFT calculations can be characterized using[14, 28, 29]

$$E_b = E_{host/H} - E_{host} - \tfrac{1}{2} E_{H_2} + E^{ZP}_{host/H} - \tfrac{1}{2} E^{ZP}_{H_2} \tag{6.1}$$

where E_{host} ($E_{host/H}$) is the total energy the system without (with) atomic H in an interstitial site of the host metal membrane, E_{H_2} is the total energy of an isolated H_2 molecule, and $E^{ZP}_{host/H}$ ($E^{ZP}_{H_2}$) is the zero point energy (ZPE) contribution of the interstitial (molecular) H. For further details refer to Chapter 2. Including ZPE contributions is crucial to capturing isotopic effects. For interstitial H, ZPEs were computed within the harmonic approximation by assuming that the vibrational modes of interstitial H are decoupled from lattice phonons[30]. Within the harmonic approximation, the ZPE for H isotopes are related to the result obtained for H by

$$E^{ZP}_{host/D} = E^{ZP}_{host/H} \Big/ \sqrt{2}, \qquad E^{ZP}_{host/T} = E^{ZP}_{host/H} \Big/ \sqrt{3} \tag{6.2}$$

Table 6.1: Zero point energy values for isotopes in an octahedral site of pure Pd (molecular gas phase) compared to experimental values[8].

Isotope	DFT calculated results [eV]	Experimental results [eV]
H (H_2)	$0.100\left(0.270\right)$	$0.102\left(0.269\right)$
D (D_2)	$0.071\left(0.191\right)$	$0.072\left(0.192\right)$
T (T_2)	$0.058\left(0.156\right)$	-

Our results for the isotopic ZPE in an O site of pure Pd and the ZPE for the molecular gas phase species are compared with experimental results in Table 6.1. There is good agreement between the experimental results and our calculated values. By comparing the ZPE between the atomic and the molecular state of each isotope to H, it can be observed that heavier isotopes have a deeper zero point level in the gas state than in the interstitial state[31-33]. This effect means that the isotopic solubility in Pd is ordered as T < D < H. This can also be seen from our calculated binding energies in the Pd O site; for H, D, T our calculations give $E_{b,H} = -0.176$ eV, $E_{b,D} = -0.166$ eV, and $E_{b,T} = -0.161$ eV respectively. This ordering is known as a reverse isotope effect[8, 33].

6.2: Solubility Calculations

For the crystalline materials we studied, the concentration of interstitial H is low at elevated temperatures, so the solubility of H can be calculated using Sieverts' Law[34]: $\Theta_H = K_s\sqrt{P_{H_2}}$. Here, Θ_H is the ratio of atomic H to metal atoms in the solid and K_s is Sieverts' constant. K_s can be defined using the partition function of the gas phase molecule, the vibrational modes of the interstitial and molecular forms of the H and E_b of the interstitial atom[23, 35]. This method was applied to calculate the solubility of H for Pd-

rich binary alloys, in Chapter 3 and for PdCu-based ternary alloys in Chapter 4. This approach can be applied independently to each H isotope. These calculations include all vibrational energy levels (within the harmonic approximation) of the molecular and interstitial H, not just the ground state that is characterized by the ZPE described above. We calculated the Sieverts' constants for H, D, and T in *c*-Fe_3B by using this approach for each of the four interstitial sites that exists in this ordered crystalline material.

For $Pd_{96}M_4$ alloys, the substitutionally disordered nature of these materials creates an enormous range of distinct interstitial sites with differing local arrangements of Pd and M atoms. We have used cluster expansion methods to derive accurate lattice models for these alloys from a large collection of DFT calculations[18]; details of these model were described in Chapter 3. For $Pd_{96}Ag_4$, $Pd_{96}Cu_4$, and $Pd_{96}Rh_4$ we reported independent models to define the binding energy and ZPE of interstitial H in Appendix B. In the results reported below, we used these models to describe interstitial D and T in these materials.

For the *a*-Fe_3B, solubility was calculated after determining the binding energy and ZPE of interstitial H in each interstitial site in a supercell of this material containing 100 Fe and B atoms. Because of the relatively high solubility of H in this material, Sieverts' law cannot be used, and Grand Canonical Monte Carlo (GCMC) calculations are required to predict the net solubility[13]. These GCMC calculations use binding energies in each site calculated with DFT. H-H interactions must be considered in this material. Hao and Sholl previously performed a series of calculations that considered interstitial H-H interactions and showed that this behavior can be described with a simple exponential function[13, 26].

Including H-H interactions in this way gives results that are qualitatively similar to but more accurate than a simpler treatment based on the Westlake criterion[13, 36].

6.3: Diffusion Calculations

Diffusion of interstitial H, D or T in dense metal membranes at elevated temperatures occurs by a series of hops between adjacent interstitial sites via a transition state (TS)[37, 38]. In the $Pd_{96}M_4$ systems, transition states were located within DFT calculations as described in Chapter 3[18, 39, 40]. For the Fe_3B systems, performing NEB calculations for all possible hops would require large computational resources. Instead, Hao and Sholl made initial approximations for the position of the interstitial atom in a transition state before performing any DFT calculations. These initial approximations were obtained by noting that the TS for diffusion of H between two interstitial sites is generally located with the H atom close to the geometric center of the polyhedral face which connects the two interstitial sites[13, 41]. These estimates made it possible to rigorously locate transition states using DFT calculation that converge to a saddle point from configurations sufficiently close to the saddle point [13]. This approach was used to find the TS of both the *a*-Fe_3B and the *c*-Fe_3B systems. The binding energy of each TS was defined using Eq.(6.1), where the vibrational frequencies of H were computed using the harmonic approximation. Once the TS are characterized in this way, we can calculated the diffusion of the interstitial atom can be computed using quantum corrected harmonic transition state theory [18, 23, 42]. The rate of hopping from site A to B via $TS_{A\to B}$, for example can be calculated using

$$k_{A\to B} = \frac{\prod_{i=1}^{3} f(h\nu_i^A / 2k_B T)}{\prod_{i=1}^{2} f(h\nu_i^{TS_{A\to B}} / 2k_B T)} \frac{\prod_{i=1}^{3} \nu_i^A}{\prod_{i=1}^{2} \nu_i^{TS_{A\to B}}} e^{\frac{-E_a}{k_B T}} \quad (6.3)$$

Here $f(x) = \sinh(x)/x$, ν_i are the real vibrational frequencies of the interstitial atom in a site or TS of the particular isotope, and E_a is the isotope-independent classical activation energy for the particular hop. The differences between the ν_i from one isotope to another control the isotopic dependence of the hopping rates.

The expression above describes the hopping rate between adjacent interstitial sites, but this information alone is not sufficient to describe the net diffusivity of interstitial atoms. In *c*-Fe_3B, the self diffusivity can be calculated exactly using the method of Braun *et al*. once the site to site hopping rates are defined because of the ordered structure of this material[43]. In order to calculate the net diffusivity of the interstitial atoms in the substitutionally disordered and amorphous materials, we used kinetic Monte Carlo (KMC) simulations. These simulations rigorously describe the dynamics of H hopping between interstitial sites once the site to site hopping rates are defined. For further details on the KMC algorithm applied to our simulations please refer to Chapter 2.

6.4: Permeability Calculations

The net transport of H, D or T across a membrane is typically quantified in terms of either the flux or the permeability. We have only considered membranes where the net transport is dominated by diffusion across the membrane, a situation that is relevant in

practical settings with all but the thinnest membranes[16, 34]. The net flux, through a membrane can be calculated by Fick's first law[44, 45],

$$N_{H_2} = \frac{1}{L}\int_{c_{H,perm}}^{c_{H,feed}} D_t(c_H)dc_H \tag{6.4}$$

where N_{H_2} is the H_2 flux, L is the thickness of the membrane, $D_t(c_H)$ is the Fickian diffusion coefficient, which is dependent on the concentration of interstitial species, and $c_{H,feed}$ and $c_{H,perm}$ are the concentration of interstitial H on the feed and permeate side respectively. We note that from our KMC simulations we obtain the tracer diffusivity, $D_s(c_H)$, which is only equal to the Fickian diffusion coefficient, $D_t(c_H)$, when the concentration of the interstitials is dilute[46-51]. The permeability, *k*, is defined by[52-54]

$$k = \frac{N_{H_2}L}{(P_{H_2,feed}^{0.5} - P_{H_2,perm}^{0.5})} \tag{6.5}$$

where $P_{H_2,feed}^{0.5}$ and $P_{H_2,perm}^{0.5}$ are the H_2 partial pressures in the feed and permeate respectively. For a material where Sieverts' Law is valid Eq.(6.5) is easily reduced to $k = D_s K_s / 2$. For *a*-Fe_3B, where Sieverts' law is not valid, the flux is obtained using the following approximation [13]:

$$N_{H_2} \approx \frac{1}{L} D_t(\bar{c}_H)(c_{H,feed} - c_{H,perm}) \tag{6.6}$$

where is an average of concentration $\bar{c}_H = (c_{H,feed} - c_{H,perm})/2$. Because we will also focus on low concentrations of interstitial atoms we can approximate Fickian diffusion to tracer diffusivity. In general, $D_t(\bar{c}_H) \geq D_s(\bar{c}_H)$, which means that by using the $D_s(\bar{c}_H)$ to approximate we are in fact analyzing the lower bound flux of the membrane[55]. Once the

value of N_{H_2} for the *a*-Fe_3B is obtained, we use Eq.(6.5) to calculate the permeability in order to compare with the crystalline systems.

6.5: Isotope Solubility in $Pd_{96}M_4$ and *c*-Fe_3B and *a*-Fe_3B Alloys

For our Pd and Pd based alloys, we calculated the Sieverts' constant K_s, while for both the *c*-Fe_3B and *a*-Fe_3B systems we performed GCMC to obtain the solubility predictions of the isotopes in these systems. We wished to compare our predicted solubilities for pure Pd with experimental data. Figure 6.1 compares our predictions for the solubility of H, D, and T in pure Pd using Sieverts' law for the temperature range of 200 – 1000 K with a model fitted by Lässer and Powell. from their experimental observations at the same temperature range[56]. In this representation of the data, a smaller value of $-\ln(K_s)$ represents higher solubility. Our results for H solubility are consistent with the observations of Lässer and Powell for temperatures below 700 K. Our predicted solubility values for D and T deviate somewhat from the results of Lässer and Powell. This is due to our harmonic treatment of the isotopic dependence of the vibrational energy levels; anharmonic effects tend to make the factor associated with the square root of the isotropic weight in Eq.(6.2) slightly larger[41]. These anharmonic effects result in slightly increased binding energies for the heavier isotopes, in turn reducing the solubility of these species relative to a purely harmonic treatment. Nevertheless, our harmonic treatment captures the main isotopic effects observed experimentally.

At temperatures above 700 K, the model developed by Lässer and Powell from their experimental data exhibits some curvature that is not present in our predictions. Lässer and Powell's model overemphasizes the strength of this effect, which is not as

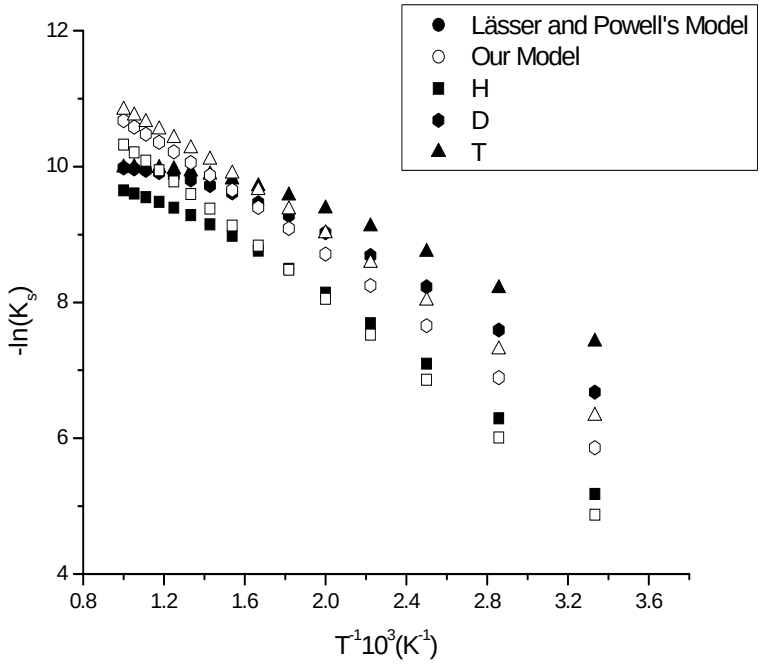

Figure 6.1: Isotope solubility in pure Pd using our models for the temperature range of 300 – 1000 K compared to the Lässer and Powell. Solid symbols represent model fitted to Lässer and Powell experimental results [56], while open symbols represent our results.

strong in their experimental data. This curvature also arises from anharmonic corrections, which become more pronounced at very high temperatures because of the increasing importance of higher vibrational energy levels under these conditions [56].

All of our analyses have been performed by examining pure H_2, D_2 and T_2, therefore in order to predict whether we can use a membrane to separate the isotopes, we define the isotopic solubility selectivity as: $\Theta_{isotope}/\Theta_H$. Figure 6.2 shows the predicted isotopic solubility selectivity for all of the metal alloys we have considered. It is clear that the crystalline alloys have similar tendencies; as temperature increases the selectivity for H relative to the heavier isotope reduces. Our results predict less variation in the selectivity as a function of temperature in pure Pd than the result from Lässer and Powell's model. The most useful contribution of our calculations is to allow a systematic

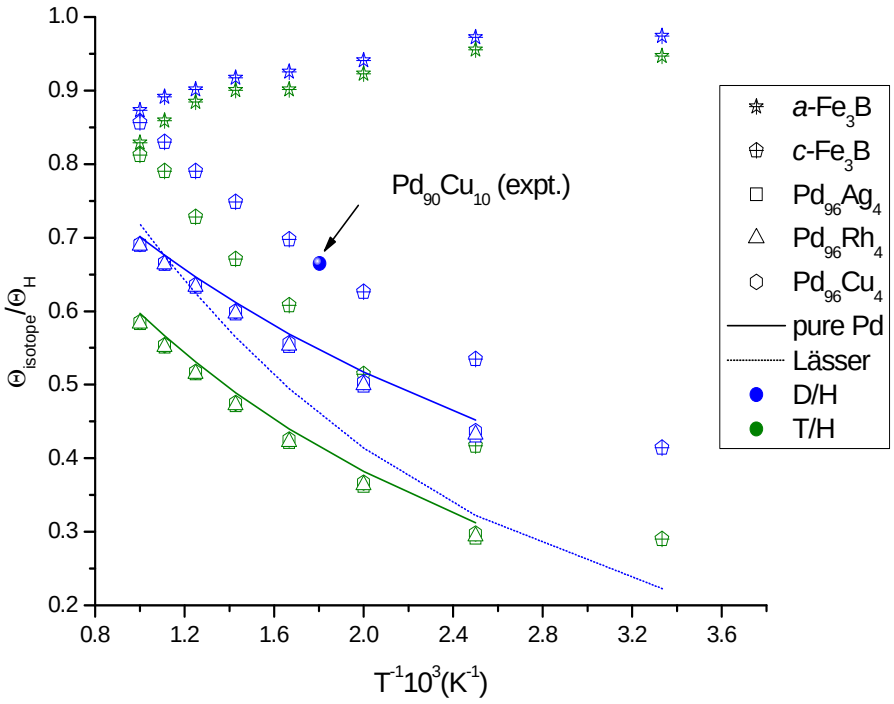

Figure 6.2: Solubility selectivity for all the metal alloys for the temperature range of 300 – 1000 K. Crossed symbols are for the Fe_3B systems. Open symbols are for the Pd-based alloys and the solid lines are for pure Pd. Blue data represents D/H, while green represents T/H selectivity.

comparison of several different alloys. For the $Pd_{96}M_4$ alloys, we find that the alloying effect makes almost no difference in the selectivity of H over the other isotopes compared to pure Pd. This does not mean that the absolute solubilities of the isotopes are the same in all the Pd-based alloys. For example, for $Pd_{96}Ag_4$ and pure Pd at 1000 K and hydrogen pressure of 1 atm we predict solubilities of $\Theta_H = 0.014$ and $\Theta_H = 0.010$ respectively. That is, the predicted solubility of H in the PdAg alloy is 40% larger than in pure Pd at these conditions. Any improvement/reduction in solubility is consistent for each of the isotopes in a given alloy, producing similar selectivities in comparison to pure Pd. Experimental isotropic selectivity from experimental data on H and D solubility in $Pd_{90}Cu_{10}$ has been reported by Kleppa *et al.*[57]. This experimental data is on a similar alloy

composition, and when we compare the solubility selectivity we observe that there is a slight decrease in the predicted selectivity at the same temperature for our Pd and Pd based alloys.

We now consider the isotopic solubility selectivity in the two Fe_3B materials we examined. For the crystalline material, *c*-Fe_3B, the trend of the isotopic selectivity is similar to the other crystalline alloys, although the selectivity of this material varies more with temperature than the Pd-based alloys. For the amorphous material, *a*-Fe_3B, the trend in the isotopic solubility selectivity is quite different than for the crystalline materials; the selectivity increases as the temperature decreases. At the lowest temperatures we examined, there is essentially no isotopic selectivity in this amorphous material. This situation is due to the very favorable binding energies found in some interstitial sites in this amorphous material. The most favorable sites in the *a*-Fe_3B material have binding energies around -0.50 eV. These values creates strong trap sites regardless of the isotope, and these trap sites dominate the overall solubility of the material. At the highest temperatures we examined, the occupancy in these strong trap sites decreases and the difference in the ZPE amongst the isotopes has a stronger effect on the solubility.

6.6: Isotope Diffusion in $Pd_{96}M_4$ and *c*-Fe_3B and *a*-Fe_3B Alloys

We first used the DFT-based KMC method reported previously[18, 42] to predict the self diffusion coefficients of H, D, and T in pure Pd. The results from these calculations are plotted our results in Figure 6.3. Above 500 K the lighter isotope diffuses fastest, while at lower temperatures a reverse isotope effect is observed. These results are in good agreement with diffusion measurements reported by Völkl and Alefeld[31, 33]. In order to

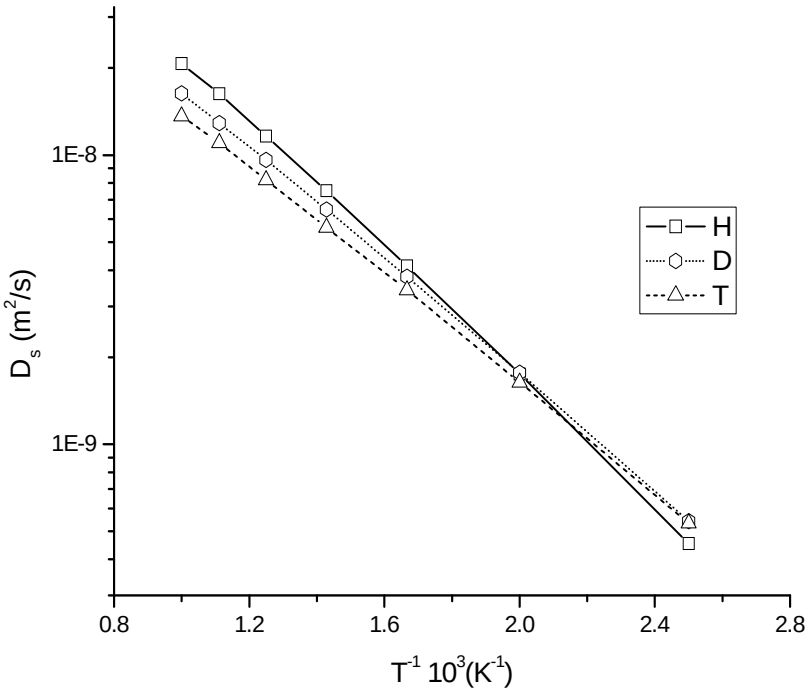

Figure 6.3: Arrhenius plot of H, D, and T self diffusion coefficient in pure Pd for the temperature range 400 – 1000 K. Curves are to guide the eye.

understand this transition from a reverse isotope effect at low temperatures to the expected behaviors at high temperatures we look at the differences in the isotopes. The vibrational frequencies and the ZPE of H at the TS are higher than those at the O site resulting in the difference in energy between these sites to decrease as the isotope mass increases[31]. The outcome of this situation is that quantum corrected energy barrier at lower temperatures decreases[33, 58]. This means that at low temperatures the effects of the first term in Eq.(6.3) will have greater influence, while at higher temperatures this term has an approximate value of 1. In Table 6.2 we compare the Arrhenius prefactor D_o for H, D, and T with experimental data by Jost[58]; our results have reasonably good agreement with the experiments.

Table 6.2: Arrhenius pre-exponential factor comparison for H, D, and T throughout the temperature range of 400 – 1200 K with experimental data[58]. In each case, the diffusivity was fitted to $D = D_o e^{-E_{act}/k_B T}$ over the temperature range indicated.

Isotope	Experimental D_o (m^2/s)	Model D_o (m^2/s)
H	2.90×10^{-7}	2.60×10^{-7}
D	1.70×10^{-7}	1.54×10^{-7}
T	0.75×10^{-7}	1.17×10^{-7}

Figure 6.4 shows the isotropic diffusion selectivity, $D_s^{isotope}/D_s^H$, for all the metal alloys we considered. The qualitative trend for every material is similar to that described above for pure Pd. Similar trends have been experimentally observed in metal alloys[31, 41, 59]. Unlike the solubility selectivity of the Pd-based alloys, where the isotopic selectivity was essentially unchanged with the addition of the alloying components, there are slight variations in the diffusion selectivity among the alloys. The isotropic diffusion selectivities of *c*-Fe_3B are also comparable to pure Pd. For *a*-Fe_3B, the concentration of the interstitial species can strongly influence the magnitude of the self diffusion coefficient[13]. For example, raising the interstitial concentration from 0.0001 to 0.1 at 600 K increases the diffusion of H by a factor of 4.5. Given that the concentration influences the diffusion, we examined the isotopic diffusion selectivity at three different interstitial concentrations, 0.0001, 0.02, and 0.1, and found that the isotopic selectivity varies little over this range. It is important to note that while the diffusion selectivities of both Fe_3B systems are comparable, the diffusion of the isotopes in these systems are orders of magnitude slower than in Pd[13].

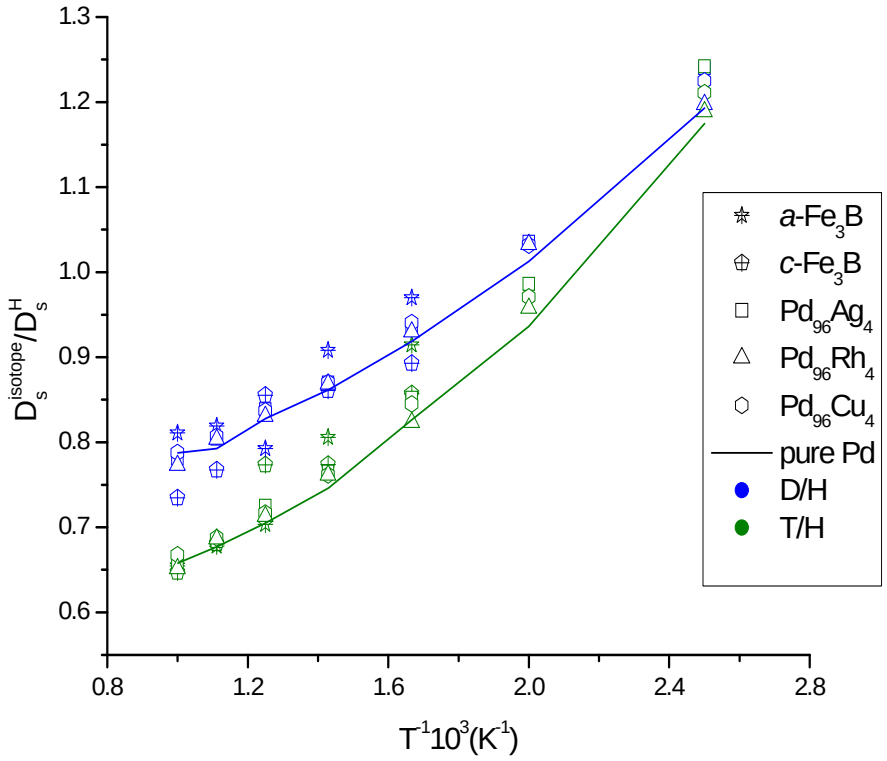

Figure 6.4: Tracer diffusion selectivity for all the metal alloys. Crossed symbols are for the Fe_3B systems. Open symbols are for the Pd-based alloys and the solid lines are for pure Pd. Blue data represents D/H, while green represents T/H selectivity.

6.7: Isotope Permeability in $Pd_{96}M_4$, *c*-Fe_3B, and *a*-Fe_3B Alloys

Our solubility and diffusion results allow us to predict the permeability of the isotopes in Pd, Pd based binary alloys and Fe_3B metal membranes. The permeability for H, D, and T was calculated using Eq.(6.5) for each system. As with our description of solubility and diffusion, we report the isotropic permeability selectivity, $k_{isotope}/k_H$, for each material metal membranes. These permeability selectivities are shown in Figure 6.5 for the temperature range for Pd and Pd based alloys of 400 – 1000 K, while a temperature range of 600 – 1000K for *c*-Fe_3B and *a*-Fe_3B.

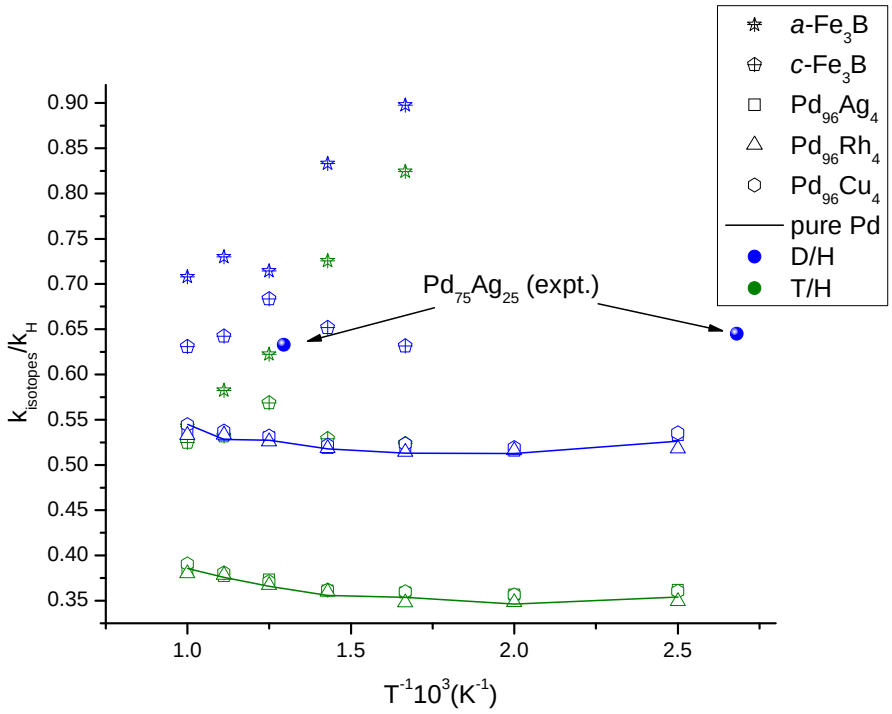

Figure 6.5: Permeability selectivity for all the metal alloys. Crossed symbols are for the Fe_3B systems. Open symbols are for the Pd-based alloys and the solid lines are for pure Pd. Blue data represents D/H, while green represents T/H selectivity.

For the Pd and Pd-based alloys, the isotopic selectivities are similar for each material. This is not surprising given the relatively weak effects of alloying in these materials on the solubility and diffusivity selectivies. It is interesting to note that throughout the entire temperature range we examined the permeability selectivity for these materials only weakly temperature dependent. This observation is supported by the experimental data of Serra *et al*. for D and H permeation through $Pd_{75}Ag_{25}$[11]. In order to obtain an approximate experimental permeability selectivity for pure Pd we took the lattice constant of pure Pd as 3.89 Å[60], solubility from Lasser and Powell's model[56], and diffusion using experimental data reported from Jost[58] to calculate the selectivity of D vs. H at 773 K to compare both our results for Pd, and Pd-based alloys, and the $Pd_{75}Ag_{25}$ alloy studied by Serra *et al*. This combination of experimental data resulted in a

permeability selectivity $k_D/k_H = 0.48$, while our calculations on pure Pd predict a selectivity of $k_D/k_H = 0.53$.

For the *c*-Fe_3B system the predicted permeability selectivities for the isotopes are less than those in Pd and Pd-based alloys. This is due to the lower solubility selectivity found at higher temperatures in this system. Although the selectivity of the *c*-Fe_3B membrane is less than the other crystalline membranes, it also shows little variation with temperature.

The amorphous Fe_3B system has a much less favorable permeability selectivity than any of the crystalline structures. From Figure 6.5, we can clearly observe that the permeability selectivity drastically decreases as the temperature decreases. This decrease in permeability selectivity is in mainly due to the poor solubility selectivity at the lowest temperatures we examined. This, combined with the fact that diffusion in this material is orders of magnitude slower than the Pd-based crystalline alloys, would make this amorphous material quite unsuitable for use in isotopic separations.

6.8: Conclusion

In this chapter, we have shown how DFT-based calculations can be used to examine the isotopic selectivity of dense metal membranes for high temperature hydrogen purification. We have reported results for the five crystalline materials, Pd, $Pd_{96}Ag_4$, $Pd_{96}Cu_4$, $Pd_{96}Rh_4$, *c*-Fe_3B, and one amorphous material, *a*-Fe_3B. Our results reliably describe the trends that have been established experimentally for pure Pd, providing a strong basis for using our methods to make predictions about materials for which experimental data is not available. One conclusion from our calculations is that

crystalline materials appear to be far better suited for isotopic separations than amorphous materials. In the amorphous Fe_3B we examined, the presence of extremely favorable binding sites for interstitial H and its isotopes strongly limited the selectivity of the material as a membrane. The existence of a broad range of interstitial site binding energies is typical in amorphous metals[61-63], so poor isotopic selectivity is likely to be common in many materials of this type. Another conclusion from our results is that the isotopic permeability selectivity of the crystalline materials is only weakly dependent on temperature over a wide range of temperatures. This observation could be very useful in considering process designs involving membranes for isotopic separations, since the operating temperature could be varied as needed to maximize flux, minimize energy usage, or to ensure compatibility of the membrane unit with other operating components in an overall system.

It is important to note that we have characterized isotopic selectivity in terms of the performance of each membrane material for isotopically pure feeds. Because net transport of H through a metal membrane occurs by molecular dissociation, transport of interstitial H atoms, and subsequent recombinative desorption of molecules, permeation of mixed feeds will inevitably lead to isotopic mixing. That is, a membrane fed with a mixture of pure H_2 and D_2 will deliver a mixture of H_2, D_2, and HD. Although it would be possible to extend the calculations we have done here to account for these mixing effects, it is beyond the scope of this initial study. As with understanding the selectivity of membranes for other kinds of gas mixtures, the predictions that can be made using pure feeds are useful in the sense that materials which are found to have poor selectivities

(e.g. the amorphous material we examined) will also perform poorly when mixture effects are included.

6.9: Reference

[1] J. Evans and I. R. Harris, J. Less-Common Metals **89**, 407 (1983).
[2] S. Tosti and V. Violante, Fusion Eng. Des. **43**, 93 (1998).
[3] K. Aoki, Y. Ogata, K. Kasakabe, and S. Morooka, Int. J. Hydrogen Energy **23**, 325 (1998).
[4] Q. Wang, S. Challa, D. S. Sholl, and K. J. Johnson, Phys. Rev. Let. **82**, 956 (1999).
[5] M. N. Polianski, T. R. Rizzo, and O. V. Boyarkin, Appl. Phys. B **83**, 311 (2006).
[6] Y. Ito, R. Takahashi, S. Mizusaki, I. Yamamoto, and M. Yamaguchi, Sci. Tech. Adv. Mater. **7**, 369 (2006).
[7] S. N. Paglieri and J. D. Way, Sep. Purif. Methods **31**, 1 (2002).
[8] G. Alefeld and J. Völkl, *Hydrogen in Metals I* (Springer-Verlag, Berlin, 1978).
[9] D. Dudek, J. Alloys and Compounds **442**, 152 (2007).
[10] M. Matsuyama, H. Sugiyama, M. Hara, and K. Watanabe, J. Nucl. Mater. **367-370**, 1096 (2007).
[11] E. Serra, A. Kemali, A. Perujo, and D. K. Ross, Metall. Mater. Trans. A **29**, 1023 (1998).
[12] B. Bhatia and D. S. Sholl, J. Chem. Phys **122**, 204707 (2005).
[13] S. Hao and D. S. Sholl, Energy Environ. Sci. **1**, 175 (2008).
[14] P. Kamakoti, B. D. Morreale, M. V. Ciocco, B. H. Howard, R. P. Killmeyer, A. V. Cugini, and D. S. Sholl, Science **307**, 569 (2005).
[15] P. Kamakoti and D. S. Sholl, J. Membr. Sci. **279**, 94 (2006).
[16] C. Ling and D. S. Sholl, J. Membr. Sci. **303**, 162 (2007).
[17] D. S. Sholl, J. Alloys and Compounds **446**, 462 (2007).
[18] L. Semidey-Flecha and D. S. Sholl, J. Chem. Phys. **128**, 144701 (2008).
[19] C. G. Sonwane, J. Wilcox, and Y. H. Ma, J. Chem. Phys **125**, 184714 (2006).
[20] C. G. Sonwane, J. Wilcox, and Y. H. Ma, J. Phys. B. **110**, 24549 (2006).
[21] B. Bhatia, X. Luo, C. A. Sholl, and D. S. Sholl, J. Phys. Cond. Mat. **16**, 8891 (2004).
[22] B. Bhatia and D. S. Sholl, Phys. Rev. B **72**, 224302 (2005).
[23] P. Kamakoti and D. S. Sholl, J. Membr. Sci. **225**, 145 (2003).
[24] E. Wimmer, W. Wolf, J. Sticht, and P. Saxe, Phys. Rev. B **77**, 13405 (2008).
[25] T. M. Nenoff, R. J. Spontak, and C. M. Aberg, MRS Bulletin **31**, 735 (2006).
[26] S. Hao and D. S. Sholl, J. Phys. Cond. Matter (2009).
[27] G. Kresse and J. Furthmuller, Comput. Mat. Sci **6**, 15 (1996).
[28] X. Ke and G. J. Kramer, Phys. Rev. B **66**, 184304 (2002).
[29] O. M. Løvvik and R. A. Olsen, J. Chem. Phys. **118**, 3268 (2003).
[30] G. J. Ackland, J. Phys.: Condens. Matter **14**, 2975 (2002).

[31] E. Wicke and H. Brodowsky, *Hydrogen in Metals II* (Springer-Verlag, Berlin, 1978).
[32] Y. Fukai, *The Metal-Hydrogen System: Basic Bulk Properties* (Springer-Verlag, Berlin, 2005).
[33] N. Sicking, J. Less-Common Metals **101**, 169 (1984).
[34] T. L. Ward and T. Dao, J. Membr. Sci. **153**, 211 (1999).
[35] B. D. Morreale, M. V. Ciocco, B. H. Howard, K. S. Rothenberger, A. V. Cugini, and R. M. Enick, J. Membr. Sci. **241**, 219 (2004).
[36] D. G. Westlake, J. Less-Common Metals **91**, 1 (1983).
[37] H. Barlag, L. Opara, and H. Zuchner, J. Alloys and Compounds **330**, 434 (2002).
[38] S. Fujita and A. Garcia, J. Phys. Chem. Solids **52**, 351 (1991).
[39] G. Henkelman, Uberuga, B.P., Jonsson, H, J. Chem. Phys **113**, 9901 (2000).
[40] G. Henkelman, Uberuga, B.P., Jonsson, H, J. Chem. Phys **113**, 9901 (2000).
[41] T. Maeda, S. Naito, M. Yamamoto, M. Mabuchi, and T. Hashino, J. Chem. Soc. Faraday Trans. **90**, 889 (1994).
[42] P. Kamakoti and D. S. Sholl, Phys. Rev. B **71**, 014301 (2005).
[43] O. M. Braun and C. A. Sholl, Phys. Rev. B **58**, 14870 (1998).
[44] B. D. Morreale, M. V. Ciocco, R. M. Enick, B. I. Morsi, B. H. Howard, A. V. Cugini, and K. S. Rothenberger, J. Membr. Sci. **212**, 87 (2003).
[45] D. S. Sholl, Ind. Eng. Chem. Res **39**, 3737 (2000).
[46] K. W. Kehr and O. Paetzold, Physica A **190**, 1 (1992).
[47] K. W. Kehr and T. Wichmann, Mater. Sci. Forum **223**, 151 (1996).
[48] F. J. Keil, R. Krishna, and M. O. Coppens, Rev. Chem. Eng **16**, 71 (2000).
[49] D. S. Sholl, Acc. Chem. Res. **39**, 403 (2006).
[50] A. I. Skoulidas and D. S. Sholl, J. Phys. Chem. B **105**, 3151 (2001).
[51] A. I. Skoulidas and D. S. Sholl, J. Phys. Chem. B **109**, 15760 (2005).
[52] R. C. Brouwer, E. Salomons, and R. Griessen, Phys. Rev. B **38**, 10217 (1988).
[53] K. S. Rothenberger, B. H. Howard, R. P. Killmeyer, A. V. Cugini, R. M. Enick, F. Baustmante, M. V. Ciocco, B. D. Morreale, and R. E. Bauxbaum, J. Membr. Sci. **218**, 19 (2003).
[54] L. Schlapbach and A. Züttel, Nature **414**, 353 (2001).
[55] S. Hao and D. S. Sholl, J. Chem. Phys. (in press).
[56] R. Lässer and G. L. Powell, Phys. Rev. B **34**, 578 (1986).
[57] O. J. Kleppa, Shamsuddin, and C. Picard, J. Chem. Phys. **71**, 1656 (1979).
[58] W. Jost, *Diffusion in Solids, Liquids, and Gases* (Academic Press, New York, 1960).
[59] G. L. Powell and J. R. Kirkpatrick, Phys. Rev. B **43**, 6968 (1991).
[60] W. B. Pearson, *A Handbook of Lattice Spacings and Structures of Metals and Alloys* (Macmillan, New York, 1958).
[61] R. Kirchheim, Prog. Mater. Sci **32**, 261 (1988).
[62] R. Kirchheim, T. M. Otschele, W. Kieninger, H. Gleiter, R. Birringer, and T. D. Koble, Mater. Sci. Eng. **99**, 457 (1988).
[63] H. Wu, W. Zhou, T. J. Udovic, and J. J. Rushm, Chem. Mater. **19**, 329 (2007).

CHAPTER 7

CONCLUSION

Metal membranes play a vital role in hydrogen purification. Defect-free membranes can exhibit infinite selectivity for H_2. High performance metal membranes must be able to provide high fluxes, be resistant to poisoning, with stand long operational lifetimes, and be of low cost[1]. Alloys offer an alternate route to improve upon membranes based on pure metal, such as Pd. Nevertheless, experimental development of new membranes is hindered by the large efforts required to make and test these materials.

In this work, we showed that a combination of first principles density functional theory (DFT) calculations and coarse grained lattice gas modeling with the aid of cluster expansion methods could be successfully used to predict hydrogen fluxes through Pd-based binary alloy membranes. First we performed atomic-scale DFT calculations of binding energies, vibrational frequencies, and energy barriers for representative alloys with composition of $Pd_{96}M_4$ for M = Au, Ag, Pt, Rh, Cu, and Ni. We used cluster expansion methods to determine lattice gas models for each of these types of calculations. H solubility, diffusivity, and permeability were calculated using these lattice gas models for each alloy of interest. The permeability results were found to be in qualitative and quantitative agreement with experimental reported H permeability in these and similar systems.

Using insight developed from our binary alloy calculations we extended our methods to calculate H macroscopic properties to PdCu-based ternary alloys. PdCu alloys have experimentally been proven to increase resistance to H_2S poisoning relative to pure

Pd membranes[1, 2]. The concept consists of using additive metal atoms that will enhance H permeability, while retaining the favorable surface chemistry of PdCu towards contaminants. We performed similar atomic-scale DFT calculations to $Pd_{70}Cu_{26}M_4$ alloys for M = Au, Ag, Pt, and Ni and two PdCu reference alloy $Pd_{74}Cu_{26}$ and $Pd_{70}Cu_{30}$. Lattice gas model based on our cluster expansion methods were developed for interstitial H in the bulk of these alloys. Using these models in conjunction with our methods we predicted the solubility, diffusivity, and permeability of H in these systems. We found that the addition of Au would produce increased H permeabilities relative to H permeability in both PdCu reference alloys.

If we had used our modeling results alone to asses the relative permeability of binary alloys as a function of temperature and alloy composition, we would have reached correct conclusion. Given this, we conclude that our ternary alloy predictions also are quantitatively correct, regardless of the lack of experimental corroboration. Our modeling methods provide an avenue to accurately predict hydrogen behavior in membrane materials without requiring experimental input. Our approach assumes that bulk diffusion is the rate limiting step in permeation. Other elementary steps such as surface to bulk diffusion play a role in the performance of ultra-thin membranes[3], but have not been explored in this work.

Although our modeling methods involving detailed DFT calculations and cluster expansion lattice models are extremely useful as a compliment to experimental studies, they require considerable computational efforts. In order to discover new materials we have developed a heuristic lattice model. Our heuristic lattice model is currently applied to Pd-based fcc binary alloys. Using a small set of DFT calculations we can qualitatively

predict whether a Pd-based alloy will have improved H permeability relative to pure Pd. Using this model we were capable of identifying four transition metals (Hf, Ir, Ta and Zr), not commonly used in hydrogen purification membranes, that at a given alloy composition result in greater H permeability when compared to pure Pd.

Most of this thesis was focused on using metal alloys as membranes for purifying hydrogen. There are applications, however, where the separation of isotopes of hydrogen is important, such as the design and operation of fusion reactors[4, 5]. Using our methods, we can easily extend our study of H macroscopic properties to include the study of isotope behavior in these dense metal alloys[6].

The methods we have developed are crucial tools for facilitating the search for new materials for H purification purposes. However, it is not limited to this research only. Our solubility and diffusion analysis combined with cluster expansion methods can be applied to a wide range of work, including but not limited to catalysis, hydrogen storage, nanoparticles, to name a few. In addition, our heuristic lattice model can be further extended to include the prediction of ternary materials, based on binary information.

References

1 P. Kamakoti, B. D. Morreale, M. V. Ciocco, B. H. Howard, R. P. Killmeyer, A. V. Cugini, and D. S. Sholl, Science **307**, 569 (2005).

2 B. D. Morreale, M. V. Ciocco, B. H. Howard, K. S. Rothenberger, A. V. Cugini, and R. M. Enick, J. Membr. Sci. **241**, 219 (2004).

3 C. Ling and D. S. Sholl, J. Membr. Sci. **303**, 162 (2007).

4 J. Evans and I. R. Harris, J. Less-Common Metals **89**, 407 (1983).

5 S. Tosti and V. Violante, Fusion Eng. Des. **43**, 93 (1998).

6 L. Semidey-Flecha, S. Hao, and D. S. Sholl, J. Taiwan Inst. Chem. Eng. **40**, 246 (2009).

APPENDIX

In our appendix we report data used in our calculations methods, results without any detailed discussion of their physical implications. In Chapter 2 we described the cluster expansion method used in determining the lattice models later used to predict macroscopic properties of interstitial H. The geometric images used to identify each of the binding sites in which H can reside within the bulk of an fcc material are described in section A. In Chapter 3 we implemented the cluster expansion method in determining a lattice model for each type of binding sites of the fcc $Pd_{96}M_4$ alloys. The coefficients pertaining to each geometric image of the individual binding sites are listed in section B. In Chapter 4 we implemented the cluster expansion method to determine the lattice model for binding sites of the fcc $Pd_{74}Cu_{26}$, $Pd_{70}Cu_{30}$, and $Pd_{70}Cu_{26}M_4$ alloys. The coefficients belonging to each of the geometric images used in describing the binding sites for these alloys are listed in section C. In Chapter 5 we developed a simple heuristic lattice model to pre-screen potential Pd-based binary alloys for H purification. The results for alloys using our heuristic lattice model are plotted in contour plots in section D.

Appendix A: Cluster Expansion Model Parameters

In this section we list all the cluster expansion model parameters used to define the fcc metal binding sites, as described in Chapter 2.

Table A.1: List of parameters used to describe the DFT calculated O sites in our fcc Pd and PdCu-based alloys. All parameters were normalized, or divided by either the shell number or the distance of the interaction. *L* represents the lattice constant in Å. Atom spacing is for the ideal fcc structures.

Parameter ID #:	Description
1	Number of Pd atoms in the $2\times N$ shell normalized by 2
2	Number of Pd atoms in the $3\times N$ shell normalized by 3
3	Number of Cu (M in the case of binary alloys) atoms in the $2\times N$ shell normalized by 2
4	Number of Cu (M in the case of binary alloys) atoms in the $3\times N$ shell normalized by 3
5	Number of M (in the ternary alloys) atoms in the $2\times N$ shell normalized by 2
6	Number of M (in the ternary alloys) atoms in the $3\times N$ shell normalized by 3
7	2 body interactions between metal atoms separated by $L/\sqrt{2}$ in the $2\times N$ shell normalized by $L/\sqrt{2}$
8	2 body interactions between metal atoms separated by L in the $2\times N$ shell normalized by L
9	2 body interactions between metal atoms separated by L in the $3\times N$ shell normalized by L
10	2 body interactions between metal atoms separated by $\sqrt{2}L$ in the $3\times N$ shell normalized by $\sqrt{2}L$
11	2 body interactions between metal atoms separated by $\sqrt{3}L$ in the $3\times N$ shell normalized by $\sqrt{3}L$
12	2 body interaction between metal atoms in the $2\times N$ shell separated by $L/\sqrt{2}$ to atoms in the $3\times N$ shell normalized by $L/\sqrt{2}$
13	3 body interactions between metal atoms in the $2\times N$ shell where each atom is separated by $L/\sqrt{2}$ normalized by $L/\sqrt{2}$
14	3 body interactions between metal atoms in the $3\times N$ shell where each atom is separated by L normalized by L
15	4 body interactions between metal atoms in the $2\times N$ shell where each atom is separated by $L/\sqrt{2}$ normalized by 2
16	4 body interactions between metal atoms in the $3\times N$ shell where each atom is separated by $\sqrt{2}L$ normalized by 3
17	Number of Pd atoms in the $4\times N$ shell normalized by 4

18	Number of Cu (M in binary alloys) atoms in the $4\times N$ shell normalized by 4
19	Number of M (in ternary alloys) atoms in the $4\times N$ shell normalized by 4
20	Number of Pd atoms in the $5\times N$ shell normalized by 5

Table A.2: List of parameters used to describe the DFT calculated T sites in our fcc Pd and PdCu-based alloys. All parameters were normalized, or divided by either the shell number or the distance of the interaction. *L* represents the lattice constant in Å. Atom spacing is for the ideal fcc structures.

Parameter ID #:	Description
1	Number of Pd atoms in the $2\times N$ shell normalized by 2
2	Number of Pd atoms in the $3\times N$ shell normalized by 3
3	Number of Cu (M in the case of binary alloys) atoms in the $2\times N$ shell normalized by 2
4	Number of Cu (M in the case of binary alloys) atoms in the $3\times N$ shell normalized by 3
5	Number of M (in the ternary alloys) atoms in the $2\times N$ shell normalized by 2
6	Number of M (in the ternary alloys) atoms in the $3\times N$ shell normalized by 3
7	2 body interactions between metal atoms separated by $L/\sqrt{2}$ in the $2\times N$ shell normalized by $L/\sqrt{2}$
8	2 body interactions between metal atoms separated by $L/\sqrt{2}$ in the $3\times N$ shell normalized by $L/\sqrt{2}$
9	2 body interactions between metal atoms separated by $\sqrt{6}L/2$ in the $3\times N$ normalized by $\sqrt{6}L/2$
10	2 body interactions between metal atoms separated by $\sqrt{2}L$ in the $3\times N$ normalized by $\sqrt{2}L$
11	2 body interactions between metal atoms separated by $\sqrt{10}L/2$ in the $3\times N$ shell normalized by $\sqrt{10}L/2$
12	2 body interaction between metal atoms in the $2\times N$ shell separated by $L/\sqrt{2}$ to atoms in the $3\times N$ shell normalized by $L/\sqrt{2}$
13	2 body interaction between metal atoms in the $2\times N$ shell separated by L to atoms in the $3\times N$ shell normalized by L
14	2 body interaction between metal atoms in the $2\times N$ shell separated by $\sqrt{6}L/2$ to atoms in the $3\times N$ shell normalized by $\sqrt{6}L/2$
15	Number of Pd atoms in the $4\times N$ shell normalized by 4
16	Number of Cu (M in binary alloys) atoms in the $4\times N$ shell normalized by 4
17	Number of M (in ternary alloys) atoms in the $4\times N$ shell normalized by 4

18	2 body interactions between metal atoms separated by $L/\sqrt{2}$ in the $4\times N$ shell normalized by $L/\sqrt{2}$
19	2 body interaction between metal atoms in the $3\times N$ shell separated by $L/\sqrt{2}$ to atoms in the $4\times N$ normalized by $L/\sqrt{2}$
20	2 body interaction between metal atoms in the $3\times N$ shell separated by L to atoms in the $4\times N$ normalized by L
21	Number of Pd atoms in the $5\times N$ shell normalized 5
22	Number of Cu (M in binary alloys) atoms in the $5\times N$ shell normalized by 5
23	Number of M (in ternary alloys) atoms in the $5\times N$ shell normalized by 5
24	3 body interactions between metal atoms in the $2\times N$ shell separated by $L/\sqrt{2}$ normalized by $L/\sqrt{2}$
25	3 body interactions between metal two metal atoms separated by $L/\sqrt{2}$ in the $2\times N$ shell to atoms in the $3\times N$ shell separated by $L/\sqrt{2}$ normalized by separated by $L/\sqrt{2}$
26	3 body interactions between metal atoms in the $3\times N$ shell separated by $L/\sqrt{2}$ normalized by $L/\sqrt{2}$
27	3 body interactions between two metal atoms separated by $L/\sqrt{2}$ in the $3\times N$ shell to atoms in the $2\times N$ shell separated by $L/\sqrt{2}$ normalized by $L/\sqrt{2}$
28	3 body interactions between two metal atoms separated by $\sqrt{6}L/2$ in the $3\times N$ shell to atoms in the $2\times N$ shell separated by $L/\sqrt{2}$ normalized by $\sqrt{6}L/2$
29	3 body interactions between atoms in the $4\times N$ shell separated by $L/\sqrt{2}$ normalized by $L/\sqrt{2}$
30	3 body interactions between two metal separated by $L/\sqrt{2}$ in the $3\times N$ shell to atoms in the $4\times N$ shell separated by $L/\sqrt{2}$ normalized by $L/\sqrt{2}$

Appendix B: $Pd_{96}M_4$ Cluster Expansion Models

In this section we list the cluster expansion model coefficients for the models used to describe interstitial H in the $Pd_{96}M_4$ (M = Au, Ag, Pt, Rh, Cu, and Ni) alloys, described in Chapter 3.

Table B.1: O site CE coefficients for the $Pd_{96}Au_4$ and $Pd_{96}Ag_4$ alloys. Parameters identified by numbers from 1 through 20 are described in detail in Table A.1. Coefficients for the CE model for E_b are listed separately from the coefficients of the ZPE for each individual alloy. All coefficients have units of eV.

	$Pd_{96}Au_4$		$Pd_{96}Ag_4$	
	E_b	ZPE	E_b	ZPE
E_o	0.7067	0.9206	0.2101	0.1182
1	0.3194	0.2929	0.1413	0.0096
2	-	-	-	-
3	-	-0.2296	-	-
4	0.0325	-	-	-
5	-	-	-	-
6	-	-	-	-
7	-	0.0169	-0.0045	-
8	0.1510	-0.0541	0.0787	-0.0139
9	-	-	-	0.0164
10	-	-	0.0057	-
11	-	-	-	-
12	-	-	0.0008	-
13	-	-	-	-
14	-	-	0.0011	0.0078
15	-	-	-	-
16	-	-	-	-
17	-	-	-	-
18	-	-	-	-
19	-	-	-	-
20	-	-	-	-

Table B.2: O site CE coefficients for the $Pd_{96}Pt_4$, $Pd_{96}Rh_4$, $Pd_{96}Cu_4$, and $Pd_{96}Ni_4$ alloys. Parameters identified by numbers from 1 through 20 are described in detail in Table A.1. Coefficients for the CE model for E_b are listed separately from the coefficients of the ZPE for each individual alloy. All coefficients have units of eV.

	$Pd_{96}Pt_4$		$Pd_{96}Rh_4$		$Pd_{96}Cu_4$		$Pd_{96}Ni_4$	
	E_b	ZPE	E_b	ZPE	E_b	ZPE	E_b	ZPE
E_o	-0.0384	-1.3120	0.3801	-0.0169	-0.3692	0.0293	-0.0999	0.0103
1	-0.0016	-0.2393	0.1478	-0.0610	-0.0363	-	0.0518	-0.0486
2	-	-0.2517	0.0963	-	-0.0652	-0.0340	-	-0.0122
3	0.1112	0.2080	-	-	-	-	0.0871	0.0010
4	-	0.2549	-	-	-	-	-	-
5	-	-	-	-	-	-	-	-
6	-	-	-	-	-	-	-	-
7	-0.0291	-	0.0206	-0.0101	-	-	0.0511	-0.0090
8	-0.0043	0.0023	0.0315	-0.0401	-	-0.0088	0.0090	-0.0129
9	-	-	0.0053	-	-0.0026	-	-	-
10	-0.0100	-	-	-	-	-0.0063	0.0050	-
11	-	-0.0085	-	-	-	-	-	-0.0077
12	-0.0003	-	0.0069	-	-0.0039	-	0.0019	-0.0025
13	-0.0166	0.0037	-	-	-	-	0.0252	-
14	-	-	-	-	-	-	-	-
15	-	0.0028	-	-	-	-	-0.0009	0.0025
16	-0.0001	-	-	-	-	-	-	-
17	-	-	-	-	-	-	-	-
18	-	-	-	-	-	-	-	-
19	-	-	-	-	-	-	-	-
20	-	-	-	-	-	-	-	0.0107

Table B.3: T site CE coefficients for the $Pd_{96}Au_4$ and $Pd_{96}Ag_4$ alloys. Parameters identified by numbers from 1 through 30 are described in detail in Table A.2. Coefficients for the CE model for E_b are listed separately from the coefficients of the ZPE for each individual alloy. All coefficients have units of eV.

	$Pd_{96}Au_4$		$Pd_{96}Ag_4$	
	E_b	ZPE	E_b	ZPE
E_o	0.8591	0.1960	0.5897	0.2321
1	0.5054	0.0100	0.3873	0.0228
2	-	-	-	-
3	-	-	-	-
4	-	-	-	-
5	-	-	-	-
6	-	-	-	-
7	0.0086	0.0043	0.0497	0.0041
8	-	-	-	-
9	-	-	-	-
10	-	-	-	-
11	-0.0040	-	0.0343	-
12	-	-	-	-
13	0.0260	-	-0.0069	-
14	-0.0056	0.0012	-0.0112	-
15	-	-	-	0.0048
16	-	-	-	-
17	-	-	-	-
18	-	-	-	-
19	-0.0005	-	-0.0028	-
20	-0.0019	-0.0013	-0.0050	-
21	-	-	-	-
22	-	-	-	-
23	-	-	-	-
24	-	-	-	-
25	-	-	-	-
26	-	-	-	-
27	-	-	-	-
28	-	-	-	-
29	-	-	-	-
30	-	-	-	-

Table B.4: T site CE coefficients for the $Pd_{96}Pt_4$, $Pd_{96}Rh_4$, $Pd_{96}Cu_4$, and $Pd_{96}Ni_4$ alloys. Parameters identified by numbers from 1 through 30 are described in detail in Table A.2 Coefficients for the CE model for E_b are listed separately from the coefficients of the ZPE for each individual alloy. All coefficients have units of eV.

	$Pd_{96}Pt_4$		$Pd_{96}Rh_4$		$Pd_{96}Cu_4$		$Pd_{96}Ni_4$	
	E_b	ZPE	E_b	ZPE	E_b	ZPE	E_b	ZPE
E_o	0.5363	0.1780	0.4890	0.1835	0.8747	0.1654	-0.4576	0.6535
1	0.2333	-0.0072	0.1271	0.0066	-	-	-0.0632	0.2311
2	0.0198	0.0016	0.0594	-	-	-	-	-
3	-	-	-	-	-	-	-	-0.2412
4	-	-	-	-	-	-	-	-0.0038
5	-	-	-	-	-	-	-	-
6	-	-	-	-	-	-	-	-
7	0.0061	-0.0011	0.0192	0.0011	0.0195	-	0.0054	0.0018
8	-	-	-	-	-	-	-	-
9	-	-	-	-	-	-0.0007	-	-0.0003
10	-0.0058	-	-0.0078	-	-	-0.0009	-	-0.0037
11	-	-	-	-	0.0294	-	-	-
12	-0.0016	-0.0002	0.0023	-	-	-	0.0009	-0.0001
13	-0.0023	-	-	-	-0.0084	-	-0.0019	-
14	-	0.0006	-	-	-	-	-	-0.0023
15	0.0113	-	0.0545	-	0.4572	-0.0076	-0.1174	-
16	-	-	-	-	-	-	-	-
17	-	-	-	-	-	-	-	-
18	-	-0.0003	0.0083	0.0011	0.0891	-	-0.0122	-
19	-	-0.0001	-	-	-	-	-0.0039	-
20	-	-	0.0050	-	-	-	0.0048	-
21	0.0071	-0.0003	0.0076	-0.0026	-	-	-	-
22	-	-	-	-	-	-	-	-
23	-	-	-	-	-	-	-	-
24	-	-	-	-	0.0103	-	-	-
25	-	-	-	-	-	-	-	-
26	-	-	-	-	0.0054	-	-	-
27	-	-	-	-	-	-	-	-
28	-	-	-	-	-	-	-	-
29	-	-	-	-	-	-	-	-
30	-	-	-	-	-	-	-	-

Table B.5: TS CE coefficients for the $Pd_{96}Au_4$ and $Pd_{96}Ag_4$ alloys. O site parameter contributions identified as O 1- O 20 and T site parameter contribution identified as T 1 – T 30 as described in Table A.1 and Table A.2. Coefficients for the CE model for E_b are listed separately from the coefficients of the ZPE for each individual alloy. All coefficients have units of eV.

	$Pd_{96}Au_4$		$Pd_{96}Ag_4$	
	E_b	ZPE	E_b	ZPE
E_o	1.4747	0.2027	-0.8336	0.1954
O 1	-	-0.0044	0.1363	0.0005
O 2	-	-	-	-
O 3	-	-	-	-
O 4	-	-	-	-
O 5	-	-	-	-
O 6	-	-	-	-
O 7	-	-	-	-
O 8	-	-	-	0.0026
O 9	-	-	-	-
O 10	-	-	-	-
O 11	-	-	-	-
O 12	-0.0081	-	-	-
O 13	-	-	-	-
O 14	-	-	-	-
O 15	-	-	-	-
O 16	-	-	-	-
O 17	-	-	0.0939	-
O 18	-	-	-	-
O 19	-	-	-	-
O 20	-	-	-	-
T 1	0.4336	0.0170	-	0.0207
T 2	-	0.0070	-0.5356	-
T 3	-	-	-	-
T 4	-	-	-	-
T 5	-	-	-	-
T 6	-	-	-	-
T 7	-	-	-	-
T 8	-	-0.0009	-0.0360	-
T 9	-0.0360	-	-	-
T 10	-	0.0024	-	-
T 11	-	-	-	-
T 12	-	0.0009	0.0144	0.0015

T 13	-	-	-0.0558	-
T 14	-	0.0022	-0.0844	-
T 15	0.2455	0.0013	-0.1223	-
T 16	-	-	-	-
T 17	-	-	-	-
T 18	-	-	-	-
T 19	-	-	-0.0302	-
T 20	0.0665	-	-	-
T 21	-	-	-	-
T 22	-	-	-	-
T 23	-	-	-	-
T 24	-	-	-	-
T 25	-	-	-	-
T 26	-	-	-	-
T 27	-	-	-	-
T 28	-	-	-	-
T 29	-	-	-	-
T 30	-	-	-	-

Table B.6: TS CE coefficients for the $Pd_{96}Pt_4$, $Pd_{96}Rh_4$, $Pd_{96}Cu_4$, and $Pd_{96}Ni_4$ alloys. O site parameter contributions identified as O 1- O 20 and T site parameter contribution identified as T 1 – T 30 as described in Table A.1 and Table A.2. Coefficients for the CE model for E_b are listed separately from the coefficients of the ZPE for each individual alloy. All coefficients have units of eV.

	$Pd_{96}Pt_4$		$Pd_{96}Rh_4$		$Pd_{96}Cu_4$		$Pd_{96}Ni_4$	
	E_b	ZPE	E_b	ZPE	E_b	ZPE	E_b	ZPE
E_o	0.4146	0.1672	0.7408	0.1718	-0.2516	0.7445	0.0776	-0.0987
O 1	-	-	-	-0.0028	-0.0421	-0.0096	-	-
O 2	-	-	-	-0.0018	-0.0478	-	-	-
O 3	-	-	-	-	-	-	-	-
O 4	-	-	-	-	-	-	-	-
O 5	-	-	-	-	-	-	-	-
O 6	-	-	-	-	-	-	-	-
O 7	-0.0077	0.0011	0.0058	-	-	-	0.0148	-
O 8	-	-	-	-	-0.0271	-	-	-
O 9	-	-	-	-	-	-	-	-0.0048
O 10	-	-	-	-	-	-	-	-0.0053
O 11	-	-	-	-	-	-	-	-
O 12	-	0.0003	-	-0.0004	-	-	-	0.0056
O 13	-	0.0006	-	-	-	-	-	-
O 14	-	-	-	-	0.0030	-	-	-
O 15	0.0073	-	-	-	-	-	-	-
O 16	-	-	-	-	-	-	-	-
O 17	-	-	-	-	-	-	-	-
O 18	-	-	-	-	-	-	-	-
O 19	-	-	-	-	-	-	-	-
O 20	-	-	-	-	-	-	-	-
T 1	0.1151	-	0.1568	-	-0.0255	0.0177	-	-0.1200
T 2	-	-	0.1359	0.0059	-	0.1907	-	-
T 3	-	-	-	-	-	-	-	0.1494
T 4	-	-	-	-	-	-	-	-
T 5	-	-	-	-	-	-	-	-
T 6	-	-	-	-	-	-	-	-
T 7	-	-0.0011	0.0157	-	-	-	0.0082	-
T 8	-	-0.0006	0.0095	0.0005	-	-	0.0146	-
T 9	-	-	0.0076	-	-	-0.0002	-	-
T 10	-0.0181	-	-0.0419	-	-	-0.0124	-0.0771	-
T 11	-	-	-	-	-	0.1014	-	-
T 12	-0.0069	-	-	-0.0003	-0.0094	-	-0.0092	-

T 13	-0.0050	-	-	-	0.0135	0.0027	-	0.0156
T 14	-	-	0.0257	-	-	0.0043	0.0341	-
T 15	-	-	-	-	-0.0235	-	-	-
T 16	-	-	-	-	-	-	-	-
T 17	-	-	-	-	-	-	-	-
T 18	-	-	-	-	-	-	0.0121	0.0010
T 19	-	-0.0004	0.0132	0.0009	-	0.0025	0.0112	-
T 20	-0.0045	-	-0.0137	-0.0007	-	-0.0024	-0.0230	-
T 21	-	-	-	-	-	-	-	-
T 22	-	-	-	-	-	-	-	-
T 23	-	-	-	-	-	-	-	-
T 24	-	-	-	-	-	-	-	-0.0020
T 25	-	-	-	-	-	-	-	-
T 26	-	-	-	-	-	-	-	-
T 27	-	-	-	-	-	-	-	-
T 28	-	-	-	-	-	-	-	-
T 29	-	-	-	-	-	-	-	-
T 30	-	-	-	-	-	-	-	-

Appendix C: $Pd_{70}Cu_{26}M_4$ Cluster Expansion Models

In this section we list the cluster expansion model coefficients for the models used to describe interstitial H in $Pd_{74}Cu_{26}$, $Pd_{70}Cu_{30}$, and $Pd_{70}Cu_{26}M_4$ (M = Au, Ag, Pt, and Ni) alloys, described in Chapter 4.

Table C.1: O site CE coefficients for the $Pd_{70}Cu_{26}Au_4$ and $Pd_{70}Cu_{26}Ag_4$ alloys. Parameters identified by numbers from 1 through 20 are described in detail in Table A.1. Coefficients for the CE model for E_b are listed separately from the coefficients of the ZPE for each individual alloy. All coefficients have units of eV.

	$Pd_{70}Cu_{26}Au_4$		$Pd_{70}Cu_{26}Ag_4$	
	E_b	ZPE	E_b	ZPE
E_o	-0.0956	-0.3524	0.5770	0.0359
1	-	-0.1354	0.1829	-0.0061
2	-	-	0.0454	-
3	-	0.1513	-0.1553	0.0209
4	-	-	-0.0687	-
5	0.7191	1.6650	-	0.3829
6	0.9169	-0.0819	-	-0.1004
7	-	-	0.0113	-
8	-	-0.0080	-	-0.0084
9	0.0126	0.0016	-	0.0016
10	-	-	0.0118	-
11	-	-	-	-
12	-0.0051	-	-0.0042	-
13	0.0062	-0.0014	0.0144	-0.0012
14	-	-	-0.0034	-
15	-	-	0.0046	-
16	-0.0105	-	-	-
17	-	0.0083	-	-0.0072
18	0.0091	-	-	-
19	0.6033	-	0.5885	-
20	-	-0.0192	-	-

Table C.2: O site CE coefficients for the $Pd_{70}Cu_{26}Pt_4$, $Pd_{70}Cu_{26}Ni_4$, $Pd_{74}Cu_{26}$, and $Pd_{70}Cu_{30}$ alloys. Parameters identified by numbers from 1 through 20 are described in detail in Table A.1. Coefficients for the CE model for E_b are listed separately from the coefficients of the ZPE for each individual alloy. All coefficients have units of eV.

	$Pd_{70}Cu_{26}Pt_4$		$Pd_{70}Cu_{26}Ni_4$		$Pd_{74}Cu_{26}$		$Pd_{70}Cu_{30}$	
	E_b	ZPE	E_b	ZPE	E_b	ZPE	E_b	ZPE
E_o	0.8625	0.0548	-0.3326	0.3285	-0.0318	-0.3016	0.0715	0.1464
1	0.3227	-	-0.1052	0.0890	-	-0.3761	0.0533	0.0195
2	-	-	-0.0278	-	-	0.2778	-	-
3	-0.2975	0.0182	0.0966	-0.0730	-	0.3928	-	-
4	-	-	-	-	-0.0494	-0.2749	-	-
5	-1.0163	-	-	-0.6242	-	-	-	-
6	1.0619	-	-	0.0520	-	-	-	-
7	0.0100	-	-	-	-	-	0.0203	-
8	-	-0.0052	-0.0119	-0.0045	-0.0156	-0.0115	-0.0185	-0.0114
9	0.0086	-	0.0072	-	-	-	0.0096	-
10	0.0125	0.0018	-	-	-	-0.0029	-	-0.0063
11	-	-	-	0.0019	-	-	-	0.0052
12	-0.0022	-	-0.0069	-	-0.0048	-	-	-
13	0.0156	-0.0020	0.0125	-0.0015	-	-	0.0120	-
14	-	-	-	-	-	-	-	-
15	0.0063	-	0.0055	-	-	-	-	-
16	-	-	-	-	-	-	-	0.0022
17	-	-0.0063	-	-	-	-	-	-
18	-	-	-	-	-	-	-	-
19	0.4737	-	-	-	-	-	-	-
20	-	-	0.0144	-0.0072	-	-	-	-

Table C.3: T site CE coefficients for the $Pd_{70}Cu_{26}Au_4$ and $Pd_{70}Cu_{26}Ag_4$ alloys. Parameters identified by numbers from 1 through 30 are described in detail in Table A.2. Coefficients for the CE model for E_b are listed separately from the coefficients of the ZPE for each individual alloy. All coefficients have units of eV.

	$Pd_{70}Cu_{26}Au_4$		$Pd_{70}Cu_{26}Ag_4$	
	E_b	ZPE	E_b	ZPE
E_o	-0.6927	0.2039	-0.7870	0.0515
1	-	-0.0086	-	-0.0832
2	-0.0522	-	-0.0639	-
3	-	-	-0.0021	0.0745
4	-	-0.0033	-	-0.0032
5	4.3617	-	3.0674	-
6	0.6058	-	0.4500	-
7	-	-0.0019	0.0055	-0.0021
8	-	-	-	-
9	-0.0004	-	-	-
10	-	-0.0008	-	-0.0007
11	-	-0.0004	-	-0.0005
12	-	-	-	-
13	-	-0.0005	-	-0.0005
14	-0.0036	-0.0011	-0.0080	-0.0010
15	-0.2099	0.0028	-0.2306	0.0015
16	0.1173	-0.0170	0.1405	-0.0160
17	2.5882	-	2.8565	-
18	-0.0128	-0.0012	-0.0099	-0.0012
19	-0.0072	-0.0005	-0.0070	-0.0005
20	0.0029	-0.0004	0.0030	-0.0005
21	-	-	-	-
22	-	-	-	-
23	-	-	-	-
24	-	-0.0005	-	-0.0007
25	-	-0.0004	-	-0.0004
26	0.0094	0.0003	0.0094	0.0004
27	0.0060	0.0003	0.0065	0.0002
28	0.0005	-	0.0025	-
29	-	-0.0008	-	-0.0008
30	0.0041	0.0001	0.0015	0.0001

Table C.4: T site CE coefficients for the $Pd_{70}Cu_{26}Pt_4$, $Pd_{70}Cu_{26}Ni_4$, $Pd_{74}Cu_{26}$, and $Pd_{70}Cu_{30}$ alloys. Parameters identified by numbers from 1 through 30 are described in detail in Table A.2. Coefficients for the CE model for E_b are listed separately from the coefficients of the ZPE for each individual alloy. All coefficients have units of eV.

	$Pd_{70}Cu_{26}Pt_4$		$Pd_{70}Cu_{26}Ni_4$		$Pd_{74}Cu_{26}$		$Pd_{70}Cu_{30}$	
	E_b	ZPE	E_b	ZPE	E_b	ZPE	E_b	ZPE
E_o	-0.3608	0.1957	-0.1746	0.1575	-0.4827	-0.2978	-0.1882	0.1630
1	-	-	-	-0.0131	-	-0.0097	0.0488	-0.0076
2	-0.0647	-	-0.0503	-	-0.1021	-0.0045	-0.0490	0.0014
3	-0.0074	-0.0161	-	0.0085	-	-	-	-
4	-	-	-	-0.0033	-	-	-	-
5	1.7606	-	-1.4918	-	-	-	-	-
6	0.8690	-	0.6391	-	-	-	-	-
7	0.0052	-	-	-	0.0108	-0.0020	0.0200	-0.0010
8	-	-	-0.0080	0.0005	-0.0069	-	-	0.0002
9	-	-	-	-	-	-0.0001	-	0.0004
10	-	-	-	-	-	-0.0006	-0.0074	-
11	-	-	-	-0.0014	-0.0112	-0.0011	-	-
12	-	-0.0006	-	0.0007	-	-	-	-
13	-	-0.0028	-	-0.0006	-0.0100	-0.0009	-	-0.0006
14	-0.0100	-	-0.0081	-0.0009	-0.0069	-0.0013	-	-0.0013
15	-0.0914	-	-0.0781	-0.0106	-0.1018	-0.1584	-0.0924	-0.0118
16	0.0021	-	-	-0.0050	-	0.1451	-	-
17	0.7527	-	0.5518	-	-	-	-	-
18	-0.0089	-	-0.0088	-0.0008	-0.0083	-0.0006	-0.0102	-0.0011
19	-0.0069	0.0012	-0.0092	-0.0007	-0.0061	-0.0004	-0.0087	-0.0004
20	0.0019	0.0021	-	-0.0010	-0.0059	-0.0005	-0.0034	-
21	-	-	0.0211	-	-	-	-	-
22	-	-	-	-	-	-	-	-
23	-	-	-	-	-	-	-	-
24	-	0.0018	-	-	-	-0.0007	-	-
25	-	0.0042	-	-	-	-0.0003	-	-
26	0.0096	-	-	0.0007	-	0.0003	0.0032	-
27	0.0061	-	0.0052	0.0006	0.0033	0.0002	-	0.0001
28	0.0018	-	0.0049	0.0001	-	-	-	-
29	-	-	-	-	-	-	-0.0046	-0.0009
30	0.0021	-	-	-	-	-	-0.0032	-

Table C.5: TS CE coefficients for the $Pd_{70}Cu_{26}Au_4$ and $Pd_{70}Cu_{26}Ag_4$ alloys. O site parameter contributions identified as O 1- O 20 and T site parameter contribution identified as T 1 – T 30 as described in Table A.1 and Table A.2. Coefficients for the CE model for E_b are listed separately from the coefficients of the ZPE for each individual alloy. All coefficients have units of eV.

	$Pd_{70}Cu_{26}Au_4$		$Pd_{70}Cu_{26}Ag_4$	
	E_b	ZPE	E_b	ZPE
E_o	0.3842	0.1711	2.3716	0.1806
O 1	0.0592	-0.0037	1.1895	-
O 2	-	-	-	-
O 3	-0.0418	-	-1.1854	-0.0104
O 4	-	-	-	-
O 5	-	-	-11.9088	-
O 6	-	-	0.0376	-
O 7	-	-	-	-
O 8	-	-	-	-
O 9	0.0083	-	0.0049	-0.0032
O 10	-	-0.0053	0.0031	-
O 11	-	-	-	-
O 12	-0.0075	-	-0.0037	-
O 13	-	-	-	-
O 14	-	-	-	-
O 15	-	-	-	-
O 16	-	-	-	-
O 17	-	-	-	-
O 18	-	-	-0.0066	-
O 19	-	-	0.2836	-
O 20	0.0110	-	-	-
T 1	-	-	-	-0.0081
T 2	0.0125	-	-0.0496	-
T 3	-	-0.0112	-	-
T 4	-	-	-	-
T 5	5.8716	-	5.1005	-
T 6	-	-	0.4181	-
T 7	-0.0055	-	-	-
T 8	-	-	-	-
T 9	0.0076	-	0.0040	-
T 10	-	-	-	-
T 11	-	-	-	-
T 12	-	0.0032	-	-

T 13	-	-	-	-
T 14	-	-0.0047	-0.0056	-
T 15	-	-	-0.4258	-
T 16	-	-0.0120	0.3382	-0.0181
T 17	-	-	4.7262	-
T 18	-	-	-0.0090	-0.0035
T 19	-	-	-0.0057	-
T 20	-	-	-	-
T 21	-	-	-	-
T 22	-	-	-	-
T 23	-	-	-	-
T 24	-	-	-	-
T 25	-	0.0034	-	-
T 26	-	-	0.0097	-
T 27	-	-	0.0041	-
T 28	0.0097	-	0.0025	-
T 29	-	-	-	-0.0040
T 30	-	-	-	-

Table C.6: TS CE coefficients for the $Pd_{70}Cu_{26}Pt_4$, $Pd_{70}Cu_{26}Ni_4$, $Pd_{74}Cu_{26}$, and $Pd_{70}Cu_{30}$ alloys. O site parameter contributions identified as O 1- O 20 and T site parameter contribution identified as T 1 – T 30 as described in Table A.1 and Table A.2. Coefficients for the CE model for E_b are listed separately from the coefficients of the ZPE for each individual alloy. All coefficients have units of eV.

	$Pd_{70}Cu_{26}Pt_4$		$Pd_{70}Cu_{26}Ni_4$		$Pd_{74}Cu_{26}$		$Pd_{70}Cu_{30}$	
	E_b	ZPE	E_b	ZPE	E_b	ZPE	E_b	ZPE
E_o	0.7124	0.1703	-0.1150	0.1368	2.9645	1.9832	0.0748	0.1052
O 1	0.0365	-	0.0311	-	0.0272	0.1765	0.0441	0.0082
O 2	-	-	-	0.0055	-	-	-	-
O 3	-0.0301	-	-0.0308	-	-	-0.1765	-	-
O 4	-	-	-	-	-	-	-	-
O 5	-	-	-	-	-	-	-	-
O 6	-	-	-	-	-	-	-	-
O 7	-	-	-	-	-	-	0.0116	-
O 8	-	0.0039	-	0.0047	-	-	-0.0202	0.0126
O 9	-	-	0.0068	-	-0.0026	-	-	-0.0028
O 10	-	-0.0032	-	-	-	-	-0.0160	-
O 11	-	-	-	-	0.0093	-	0.0122	-0.0137
O 12	-0.0050	-	-0.0017	-	-	0.0010	-	-
O 13	-	-0.0009	-	-	-	-	0.0075	-
O 14	-	-	-	-	-	-	-	-
O 15	-	-	-	-	0.0040	-	-	-
O 16	-	-	-	-	0.0083	-	0.0058	0.0036
O 17	-	-	-	-	-0.0077	0.2050	-	-
O 18	-	-	-	-	-	-0.2116	-	-
O 19	-	-	-	-	-	-	-	-
O 20	-	-0.0040	-0.0246	-0.0050	-	-	-	-
T 1	0.1138	-	-	-	-	-	0.0427	-0.0225
T 2	0.0223	-	-0.0392	-	-	-	-0.0443	-0.0071
T 3	-0.1079	-0.0174	-	-	-	-0.0299	-	-
T 4	-0.1078	-	-	-	-0.0746	-0.0168	-	-
T 5	-	-	0.4960	-	-	-	-	-
T 6	-	-	-	-	-	-	-	-
T 7	0.0077	-	0.0064	0.0031	0.0100	-	0.0197	-
T 8	-0.0058	-	-	-	-0.0072	-	-	-
T 9	-	-	0.0056	-0.0019	-	-	-	-
T 10	-	-	-	-	-	-	-0.0104	-
T 11	-	-	-	-	-	-0.0057	-	-
T 12	-	-	-	-	-	-	-	-

T 13	-	-	-	-	-0.0151	-	-	-0.0043
T 14	-0.0109	-0.0020	-	-	-	-0.0052	-	-
T 15	-0.0189	-	-0.0878	-0.0098	0.8850	-	-0.0749	-0.0147
T 16	-0.0804	-0.0114	-	-	-0.9465	-0.0159	-	-
T 17	-	-	0.1576	0.0900	-	-	-	-
T 18	-0.0094	-	-0.0052	-	-	-	-0.0093	-
T 19	-0.0081	-	-0.0040	-	-0.0039	-	-0.0061	-
T 20	-	-	-	-	-	-	-	-
T 21	-	-	-	-	-	-	-	-
T 22	-	-	-	-	-	-	-	-
T 23	-	-	-	-	-	-	-	-
T 24	-	0.0025	-	-	-	0.0036	-	-
T 25	-	-	-	-	-	-	-	-
T 26	0.0087	-	0.0124	-	-	-	-	0.0031
T 27	0.0031	-	-	-	-	-	-	-0.0020
T 28	0.0025	-	0.0038	-0.0024	-	-	-	-
T 29	-	-	-	-	-	-	-0.0065	-
T 30	-	-	-	-	-	0.0016	-0.0038	-

Appendix D: Heuristic Lattice Model H Macroscopic Property Predictions

In this section we plot the H solubility, diffusion, and permeability predictions from the heuristic lattice model described in Chapter 5 for a series of Pd-based binary alloys with composition $Pd_{100-x}M_x$ for $x = 4$, 11, 19, 26, 33, and 41 at.%. Each plot has a fixed alloy composition. Data is for T = 600 K.

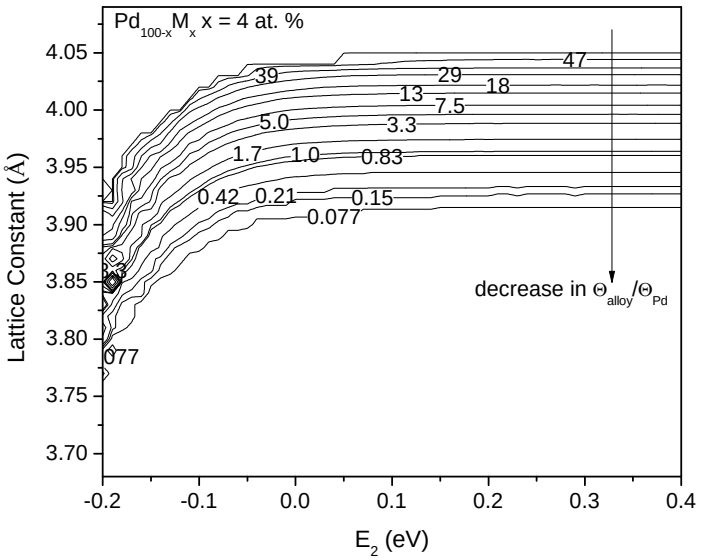

Figure D.1: Solubility predictions using heuristic lattice model for Pd-rich binary alloys with composition $Pd_{96}M_4$. The alloy solubility results have been normalized with respect to the hydrogen solubility of pure Pd, so the contours show values of $\Theta_{alloy}/\Theta_{Pd}$ at 600 K.

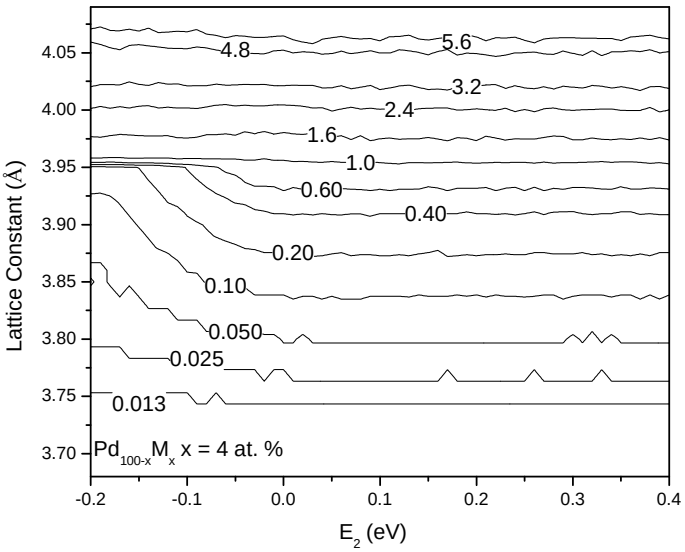

Figure D.2: Diffusion predictions using heuristic lattice model for Pd-rich binary alloys with composition $Pd_{96}M_4$. The alloy diffusion results have been normalized with respect to the hydrogen diffusion of pure Pd, so the contours show values of $D_{s,alloy}/D_{s,Pd}$ at 600 K.

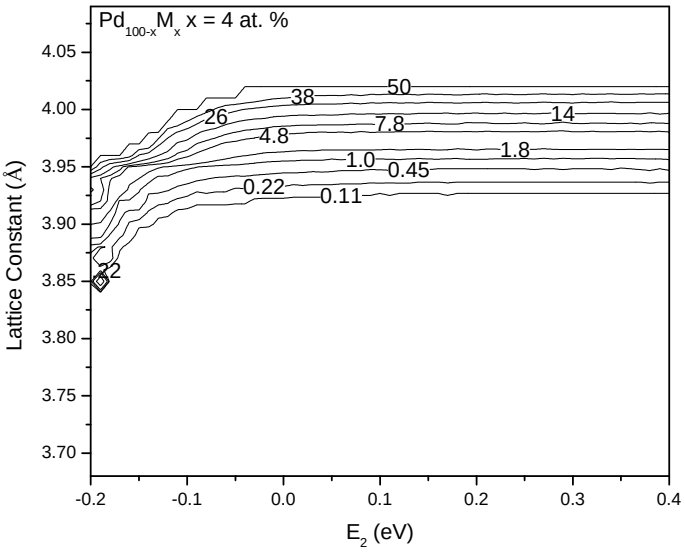

Figure D.3: Permeability predictions using heuristic lattice model for Pd-rich binary alloys with composition $Pd_{96}M_4$. The alloy permeability results have been normalized with respect to the hydrogen permeability of pure Pd, so the contours show values of k_{alloy}/k_{Pd} at 600 K.

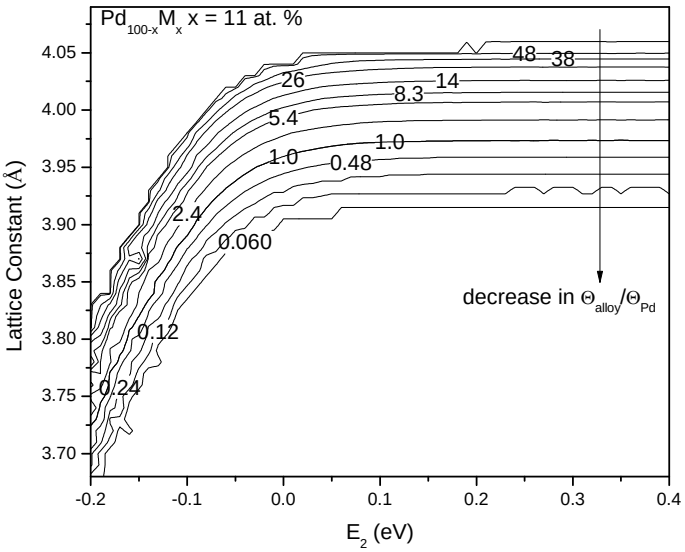

Figure D.4: Solubility predictions using heuristic lattice model for Pd-based binary alloys with composition $Pd_{89}M_{11}$. The alloy solubility results have been normalized with respect to the hydrogen solubility of pure Pd, so the contours show values of $\Theta_{alloy}/\Theta_{Pd}$ at 600 K

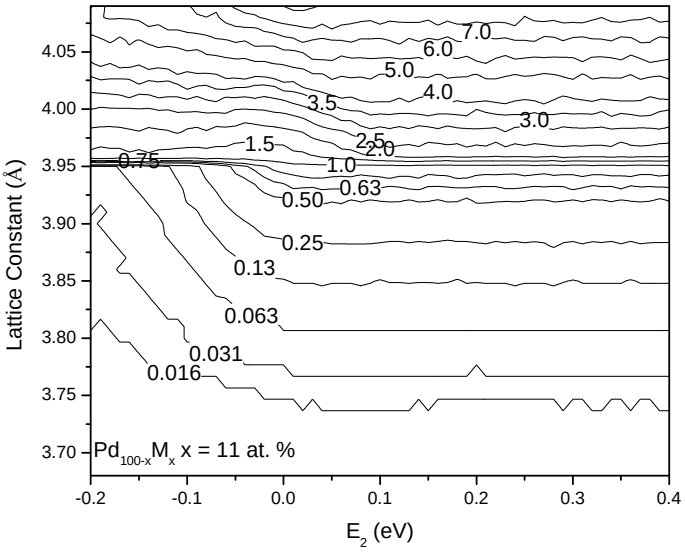

Figure D.5: Diffusion predictions using heuristic lattice model for Pd-based binary alloys with composition $Pd_{89}M_{11}$. The alloy diffusion results have been normalized with respect to the hydrogen diffusion of pure Pd, so the contours show values of $D_{s,alloy}/D_{s,Pd}$ at 600 K.

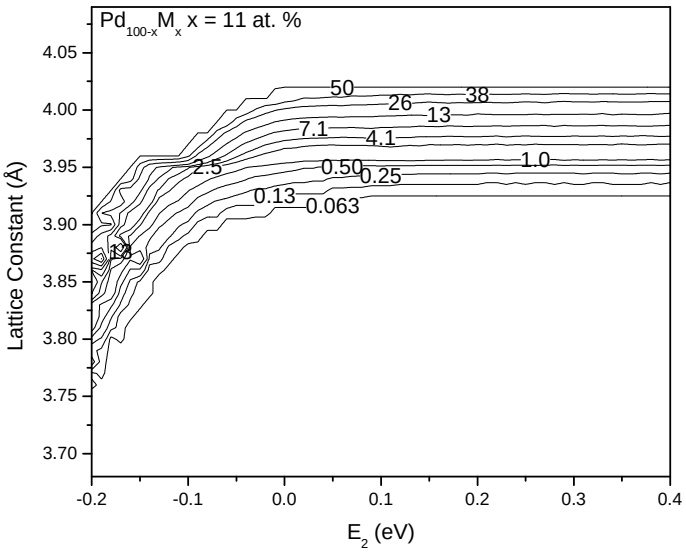

Figure D.6: Permeability predictions using heuristic lattice model for Pd-based binary alloys with composition $Pd_{89}M_{11}$. The alloy permeability results have been normalized with respect to the hydrogen permeability of pure Pd, so the contours show values of k_{alloy}/k_{Pd} at 600 K.

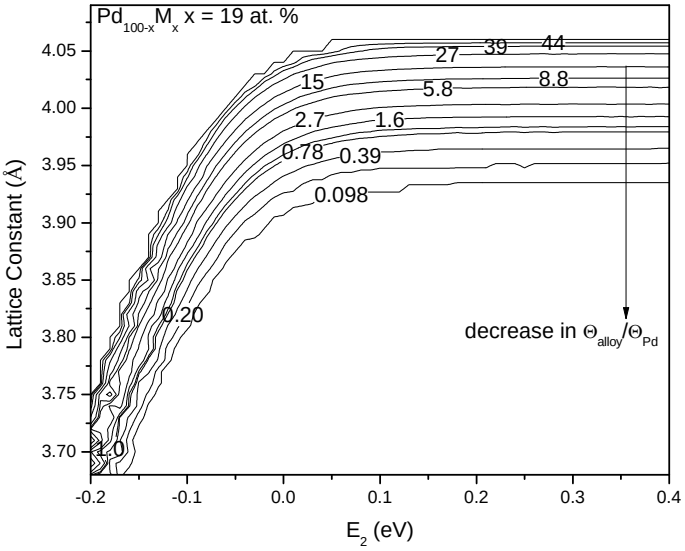

Figure D.7: Solubility predictions using heuristic lattice model for Pd-based binary alloys with composition $Pd_{81}M_{19}$. The alloy solubility results have been normalized with respect to the hydrogen solubility of pure Pd, so the contours show values of $\Theta_{alloy}/\Theta_{Pd}$ at 600 K.

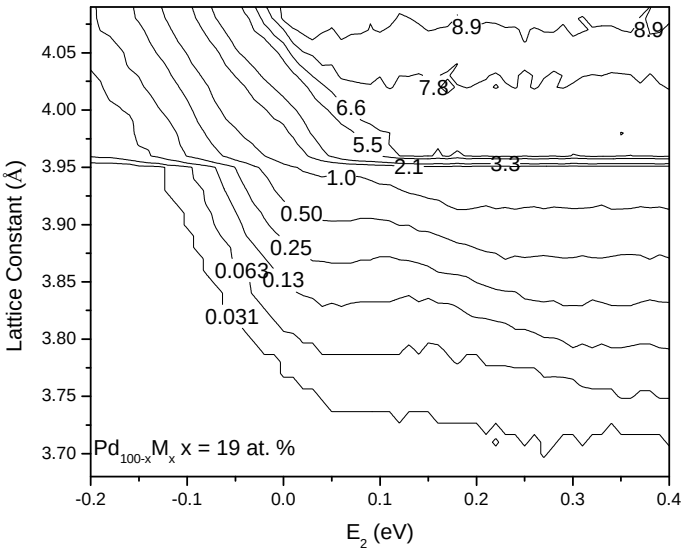

Figure D.8: Diffusion predictions using heuristic lattice model for Pd-based binary alloys with composition $Pd_{81}M_{19}$. The alloy diffusion results have been normalized with respect to the hydrogen diffusion of pure Pd, so the contours show values of $D_{s,alloy}/D_{s,Pd}$ at 600 K.

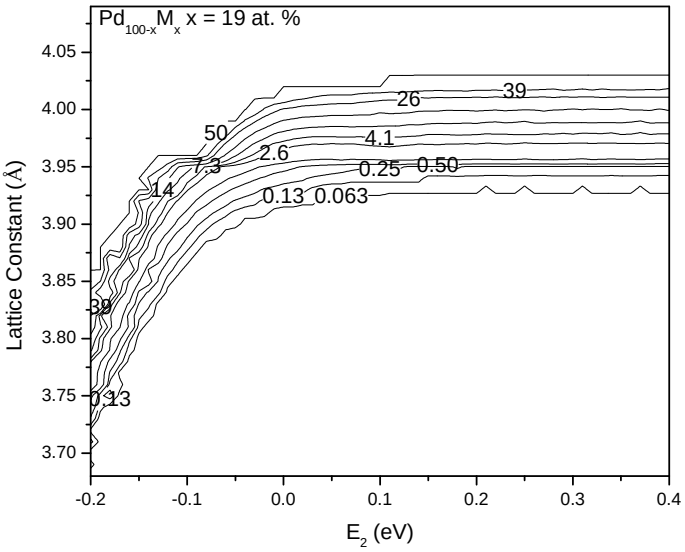

Figure D.9: Permeability predictions using heuristic lattice model for Pd-based binary alloys with composition $Pd_{81}M_{19}$. The alloy permeability results have been normalized with respect to the hydrogen permeability of pure Pd, so the contours show values of k_{alloy}/k_{Pd} at 600 K.

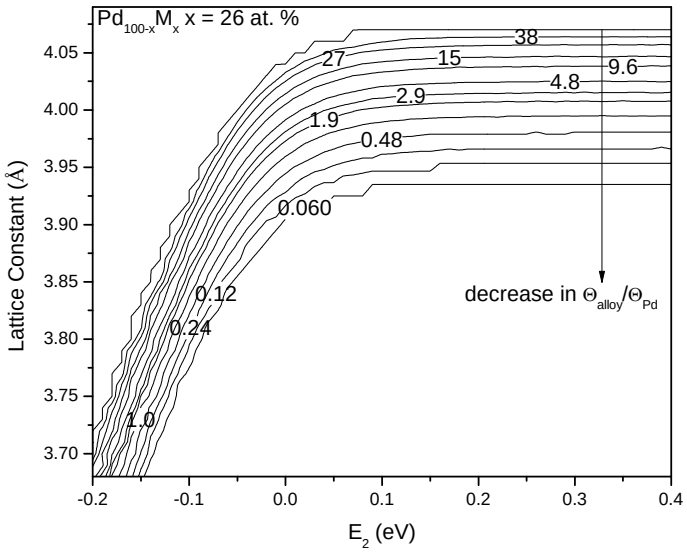

Figure D.10: Solubility predictions using heuristic lattice model for Pd-based binary alloys with composition $Pd_{74}M_{26}$. The alloy solubility results have been normalized with respect to the hydrogen solubility of pure Pd, so the contours show values of $\Theta_{alloy}/\Theta_{Pd}$ at 600 K.

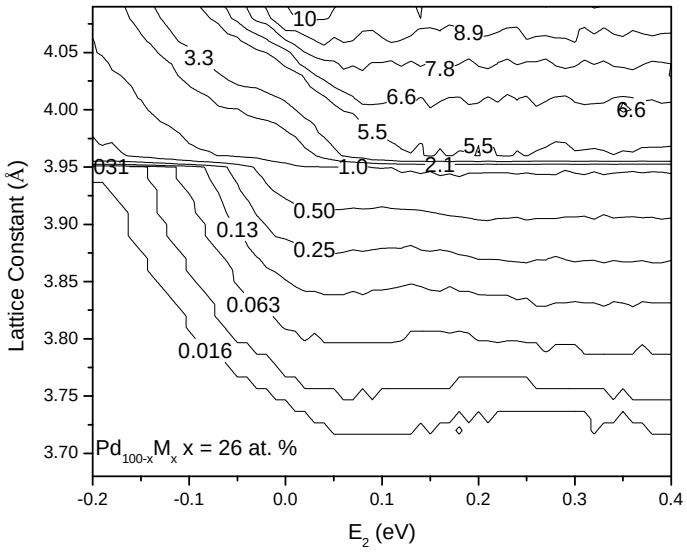

Figure D.11: Diffusion predictions using heuristic lattice model for Pd-based binary alloys with composition $Pd_{74}M_{26}$. The alloy diffusion results have been normalized with respect to the hydrogen diffusion of pure Pd, so the contours show values of $D_{s,alloy}/D_{s,Pd}$ at 600 K.

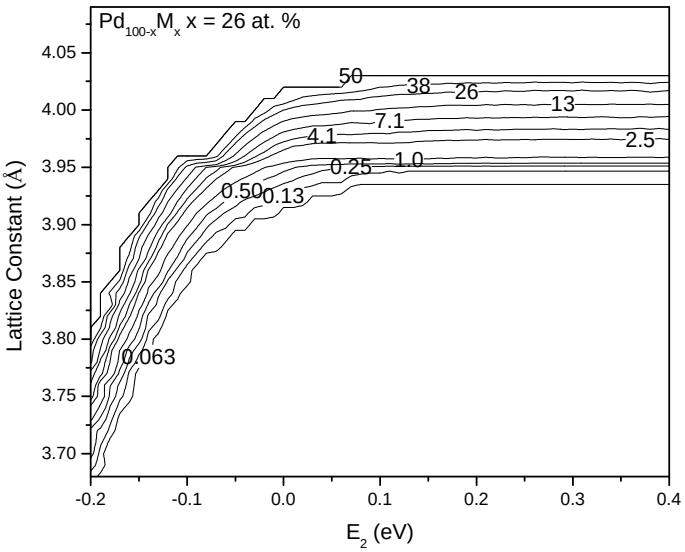

Figure D.12: Permeability predictions using heuristic lattice model for Pd-based binary alloys with composition $Pd_{74}M_{26}$. The alloy permeability results have been normalized with respect to the hydrogen permeability of pure Pd, so the contours show values of k_{alloy}/k_{Pd} at 600 K.

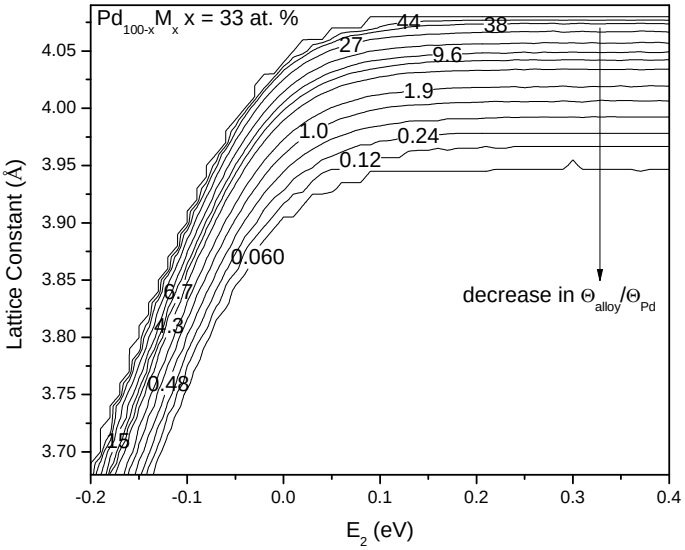

Figure D.13: Solubility predictions using heuristic lattice model for Pd-based binary alloys with composition $Pd_{67}M_{33}$. The alloy solubility results have been normalized with respect to the hydrogen solubility of pure Pd, so the contours show values of $\Theta_{alloy}/\Theta_{Pd}$ at 600 K.

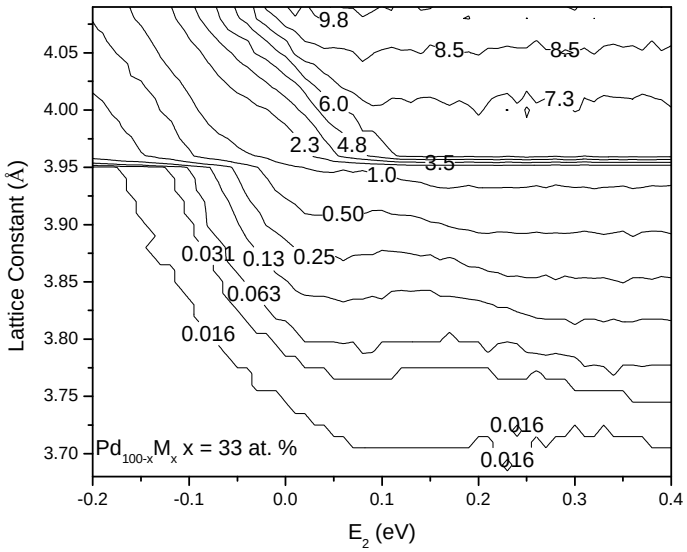

Figure D.14: Diffusion predictions using heuristic lattice model for Pd-based binary alloys with composition $Pd_{67}M_{33}$. The alloy diffusion results have been normalized with respect to the hydrogen diffusion of pure Pd, so the contours show values of $D_{s,alloy}/D_{s,Pd}$ at 600 K.

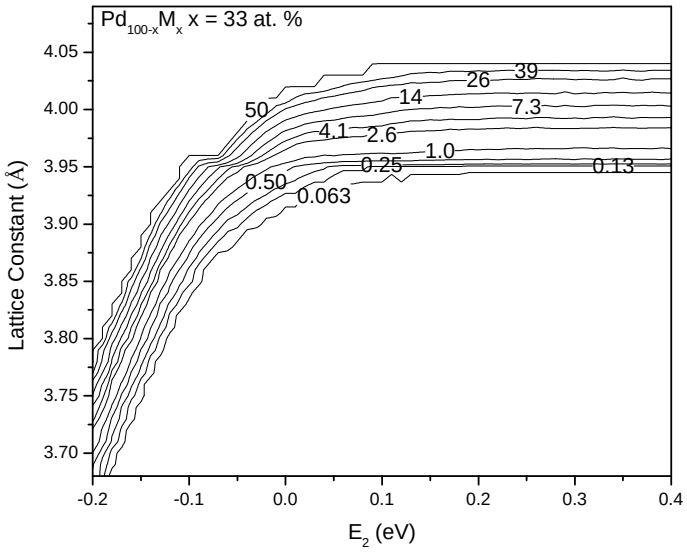

Figure D.15: Permeability predictions using heuristic lattice model for Pd-based binary alloys with composition $Pd_{67}M_{33}$. The alloy permeability results have been normalized with respect to the hydrogen permeability of pure Pd, so the contours show values of k_{alloy}/k_{Pd} at 600 K.

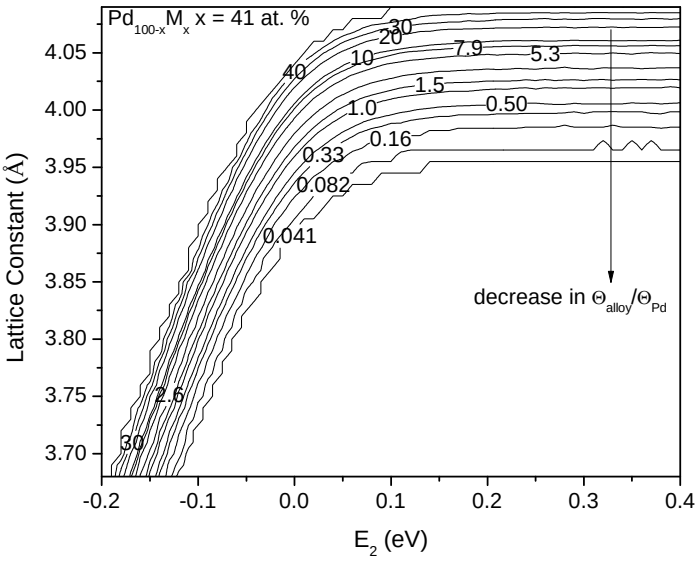

Figure D.16: Solubility predictions using heuristic lattice model for Pd-based binary alloys with composition $Pd_{59}M_{41}$. The alloy solubility results have been normalized with respect to the hydrogen solubility of pure Pd, so the contours show values of $\Theta_{alloy}/\Theta_{Pd}$ at 600 K.

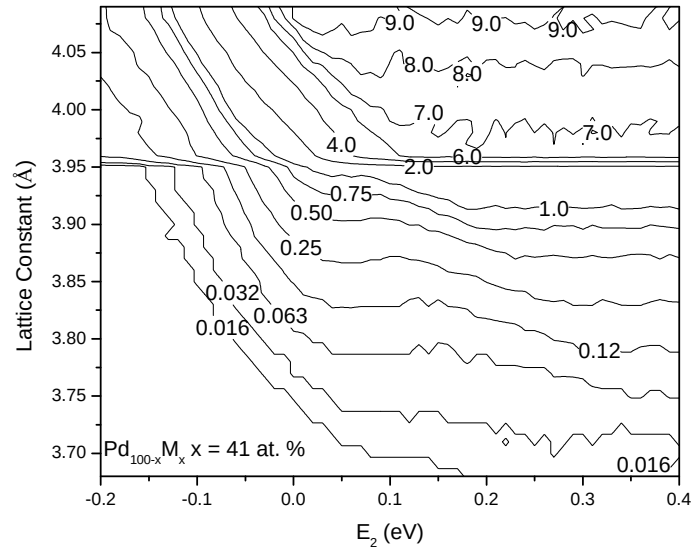

Figure D.17: Diffusion predictions using heuristic lattice model for Pd-based binary alloys with composition $Pd_{59}M_{41}$. The alloy diffusion results have been normalized with respect to the hydrogen diffusion of pure Pd, so the contours show values of $D_{s,alloy}/D_{s,Pd}$ at 600 K.

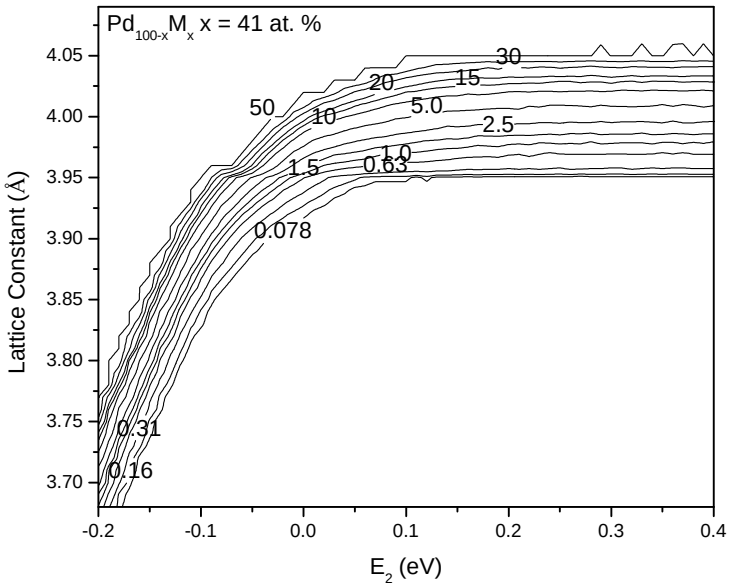

Figure D.18: Permeability predictions using heuristic lattice model for Pd-based binary alloys with composition $Pd_{59}M_{41}$. The alloy permeability results have been normalized with respect to the hydrogen permeability of pure Pd, so the contours show values of k_{alloy}/k_{Pd} at 600 K.